DOE/ER-0046/19

Damage Analysis and Fundamental Studies

Quarterly Progress Report
July-September 1984

November 1984

U.S. Department of Energy
Office of Energy Research
Office of Fusion Energy
Washington, DC 20545

NOTICE

Printed in the United States of America
Available from
National Technical Information Service
U.S. Department of Commerce
5285 Port Royal Road
Springfield, VA 22161

NTIS price codes
Printed copy: A09
Microfiche copy: A01

DOE/ER-0046/19
UC-20,20c

Damage Analysis and Fundamental Studies

Quarterly Progress Report
July-September 1984

November 1984

U.S. Department of Energy
Office of Energy Research
Office of Fusion Energy
Washington, DC 20545
B&R No. AT-15-02-03-04

FOREWORD

This report is the twenty-seventh in a series of Quarterly Technical Progress Reports on ***Damage Analysis and Fundamental Studies*** (OAFS), which is one element of the Fusion Reactor Materials Program, conducted in support of the Magnetic Fusion Energy Program of the U.S. Department of Energy (DOE). The first eight reports in this series were numbered DOE/ET-0065/1 through 8. Other elements of the Fusion Materials Program are:

- Alloy Development for Irradiation Performance (ADIP)
- Plasma-Materials Interaction (PMI)
- Special Purpose Materials (SPM).

The OAFS program element is a national effort composed of contributions from a number of National Laboratories and other government laboratories, universities, and industrial laboratories. It was organized by the Materials and Radiation Effects Branch, DOE/Office of Fusion Energy, and a Task Group on ***Damage Analysis and Fundamental Studies,*** which operates under the auspices of that branch. The purpose of this series of reports is to provide a working technical record of that effort for the use of the program participants, the fusion energy program in general, and the OOE.

This report is organized along topical lines in parallel to a Program Plan of the same title so that activities and accomplishments may be followed readily, relative to that Program Plan. Thus, the work of a given laboratory may appear throughout the report. A chapter has been added on Reduced Activation Materials to accommodate work on a topic not included in the early proqram plan. The Contents is annotated for the convenience of the reader.

This report has been compiled and edited under the guidance of the Chairman of the Task Group on ***Damage Analysis and Fundamental Studies, 0.*** G. Ooran, Hanford Engineering Development Laboratory (HEOL). His efforts, those of the supporting staff of HEOL, and the many persons who made technical contributions are gratefully acknowledged. T. C. Reuther, Fusion Technologies Branch, is the DOE counterpart to the Task Group Chairman and has responsibility for the DAFS program within DOE.

G. M. Haas, Chief
Fusion Technologies Branch
Office of Fusion Energy

CONTENTS

CHAPTER 1

IRRADIATION TEST FACILITIES

RTNS-II IRRADIATIONS AND OPERATIONS

C.M. Logan and D. W. Heikkinen
Lawrence Livermore National Laboratory

1.0 Objective

The objectives of this work are operation of RTNS-II (a 14-MeV neutron source facility). machine development, and support of the experimtal program that utilizes this facility. Experimenter services include dosimetry, handling, scheduling, coordination, and reporting. RTNS-II is supported jointly by the U.S. and Japan and is dedicated to mterials research for the fusion power program. Its primary use is to aid in the development of models of high-energy neutron effects. Such models are needed in interpreting and projecting to the fusion environment, engineering data obtained in other spectra.

2.0 Summary

Nine different experiments were irradiated during this quarter. Ion Source development work continues. An accelerator electrode water leak caused a major outage. The right target came off after a power outage. A new materials testing lab is now in use.

3.0 Program

Title: RTNS-II Operations (WZJ-16)
Principal Investigator: C. M. Logan
Affiliation: Lawrence Livermore National Laboratory

4.0 Relevant DAFS Program Plan Task/Subtask

TASK II,A,2,3,4,
TASK II,B,3,4
TASK II,C,1,2,6,11,18,

5.0 Irradiation - C. M. Logan, D. W. Heikkinen and N. W. Quinan

During this quarter, irradiations (both dedicated and add-on) were done for the following people.

Experimenter	P or A*	Sample Irradiated
R. Smither (ANL)	A	Al - the $^{27}Al(n,2n)^{26}Al$ cross section near threshold
D. Heikkinen (LLNL)	A	Nb - dosimetry calibration
H. Heinisch (HEDL) H. Matsui (Tohoku) N. Yoshida (Kyushu) M. Kiritani (Hokkaido) H. Takahashi (Hokkaido) K. Abe (Tohoku) S. Ishino (Tokyo) Y. Shimamura (Hiroshima) E. Kuramoto (Kyushu)	P	Metals - microstructure and mechanical properties at 90°C and 290°C

Experimenter	P or A*	Sample Irradiated
H. Kawamura (TiT)	A	$Pd_{80}Si_{20}$ - property changes
H. Matsui (Tohoku) and M. Guinan (LLNL) M. Kiritani (Hokkaido) H. Takahashi (Hokkaido) H. Kayano (Tohoku) K. Abe (Tohoku) A. Kohyama (Tokyo) S. Nanao (Tokyo) H. Kawanishi (Tokyo) M. Iseki (Nagoya) Y. Shimamura (Hiroshima) N. Yoshida (Kyushu) E. Kuramoto (Kyushu)	P	Metals - low temperature experiment - microstructure and mechanical properties
R. Jalbert (LANL)	A	Measurement of HT and HTO in activated air
P. Cannon (HEDL) C. Snead (BNL) R. Flukiger (Karlsruhe) M. Guinan (LLNL)	P	FMIT - instrumentation Nb_3Sn-Ti mo-filaments and Nb_3Sn multi-filaments, critical field, current and temperature
L. Lucht (LLNL)	A	Oil shale tracer transport in fluidized bed
P. Pawlikowski (LLNL) G. Coleman (LLNL)	P	(n,2n) cross section

*P - primary, A = Add-on

5.1 RTNS-II Stat - M. Logan and D. W. Heikkinen

Ion source system development continues on the right mchine.

General cleanup was concluded in July on all areas of the facility.

The right neutron source target came off after a power outage causing some damage.

A new terminal isolation-transformer was installed on the right mchine.

The new mterials lab testing has been occupied.

An accelerator column electrode developed a water leak and was the cause of a major unscheduled outage on the left neutron source in August.

6.0 Future Work

Irradiations will be continued for R. Smither (ANL), P. Pawlikowski, G. Coleman (LLNL), D. Heikkinen (LLNL), H. Matsui (Tohoku)/M. Guinan (LLNL) et al., P. Cannon (HEDL), et al. Also during this period, irradiations for N. Yoshida (Kyushu) et al., R. Haight (LLNL), Y. Shimomura (Hiroshima) and C. Kinoshita (Kyushu) will be initiated.

A new bypass and filtering system will be installed on the target cooling water system. In addition, new turbo pump vacuum stations for the target rooms are scheduled for installation.

CHAPTER 2

DOSIMETRY AND DAMAGE PARAMETERS

FISSION REACTOR DOSIMETRY - HFIR - CTR40-45

L. R. Greenwood (Argonne National Laboratory)

1.0 Objective

To characterize neutron irradiation facilities in tens of neutron flux, spectra, and damage parameters (dpa, gas generation, transmutation) and to measure these exposure parameters during fusion materials irradiations.

2.0 Summary

Oosimetry measurements and damage calculations have been completed for the CTR40-45 irradiations in HFIR. Neutron fluence, dpa, and helium production values are reported. The status of all other experiments is summarized in Table I.

TABLE I

STATUS OF DOSIMETRY EXPERIMENTS

	Facility/Experiment	Status/Comments
ORR	- MFE 1	Completed 12/79
	- MFE 2	Completed 06/81
	- MFE 4A1	Completed 12/81
	- MFE 4A2	Completed 11/82
	- MFE 48	Completed 04/84
	- TBC 07	Completed 07/80
	- TRIO-Test	Completed 07/82
	- TRIO-1	Completed 12/83
	- Hf Test	Completed 03/84
	- JP Test	Samples Sent 06/84
HFIR	- CTR 32	Completed 04/82
	- CTR 31, 34. 35	Completed 04/83
	- T2, RB1	Completed 09/83
	- T1, CTR 39	Completed 01/84
	- CTR 40-45	Completed 09/84
	- RB2, RB3. T2	Irradiations in Progress
	- CTR 30, 46-52	Irradiations in Progress
	- JP 1-8	Irradiations in Progress
Omega West	- Spectral Analysis	Completed 10/80
	- HEDL1	Completed 05/81
	- HEDL2	Samples Sent 05/83
	- LANL 1	Completed 08/84
EBA II	- X287	Completed 09/81
IPNS	- Spectral Analysis	Completed 01/82
	- LANL1 (Hurley)	Completed 06/82
	- Hurley	Completed 02/83
	- Coltman	Completed 08/83

3.0 Program

Title: Oosimetry and Damage Analysis
Principal Investigator: L. R. Greenwood
Affiliation: Argonne National Laboratory

4.0 Relevant DAFS Program Plan Task/Subtask

Task II.A.1 Fission Reactor Dosimetry

5.0 Accomplishments and Status

Dosimetry measurements and damage calculations have been completed for six irradiations labeled CTR40-45 in the peripheral target position (PTP) of HFIR. The exposure histories are, as follows:

Experiment	Dates	Exposure, MWD
40	7/18/82 to 12/12/82	13,172
41	8/10/82 to 1/5/83	13,208
42, 43	10/25/82 to 6/18/83	21,604
44, 45	1/30/82 to 5/27/83	10,655

Since the CTR40 and 41 exposures are nearly identical, we decided to report these results together. as we have done for the 42-43 and 44-45 data Sets. Detailed comparisons of activities between these subsets show no significant differences.

Dosimetry capsules were located at three different heights in the CTR40, 41, 44, and 45 irradiations and at five heights in the larger CTR42 and 43 experiments. All dosimetry capsules were nearly identical consisting of Co-Al, Fe, Ti, and Mn-Cu wires. Contrary to previous experience, many of the Ti dosimeters were severely degraded, possibly due to the long delay in receiving the dosimeters following the irradiation. The measured activation rates are listed in Table II. All activity rates have been corrected for burnup and the present results agree quite well with previous experiments in the PTP.[1,2,3]

TABLE II

ACTIVITY RATES MEASURED IN HFIR-PTP
(Values normalized to 100 MW, corrected for burnup)

	Activity Rate, atom/atom-s			
Height, cm	$^{59}Co(n,\gamma)$	$^{58}Fe(n,\gamma)$	$^{54}Fe(n,p)$	$^{55}Mn(n,2n)$
CTR40/41:	(10-8)	(10-9)	(10-11)	(10-13)
19.8	3.83	1.32	4.62	1.38
10.9	6.50	1.72	6.52	1.99
2.0	7.33	2.19	7.50	2.25
-2.4	7.40	2.00	7.24	2.21
-11.3	6.10	1.72	6.32	1.88
-20.2	4.35	1.18	4.30	1.29
CTR42/43:				
19.8	4.38	1.27	4.60	1.38
15.4	5.21	1.51	5.71	1.67
10.9	6.34	1.80	6.40	1.91
6.5	6.68	1.90	6.90	2.11
2.0	7.20	2.08	7.02	2.06
-6.9	6.86	1.97	6.65	1.99
-11.3	6.20	1.76	6.20	1.83
CTR44/45:				
19.8	4.46	1.20	4.22	1.35
10.9	6.44	1.79	6.56	1.90
2.0	7.29	1.98	7.28	2.20
-2.4	7.38	2.08	7.33	2.17
-11.3	6.17	1.72	6.24	1.88
-20.2	4.29	1.24	4.39	1.28

The activity rates in Table II are well-described by a quadratic polynomial using the same coefficients determined previously for the HFIR-PTP.[3] This polynomial, as described in Table III, was used to determine the maximum activities for each irradiation set. These maximum activities were then used to adjust the neutron flux spectrum with the STAY'SL computer code. Flux levels were found to also be in excellent agreement with previous experiments.[1,2,3]

Neutron fluences and damage calculations from SPECTER are listed in Table III. Using the polynomial at the top of Table III and the maximum values for the parameter a, one can easily determine the desired fluence. damage, or helium production for any specified height, z, in a given subassembly. For simplicity, the gradient is very nearly symnetric and the b term can usually be neglected.

TABLE III

NEUTRON FLUENCE AND OAMAGE PARAMETERS FOR HFIR-PTP
Values are listed at midplane; gradients are described by
$f = a(1+bz+cz^2)$ where $b = 1.95 \times 10^{-4}$ and $c = -9.75 \times 10^{-4}$

Energy	CTR40/41		CTR42/43		CTR44/45	
	Neutron Fluence, x 10^{22} n/cm^2:					
Total	5.87		9.45		4.72	
Thermal (<.5 eV)[a]	2.45		3.94		1.98	
0.5 eV - 0.1 MeV	1.89		3.04		1.52	
>.1 MeV	1.53		2.46		1.23	
	DPA	He	DPA	He	DPA	He
Al	20.2	9.86	32.3	15.7	16.1	7.87
Ti	12.8	6.58	20.5	10.5	10.3	5.25
V	14.4	0.33	23.0	0.53	11.5	0.26
Cr	12.7	2.27	20.3	3.61	10.1	1.81
Mn[b]	14.0	2.00	22.4	3.18	11.2	1.59
Fe	11.2	4.02	17.9	6.41	9.0	3.21
Co[b]	14.2	1.98	22.7	3.15	11.3	1.58
Ni[c] Fast	12.1	53.33	19.3	84.9	9.6	42.53
Ni[c] ^{59}Ni	8.0	4532	15.5	8789	5.7	3253
Ni[c] Total	20.1	4585	34.8	8874	15.3	3296
cu	10.9	3.58	17.5	5.72	8.7	2.86
Nb	10.8	0.73	17.3	1.17	8.7	0.59
Mo	8.1	--	12.9	--	6.4	--
316 ss[d]	12.6	599.0	20.5	1158.0	10.0	431.0

[a] The thermal fluence is equal to 1.15 times the 2200 m/s value

[b] Thermal self-shielding may lower damage rates

[c] See Table IV for nickel gradients

[d] 316 ss: Fe(0.645), Ni(0.13), Cr(0.18), Mn(0.019), Mo(0.026)

Helium production in nickel is not so easily determined due to the two-step thermal production from ^{58}Ni. These calculations are thus listed separately in Table IV along with the resultant extra damage (He/567) due to the energetic ^{56}Fe recoils.[4] These helium calculations were found to agree quite well with experimental measurements by Rockwell International, as reported in a recent publication.5

6.0 References

1. L. R. Greenwood, Fission Reactor Oosimetry - HFIR-CTR31, 32, 34, and 35, Damage Analysis and Fundamental Studies Quarterly Progress Report, DOE/ER-0046/13, pp. 17-26, May 1983.

2. L. R. Greenwood, Fission Reactor Oosimetry - HFIR-T2 and RB1, IBID, DOE/ER-0046/15, pp. 6-9, November 1983.

3. L. R. Greenwood, Fission Reactor Dosimetry - HFIR-T1 and CTR39, IBID, DOE/ER-0046/16, pp. 5-8, February 1984.

4. L. R. Greenwood, A New Calculation of Thermal Neutron Damage and Helium Production in Nickel, J. Nucl. Mater. 115, 137-142 (1983).

TABLE IV

NICKEL HELIUM AND DPA GRADIENTS FOR HFIR
(He(appm) and DPA include thermal and fast effects)

	CTR40-41		CTR42-43		CTR44-45	
Height, cm	He	DPA	He	DPA	He	DPA
0	4585	20.1	8874	34.8	3296	15.3
3	4532	19.9	8782	34.4	3255	15.1
6	4357	19.3	8483	33.4	3123	14.7
9	4070	18.3	7989	31.8	2908	14.0
12	3669	16.8	7290	29.3	2609	12.8
15	3170	15.0	6402	26.3	2239	11.4
18	2579	12.8	5321	22.6	1806	9.7
	1921	10.2	4077	18.2	1331	7.8
24	1242	7.5	2731	13.2	850	5.8

5. L. R. Greenwood, D. W. Kneff, R. P. Skowronski, and F. M. Mann, A Comparison of Measured and Calculated Helium Production in Nickel Using Newly Evaluated Neutron Cross Sections for ^{59}Ni, J. Nucl. Mater. 122, 1002-1010, (1984).

7.0 Future Work

Further irradiations are in progress in HFIR, as listed in Table I.

8.0 Publications

See references 4 and 5.

HELIUM GENERATION MEASUREMENTS FOR IRON FROM HFIR

D. W. Kneff, B. M. Oliver, and R. P. Skowronski (Rockwell International)

1.0 Objective

The objectives of this work are to apply helium accumulation neutron dosimetry to the measurement of neutron fluences and energy spectra in mixed-spectrum fission reactors utilized for fusion materials testing, and to measure helium generation rates of materials in these irradiation environments.

2.0 *Summary*

Helium generation measurements have been made for iron samples irradiated in the High Flux Isotopes Reactor (HFIR) experiments CTR31 and CTR32. Comparison of these spectrum-integrated results with helium predictions based on ENDF/B-V evaluated nuclear data files shows agreement to within 7%. This agreement indicates that the iron ENDF/B-V cross section, combined with the unfolded HFIR neutron spectrum, can be used with confidence in predicting helium generation in HFIR-irradiated iron.

3.0 Program

Title: Helium Generation in Fusion Reactor Materials
Principal Investigators: D. W. Kneff and H. Farrar IV
Affiliation: Rockwell International

4.0 Relevant DAFS Program Plan Task/Subtask

Task II.A.1	Fission Reactor Dosimetry
Task II.A.4	Gas Generation Rates
Subtask II.A.5.1	Helium Accumulation Monitor Development

5.0 Accomplishments and Status

Helium generation measurements have been performed for iron samples irradiated in HFIR as part of experiments CTR31 and CTR32. These measurements are part of a joint Rockwell-Argonne National Laboratory (ANL) program to measure total helium production rates over the range of fission reactor neutron spectra and fluences used for fusion materials testing, and to use the results to integrally test helium production cross section evaluations used in damage calculations. The present work extends the measurements previously reported for Ni, Fe, Ti, and Cu samples irradiated in the Oak Ridge Research Reactor (ORR) and the Experimental Breeder Reactor-11 (EBR-II),[1-3] and Ni samples from HFIR.[1]

The analyzed iron samples from HFIR were incorporated in the CTR31 and CTR32 experiments as bare wire segments for both helium accumulation and radiometric dosimetry measurements. The samples are listed in Column 2 of Table 1. The sample number identifies the ANL dosimetry capsule in which each wire sample was irradiated. After irradiation, the samples were radiometrically counted at ANL and then shipped to Rockwell for helium analysis.

At Rockwell, the irradiated materials were etched, to remove all possible surface effects of helium recoil, and then segmented and analyzed by high-sensitivity gas mass spectrometry[4] for their irradiation-generated helium concentrations. Multiple specimens were analyzed for each sample location, with good reproducibility. The absolute uncertainty in each helium analysis was ±1-2%. Selected samples were also

TABLE 1

HELIUM PRODUCTION MEASUREMENTS FOR IRON IRRADIATED IN HFIR

Experiment	Sample	Core Height[a] (cm)	4He Concentration Measured (appm)[b]	4He Concentration Calculated[c] (appm)[b]	Calculated / Measured
CTR31	Fe-1	+21.07	3.66	3.91	1.07
	Fe-3	+ 4.41	6.76	6.72	0.99
	Fe-5	-12.26	5.73	5.82	1.02
CTR32	Fe-3	+ 4.41	3.12	3.28	1.05

[a] Distance above core midplane
[b] Atomic parts per million (10^{-6} atom fraction)
[c] Based on calculations by L. R. Greenwood (Ref. 5) using ENDF/B-V

analyzed for ^3He, which is formed from the decay of tritium often found in reactor environments. The ^3He concentration in each case was measured to be less than 1 appb (10^{-9} atom fraction).

The measured helium concentrations for the irradiated iron samples are given in Column 4 of Table 1. For comparison, Column 5 gives the predicted helium concentrations in iron for these irradiation positions. The predictions are based on L. R. Greenwood's calculations at core midplane for each experiment, (5) using the helium production cross section evaluations from the ENDF/B-V Gas Production File. These calculated concentrations were adjusted for the samples' distances from core midplane using Greenwood's empirical expression for the effects of reactor gradients. (5)

Comparisons between the measured and predicted helium concentrations agree within 7%. with the predictions averaging about 3% higher than the measurements. This good agreement indicates that the iron ENDF/B-V cross section, combined with the unfolded HFIR neutron spectrum, can be used with confidence in predicting helium generation in HFIR-irradiated iron. However, the results show some inconsistency with results previously obtained for ORR and EBR-II. (2) For DRR experiment MFE4A2, the predictions were about 10% below the measurements; this may be due in part to the ~10% uncertainty in the shape of the ORR-MFE4A2 spectrum. For EBR-II the predictions were found to be -30% low, using iron cross sections from the ENDF/B-V General Purpose File, (2) and ~25% low when recalculated using the ENDF/B-V Gas Production File. (6) This inconsistency with the HFIR and ORR results may be associated with the different neutron spectrum shape.

6.0 References

1. D. W. Kneff, R. P. Skowronski, B. M. Oliver, and L. R. Greenwood, "A Comparison of Measured and Calculated Helium Production in Nickel for Fission Reactor Irradiations," in Damage Analysis and Fundamental Studies, Quarterly Progress Report July-September 1983, DOE/ER-0046/15, U.S. Department of Energy, 12 (1983).

2. B. M. Oliver, D. W. Kneff, and R. P. Skowronski, "Helium Generation Measurements for EBR-II and ORR," in Damage Analysis and Fundamental Studies, quarterly Progress Report January-March 1984, DOE/ER-0046/17, U.S. Department of Energy, 14 (1984).

3. B. M. Oliver, D. W. Kneff, and R. P. Skowronski, "Helium Generation Measurements for Ti and Cu from ORR," in Damage Analysis and Fundamental Studies, Quarterly Progress Report April-June 1984, DOE/ER-0046/18, U.S. Department of Energy, 18 (1984).

4. H. Farrar IV, W. N. McElroy, and E. P. Lippincott, "Helium Production Cross Section of Boron for Fast-Reactor Neutron Spectra," Nucl. Technol., 25, 305 (1975).

5. L. R. Greenwood, "Fission Reactor Dosimetry - HFIR - CTR 31, 32, 34, and 35," in Damage Analysis and Fundamental Studies, Quarterly Progress Report April-June 1983, DOE/ER-0046/14, U.S. Department of Energy, 9 (1983).

6. L. R. Greenwood, personal communication.

7.0 Future Work

Helium measurements and integral cross section testing are continuing, in a joint effort with ANL. Analyses are in progress for several samples of HFIR-irradiated Cu, Ti, and Nb, and ORR-irradiated Nb. New materials will be incorporated in future mixed-spectrum reactor irradiations. The goals of this work are the accurate prediction of helium generation in materials irradiation experiments and the further development of helium accumulation fluence monitors.

8.0 Publications

A paper entitled "Helium Production Crass Sections I: ^{4}He Production in Pure Elements, Isotopes, and Alloy Steels by 14.8-MeV Neutrons," by D. W. Kneff, B. M. Oliver, H. Farrar IV (Rockwell), L. R. Greenwood (ANL), and F. M. Mann (HEDL), has been submitted for publication in Nuclear Science and Engineering.

OISPLACEMENT AND HELIUM GENERATION RATES IN THE MATERIALS OPEN TEST ASSEMBLY OF THE FAST FLUX TEST FACILITY

R. L. Simons (Hanford Engineering Development Laboratory)

1.0 Objective

The objective of this effort is to calculate the irradiation damage parameters displacement rate (dpa/sec) and helium generation rate (hpa/sec) in the Materials Open Test Assembly (MOTA) of the Fast Flux Test Facility (FFTF).

2.0 *Summary*

The axial distribution of dpa/sec and hpa/sec for the FFTF MOTA were calculated for the following elements: AI, Si, Ti, V, Cr, Mn, Fe, Ni, Cu, Nb, and Mo.

3.0 Program

Title: Irradiation Effects Analysis (AKJ)
Principal Investigator: O. G. Ooran
Affiliation: Hanford Engineering Development Laboratory

4.0 Relevant DAFS Plan Task/Subtask

Subtask II.A.l Fission Reactor Dosimetry

5.0 Accomplishments and Status

5.1 Introduction

The FFTF MOTA is an excellent facility for fusion materials irradiation experiments for a number of reasons including: 1) high displacement rate and subsequent dpa, 2) large test volumes, 3) controlled and measured irradiation temperatures, and 4) quick recharging of metallurgical specimens between reactor cycles.

For purposes of planning irradiation experiments in the FFTF MOTA, dpa/sec and hpa/sec were calculated for a number of elements relevant to the MFE program. Also calculated is the axial distribution of flux for energies greater than 0.0, 0.1, and 1.0 MeV.

5.2 Data Source

The reaction rate (R) is calculated with the enuation

$$R = \sum_g \phi_g \sigma_g$$

where ϕ_g are the multigroup fluxes and σ_g are the multigroup reaction cross sections.

The fluxes for MOTA are from a three dimensional, 53 energy group-diffusion theory calculation of the FFTF for the pre-startup fuel loading condition.) The MOTA fluxes used in this calculation are from the subassembly 3404. Subassembly 3404 is a shim suhassembly (filled with stainless steel pins) in a location with surrounding fuel and control rods which were identical to those around MOTA. The diffusion theory calculations used six mesh points in each hexagonal subassembly. The fluxes used in this calculation were the average values of the six mesh points for each axial location. There is no significant radial gradient across the subassembly. Variation in fuel loading and fuel burn-up in the subassemblies around MOTA may cause up to 15% variation in the actual fluxes and reaction rates reported here.

The rnultigroup cross sections were calculated by Mann[2,3] using the NJOY[4] code and ENDF/B-V nuclear cross sections[5]. The NJOY code calculates damage energy cross sections. These were converted to displacement cross sections using the threshold energies (E_d) in Table 1. A stainless steel (Fe18Cr10Ni) displacement cross section froni previous work of Doran and Graves[6] based on ENDF/B-IV cross sections was also used.

TABLE 1

OAIMPGE THRESHOLD ENERGIES

Element	E_d (eV)
Al	25
Si	20
Ti	30
V	40
Cr	40
Mn	40
Fe	40
Ni	40
Cu	30
Nb	60
Mo	60

5.3 Results

Figures 1 through 11 show dpalsec and μhpa/sec (i.e., appm helium/second) for the elements listed in Table 1. A Mo(n,He) cross section is not available on ENDF/B-V data files. Therefore, Nb(n,He) was used in place of Mo(n,He) in Figure 11. Typical FFTF irradiation cycles last 115 days (~10^7 seconds). The legend at the bottom of each figure gives the location of each MOTA canister, including the below core canister (BCC). For all elements except nickel, a relatively high producer of helium, the μhpa/sec curve falls below the dpa/sec curve.

Figure 12 shows hpa/sec from the $^{59}Ni(n,\alpha)^{56}Fe$ reaction. Because of the resonance at 203 eV, helium production from this reaction peaks just outside the core of FFTF. Figure 13 shows the stainless steel dpa/sec reaction rate. The peak rate is 2 x 10^{-6} dpa/sec. The lowest rate, at the top of the level 8 canister, is 7.5 x 10^{-9} dpa/sec, about twice the rate obtained in RTNS-II. Figures 14 through 16 shows the axial distribution of fluxes >0.0, 0.1, and 1.0 MeV in MOTA.

A proposed experiment to simulate the heliumldpa ratio expected at a first wall location in a MFE device will use type 316 stainless steel enriched with 0.15% of the irradiation produced isotope ^{59}Ni. The ^{59}Ni enriched isotope is best utilized in a MOTA spectrum which activates the 203 eV resonance. Figure 17 shows the heliumldpa ratio expected from the ^{59}Ni enriched 316 stainless steel. In core the ratio will be ~0.75. This is about three times larger than a nonenriched sample. Outside the core the 203 eV resonance enhances the helium/dpa ratio to values of 8 and 15 at the far ends of MOTA. However, the optimum displacement rate is just outside the core top and bottom. The second curve shows the stainless steel displacement rate in units of 10^{-6} dpa/sec. At the top of the BCC and the bottom of canister 6 one can expect 4-5 dpa/cycle and a heliumldpa ratio of ~4-5. Compared to a nonenriched sample this should give a factor of 10-20 enhancement in the helium/dpa ratio.

This approach provides a constant, high value of helium/dpa during the void nucleation phase, in contrast to the low but increasing value obtained in a mixed spectrum reactor like HFIR. The nonlinearity in the latter case is due to the production of ^{59}Ni which is not present in natural nickel.

6.0 References

1. D. W. Wootan, J. A. Rawlins, K. D. Dobbins, "Reaction Rates and Neutron Spectra in the FFTF at Full Power," American Nuclear Society Transaction, Vol. 46, 1984.

2. F. M. Mann, "^{59}Ni t n Cross Section Evaluation," UAFS Quarterly Report DOE/ER-0046/12, February 1983.

3. F. M. Mann, "Calculations of Damage Parameters," DAFS Quarterly Report DOE/ER-0046/6, August 1981.

4. R. E. Macfarlane, D. W. Muir, and F. M. Mann, "Radiation Damage Calculations with NJOY," Journal of Nuclear Materials 122 & 123 (1984) pp. 1041-1046.

5. R. Kinsey, "ENDF-I02 Data Formats and Procedures for the Evaluated Nuclear Data Files, ENDF," Brookhaven National Laboratory report BNL-NCS-50496 (ENDF-102) 2nd Ed. (ENDFIB-V) (1979).

6. D. G. Doran and N. J. Graves, "Neutron Displacement Damage Cross Sections for Structural Metals", in Irradiation Effects on the Microstructure and Properties of Metals, ASTM STP 611, 1976, P. 463.

7.0 Future Work

In the next reporting period hpa and dpa rates for Zr, Ta, and W will be calculated.

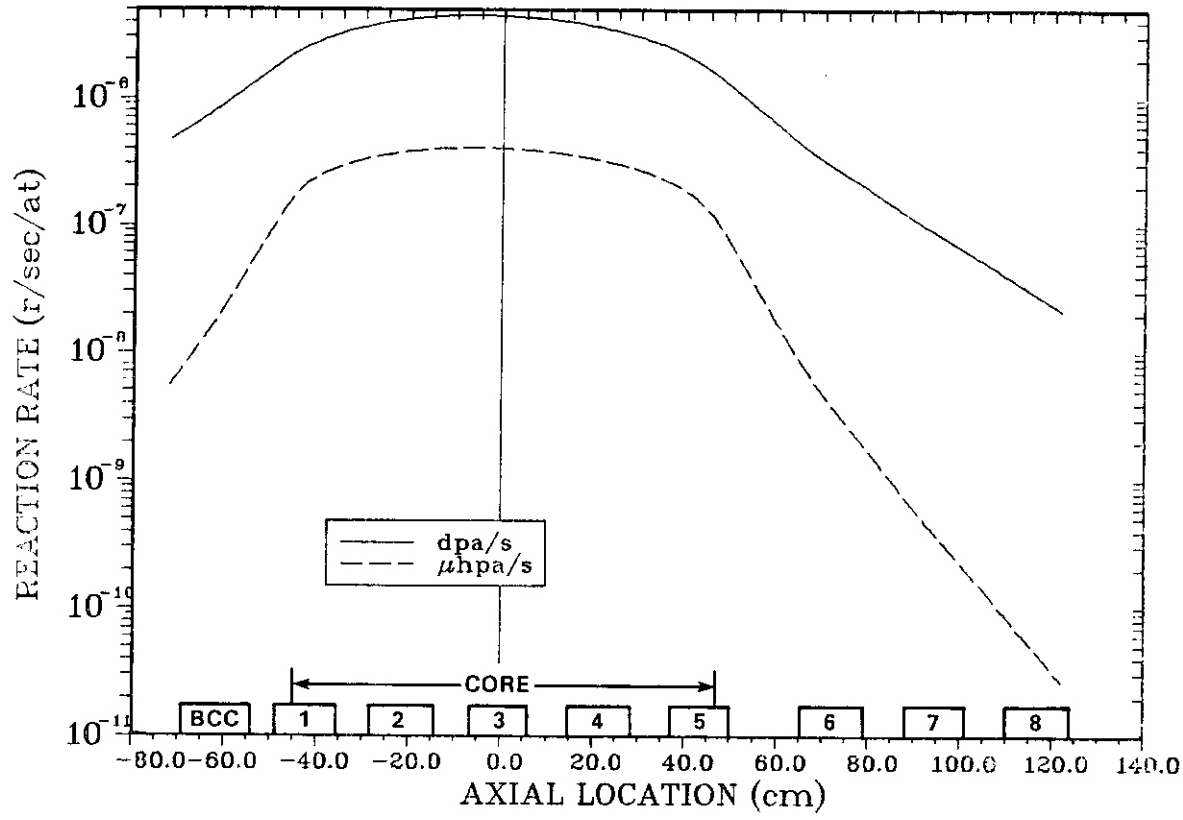

Figure 1 Al(n,dpa) and Al(n,He) reaction rate per atom in MOTA

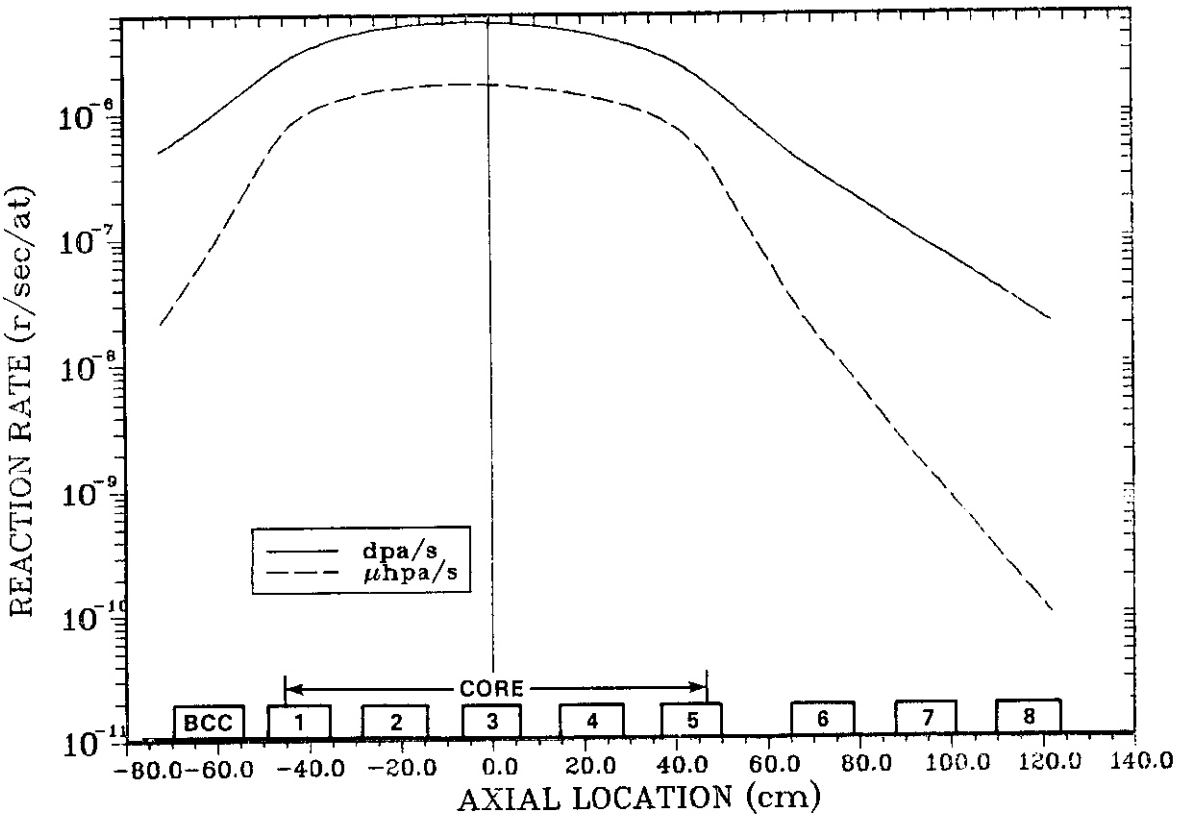

Figure 2 Si(n,dpa) and Si(n,He) reaction rate in MOTA.

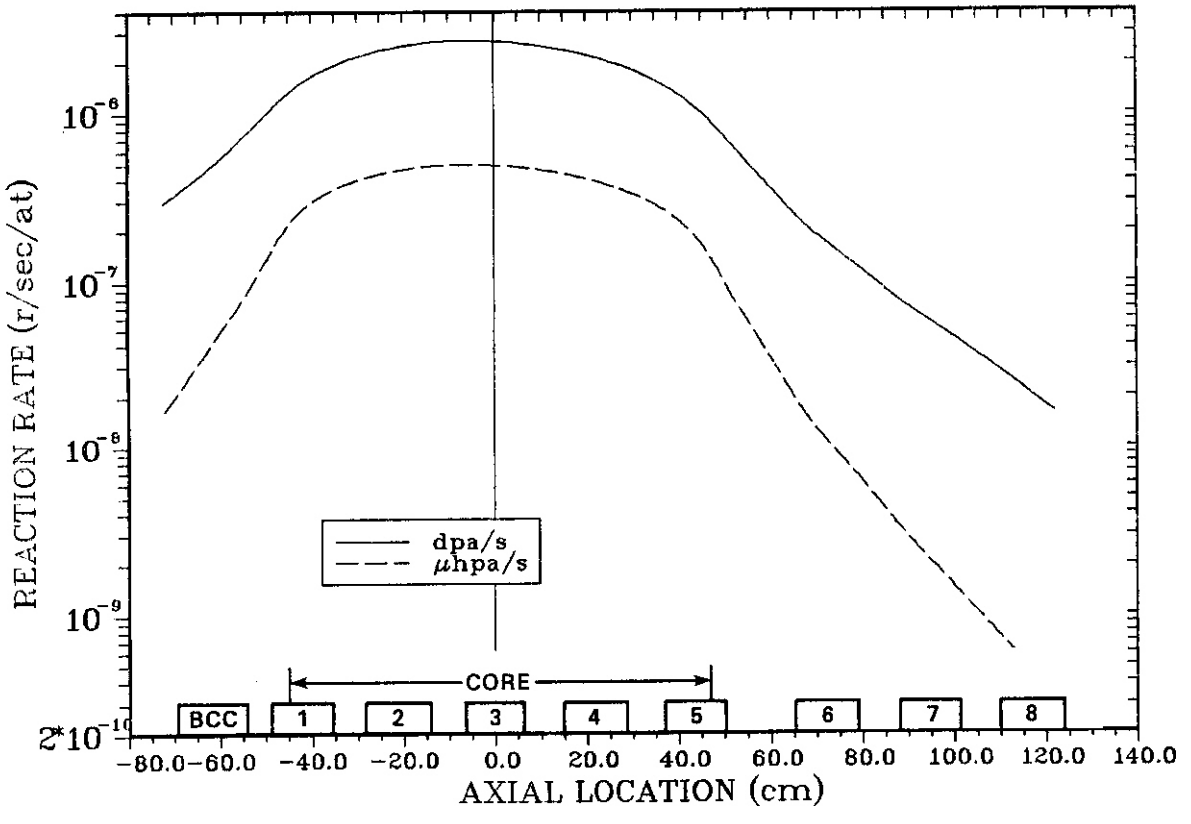

Figure 3 Ti(n,dpa) and Ti(n,He) reaction rate in MOTA.

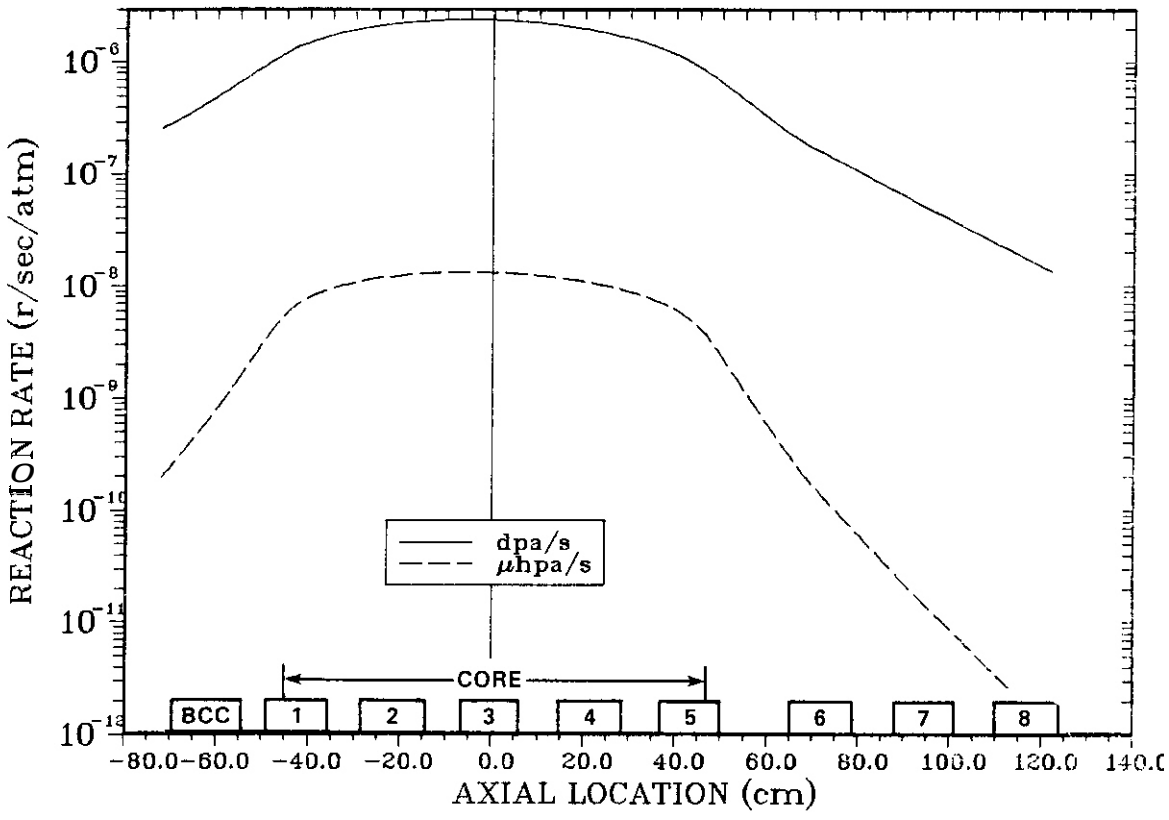

Figure 4 V(n,dpa) and V(n,He) reaction rate in MOTA.

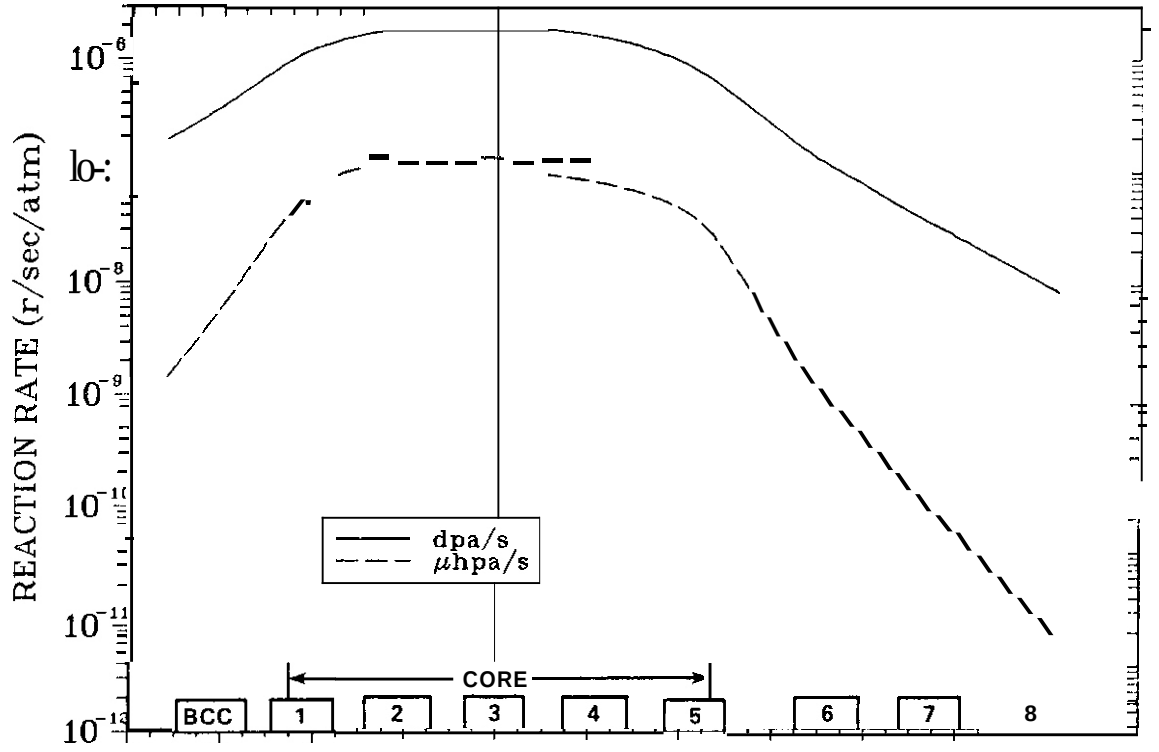

Figure

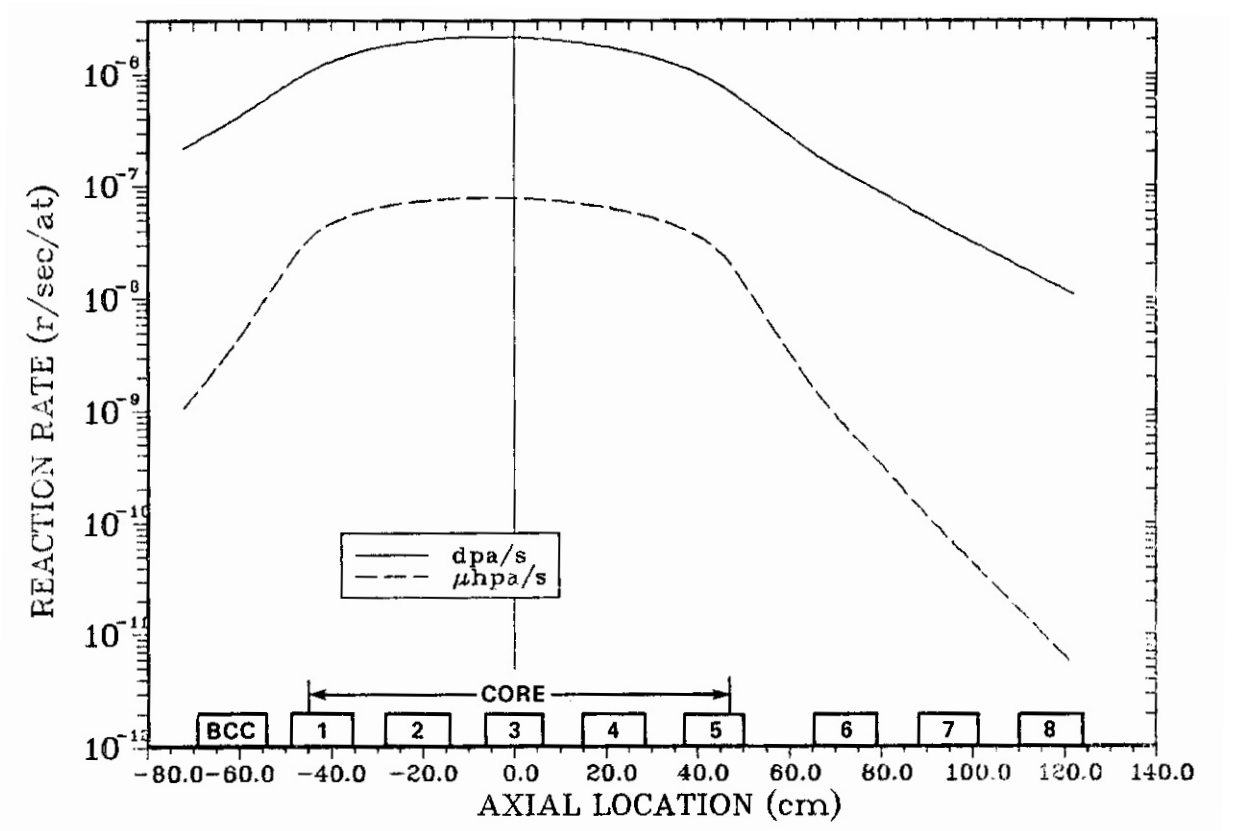

Figure 6 Mn(n,dpa) and Mn(n,He) reaction rate in MOTA.

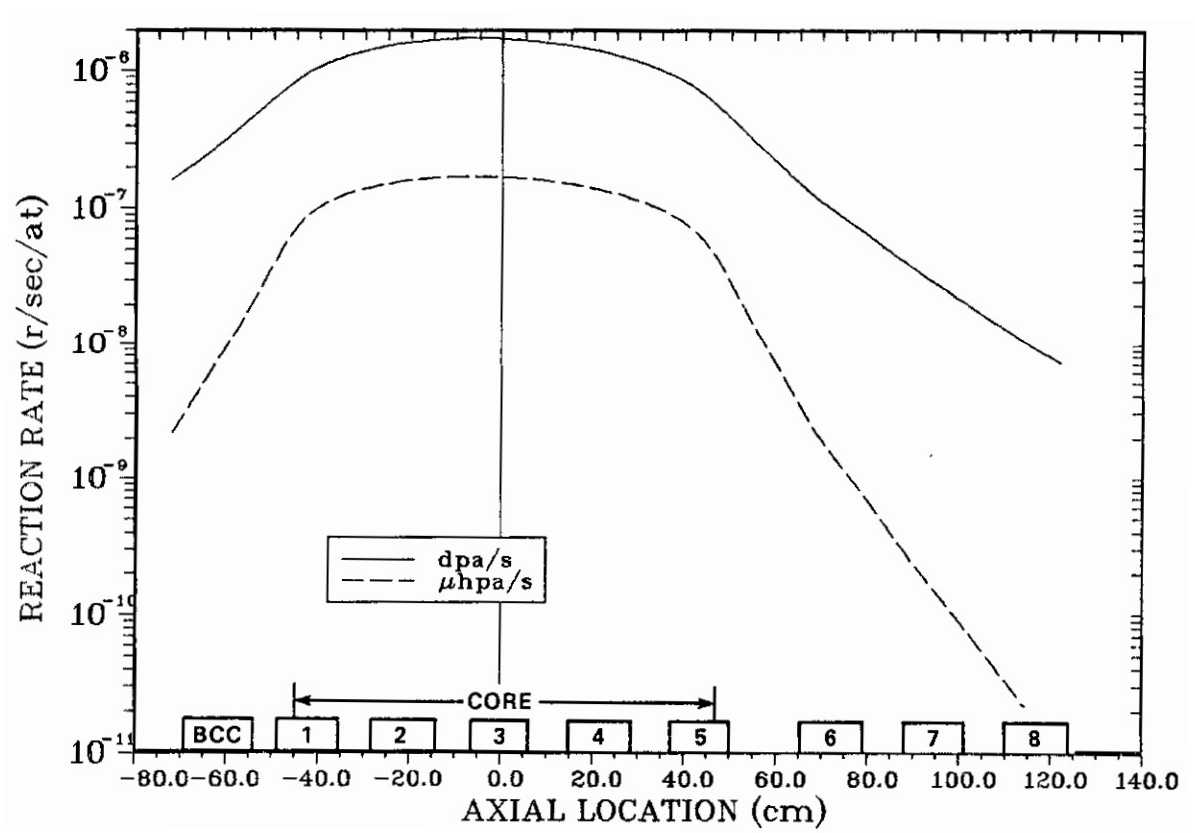

Figure 7 Fe(n,dpa) and Fe(n,He) reaction rate in MOTA.

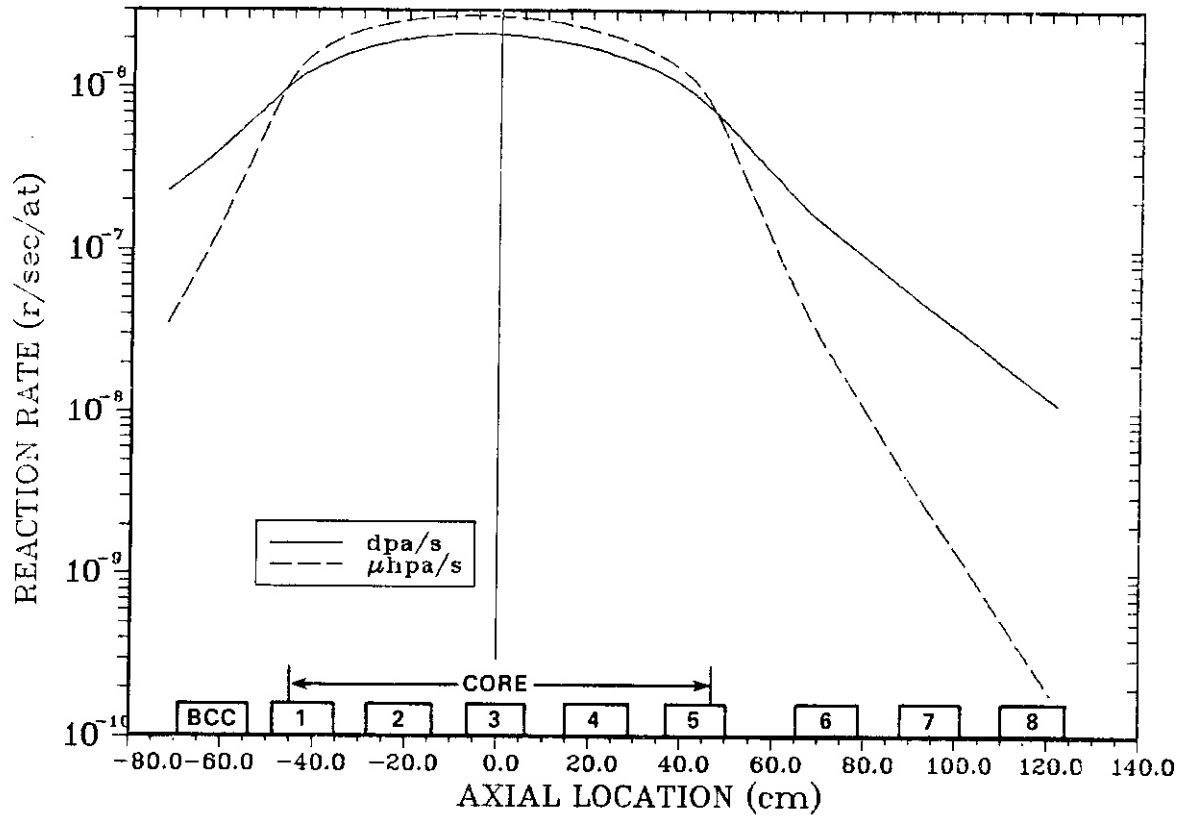

Figure 8 Ni(n,dpa) and Ni(n,He) reaction rate in MOTA.

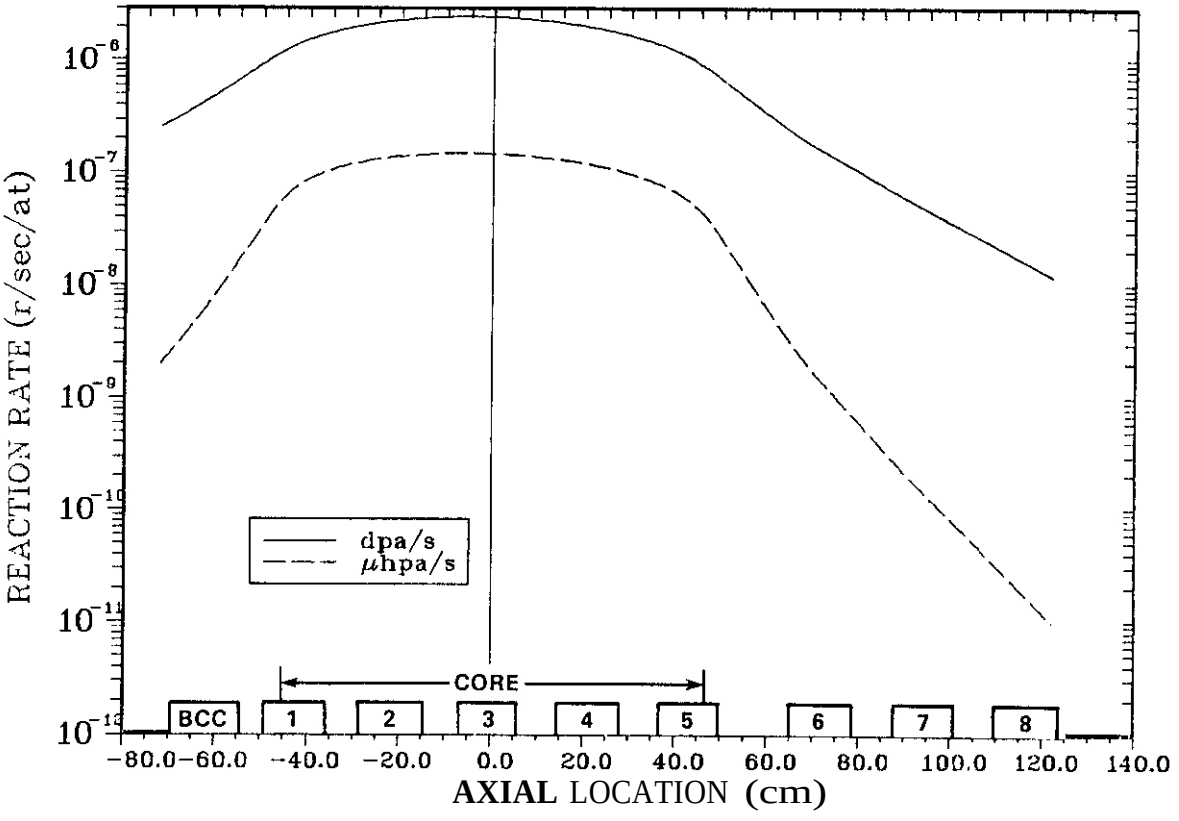

Figure 9 Cu(n,dpa) and Cu(n,He) reaction rate in MOTA.

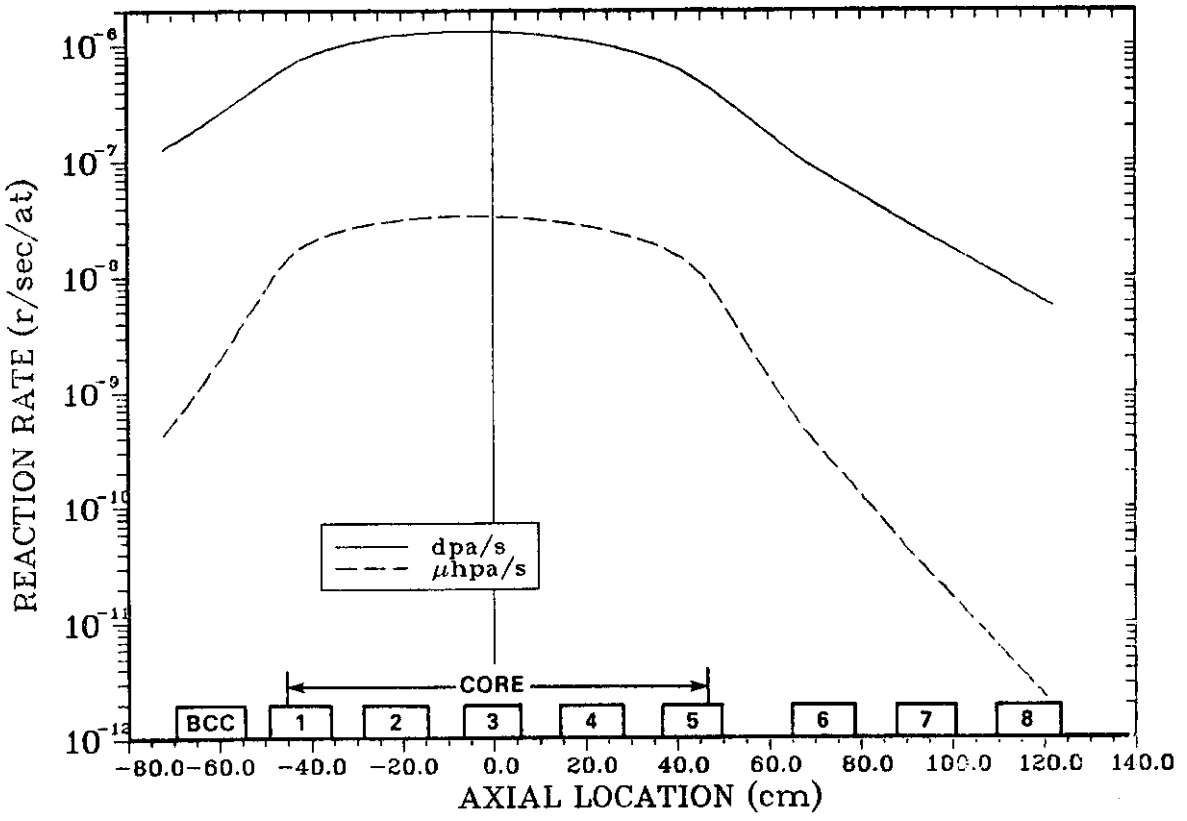

Figure 10 Nb(n,dpa) and Nb(n,He) reaction rate in MOTA.

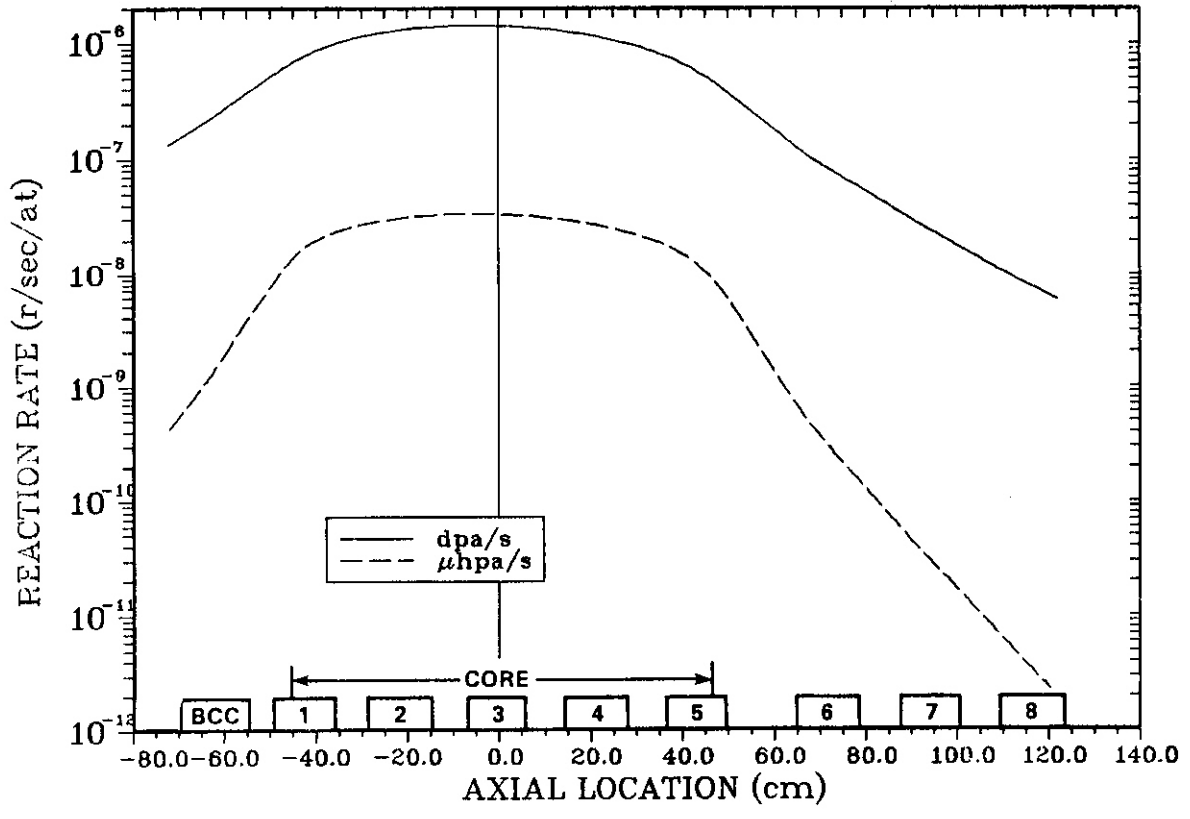

Figure 11 Mo(n,dpa) and Nb(n,He) reaction rate in MOTA.

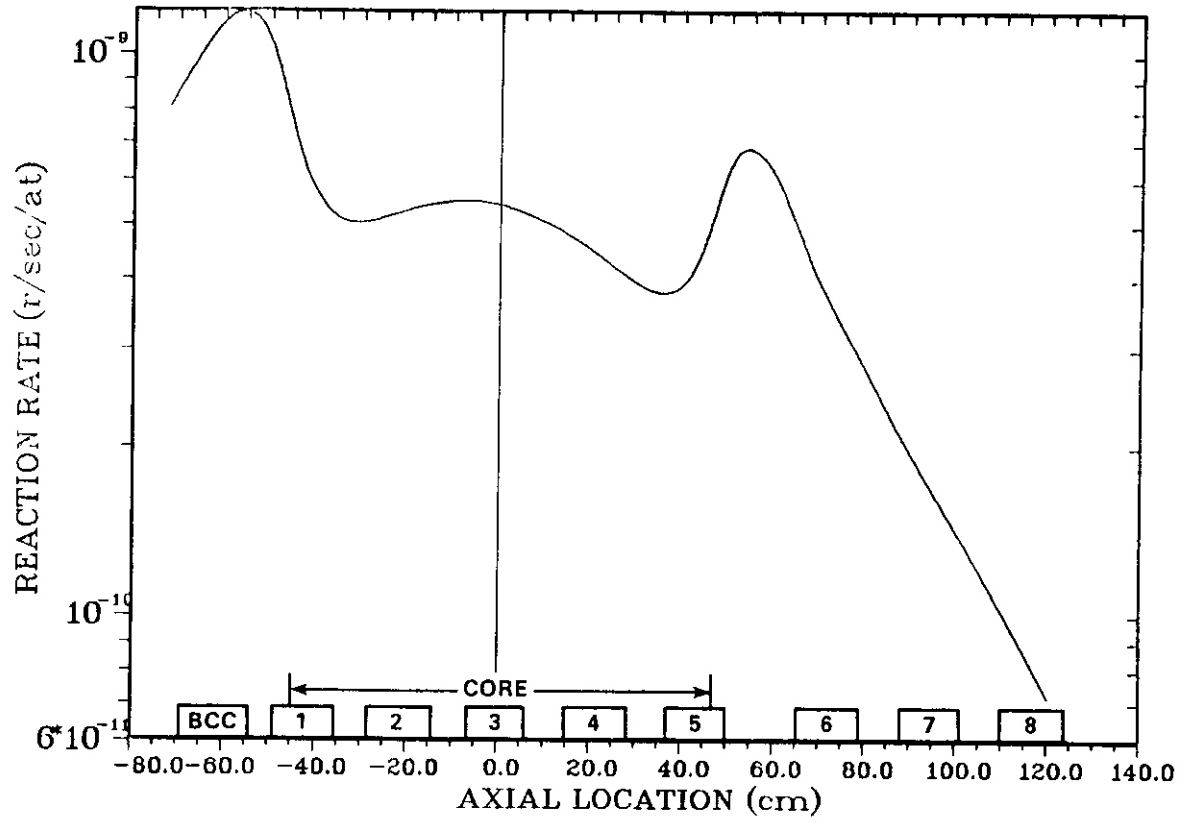

Figure 12 ^{59}Ni (n,He) reaction rate in MOTA.

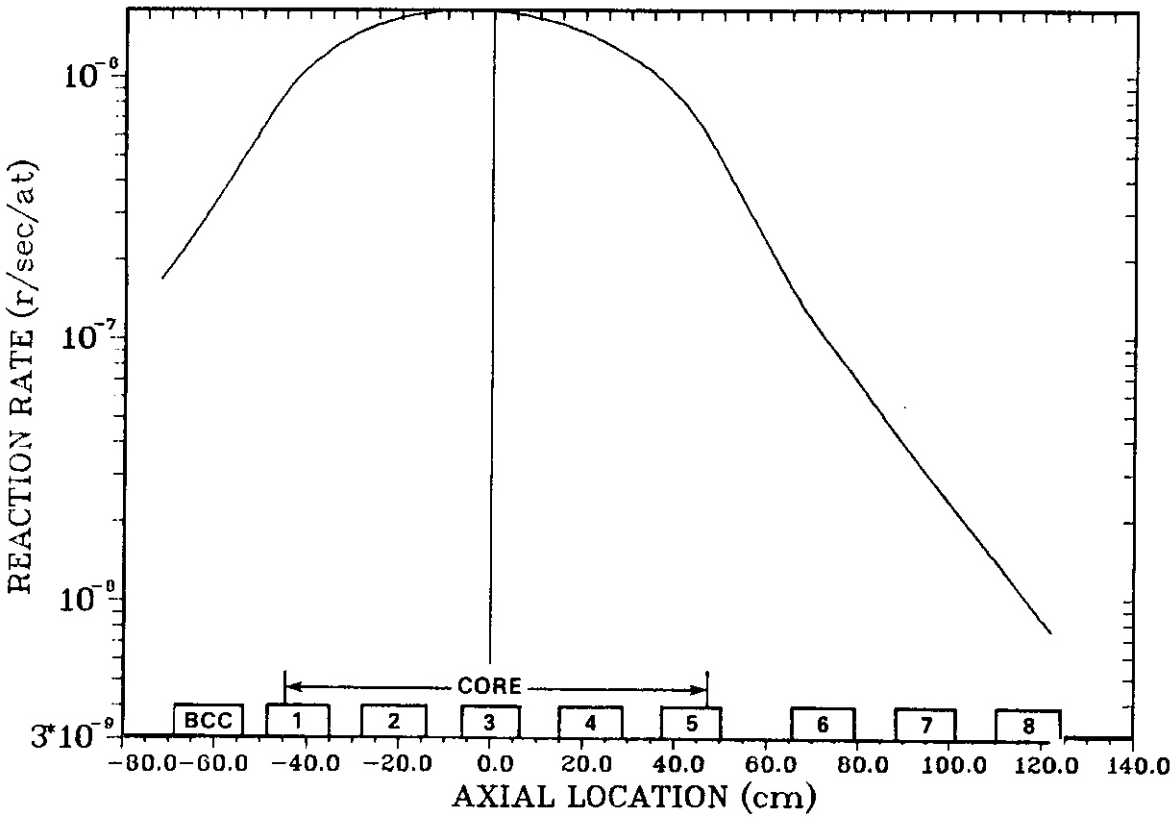

Figure 13 (Fe18Cr10Ni) reaction rate in MOTA.

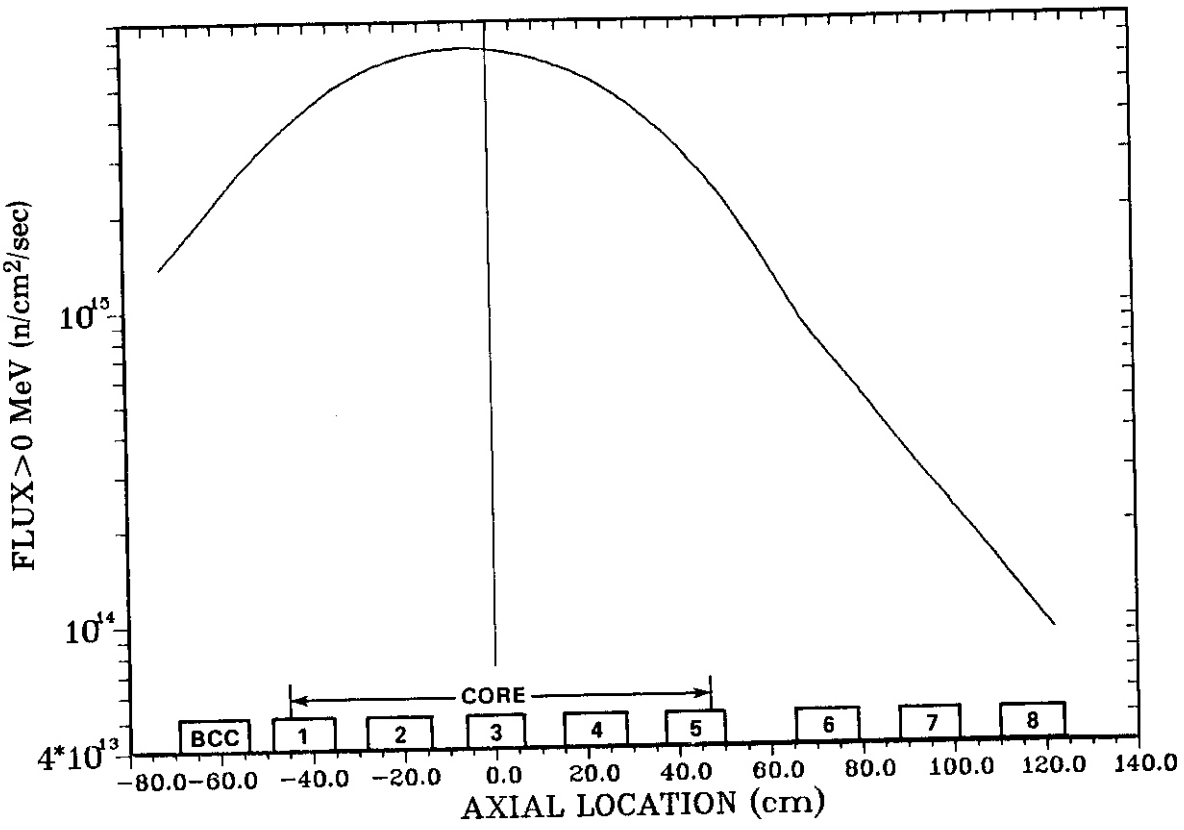

Figure 14 Flux > 0.0 MeV in MOTA.

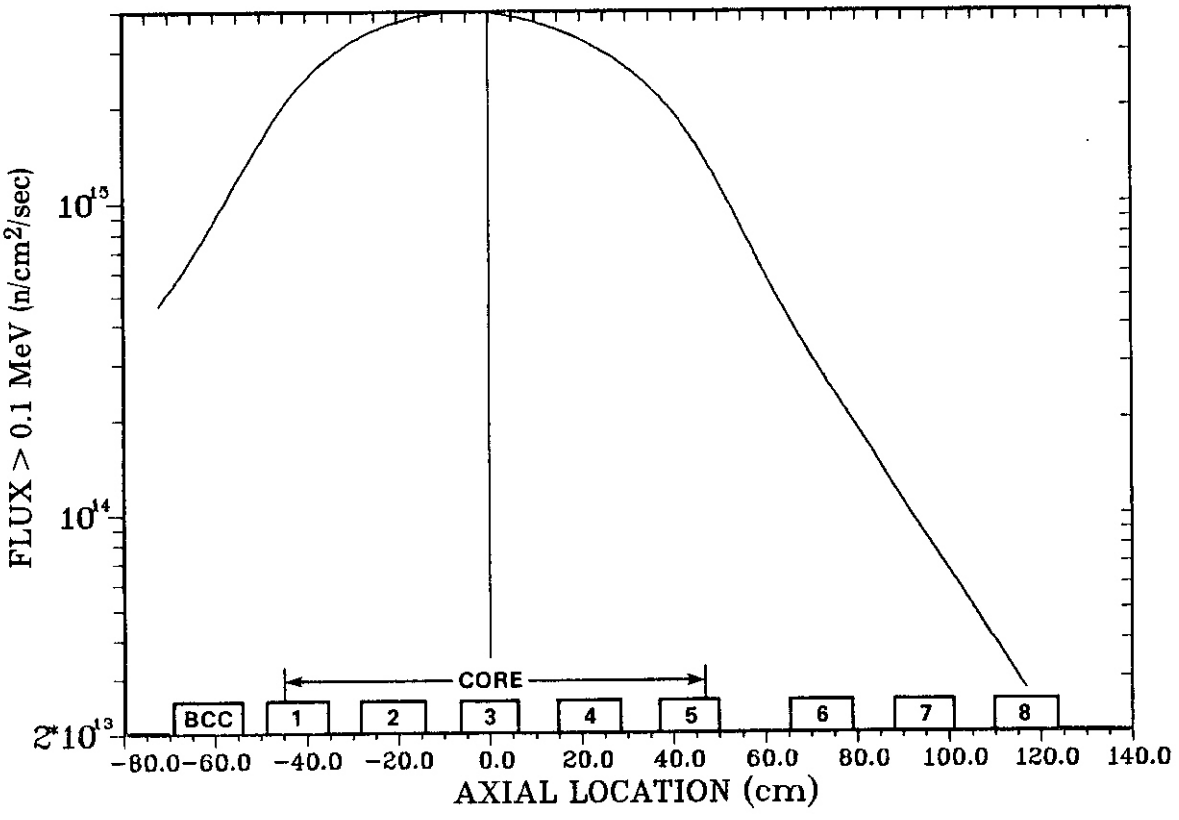

Figure 15 Flux > 0.1 MeV in MOTA.

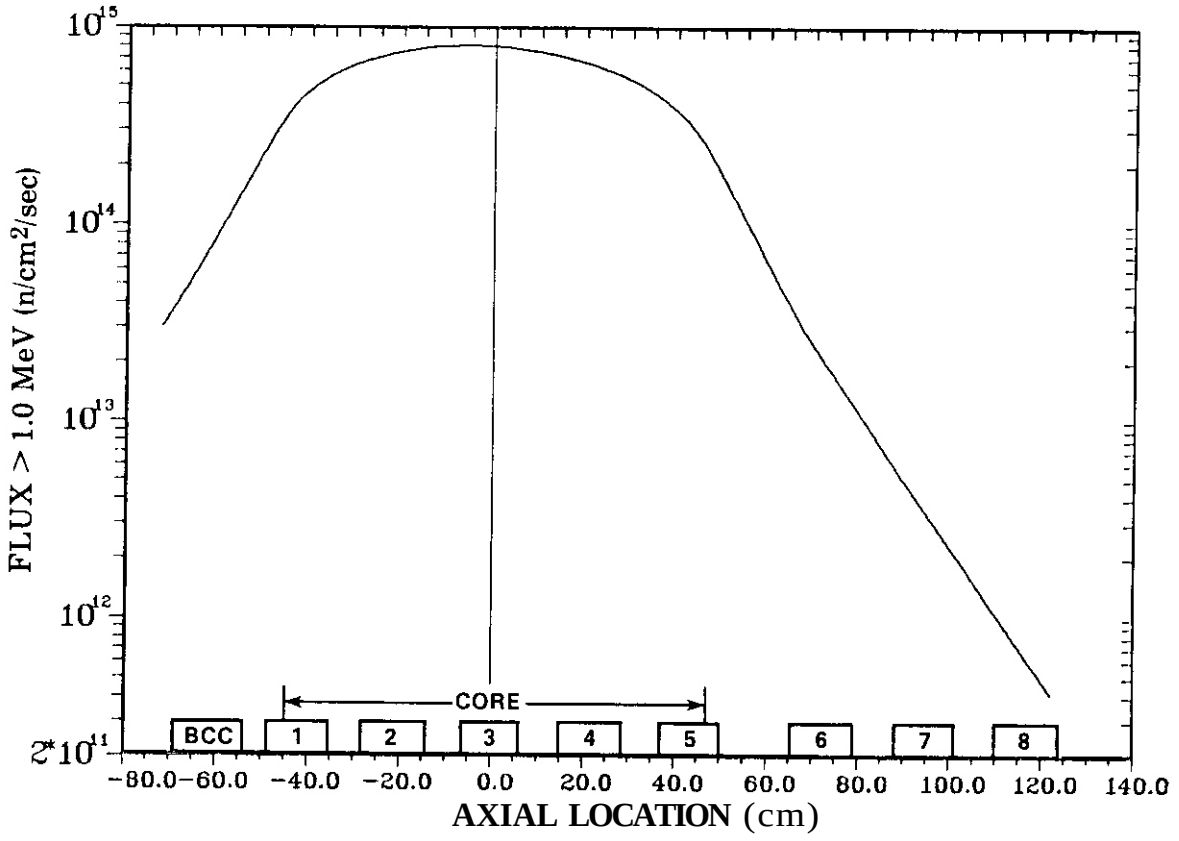

Figure 16 Flux > 1.0 MeV in MOTA.

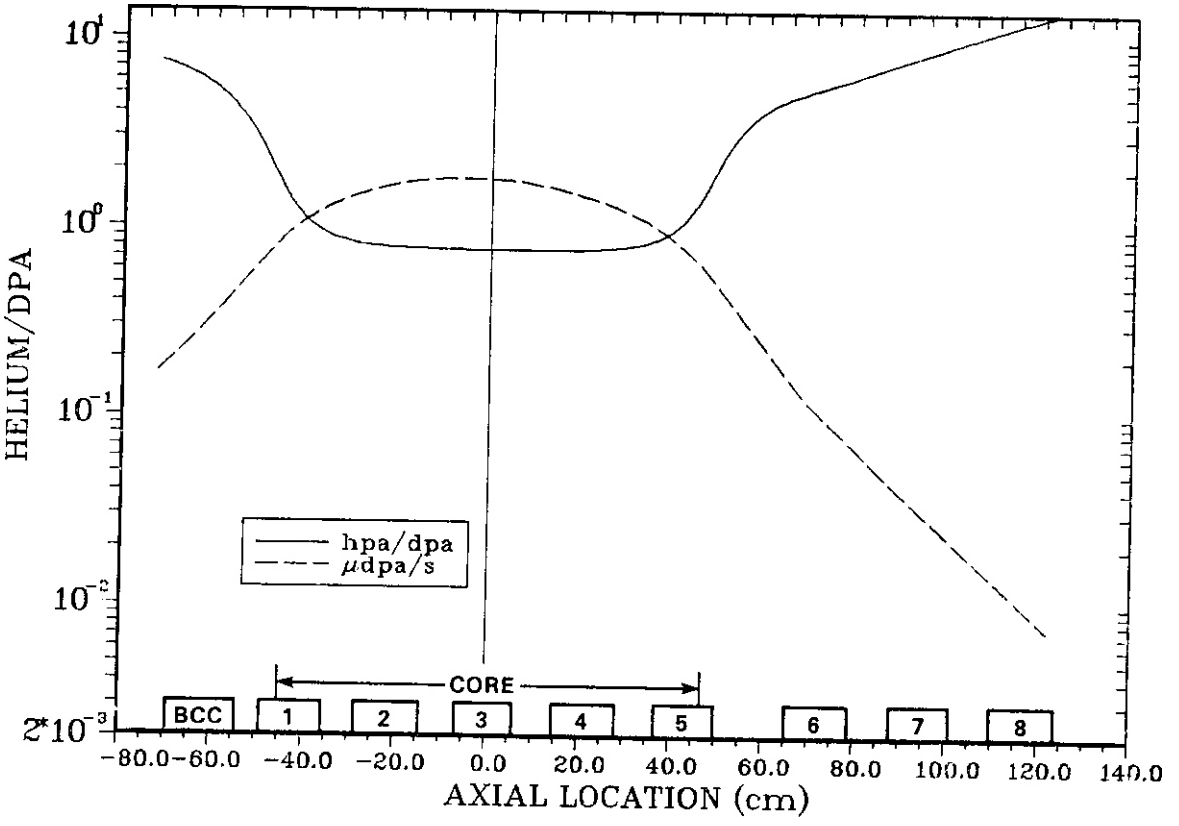

Figure 17 Helium/dpa ratio in type 316 stainless steel enriched with 0.15% ^{59}Ni and μdpa/sec in Fe18Cr10Ni type stainless steel.

CHAPTER 3

REDUCED ACTIVATION MATERIALS

REDUCED ACTIVATION GUIDELINES IN PERSPECTIVE

D. G. Doran, H. L. Heinisch, and F. M. Mann (Hanford Engineering Development Laboratory)

1.0 Objective

A goal of reducing the activation of materials and components of fusion devices has been adopted by the Fusion Materials Program. Consequently, decisions that have long term ramifications are being made on acceptable material compositions. The purpose of this work is to provide a perspective for the guidelines under which these decisions are being made.

2.0 *Summary*

The Fusion Materials program recently adopted a requirement that structural alloys qualify for shallow land burial at end of life. In the absence of a directly applicable regulation, the activation limits currently being used are taken from a Nuclear Regulatory Commission regulation, 10CFR61, developed to handle existing waste streams from the commercial nuclear industry. Activation calculations are characterized by many uncertainties, e.g., in nuclear data, in handling of multi-step reactions, in appropriate neutron flux-spectra, in component lifetimes, and in the viability of isotopic tailoring. These uncertainties, coupled with uncertain regulatory criteria, mean that calculated concentration limits should be viewed only as a qualitative guide in developing reduced activation materials.

3.0

Title: Irradiation Effects Analysis
Principal Investigator: D. G. Doran
Affiliation: Hanford Engineering Development Laboratory

4.0 Relevant Program Plan Task/Subtask

No tasks on reduced activation were identified in the original DAFS Program Plan.

5.0 Accomplishments and Status

5.1 Introductio?

The current status of nuclear power makes it clear that public acceptance of fusion power may be as important as feasibility issues. A key element in achieving public acceptance is to reduce the environmental impact as much as is reasonably achievable. To the fusion materials community, this generally means selecting and developing materials so as to reduce the level of radioactivity associated with a fusion reactor.[1]

Reducing the level of activation is a valid general goal, but devising a strategy for doing so requires consideration of specific objectives. Four objectives can be identified: increased hands-on maintenance, improved safety, meeting criteria for low-level waste (hence avoiding the need for geologic disposal), and recycling of certain materials. Each of these objectives places constraints on materials--some are common to one or more of the objectives, some are unique.

Of primary concern for maintenance and safety issues are short-lived radioisotopes. These issues are outside the scope of this paper. We are concerned here with the long-lived radioisotopes that must be controlled if

criteria for low-level waste disposal and recycling are to be met.

It is widely recognized that the development of radiation resistant materials is a key element in demonstrating the engineering and economic viability of fusion power. In developing such materials, there are constraints on material availability, joining techniques, test facilities, etc. An important new constraint in the U.S. fusion materials program is that materials should qualify as low-level radioactive waste (radwaste) that can be disposed of by shallow land burial. Consideration of recycling is at a more preliminary stage, but we believe that incentives to recycle certain elements (and possibly even compounds, such as breeder and magnet materials) will be sufficient that the recycling potential should be part of the evaluation of new materials.

Disposal of radwastes and recycling are two important aspects of fusion materials management that are affected by induced radioactivity. This paper discusses some of the issues that must be addressed early in materials development to aid in that management.

5.2 Materials Management

5.2.1 Regulatory Issues

Radwaste regulations specifically for fusion materials have not yet been prepared. The most applicable regulation appears to be the recently published Part 61 of Title 10 *of* the U.S. Code of Federal Regulations (10CFR61). It was prepared by the U. S. Nuclear Regulatory Commission (NRC) to cover shallow land burial of low level waste produced by the nuclear fission industry. This NRC reuulation soecifies the maximum permitted specific activity of certain radioisotopes for three classes of-low level' waste, Class C being the least restrictive. Although not stated explicitly, this regulation reflects the character of the waste streams from the commerciai nuclear industry. Only a small volume, less than one percent, is expected to be Class C waste, and only a small fraction of that would be activated metals. In fact, a small volume of currently generated waste exceeding Class C criteria may be covered by a new Class D which is under consideration by the NRC. This would also cover some activated metals from the future decommissioning of light water reactors. No consideration has yet been given to the disposal of large volumes of activated metals. It is likely that the methodology for setting disposal criteria would be quite different from that used for 10CFR61.

In the absence of a clearly applicable regulation, the Class C criteria have been adopted by the U.S. Office of Fusion Energy as requirements for fusion materials. Activation calculations at this laboratory [2] and others [3-5] have been compared with 10CFR61 to determine acceptable concentration limits for alloying elements and impurities. However, the 10CFR61 list of isotopes must be supplemented for fusion applications. Not surprisingly, this has introduced discrepancies among laboratories because setting acceptable limits on radioactivity is not straightforward. It involves analysis of pathways by which an isotope in waste material can add to the radiation burden of an individual or the general population. While we did not attempt to reproduce the full NRC analysis in order to supplement 10CFR61, we did employ scenario-specific factors (calculated by Kennedy and Peloquin of Battelle-Pacific Northwest Laboratory [6]) to convert the specific activity of each new radionuclide to total body dose. Waste disposal limits were then estimated by comparing the new conversion factors with that for Ni-59, a long-lived product included in 10CFR61.

There is no simple answer *to* the question of what constitutes an acceptable dose for recycling. Although there is no specific applicable U. S. regulation, it is clear that, for irradiated material to be returned to an unregulated status, associated dose levels would have to be near or below background. This appears to be generally unobtainable. For recycling within a regulated fusion industry, a more reasonable level, which would permit extensive handling of a material, is 2.5 mremlhr or 5 remlyr. This would comply with the U.S. NRC's Standards for Protection Against Radiation (10CFR20). (Air and water quality standards are covered by this standard also.) Techniques for remote handling are improving rapidly, however, so that many operations could be performed on material having a higher contact dose. If the incentives to recycle are sufficient, many limits may have to be determined on a case by case basis, taking account of the component involved.

5.2.2 Activation Issues

5.2.2.1 Nuclear Data

For waste management, the object of an activation calculation is the activity per unit volume for each

radionuclide hdving a halflife of about five years or more. Differences in existing activation calculations are due in part to differences in nuclear data bases. Two major activation cross section libraries in the U. S. are ACTL [7], developed at Lawrence Livermore National Laboratory, and FMITACTIVLIB [8], developed at our laboratory. The latter uses Evaluated Nuclear Data File (ENDF/B) [9] data, supplemented where necessary by ACTL and special evaluations using scarce experimental data and nuclear model calculations. This file is currently being expanded--the greatest need is cross sections for radioactive species--by using the relatively crude, nuclear systematics code THRESH.[10] Cross sections for several thousand reactions are required. The objective is to achieve completeness in activation calculations. Cross sections for reactions shown by the calculations to have the potential to influence materials development or application will be reviewed to determine if improved accuracy is warranted. In addition to cross sections, one needs decay data for product nuclides, including branching ratios for isomeric states.

To evaluate recycling possibilities, personnel dose calculations are needed for direct gammas and for bremsstrahlung from high energy beta emitters. Alpha and beta emissions are generally considered easily shielded against for handling of stable solids. Cooling times up to 100 years are of interest, hence intermediate halflives are important--some so short that they are not a concern for Class C waste. On the other hand, Class C waste analysis must include alpha and beta emitters that are hazardous if inhaled or ingested. (Concern for the effect of recycling procedures on air dnd water quality also may require that alpha and beta activity be considered in specific recycling cases.)

The status of nuclear data necessary for activation and dose calculations is about the same. In both cases, the data used leans heavily on systematics because the cross sections for many important reactions are difficult to measure. The large amount of data needed — cross sections for about 5000 reactions and decay data for about 1000 isotopes--almost ensures that initial data files will be incomplete and of inconsistent accuracy.

5.2.2.2 Activation Calculations

Activation calculations have been published for a variety of materials irradiated in a variety of fusion spectra.[1-5, 11-14] Quantitative agreement is often poor. One reason for discrepancies in published work is the use of different data bases and differing methodologies in the various codes. These sources have been investigated in a recent interlaboratory study coordinated by E. Cheng of General Atomic. All participants made activation calculations for the same fusion device. The final analysis is not yet available, but some order-of-magnitude inconsistencies have already been revealed. Table 1 gives examples of elements for which there is general agreement that concentration limits are necessary if low level waste criteria are to be met. Examples of borderline elements, for which limits might be necessary, are Al, Zr, and Pb.

A number of caveats must accompany Table 1: (1) The dose is arbitrary--relevant doses are specific component lifetime doses. For radionuclides that are products of single-stage reactions, the concentration limits for a component lifetime dose are easily obtained by ratioing. (For very high doses, burnout may reduce the activity, hence raise the concentration limit.) On the other hand, oxygen, copper, and molybdenum produce significant radionuclides by multi-step reactions, hence activities increase as a power of the dose. For example, the fraction of Ni-63 activity in copper due to multi-step reactions increases from less than 20 % to over 50 % between 10 and 40 MW-y/m^2.[15]

(2) The composition limits are device dependent. (Even for a single reactor concept, the calculations apply rigorously only if the element does not perturb the first wall flux-spectrum associated with that concept.) Comparative calculations at 10 MW-ylm2 were made [15] for first wall spectra in STARFIRE, a water-cooled, solid breeder ($LiAlO_2$) tokamak [16]; MARS, a lead-lithium cooled mirror machine [17]; and a General Atomic conceptual tokamak reactor blanket featuring helium gas cooling and a Li_2O breeder.[18] It was found that the low energy tail of the STARFIRE spectrum, the result of moderation by the water coolant, generally caused higher levels of activation--up to a factor of five higher than for the other spectra. The same critical isotopes were identified in each spectrum, however.

(3) The nuclear data used in the calculations carries uncertainties as discussed above.

(4) The calculated composition limits are for natural isotopic abundances. As has been pointed out by others, [19] isotopic tailoring can in principle make some elements more benign, e.g., Cu and Mo. [1,2,4]

(5) The low level waste criteria estimates, especially for radionuclides not included in 10CFR61, must be considered uncertain, possibly by large factors. Such estimates must be reviewed and consensus obtained.

Because of the above considerations, the concentration limits in Table 1 should not be considered rigid boundaries on materials development.

5.2.2.3 Personnel Dose Calculations

Personnel dose estimates have been included in a number of activation studies. The calculations by Jarvis are probably the most extensive on recycling of specific elements.[20]. Although preliminary and carrying large uncertainties, they point to a number of potential problem elements, especially impurities at very low concentrations. Order of maqnitude estimates for some of these are given in Table 2. Of those included, only copper (dose due to Co-60) is very sensitive to the assumed cooling time of 100 years.

5.2.2.4 Impurity Control

The general subject of impurity analysis and control is generic to waste management and recycling--it may be the controlling factor in both. The problem is being attacked in several stages: determine the elements that dominate the radioactivity, determine the impurity elements that are present in current commercial feedstocks, identify problem elements, and investigate the potential for effectively eliminating the problem elements at various stages of material fabrication. Some potential problem impurity elements are Nb, Ag, Sn, Bi, and some rare earths. Some, such as Nb in V, are specific impurities that compromise the use of otherwise low activation metals. Others, such as the rare earths, are not routinely analyzed for, so their concentrations in current materials are unknown. Because materials fabrication techniques can evolve greatly in the future to meet the needs of materials-intensive fusion development, it is premature to conclude from current impurity considerations that certain materials cannot meet waste or recycling criteria.

5.2.3 Decommissioning Scenarios

Materials management must be an important aspect of decommissioning a fusion facility, or of interim component replacement operations. The reprocessing or reuse of materials, as an alternative to disposal as radwaste, must be evaluated in terms of materials resources, economics, and public perception. Such considerations must eventually be included in facility design.

The actual radionuclide concentrations in radwaste depend on the manner in which it is packaged. In particular, some dilution of the most active material with less active material is to be expected, or dilution can be an integral part of a disposal scenario. There is an apparent tradeoff between isolating the most active material or diluting it to meet concentration limits. The isolation facilitates handling of both the high and low activity portions, the latter generally being the dominant volume fraction. Some dilution of the high activity portion could follow its isolation, but incentives to keep the volume low can be expected.

The STARFIRE studies emphasized environmental concerns; they provide much insight into the relative activation of different reactor components. They also provide examples of integrated materials management. Vogler et al carried out an interesting exercise in which detailed scenarios were developed for disposing of STARFIRE blanket and magnet materials, some through recycling and some as waste.[21] For example. they concluded that, while recycling possibilities for magnet materials could be enhanced by dilution of highly active material with less active or virgin material, this was not a viable approach for a mature fusion economy because it would lead to a surplus of magnet materials.

5.3 Conclusion

Developing reduced activation materials is an important objective that should be diligently pursued. It will not only reduce the environmental impact of fusion power, but will reduce the complexity and costs of material handling and disposal. At this time, however, evaluation criteria are not developed sufficiently to define composition limits accurately for fusion reactor materials in terms of neutron activation.

The straightforward work, the identification of the dominant radionuclides, will SOON be complete. It is important to maintain the results of this work in perspective. Even if the computational uncertainties are made negligible, the requirements on material composition will remain soft for a long time. Waste management and recycling criteria must be developed. Attainable impurity levels will evolve. And, most importantly, the methods by which a component is recovered, dismantled, and packaged will strongly influence what compositions are acceptable for the materials of the component. The activation of the component will, in turn, affect how the component is decommissioned.

In the near term, then, fusion materials programs should use activation calculations as a guide. The consequences should be determined of reducing common alloying constituents such as Ni and Ma to even lower levels than suggested by Table 1. But it would be premature to accept any degradation of desirable properties on the basis of activation.

Impurities have taken on a new significance. Sample materials must be analyzed more thoroughly than heretofore to determine possible low levels of unusual impurities. This information will be the basis for assessing the need for long-range impurity control programs.

Some elements could be subject to more restrictive composition restraints than currently indicated through increases in required component lifetime fluences, changes in neutron spectra, or changes in regulatory criteria. It is well to remember also that it is the total activity of, or dose from, a component that is important, so that reducing the contribution from one element provides more flexibility for accommoddting the others.

5.0 Acknowledgements

The authors are indebted to W. Kennedy, Battelle-Pacific Northwest Laboratories, and G. Roles, US NRC, for helpful discussions regarding regulatory issues.

7.0 References

1. R. W. Conn et al., Nucl. Tech./Fusion 5, p. 219, 1984.

2. F. M. Mann. Nucl. Tech./Fusion 6, p. 213, 1984

3. S. Vogler, M. J. Steindler, and J. Jung, Nucl. Tech./Fusion 4, p. 415, 1983.

4. J. A. Blink, D. W. Dorn, and R. C. Mdninger, J. Nucl. Mat. 122 & 123, p. 977, 1984

5. F. W. Wiffen and R. T. Santoro, in Proc. Topical Conf. on Ferritic Alloys for use in Nuclear Energy Technologies, June 19-23, 1983, Metallurgical Society of AIME, in press.

6. W. E. Kennedy, Jr. and R. A. Peloquin, "Potential Low-Level Waste Disposal Limits for Activation Products from Fusion", Battelle-Pacific Northwest Laboratory Report, PNL-484, Sept. 1983.

7. M. A. Gardner and R. J. Howerton, "ACTL: Evaluated Neutron Activation Cross Section Library - Evaluation Techniques and Reaction Index," Lawrence Livermore National Laboratory Report, UCRL-50400, Vol. 18. Oct. 1978.

8. F. M. Mann, "Transmutation of Alloys in MFE Facilities as Calculated by REAC," Hanford Engineering Development laboratory Report, HEDL-TME 81-37, Rug. 1982.

9. R. Kinsey, Compiler, ENDF/B Summary Documentation (ENDF-201), 3rd ed. (ENDFIB-V), Brookhaven National Laboratory Report, BNL-NCS-17451, July 1979.

10. S. Pearlstein, in Proc. Conf. on Nuclear Cross Sections and Technology, Wash. D.C., Mar. 1975, COM-75-11469, Oct. 1975.

11. E. T. Cheng, Nucl. Tech./Fusion 4, p. 545, 1983.

12. J. Jung, ibid., p. 566.

13. M. 2. Youssef and R. W. Conn, Nucl. Tech./Fusion 3, p. 361, 1983

14. G. J. Butterworth and O. N. Jarvis, J. Nucl. Mat. 122 & 123, p. 982, 1984

15. H. L. Heinisch, F. M. Mann and D. G. Doran, submitted for publication in Fusion Tech.; Hanford Engineering Development Laboratory Report, HEDL-SA-3219.

16. C. C. Baker et al., "STARFIRE - A Commercial Tokamak Fusion Power Plant Study," Argonne National Laboratory Report, ANL/FPO-80-1, Sept. 1980.

17. B. G. Logan et al., "Mirror Advanced Reactor Study: Final Design Report," Lawrence Livermore National Laboratory Report, UCRL-53480.1984. Also, B. G. Logan, Nucl. Tech./Fusion 4, p. 563, 1983.

18. M. Huggenberger and K. R. Schultz, in Proc. IEEE 9th Symposium on Engineering Problems of Fusion Research, Oct. 1981.

19. M. Z. Youssef and R. W. Conn, ibid. Ref. 11, p. 1177

20. 0. N. Jarvis, "Low Activity Materials: Reuse and Disposal", UKAEA Harwell Report AERE-R 10860, July, 1983.

21. S. Vogler et al., "Materials Recycle and Waste Management in Fusion Power Reactors. Prog. Rept. for 1982," Argonne National Laboratory Report, ANLIFPPITM-163, Jan. 1983.

8.0 Future Work

Work on the contextual framework of reduced activation materials studies will continue,

9.0 Publications

The work reported here is the content of a paper to be presented at the International Conference on Fusion Reactor Materials in Tokyo on Dec. 3-6, 1884.

TABLE 1

SOME ELEMENTS HAVING CONCENTRATION LIMITS UNOER SHALLOW BURIAL GUIDELINES FOR RADWASTE

Element	Controlling Isotope	Halflife (yr)	(a) Class C Limit (Ci/m^3)	(b) Concentration Limit (vol.%)
N	C-14	5.7 (3)	80.	0.3
Ni	Ni-63	1.0 (2)	7000.	0.9
cu	Ni-63	1.0 (2)	7000.	1.
Mb	**Nb-94**	2.0 (4)	0.2	3 (-4)
Mo	Mo-93	3.5 (3)	[30]	[0.05]
Ag	Ag-108	1.3 (2)	[3]	[1 (-4)]
Bi	Bi-208	3.7 (5)	[0.1]	[1 (-3)]

[a) Brackets [] indicate that limit **was** estimated because it is not included in 10CFR61.

(b) Note that this "limit" is for a 10 $MW-y/m^2$ firstwall exposure in STARFIRE.

TABLE 2

SOME ELEMENTS THAT ARE EXPECTED *TO* HAVE CONCENTRATION LIMITS UNDER RECYCLING CRITERIA.*

Concentration Level	Element
1-10%	Si, Cu
0.01-1%	**Ni, Zr, Mo**
10-100 ppm	Al, Er
1-10 ppm	K, Nb, Ag, Ba, Ho
<1 ppm	Eu, Tb, **Ir**, Bi, Th, U

* Assumptions are 10 $MW-y/m^2$ at STARFIRE first wall position, 100 yr decay, and surface dose limit of 2.5 mremlhr.

Swelling of Fe-Cr-Mn Ternary Alloys in FFTF

H. R. Brager and F. A. Garner (Hanford Engineering Development Laboratory)

1.0 Objective

The object of this effort is to determine those factors which control the swelling of alloy systems which have the potential for reduced activation.

2.0 Summary

The swelling of nine simple Fe-Mn binary and Fe-Cr-Mn ternary alloys has been measured by an immersion density technique after irradiation at ~520°C to 3.2 x 10^{22} n/cm^2, E > 0.1 MeV, or ~15 dpa. The swelling of these alloys decreases with manganese but exhibits a dependence on manganese content that is weaker than that of nickel in Fe-Cr-Ni alloys. The dependence on chromium is even weaker, in sharp contrast to the behavior observed in Fe-Cr-Ni alloys.

3.0 Program

Title: Irradiation Effects Analysis (AKJ)
Principal Investigator: D. G. Doran
Affiliation: Hanford Engineering Development Laboratory

4.0 Relevant DAFS Program Plan Task/Subtask

Subtask II.C.I. Effects *of* Material Parameters on Microstructure.

5.0 Accomplishments and Status

5.1 Introduction

In an earlier report it was noted that a series of austenitic alloys based on manganese substitution for nickel was included in the MOTA-1B experiment for irradiation in FFTF.(1) MOTA-1B has been discharged from the reactor and the measurement of density changes is in progress. While data will eventually be available for irradiations at 400, 520 and 600°C on manganese stabilized commercial alloys, developmental alloys and simple binary and ternary alloys, only data on the latter irradiated at 520°C are available at this time. The specimens were standard TEM microscopy disks which were irradiated to 3.2 x 10^{22} n/cm^2 (E > 0.1 MeV) or n15 dpa.

5.2 Results

Figure 1 shows the density changes measured in these alloys. Figure 2 shows a comparison with Fe-Cr-Ni ternary alloys irradiated in the AA-VII experiment in EBR-II.(2) The irradiation conditions depicted in Figure 2 for Fe-Cr-Ni alloys bracket the Fe-Cr-Mn data, both in irradiation temperature and exposure level

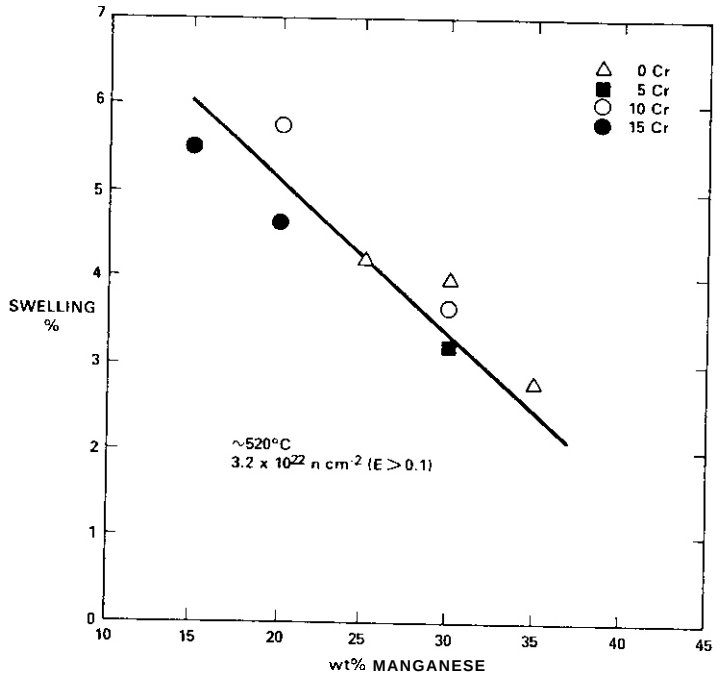

FIGURE 1. Swelling Observed in Fe-Cr-Mn Alloys Irradiated in FFTF to 3.2 x 10^{22} n/cm^2 (E **> 0.1** MeV) **at** ~520°C.

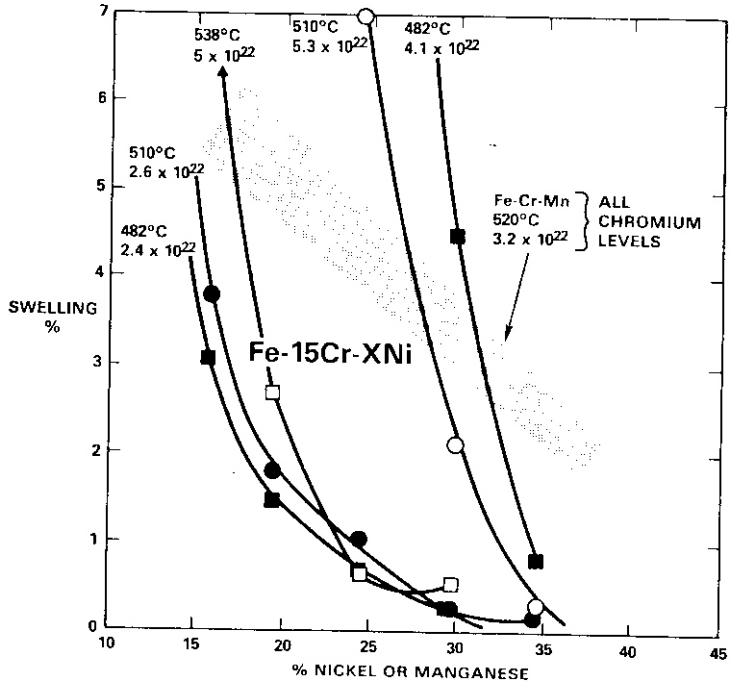

FIGURE 2. **Comparison** of Swelling of **Fe-Cr-Ni Alloys** in EBR-II **and Fe-Cr-Mn Alloys in FFTF Under Comparable Irradiation Conditions.**

5.3 Discussion

While swelling decreases with manganese content, it does so at a much lower rate than would occur if the alloys were stabilized with nickel. Even more importantly, there is very little dependence of swelling on chromium level, in sharp contrast to the behavior of Fe-Cr-Ni alloys. The lesser impact of manganese level on swelling is similar to the reduced effectiveness of manganese relative to nickel in promoting the stability of the austenite phase.

The MOTA irradiation temperature of 520°C lies right between the 510 and 538°C irradiation temperatures of the AA-VII experiment in EBR-II. It was in the range 510-538°C that Fe-Cr-Ni alloys with low nickel levels departed from their temperature-independent behavior and began to develop longer transient regimes of swelling. The maximum swelling of ~5% in the Fe-Cr-Mn alloys at 15 dpa is quite consistent with the swelling behavior developed by the Fe-Cr-Ni alloys below 510°C. These data suggest that the swelling rate of the Fe-Cr-Mn system is also ~1%/dpa.

6.0 References

1. H. R. Brager and F. A. Garner, "Fundamental Alloy Studies," DAFS Quarterly Progress Report DOE/ER-0046/17, May 1984, p. 93.

2. F. A. Garner and H. R. Brager, "Swelling of Fe-Ni-Cr Ternary Alloys at High Exposure," DAFS Quarterly Progress Report DOE/ER-0046/16, February 1984, p. 38.

7.0 Future Work

Density change measurements will continue on the other alloys irradiated at 520°C and on alloys irradiated at ~420 and ~620°C. Electron microscopy examination will also be initiated.

8.0 Publications

None

COMPOSITIONAL DEPENDENCE OF ION-INDUCED SWELLING IN Fe-Cr-Mn ALLOYS

E. H. Lee and L. K. Mansur (Oak Ridge National Laboratory)
F. A. Garner and H. R. Brager (Hanford Engineering Development Laboratory)

1.0 Objective

The object of this effort is to determine the response of swelling with composition in simple Fe-Cr-Mn alloys. These data will be used to guide the search for swelling-resistant austenitic alloys with low activation characteristics.

2.0 Summary

A series of simple Fe-Cr-Mn alloys has been prepared and will be irradiated with iron ions in order to determine the influence of alloy composition on void swelling.

3.0 Program

Title: Irradiation Effects Analysis
Principal Investigator: D. G. Doran
Affiliation: Hanford Engineering Development Laboratory

4.0 Relevant Program Plan Task/Subtask

Subtdsk II.C.l, Effect of Material Parameters on Microstructure

5.0 Accomplishments and Status

5.1 Introduction

Earlier it was reported that a series of Fe-Cr-Mn alloys had been irradiated as TEM disks in the MOTA-1B experiment in FFTF.[1] These alloys comprised two compositional ranges. The first was Fe-15Mn-(5-15)Cr which covered the base composition range of existing commercial alloys. The second set of alloys was Fe-30Mn-(0-10)Cr, which were selected in the hope that the correlation observed in Fe-Cr-Ni alloys between swelling resistance and Invar-like anomalous properties also existed in the Fe-Cr-Mn system.

The potential for development of Fe-Cr-Mn alloys depends strongly on their swelling resistance relative to that of other alloys. However, high fluence data are needed to study swelling resistance and such data necessarily take years to generate in fission reactors. It has been demonstrated, however, that the early ion bomhardment studies of Johnston and coworkers2 yielded a correct description of the relative compositional dependence of swelling in neutron-irradiated Fe-Cr-Ni alloys.[3,4]

Therefore a similar set of ion irradiations will be conducted on a wide range of compositions in the Fe-Cr-Mn system to determine the swelling behavior. Since the objectives of this experiment are of interest to both fundamental and applied programs, it will be conducted jointly by the OAFS and ADIP activities of the DOE Fusion Materials program and also the Basic Energy Science (BES) program of DOE. In addition, T. Lauritzeri and W. G. Johnston of General Electric agreed to provide assistance and guidance on how the previous irradiations on Fe-Cr-Ni alloys were performed.

5.2 Status of Experiment

The dual-ion irradiations will be conducted at Oak Ridge National Laboratory using coinjected helium and 4 MeV Fe^+ ions. Specimen examination and data analysis will he done primarily by the BES program and assisted by the participants of the fusion programs. Some Fe-Cr-Ni alloys will also be irradiated in order to determine the consequences (relative to the work of Johnston) of using Fe^+ rather than Ni^+ ions and a different ion energy. Simultaneous helium injection will also be employed in the present study, while 15 appm preinjection was used in the earlier experiments. The data will he extracted both by step-height measurement and electron microscopy. This requires a special mask for the specimens. Approximately 600 of these masks were specially manufactured for this experiment by Johnston. They are made of pure molybdenum and are 3 mm in diameter and 0.025 mm thick.

The Fe-Cr-Ni alloys were provided by Lauritzen and Johnston and are identical to those of their earlier studies. These alloys, as well as the Fe-Cr-Mn alloys, were processed at HEDL to sheet form (0.015 in. thick) and vacuum annealed at 1030°C for 1/2 hour, followed by air cooling. Final preparation of specimens for irradiation was completed at ORNL.

It is anticipated that two holders with nine specimens each will be irradiated at both 625°C and 675°C to a dose of ~120 dpa. A fifth holder will contain Fe-Cr-Ni specimens. The sixth holder will provide lower doses and perhaps different heliumldpa ratios for selected specimens, depending on the results obtained from the other specimens.

Preirradiation electron microscopy of the Fe-Cr-Mn alloys is nearing completion at ORNL.

6.0 References

1. H. R. Brager and F. A. Garner, "Fundamental Alloy Studies," DAFS Quarterly Progress Report DOE/ER-0046/17, May 1984, p. 93.

2. W. G. Johnston et al., "The Effect of Metallurgical Variables on Void Swelling," Radiation Damage in Metals, N. L. Peterson and S. D. Harkness, Eds., Am. Soc. of Metals, 1976, p. 227.

3. F. A. Garner, J. Nucl. Mater., 117 (1983), p. 177.

4. F. A. Garner and H. R. Brager, "Swelling of Austenitic Fe-Ni-Cr Ternary Alloys During Fast Neutron Irradiation," ASTM STP 8970, in press.

7.0 Future Work

This effort will continue, focusing primarily on the ion irradiation at ORNL. The irradiation experiment is anticipated to commence in the near future.

8.0 Publications

None

CHAPTER 4

FUNDAMENTAL MECHANICAL BEHAVIOR

SHEAR PUNCH AND BALL MICROHARDNESS MEASUREMENTS OF 14-MeV NEUTRON IRRADIATION HARDENING IN FIVE METALS

G.E. Lucas, K. Shinohara*, and G.R. Odette (University of California, Santa Barbara)

1.0 Objectives

This study was performed to investigate the combined use of ball microhardness and shear punch tests to determine strength and ductility changes in specimens irradiated by high energy neutrons.

2.0 *Summary*

The irradiation hardening response of five metals irradiated in RTNS-II was investigated using a combination of ball microhardness and shear punch test techniques. The metal specimens were transmission electron microscopy disks of pure nickel, Ni-5 wt % Si, pure iron, solution annealed prime candidate alloy (PCA) for Path A, and 40% cold worked MFE 316 stainless steel. Specimens were irradiated in RTNS-II to fluences in the range 6 x 10^{16} to 6 x 10^{17} n/cm^2. Only limited ball microhardness data could be obtained because of disk thickness. However, the ball microhardness data obtained were in good agreement with shear punch data. It was found that the pure metals exhibited little hardening after exposure to fluences of ~1 x 10^{17} n/cm^2, but Ni-5 Si exhibited significant hardening after 6 x 10^{17} n/cm^2. Hardening in PCA was similar to that observed in solution annealed 316 stainless steel; and hardening in 40% cold worked MFE 316 was relatively small after 6 x 10^{17} n/cm^2.

3.0

Title: Damage Analysis and Fundamental Studies for Fusion Reactor Materials Development
Principal Investigators: G.R. Odette and G.E. Lucas
Affiliation: University of California, Santa Barbara

4.0 Relevant DAFS Program Plan Task/Subtask

Subtask B Mechanical Properties

5.0 Accomplishments and Status

5.1 Introduction

The development of materials for fusion reactors and ultimately the design of the fusion reactor necessitates the application of a fission reactor irradiation data base to fusion conditions. Such fission-fusion correlations will in turn require a fundamental understanding of the comparative behavior of materials in different neutron environments. One of the steps in developing this understanding is the generation of a microstructure and mechanical property data base for materials irradiated in 14 MeV neutron environments; and because of the volume limitations of current and near term high energy neutron sources, the specimens used for these purposes are necessarily small.

For this reason, we have been engaged in the development of a variety of test techniques which can be applied to relatively small specimens to extract mechanical property information.[1-7] Two of these techniques, the ball microhardness test and the shear punch test,[6] have been developed most extensively. Although each test Drovides strenoth and flow oroperty information. the nature of the data provided by each technique is somewhat different. "Consequently, the purpose of this investigation was twofoid. First, we attempted to demonstrate that the shear punch and ball microhardness tests are complementary, both in the

*Visiting scientist *from Department* of Nuclear Engineering, Kyushu University, Japan

way the test is conducted and in the way the data from each test can be interpreted. Secondly, we applied this combination of test techniques to investigate the high energy neutron irradiation hardening response of five metals for which results have not been reported previously.

5.2 Materials

We investigated a total of 19 specimens in the form of transmission electron microscopy (TEM) disks taken from five different materials. These were provided courtesy of Ur. H. Heinisch, Westinghouse Hanford Co. The disks were fabricated by punching from sheet stock and deburring by a mechanical polish technique. Each disk carried its own laser-engraved, four digit identification. Approximately half of the discs were unirradiated, while the other half were irradiated at ambient temperature (~ °C) in RTNS-II at Lawrence Livemore National Laboratory as part of HEDL experiments II, III, and IV.[8-9] A summary of the materials, their metallurgical conditions, the specimen identification, and the neutron fluence for each specimen is given in Table 1.

5.3 Experimental Procedure

Both unirradiated and irradiated specimens were first tested using ball microhardness techniques with an automated Tukon® microhardness tester. The technique and equipment are described elsewhere.[6] Unfortunately, the available ball sizes and specimen thicknesses (~ .25 mm) precluded obtaining many data points per specimen. The identation size criteria[6] were violated at intermediate to high loads, and the indentations either became too difficult to see (specimen surfaces were in the as-rolled condition, not highly polished) or too small at low loads. Hence only data obtained with a 0.25 mm diameter ball for loads on the order of 200-700 g were of a valid and observable size. If the specimens had been thicker (~.5mm) or if better surface conditions had been achieved, considerably more data could have been obtained and with a wider range of ball sizes and loads; this in turn means that flow stress over a wider strain range could have been obtained. It is recommended that future irradiations of TEM disks for use a5 microhardness specimens be fabricated with at least 0.5 mm thickness. In addition, specimen surfaces could be improved by polishing prior to testing to extend the strain range of the data obtainable.

Following ball microhardness testing, each specimen was subjected to a shear punch test at room temperature using a 1 mm punch. The technique and apparatus are described in more detail elsewhere.[6] Precautions were taken in the case of both ball microhardness and shear punch testing of irradiated material to minimize personnel doses and contamination of test equipment. However, doses at contact of individual disks were very small (< 2mr/h), and no contamination of either microhardness or shear punch equipment was found after testing and wiping.

5.4 Results and Discussion

Using the correlations described elsewhere, the shear punch data were used to determine yield stress (σ_y), ultimate tensile strength (UTS), work hardening exponent (n), and reduction in area (RA) values for each of the specimens tested. The results of this analysis are shown in Table 2. Tensile data on these specific materials are not available so direct quantitative comparisons cannot be made. However, these data are qualitatively correct and some indirect comparisons can be made. The unirradiated recrystallized materials have relatively low yield strengths (100-200 MPa), high work hardening exponents (n ~.2), and high RA (70-80%); whereas the cold worked material has high yield strength (700 MPa), and low values of n and RA. The values of yield stress (100-200 MPa) for unirradiated Ni and Fe are in agreement with published values of pure fine-grained materials.[10] The values of yield stress and ultimate tensile strength for unirradiated PCA and MFE 316 SS are similar to those reported by Braski and Maziasz[11,12] for PCA in the fully recrystallized condition (σ_y ~ 220 MPa and UTS ~ 529 MPa) and MFE 316 stainless steel in the 20% cold worked condition (σ_y ~ 688 MPa, UTS ~ 791 MPa). Furthermore, the change in yield strength after irradiation can be compared to some literature data, and this point is addressed shortly.

To compare the shear punch data to ball microhardness data, the following was done. A true stress strain curve was determined in log σ-log ε_p space from the shear punch data assuming a relationship log σ = A + n log ε_p, where σ is the true flow stress and ε_p a true plastic strain. The lower terminus was set by $\sigma = \sigma_y$ at ε = .002. Where multiple values of σ were available, the spread in values was treated as an uncertainty range. The upper terminus was determined by σ = UTS at $\varepsilon_p = \varepsilon_u$ = n, assuming the validity of the constitutive relation and Considere's criteria.[13] However, we have noted in previous tensile tests[14] that the value of uniform elongation ε_u can be significantly less than n by as much as a factor of two or more. Hence, we have treated this by evaluating an alternative second terminus at σ_y = UTS at ε_p = 0.5 n and treating the two termini as an uncertainty range. The stress strain curves so constructed are shown in Fig. 1. Superimposed on these are the true stress-strain points evaluated from ball microhardness tests.

TABLE 1

Characteristics of Test Materials

Material	Designation	Condition	ID	Neutron Fluence (n/cm^2)
Pure Nickel	Ni	Fully Recrystallized	1T4X	- -
			1T53	- -
			1TF6	1.057×10^{17}
			1THV	1.105×10^{17}
Pure Iron	Fe	Fully Recrystallized	7XUV	- -
			7XZT	- -
			7XVU	9.60×10^{16}
			7XXT	9.74×10^{16}
Nickel-5 wt% Silicon	Ni-5 Si	Fully Recrystallized	55N4	- -
			55N4	- -
			55U3	6.12×10^{17}
			55V1	6.36×10^{17}
Prime Candidate Alloy for Path A, Austenitics	PCA	Fully Recrystallized	46ZE	- -
			46XT	- -
			46AT	6.18×10^{16}
			46U5	2.87×10^{17}
MFE 316 Stainless Steel	MFE 316 SS	40% Cold Worked	4914	- -
			493E	- -
			49A5	6.14×10^{17}

TABLE 2

Mechanical Properties Derived from Shear Punch Tests

Material	Fluence (n/cm^2)	σ_y (MPa)	(avg)	UTS (MPa)	(avg)	n	(avg)	RA (%)	(avg)
Ni	- -	110		320		.20		68	
	- -	112	> (111)	348	> (334)	.24	> (.22)	88	> (78)
	1.1×10^{17}	118		328		.22		84	
	1.1×10^{17}	98	> (108)	329	> (329)	.25	> (.24)	81	> (83)
Ni-5 Si	- -	96		380		.28		72	
	- -	122	> (109)	428	> (404)	.26	> (.27)	88	> (80)
	6.1×10^{17}	255		414		.12		79	
	6.4×10^{17}	250	> (253)	352	> (383)	.10	> (.11)	70	> (75)
Fe	- -	193		336		.13		- -*	
	- -	135	> (164)	336	> (336)	.20	> (.17)	81	
	9.6×10^{16}	193		383		.16		81	
	9.7×10^{16}	167	> (180)	373	> (378)	.18	> (.17)	81	> (81)
PCA	- -	200		684		.26		- -*	
	- -	191	> (195)	693	> (689)	.26	> (.26)	- -*	
	6.2×10^{16}	224		734		.25		- -*	
	2.9×10^{17}	237		685		.23		- -*	
MFE	- -	685		1066		.11		- -*	
	- -	685	> (685)	1070	> (1068)	.11	> (.11)	42.4	
	6.1×10^{17}	740		1029		.09		49.6	

*Scale change during tests resulted in uncertain displacement evaluations in the latter portion of the test, hence disallowing RA determinations.

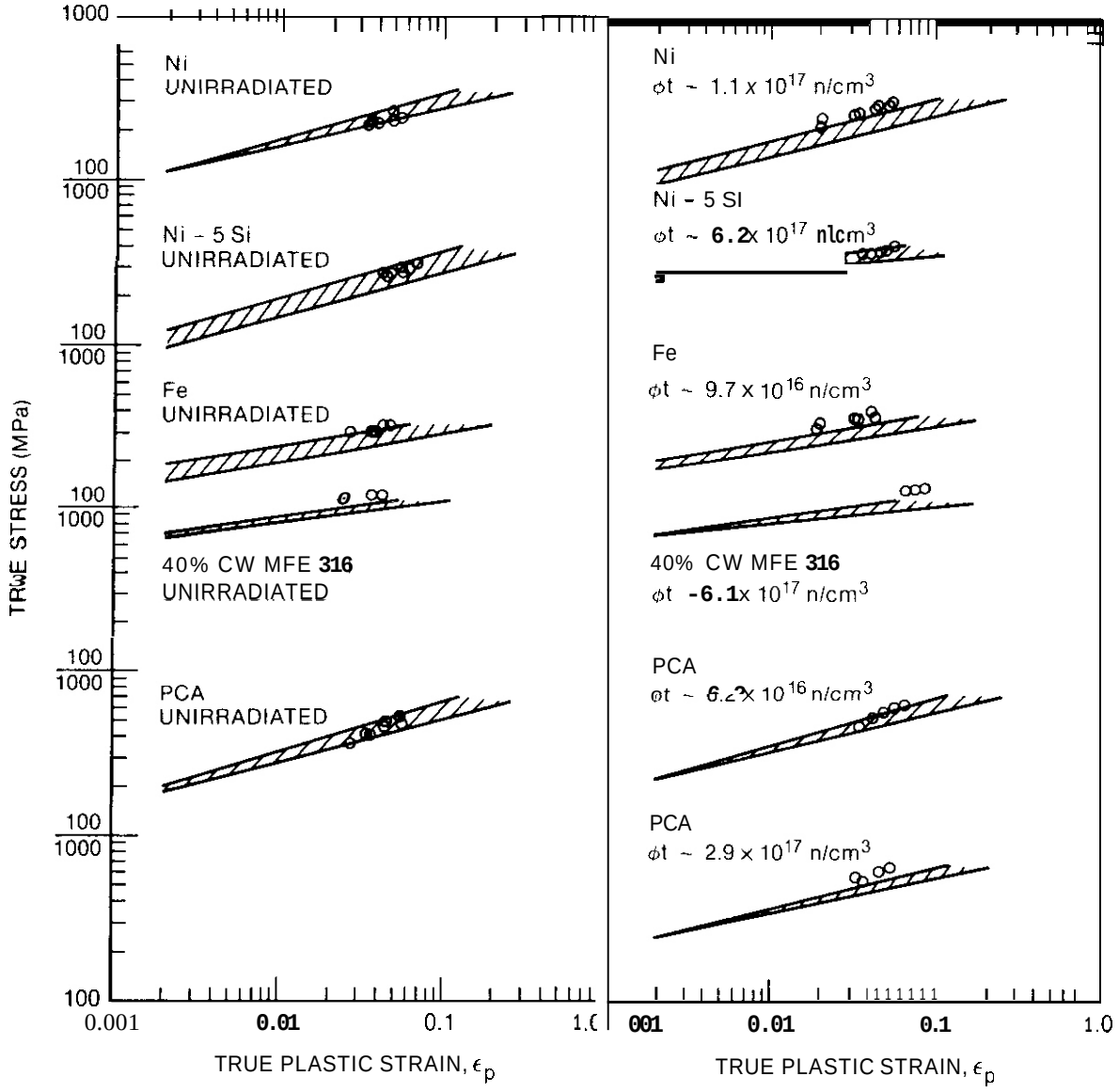

Figure 1: Comparison of ball microhardness data with stress-strain curves derived from shear punch data for both unirradiated and irradiated material.

Agreement between ball microhardness data and curves derived from shear punch data is quite good except in a few instances. In the case of Fe, the ball microhardness data were corrected for strain rate sensitivity effects by procedures outlined elsewhere[6] using an assumed strain rate sensitivity of $m = d \log \sigma / d \log \dot{\varepsilon} \sim .06$ which is typical for mild steels. If m were actually larger than this, the microhardness data would be shifted down relative to the stress strain curves. In the case of MFE 316 SS, the yield strength of the material approaches 1/2.5 the yield strength of the ball material. Hence, there may have been some ball deformation in these tests which would lead effectively to higher predicted values of stress.[15] In the remaining cases, small discrepancies might be attributable to uncertainties in both shear punch and microhardness data and to uncertainties arising from the procedures by which the stress strain curves were constructed. Indeed, we have found that ball microhardness data tend to be systematically high relative to actual tensile data for a majority of materials. However, even for those cases where microhardness data do not fall on the stress-strain curves, the slopes of the two data sets are comparable. In any event, the overall agreement between microhardness and shear punch data suggests that the procedure by which shear data were used to construct stress strain curves is a good approximation. Moreover, the use of microhardness data to evaluate shear data demonstrates the complementary nature of the test data and the usefulness of performing more than one test technique.

The effects of irradiation determined from shear punch tests are given in Table 2. Except for the case of Ni-5 Si, the effects of irradiation on σ_y, UTS, n, and RA are small or negligible. For purposes of comparison, we have evaluated the change in yield stress as a function of fluence for the metals in Table 2 and plotted these data against curves determined for similar materials by other researchers.[16-23] Figure 2 compares the data obtained for PCA and MFE 316 SS with the trend curves determined for solution annealed 316 stainless steel by Vandervoort et al.[20] at LLNL using miniature tensile specimens, and by Panayotou et al. at HEDL using miniature tensile specimens[18] and conventional microhardness tests.[19] Different heats of steel were used in each case, which may explain in part why the two trend curves do not completely overlap. Although PCA is a Ti modified 316 stainless steel and thus has a somewhat different composition than 316 stainless steel, the data fall in the trend band of solution annealed 316 stainless steel data. However, the yield strength change for the cold worked MFE 316 of $\Delta\sigma_y \sim 55$ MPa at 6.4 x 10^{17} n/cm^2 falls slightly below the trend band. While this yield strength change is small relative to the unirradiated value of σ, and thus is subject to a greater uncertainty than values of $\Delta\sigma_y$ for the PCA and pure metals, it suggests that the pre-existing dislocation network has suppressed the initial hardening response. This is in agreement with low temperature fission reactor irradiation data on 316 stainless steel.[22]

Figure 3 compares yield strength changes for Fe, Ni, and Ni-5 Si to yield strength versus fluence curves determined for V and Ti by Bradley and Jones[16] and for Cu, Cu-5 Al, Cu-5 Ni and Cu-5 Mn by Zinkel and Kulcinski.[17] The trend curve determined by Zinkle and Kulcinski for Cu, Cu-5 Al, and Cu-5 Ni is in agreement with that determined by Brager et al.[21] for the same materials and with Mitchell et al.[23] for pure Cu. (It's also interesting to note that the trend lines for Cu and PCA are similar.) However, while Brager et al. found no differences between the response of Cu-5 Mn and pure Cu, Zinkle and Kulcinski reported a shorter incubation time for hardening and hence a greater hardening at a given fluence for Cu-5 Mn, as shown in Fig. 3. The data obtained on Fe and Ni in this study show little hardening at 1 x 10^{17} n/cm^2 in agreement with the response observed for V and Ti. However, the hardening was less than that observed for Cu at the same fluence; in addition, Panayotou reported ~20% increase in hardness in Ni after 1 x 10^{17} n/cm^2.[27] The hardening response of Ni-5 Si on the other hand was quite large and similar to the response observed by Zinkle and Kulcinski for Cu-5 Mn.

It is interesting to note that the ratio of atomic radii for Si/Ni (1.94) and Mn/Cu (1.88) are significantly less than 1, whereas Ni and Cu have similar radii and Al has a larger radius than Cu. Moreover, at room temperature, the Mn in Cu and Si in Ni are close to the solubility limits, whereas Al is well below its solubility limit and Cu-Ni is an isomorphic system.[24] Hence, there may be an irradiation induced precipitation response occurring in both Ni-5 Si and Cu-5 Mn. Although Brager et al.[21] reported only defect clusters in Cu-5 Mn which were similar in size and number density to those observed in Cu and Cu-5 Ni, they also concluded that 70% of the defects in Cu-5 Mn were smaller than the resolution limit of their microscope. In addition, it can be seen from Table 2, that for Ni-5 Si, the predicted work hardening exponent decreases dramatically with increasing hardening. This suggests that the defects formed might be shearable, hence contributing to work softening; and such a response would be expected to give rise to flow localization. This behavior is typical of Fe-Cu alloys, for instance, where small shearable bcc copper precipitates, invisible in TEM, can be nucleated by either thermal aging[25] or irradiation[26] and give rise to both hardening and flow localization. Hence, for future research, it would be interesting to examine the microstructure of this alloy and look for evidence of flow localization with techniques applicable to small specimens.[5,14]

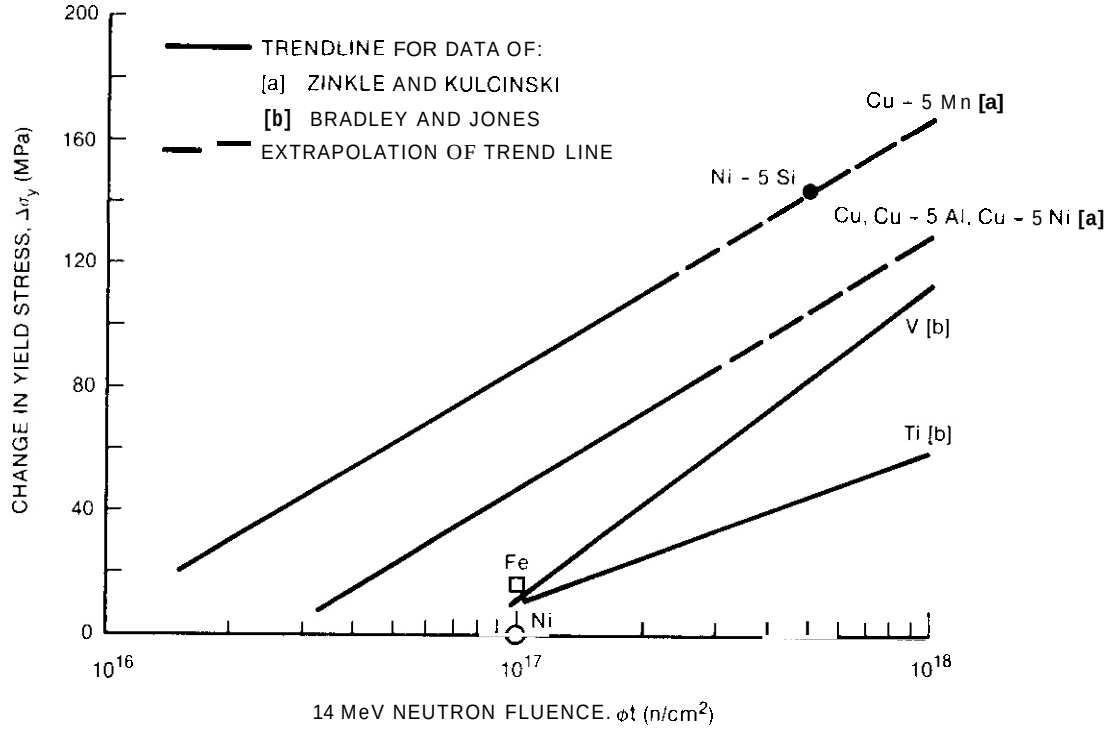

Figure 3: Comparison of yield strength changes of Ni, Fe, and Ni-5 Si with $\Delta\sigma_Y$ vs. ϕt curves determined in other investigations.

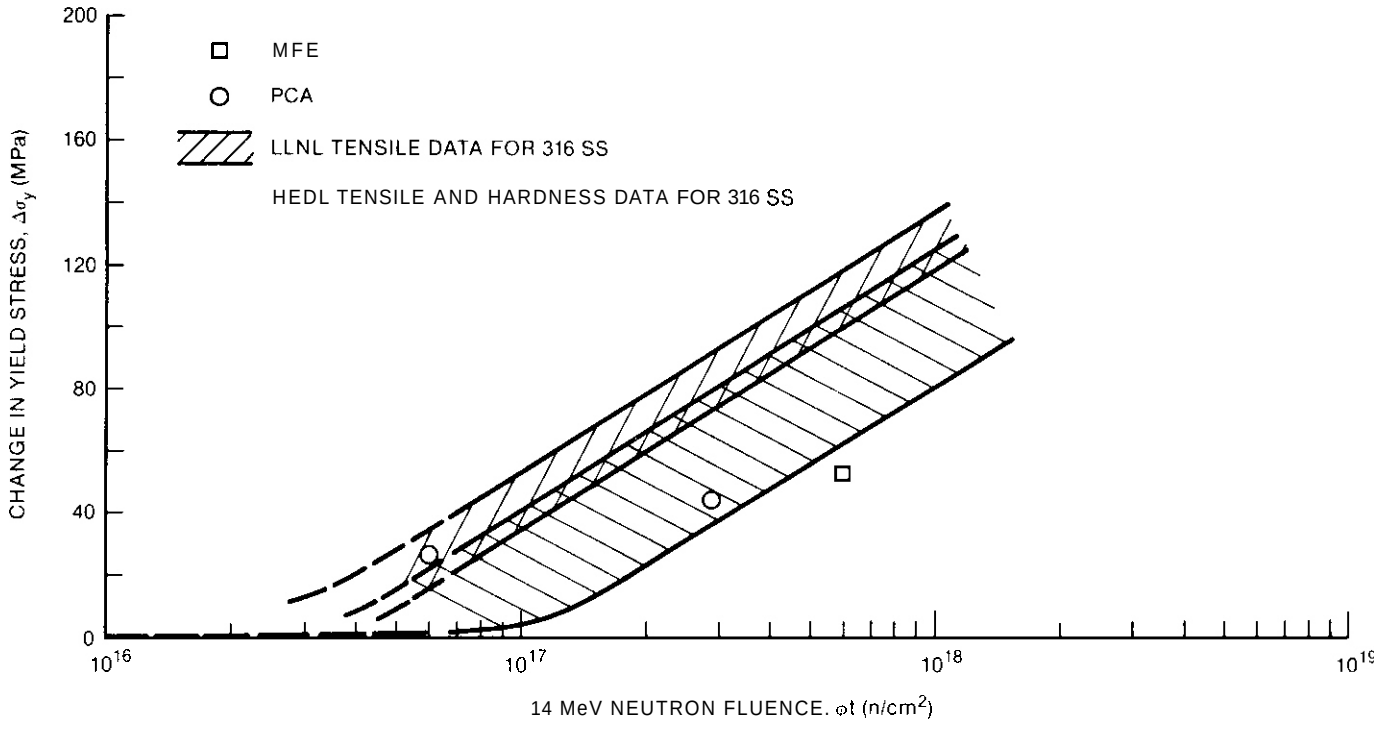

Figure 2: Comparison of yield strength changes of PCA and MFE with $\Delta\sigma_Y$ vs. ϕt curves determined in other studies for solution annealed 316 stainless steel.

5.5 Conclusions

We have investigated the irradiation hardening response of 5 metals irradiated in RTNS-II to fluences up to 6.4×10^{17} n/cm^2. Both ball microhardness techniques and shear punch test techniques were used to evaluate mechanical property changes. It was found that:

1. Only a limited amount of microhardness data could be obtained because of indentation size constraints imposed by specimen thickness and indentation observability. It is recommended that future hardness disks be fabricated at least 0.5 mm thick. Additional data could also be obtained if specimen surfaces were polished prior to testing.

2. Ball microhardness data and shear punch data are complementary and can be used to construct approximate stress-strain curves for the test material.

3. Both unirradiated and irradiated values of mechanical properties were in reasonable agreement with data obtained in other studies on comparable material.

4. The irradiation hardening response was greatest for Ni-5 Si and similar to that reported by Zinkle and Kulcinski for Cu-5 Mn. Irradiation hardening in Ni-5 Si was accompanied by a drop in work hardening exponent, suggesting that the extended defects produced by irradiation might be shearable. This may be an irradiation induced precipitation effect similar to that observed in Fe-Cu alloys and warrants further investigation.

6.0 References

1. G.E. Lucas and N. Panayotou, J. Nucl. Mater., 103/104 (1981) 1527.
2. G.E. Lucas and C. Pendleton, J. Nucl. Mater., 103/104 (1981) 1539.
3. M. Dooley, G.E. Lucas, J.W. Sheckherd, J. Nucl. Mater. (1981) 1533.
4. G.E. Lucas, J. Nucl. Mater., 117 (1983) 327.
5. M. Jayakumar and G.E. Lucas, J. Nucl. Mater., 122/123 (1984) 840.
6. G.E. Lucas, J.W. Sheckherd, G.R. Odette, "Shear Punch and Microhardness Tests for Strength and Ductility Measurements", Proc. of Symp. on Use of Nonstandard Subsized Specimens for Irradiated Testing, ASTM, Albuquerque, NM, 9/83.
7. G.E. Lucas, G.R. Odette, J.W. Sheckherd, P. McConnel, J. Perrin, "Subsized Bend and CVN Specimens for Irradiated Testing", *Ibid*.
8. N.F. Panayotou, R.W. Powell, E.K. Opperman, DOE/ET-0065/6, Department of Energy (1979) 84.
9. N.F. Panayotou and E.K. Opperman, DOE/ET-0065/7, Department of Energy (1979) 65.
10 Metals Handbook, Vol. 1, ASM, Metals Park, OH, 1980.
11 D.N. Braski and P.J. Maziasz, DOE/ER-0045/9, Department of Energy (1982).
12 D.N. Braski and P.J. Maziasz. DOE/ER-0045/10, Department of Energy (1983)
13 Considére, Ann. ponts et chaussees, 9, *6* (1885) 574
14 M. Jayakumar, M.S. Thesis, Dept. of Chemical and Nuclear Engineering, University of California, Santa Barbara.
15 D. Tabor, The Hardness of Metals, Clarendon Press, Oxford (1951).
16. E.R. Bradley and R. Jones, J. Nucl. Mater., 103/104 (1981) 901

17. S. Zinkle and G. Kulcinski, "14 MeV Neutron Radiation-Induced Microhardness Changes in Copper Alloys", in Proc. Symp. on Use of Nonstandard Subsized Specimens for Irradiated Testing, ASTM, Albuquerque, NM, Sept., 1983.

18. N.F. Panayotou, R.J. Puigh, E.K. Opperman, J. Nucl. Mater., 103/104 (1981) 1523.

19. N. F. Panayotou, DOE/ER-0046/10, Department of Energy (1982) 77.

20. R.R. Vandervourt, E.L. Raymond, C.J. Echer, Rad. Eff., 45 (1980) 191.

21. H.R. Brager, F.A. Garner, N.F. Panayotou, DOE/ER-0046/6, Department of Energy (1981) 81.

22. F.A. Garner, M.L. Hamilton, N.F. Panayotou, G.O. Johnson, J. Nucl. Mater., 103/104 (1981) 803.

23. J.B. Mitchell, R.A. Van Konynenburg, C.J. Echer, O.M. Parkin, UCRL Preprint, UCRL-77357, Rev. 1.

24. R. Hultgren et al., Selected Values of the Thermodynamic Properties of Binary Alloys, ASM, Metals Park, OH, 1973.

25. E. Hornbogen and R.C. Glenn, Trans. TMS-AIME, 218 (1960) 1064.

26. G.R. Odette, Scripta Met., 11 (1983) 1183.

27. N.F. Panayotou, DOE/ER-0046/1, Department of Energy (1980) 69.

RADIATION-INDUCED SEGREGATION OF PHOSPHORUS IN FUSION REACTOR MATERIPLS

J.L. Rrimhall, D.R. Baer, R.H. Jones (Pacific Northwest Laboratory)

1.0 Objective

The purpose of this study is to determine the critical material and irradiation parameters which control the radiation induced segregation of impurity elements in fusion reactor materials.

2.0 Sumnary

Bombardment of iror-phosphorus and nickel phosphorus alloys to very low **dose** levels has not produced significant surface segregation of phosphorus. These ohservstions rule out the possibility that radiation induced segregation may **he** very rapid in there alloys and the phosphorus laver formed at low dose would be subsequently removed by ion sputterinp as radiation continued. The observation confirms the conclusion that the magnitude of radiation induced segrcnation is inherently much less in these alloys compared t.o 316 stainless steel. Radiation induced segregation of phosphorus in an Fe t 25% Ni t .022% P 7-phase alloy was somewhat greater than in the ferritic alloys, hut also considerably less than in 316 SS.

3.0 Prnqram

Title: Mechanical Properties
Principal Investigator: R. H. Jones
Affiliation: Pacific Northwest Laboratory

4.0 Relevant OAFS Program Plan Task/Sub-Task

Subtask II.C.14 Models of Flow and Fracture Under Irradiation
Suhtask II.C.1 Effect of Material Parameters on Microstructure

5.0 Accomplishments and Status

5.1 Introductinn

Radiation induced segregation (RIS) of alloying elements to interfacial sinks is a well established phenomenon. Various physical and mechanical properties can be altered by radiation induced segregation of certain elements. Segregation of such impurity elements as phosphorus to the qrain boundaries may have a marked effect on such properties as fracture toughness, hydrogen embrittlement, stress corrosion or corrosion fatigue. The radiation induced segregation of impurity elements has not been widely studied, however, and is the main subject of the current research reported here.

The radiation induced segregation of phosphorus and other impurity elements in a variety of candidate fusion reactor alloys has been previously reported **(1-3).** This research bas utilized heavy ion irradiation to induce segregation near the free surface of the alloys. In the present work, the dose dependence *of* the phosphorus segregation in iron and nickel alloys **was** extended to very low doses. In addition, a phosphorus-containina, iron-nickel γ-phase alloy has also been studied.

5.2 Experimental Details

The surface segregation of phosphorus was analyzed in ferritic HT-9, Fe + .03 %P, Fe + .1 %P, Ni + .03 %P and Fe + 25% Ni + .022 %P. The HT-9 was obtained from the fusion materials stockpile and the prior heat treatment reported previously (1). The iron-phosphorus, nickel-phosphorus and iron-nickel-phosphorus alloys were annealed at 1325K for 30 min. and furnace cooled. The specimens were mechanically polished and oiven a final electrnpolish after the heat treatments to remove any degree of thermal segregation. All the alloys were irradiated with 5 MeV Ni^{++} ions to dose levels ranginq from 0.02 to 1.2 dpa at 875 K. The near surface composition after irradiation was analyzed by Auger Flectron Spectroscopy (AES). The concentration profiles of up to six elements were obtained by sputter profiling using Ar ions in the AES chamber. A sputter removal rate of 0.05nm/min was used for the near surface region and the rate was increased at. greater depths from the surface. Full range AES scans were periodically taken to check the entire compositional spectrum. The data is presented as the peak height ratio (PHR) of the particular element to the bulk iron (or nickel) signal. The iron signal was changinq rapidly in the region of maximum phosphorus roncentration, so the iron signal in the bulk reqion was considered more appropriate for normalizinq the data.

5.3 Results and Discussion

The PHR for phosphorus as a function of the radiation dose in dpa is shown in Figure 1 for a number of alloys. Although some phosphorus segregation was evident at 0.02 dpa in the Fe+.03P and Ni+.03P alloys, the maximum segregation occurred at doses nearer to 0.2 dpa. The segregation decreased at still higher doses. The segreaation in the Fe+0.1%P alloy did not show much variation with dose up to 1 dpa. The absolute values of the phosphorus peak heights in these alloys are not much ahove background so there is considerahle uncertainty in the data. HT-9 shows the least amount of radiation induced segregation of all the alloys studied. For comparison, the dose dependence for phosphorus segregation in 31655, taken from the previous work (3), is also shown.

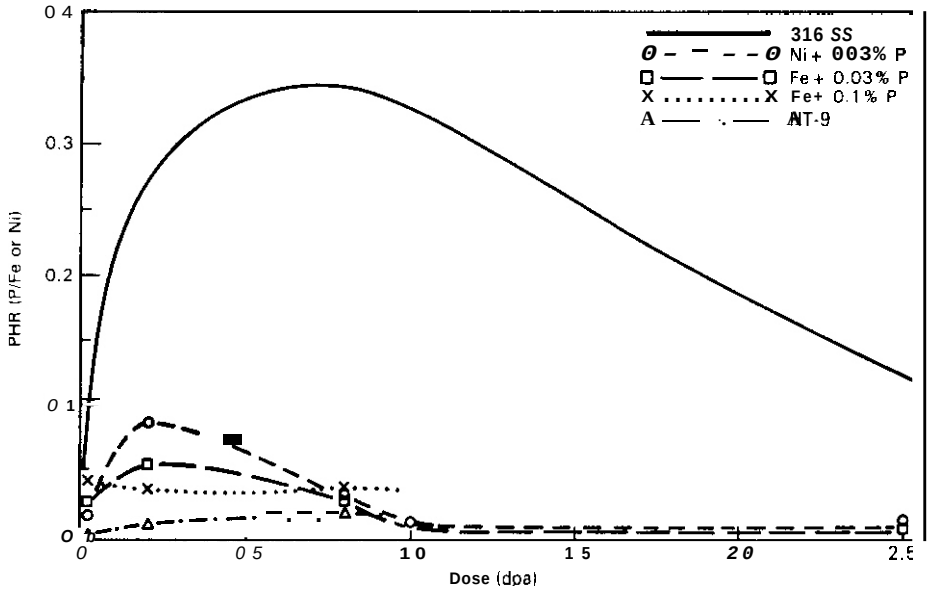

FIGURE 1. The dose dependence of the surfare seqregation of phosphorus in ferritic and nickel alloys during ion bombardment at 600°C. The curve for 316SS is shown for comparison.

A small, but measurable, degree of phosphorus segregated to the free surface during irradiation of an Fe + 25% Ni + .022% P alloy. This alloy represents a simple austenitic alloy with a low level of minor alloying and impurity elements. The radiation induced seoregation is comparable t.o that observed in the Fe-P and Ni-P alloys. Typical sputter profiles are shown in Figure 2.

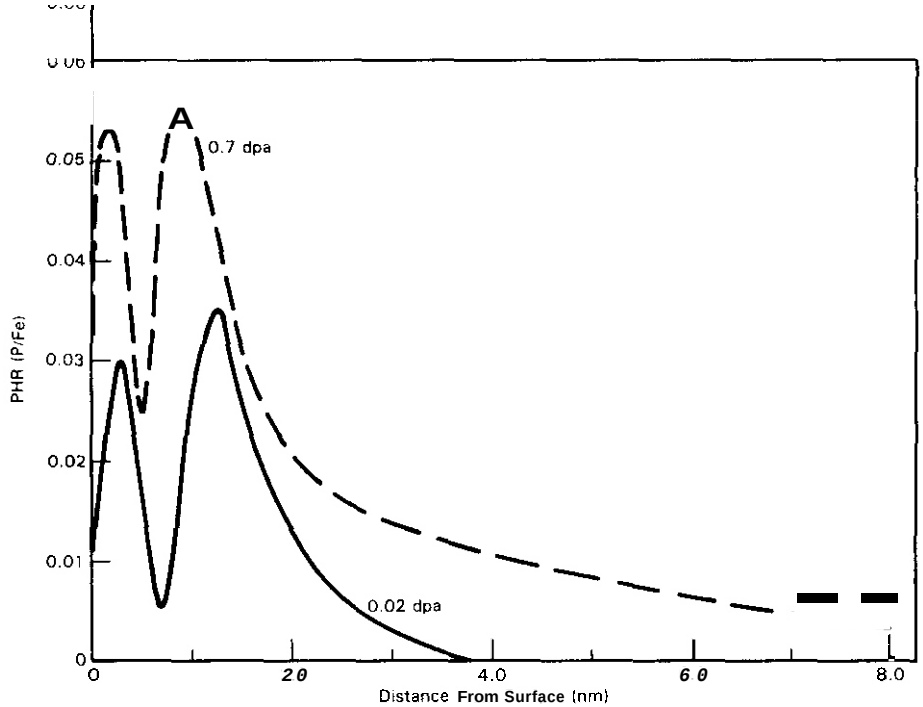

FIGURE 2. AES sputter profile for phosphorus in an Fe + 25 Ni + .022 P alloy after ion bombardment at 600°C. Two ion dose levels are shown.

The douhle peak in the sputter profiles for phosphorus shown in Figure ? was observed in other alloys as well. The minimum in the phosphorus concentration generally coincided with a maximum in the sulfur concentration. It is likely that the sulfur is replacinp the phosphorus in the near surface region. The behavior of the sulfur was erratic and nonreproducible however, i.e., there was no clear indication of a radiation induced segregatior or depletion of sulfur. Sulfur sometimes segregated in thermal control specimens as well. Ihe sulfur effect exemplified hy the dnuhle peak makes it difficult to know what the true phosphorus segregation would be in the absence of sulfur.

The observation of only a small degree of phosphorus segregation in the alloys at very low doses eliminates the possibility that RIS could he very rapid in ferritics. The reasoning is that rapid segregation would produce a segregated phosphorus layer at very low doses. This layer would already have been removed by sputtering if the initial observations were made at higher dose levels. However, the trend in the dose dependence in the ferrous and nickel alloys is similar to that in stainless steel in that a maximum in the segregation occurs at a moderate dose level hetween 0.5 to 1.0 dpa. It is concluded that less RIS of phosphorus in ferritic alloys compared to 316SS as an inherent alloy property and not a result of experimental anomalies.

RIS of phosphorus is also less in alloys with the same crystal structure as 316SS, namely the Ni+.03P alloy and Fe+25Ni+.03P alloy. This suggests that the 316SS mav he somewhat anomalous in showing such a strong RIS of phosphorus. High energy electron irradiation in an HVEM was also ohserved to produce a strong RIS of phosphorus to grain boundaries in 316 stainless steel (4). The austenitic stainless steels are complex alloys with many minor and impurity elements and a plausible reason for the stronq effects of radiation or segrepation is not possihle at this time.

5.4 References

1. J. L. Brimhall, D. R. Baer and R. H. Jones, "Radiation Induced Segregation in Candidate Fusion Reactor Alloys", J. Nucl. Mat., 103 & 104 (1981) 1379.

2. J. L. Brimhall, D. R. Baer and R. H. Jones, "Effect of Radiation on Phosphorus Segregation", J. Nucl. Mat. 117 (1983) *218.*

3. J. L. Brimhall, D. R. Baer and R. H. Jones, "Radiation Induced Phosphorus Segregation in Austenitic and Ferritic Alloys", J. Nucl. flat., 127 & 1.23, (1984) 196.

4. K. Nakata, I. Masaoka, Y. Katano, K. Shiraishi, "Radiation Induced Segregation of P, Si and Cr at Grain Boundaries in Type 316 Stainless Steel", to be published.

CHAPTER 5

CORRELATION METHODOLOGY

REIRRADIATION OF HFIR SPECIMENS IN FFTF

H. R. Brager and F. A. Garner (Hanford Engineering Oevelopment Laboratory)
P. J. Maziasz (Oak Ridge National Laboratory)

1.0 Objective

The object of this effort is to determine whether large levels of helium substantially alter the development of neutron-induced swelling in austenitic alloys.

2.0 Summary

A series of AISI 316 and PCA specimens previously irradiated in HFIR to doses ranging from 10 to 44 dpa have been measured to determine their density and then included in the MOTA irradiation experiment for continued irradiation in FFTF. These specimens were divided into two subsets to he discharged after 30 and 60 dpa.

3.0 Program

Title: Irradiation Effects Analysis (AKJ)
Principal Investigator: D. G. Doran
Affiliation: Hanford Engineerinq Development Laboratory

4.0 Relevant Program Plan Task/Subtask

Task II.C.2 Effects of Helium on Microstructure

5.0 Accomplishments and Status

5.1 Introduction

Two alternative interpretations of a unique but limited set of data have been advanced in an attempt to predict the influence of large levels of helium on the swelling of AISI 316[1,2]. Whether or not large amounts of helium can preclude the development of the ~1%/dpa swelling rate typical of the Fe-Ni-Cr austenitic system[3] has not yet been demonstrated to everyones satisfaction. It has also been proposed that interactions between helium huhbles and TiC precipitates in titanium-modified steels can substantially alter the swelling behavior[4]. In the absence of large helium levels Ti-modified steels have been shown to swell like 316 in the post-transient regime[5,6].

In an attempt to test the various predictions a series of specimens irradiated in the HFIR reactor have been incorporated into the MOTA experiment to accumulate large displacement levels (30 and 60 dpa) without adding significantly to the large helium levels (500-3600 appm) already attained in HFIR. The specimens are in the form of TEM disks and were irradiated to doses of 10.5, 22 and 44 dpa at nominal temperatures of 400, 500 and 600°C. The alloys included in the experiment are the N-lot heat of AISI 316 and PCA, both in the annealed and cold-worked conditions.

TABLE 1

SPECIMEN IRRADIATION CONDITIONS AND MICROSTRUCTURE

Alloy/ Condition	Specimen Identification	HFIR Irradiation Conditions			Microstructural Conditions		Total cvf Swelling (%)	Dislocation Structure	Precipate Microstructure
		Temperature (°C)	dpa	Helium (at. ppm)	Cavity Size (d. nm)	Concentration (m-3)			
PCA. SA	(6) ED-65, -98, -70. -80, -69. -94		None				None	Solution annealed	Same medium-sized MC particles from fabrication
	(1) ED-16	400	~10.5	~520	None detectable	(n.d)	(n.d)	High concentration of Frank loops	n.d.
	(1) ED-19	400	~22	~1700 (bimodal)	2.5 6.9	1.5×10^{23} 3×10^{21}	0.2	Some network and many Frank loops	Coarser MC, some γ', and possibly some G phase
	(1) ED-90	400	4 4	6600	5.9	8.2×10^{22}	0.94	Some network and and many Frank loops	Coarser MC and some γ'
	(2) ED-15. -18	500	~22	~1700 (bimodal)	2.2 10.1	7.8×10^{22} 9.1×10^{21}	0.84	Network and Frank loops	Coarser γ', a little MC, possibly some G
	(1) ED-01	600	~22	1750 bubbler. matrix voids. ppt. voids	6.1 21.9 53	1.3×10^{22} 1.3×10^{21} 3.3×10^{19}	1.7	Network and larger frank loops	Coarse G phase, some fine MC, and γ'
	(1) EO-72	600	"44	~3600 bubbles, matrix voids, ppt. voids	4.9 28 41	2.1×10^{22} 1.1×10^{21} 1.13×10^{21}	6.9	Network and some small Frank loops	Coarse G phase, little or no MC and γ'
PCA. 25% CY	(2) EC-99. -68	None			None		None	Cold worked network	None
PCA. 25% CY	(1) EC-04	400	-22	~1700	2.3	2.1×10^{23}	0.13	Network plus many Frank loops	Tremendous concentration of fine HC
	(1) EC-92	400	"44	~3600	3.0	2.4×10^{23}	0.37	Network plus many frank loops	Fine and coarser MC
N-lot 316, 20% CW	(1) AD-04	400	~22	~1475 (bimodal)	3.2 5.4	7.4×10^{22} 1.6×10^{21}	0.14	Network plus many Frank loops	Some coarser MC (VC?), very little γ'
	(2) AO-19 -34	500	-22	4475 (bimodal)	4.0 9.8	3.7×10^{22} 1.7×10^{21}	0.25 0.25	Network plus Frank loops	Many medium-sired M_6C particles
	(I) AD-20	500	4 4	~3000 bubbler, matrix voids, ppt. voids	5.8 13.3 60	7.2×10^{22} 9.9×10^{21} 1.7×10^{19}	3.6	Network plus Frank loops	Tremendous density of medium and coarse M_6C
	(I) AD-53 -56	600	~22	~1475 bubbler, matrix voids	4.5 11.8	2.2×10^{22} 3×10^{21}	0.52	Network plus Frank loops	Some γ' in matrix. coarse M_6C on faulted bands
	(2) AD-?	600	4 4	~3000 bubbler, matrix voids, ppt. voids	9.3 29.3 86	2.5×10^{21} 2.7×10^{21} 1.86×10^{19}	5.9	Loose network	A tremendous amount of coarser M_6C
N-lot 316, SA	(2) AG-3, -6	500	~22	~1475 Not measured (n.m.)				n.m.	n.m.
	(2) AG-5, -9	600	~22	~1475 (n.m.)				n.m.	n.m.

Duplicate specimens were exdnlined hy transmission electron microscopy at Oak Ridge National Laboratory and were chosen to provide a large variety of starting microstructures. A description of these microstructures is given in Table I.

5.2 Status of Experiment

Density measurements have been made at Westinghouse Hanford Company on all specimens. The specimens were then suhdivided into eleven groups. Each group consists of one alloy (316 or PCA) to he irradiated at one irradiation temperature (400, 500 and 600°C) to one dose level (either 30 or 60 dpa). Due to specimen limitations there are no 316 specimens at 400°C and 30 dpa, although there are 316 specimens at 400°C and 60 dpa. All eleven groups of specimens are now being irradiated in FFTF.

6.0 REFERENCES

1. H. R. Brager and F. A. Garner, J. Nucl. Mater., 117 (1983) 159-176.
2. G. R. Odette, P. J. Maziasz and J. A. Spitrnagel, J. Nucl. Mater., 103-104 (1981) 1289.
3. F. A. Garner, J. Nucl. Mater., 122 & 123 (1984) 459.
4. P. J. Maziasz, J. Maziasz, J. Nucl. Mater., 122 & 123 (1984) 472.
5. F. A. Garner, Swelling Behavior of Titanium-Modified AISI 316 Alloys, DAFS Quarterly Progress Report DOE/ER-0046/17, May 1984, p. 102.
6. F. A. Garner and H. R. Brager, "Influence of Titanium on the Neutron-Induced Swelling of Austenitic Alloys," this report.

7.0 Future Work

This effort will resume upon discharge of the MOTA-IC and MOTA-1D experiments.

8.0 Publications

None

INFLUENCE OF TITANIUM ON THE NEUTRON-INDUCED SWELLING OF AUSTENITIC ALLOYS

F. A. Garner and H. R. Brager (Hanford Engineering Development Laboratory)

1.0 Objective

The object of this effort is to use breeder reactor data to forecast the potential swelling behavior in fusion devices of titanium-modified alloys such as the fusion candidate alloy designated PCA.

2.0 Sumnary

Addition of titanium to variants of AISI 316 stainless steel does not significantly alter the eventual swelling behavior of this class of steel during neutron irradiation. In qeneral, titanium additions only temporarily suppress the onset of swellinq.

3.0 Program

Title: Irradiation Effects Analysis (AKJ)
Principal Investigator: D. G. Doran
Affiliation: Hanford Engineering Development Laboratory

4.0 Relevant OAFS Program Plan Task/Subtask

Substask II.C.l Effects of Material Parameters on Microstructure

5.0 Accomplishments and Status

5.1 Introduction

It now appears that all austenitic alloys eventually swell at ~1%/dpa during fast reactor irradiation.[1] This swelling regime is preceded by a transient regime which is sensitive to many environmental and material variables. The transient regimes of austenitic alloys are longest for solute-laden and cold-worked alloys, of intermediate duration for annealed solute-modified alloys and shortest for solute-free or aged solute-modified alloys. Aged alloys also exhibit the most abrupt transition reqime, the least temperature dependence of swelling and the least curvature in swelling. This pattern of behavior continues to be observed in more recently acquired data sets, an example of which is shown in Figure 1 for a common Russian steel.[2]

In another report it was shown that the addition of titanium and other solutes to alloys with composition similar to that of AISI 316 does not change their basic swelling behavior from that of unmodified 316 stainless steel.[3] While the transient reqimes of Ti-modified alloys at 540°C were shown to he somewhat longer than that of AISI 316, both modified and unmodified alloys eventually approached the 1%/dpa swelling rate characteristic of all Fe-Ni-Cr austenitic alloys.[1]

In the previous report,[3] however, it was not demonstrated that 1%/dpa had actually been reached in that series of annealed Ti-modified steels. Additional data are now available to prove this point. It was also not demonstrated in that report that the conclusions drawn at 540°C held equally well at other irradiation temperatures.

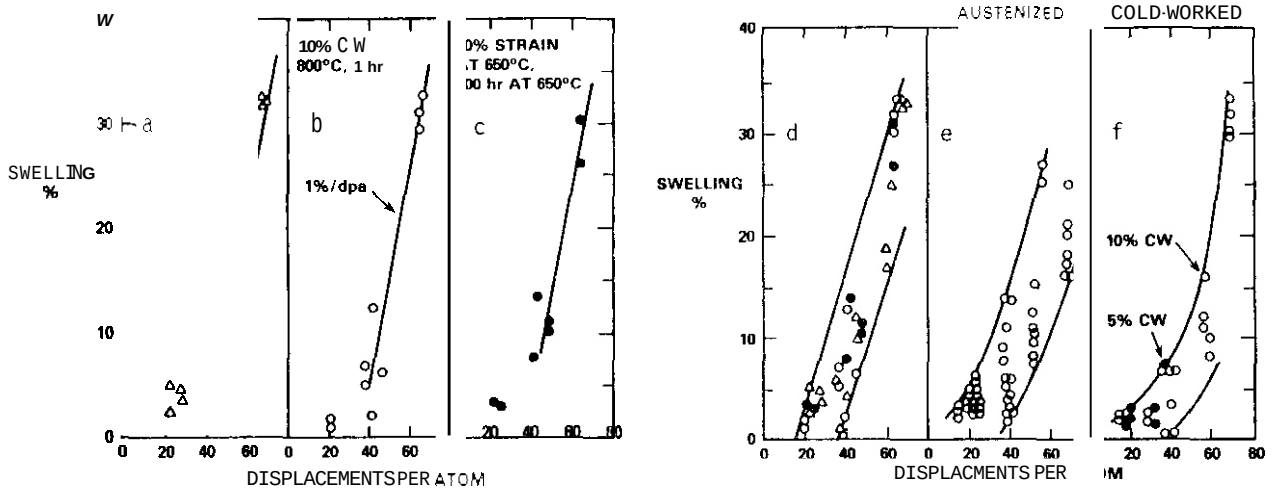

FIGURE 1. Swelling Observed in OKh16N15M3B steel at 400 - 550°C in the BOR-60 Fast Reactor After Various Thermomechanical and Ageing Treatments.(2) Fig. 1d is a compilation of a, b, and c.

This latter consideration is particularly important when one considers the nature of swelling of AISI 316 in response to irradiation temperature. In general, the swelling of annealed 316 exhibits two peaks with temperature, the relative maqnitudes of which are determined by solute levels (particularly carbon) and the relative flux and temperature profiles across the irradiated component.(4-6) While cold-working temporarily suppresses both peaks, its influence is most pronounced for the low temperature peak. Titanium additions, however, tend to temporarily suppress the hiqh temperature peak and accentuate the low temperature peak. Given this opposing interaction between titanium and cold-work at lower temperatures, it is important to establish whether titanium-modified steels exhibit swelling hehavior typical of titanium-free austenitic alloys in this temperature regime. Additional data are now available *to* address this question.

5.2 Results

In the previous report,(3) swelling data at 540°C were provided for twenty-one solution-annealed Ti-modified alloys irradiated in the MV-III experiment to 6.3 and 10.0 x 10^{22} n cm^{-2} (E > 0.1 MeV). This corresponds to 32 and 50 dpa. Data is now available for some of these alloys at 14.9 x 10^{22} n/cm^{-2} (~75 dpa) and can be used to test the assertion that titanium modifications do not preclude the inevitability of swelling rates of ~1%/dpa. Figure 2 shows that as the swelling level increases at 540°C, the swelling rate indeed approaches 1%/dpa.

In an earlier report it was shown that one way to demonstrate the comparable rate of swelling development in various related alloys is to plot the average swelling rate over an exposure interval vs. the maximum swelling observed in that interval.(7) This approach allows comparison of relative swelling rates while reducing the impact of variations in transient duration. Figure 3 shows that the average swelling rate over the two fluence intervals at 540°C indeed approaches 1%/dpa in a consistent manner. It is important to recognize that at low swelling levels the average swelling rates are strong underestimates of the actual swelling rate at the end of the exposure interval.

Figure 3 also contains comparable data for many of these same alloys irradiated at 425°C to 7.6 and 11.3 x 10^{22} ncm^{-2} (E > 0.1 MeV). This corresponds to 38 and 56.5 dpa. Note that at 540 and 425°C the swelling rates are quite consistent, even though, as shown in Figure 4, the transient regimes in this particular alloy series are longer at 475°C than at 540°C.

5.3 Discussion

While the preceeding section demonstrates that the swelling rate at 425°C evolves in a comparable manner to that of 540°C, it does not conclusively prove by itself that swelling at 425°C will not divert from that trend later. The earlier report did show, however, that the LS-1 alloy irradiated in another experiment exhibited swelling behavior at high fluence typical of AISI 316 even in the lower temperature range.(3) Whereas the current study concentrates on annealed steel, this inevitability of 1%/dpa behavior was demonstrated earlier for LS-1 in both the annealed and cold-worked conditions.(3)

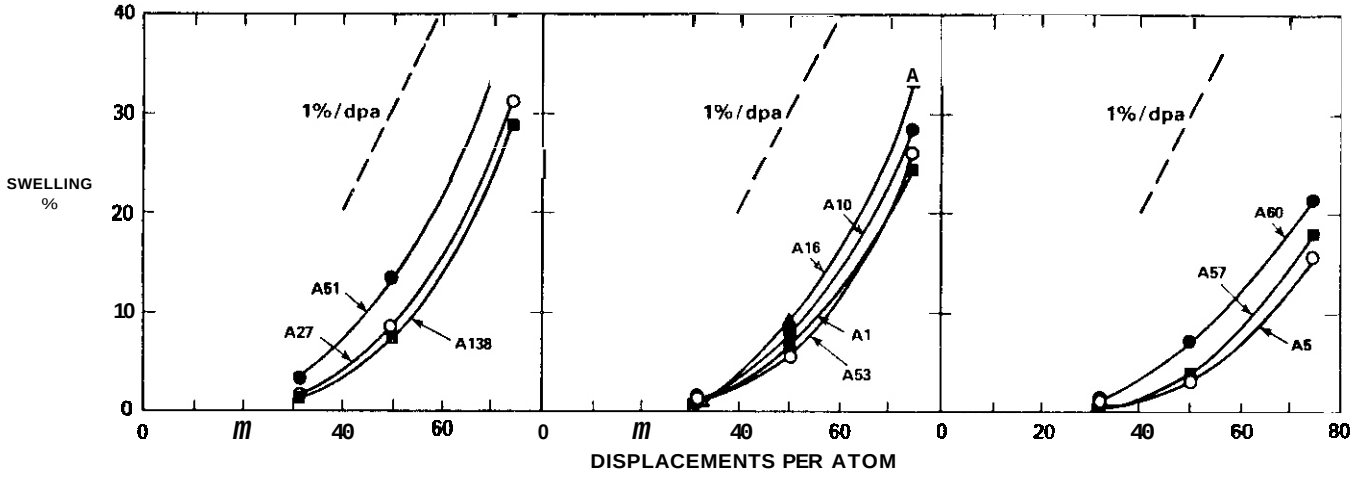

FIGURE 2. Swelling of Various Annealed Titanium-Modified AISI 316 Steels at 540°C in EBR-II. The alloy compositions are given in reference 3.

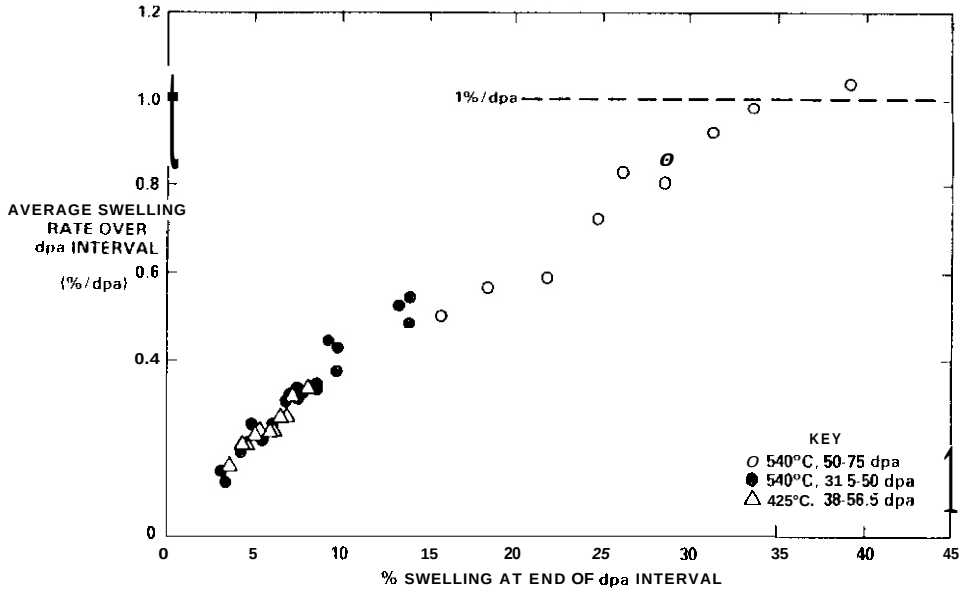

FIGURE 3. Average Swelling Rate Observed in Annealed Ti-modified Steels at 425 and 540°C, Showing Approach of Swelling Rate to 1%/dpa with Increasing Swelling.

5.4 Conclusions

Addition of titanium to variants of AISI 316 stainless steel does not appear to alter the eventual swelling behavior of this class of steels. In general, titanium additions only prolong the duration of the transient regime of swelling.

6.0 References

1. F. A. Garner, J. Nucl. Mater. 122 & 123 (1984) 459-471.

2. V. A. Krasnoselov, V. I. Prokhorov, A. N. Kolesnikov, and Z. A. Ostrovskii, Atomnaya Energiya, 54 (2) 1983, 111-114.

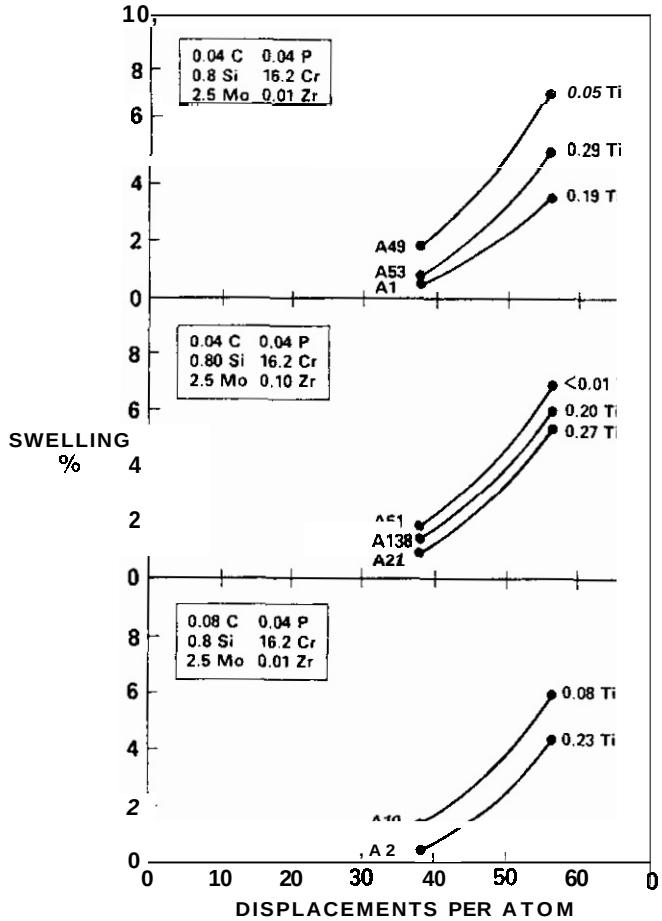

FIGURE 4. Swelling of Various Titanium-Modified AISI 316 Steels at 425°C in EBR-II.

3. F. A. Garner, "Swelling Behavior of Titanium-Modified AISI 316 Alloys," Damage Analysis and Fundamental Studies Quarterly Progress Report DOE/ER-0046/17, May 1984, 102-108.

4. F. A. Garner, in Proc. of AIME Symp. on Phase Stability During Irradiation, Pittsburgh, PA (Oct. 5-9, 1980) 165-190.

5. L. A. Lawrence and J. W. Weber, Trans. ANS (Poster Session), San Diego, CA, June 18-23, 1978, 225.

6. R. A. Weiner and A. Boltax, "Comparison of High Fluence Swelling Behavior of Austenitic Stainless Steels," Effects of Radiation on Materials, ASTM STP 725, D. Kramer, H. R. Brager and J. S. Perrin (Eds.) ASTM (1981) 484-499.

7. F. A. Garner, The Influence of Reactor Spectra and Irradiation Temperature on the Swelling of AISI 316 Stainless Steel, Damage Analysis and Fundamental Studies Ouarterly Progress Report DOE/ER-0046/12 (Feb. 1983) 178-193.

7.0 Future Work

None planned.

8.0 Publications

None

Compositional Micro-Oscillations in Ion-Bombarded Fe-35.0Ni-7.0Cr

H. R. Brager, F. A. Garner (Hanford Engineering Development Laboratory)
T. Lauritren (General Electric Company, Sunnyvale, CA)

1.0 Objective

The object of this effort is to determine the origins of the cornpositional dependence of swelling in Fe-Ni-Cr alloys.

2.0 Summary

The compositional micro-oscillations observed in neutron-irradiated Fe-35.5Ni-7.5Cr at 593°C and 38 dpa have also been found in Fe-35.0Ni-7.0Cr irradiated with nickel ions to 117 dpa at 625°C. The period of the oscillations found in both specimens is on the order of 200-400 nm. During irradiation the matrix of this alloy subdivides toward near-stoichiometric Zones of Fe_3Ni and FeNi, with chromium substituting for iron.

3.0 Program

Title: Irradiation Effects Analysis
Principal Investigator: D. G. Doran
Affiliation: Hanford Engineering Development Labordtory

4.0 Relevant DAFS Program Plan Task/Subtask

Subtask II.C.l Effect of Material Parameters on Microstructure

5.0 Accomplishments and Status

5.1 Introduction

In an earlier report it was shown that the alloy E37, often designated as Elinvar, Fe-35.5Ni-7.5Cr (wt %), exhibited a densification upon irradiation that arose as a consequence of a spinodal-like decomposition of the alloy matrix.[1] This decomposition produced micro-oscillations in composition at 593°C and 38 dpa which involved the enrichment of nickel in some areas while iron and chromium were enriched in others. The peak-to-peak distance between these fluctuations was on the order of 100-200 nm. A hypothesis was advanced that the decomposition of this alloy was related to the gradual loss of swelling resistance during irradiation. It was also proposed that the increasing tendency toward decomposition with increasing nickel content was the mechanism operating to produce the minimum in swelling observed in Fe-Ni-Cr alloys in the vicinity of 40% nickel.[2]

Since the minimum in swelling was observed in both neutron and ion-irradiated alloys,[3] it therefore followed that such micro-oscillations must have occurred in the 5 MeV Ni+ ion-irradiated specimens as well. Since the Fe-Cr-Ni specimens of Johnston and co-workers[3] were still available in the post-irradiation thinned condition, these specimens were forwarded to HEDL for examination by conventional energy dispersive X-ray (EDX) analysis. The regions available for examination were 850-1050 nm from the original foil surface, which corresponds to the peak displacement region examined by Johnston and co-workers. The procedures used in the EDX analysis were identical to those used for the neutron-irradiated specimen. To date, one specimen has been examined, that of Fe-35.0Ni-7.0Cr irradiated to 117 dpa at 625°C. Very little swelling (<0.1%) was found by Johnston to have occurred in that specimen.[3]

5.2 Results

Few areas of the as-received specimen were acceptable for the requirements of this analysis. Since the micro-oscillations occur over a small scale, they must be measured in uniformly thin sections which are also relatively large in extent. Such areas must also contain a minimum of microstructural sinks which would tend to alter the composition.

Although there were very few microstructural features in suitable areas of the specimen, compositional traces were obtained starting at features which appeared to be surface contamination particles. Figure 1 shows four such sets of measurements. Note that the period of the oscillations is on the order of 200-400 nm and that the chromium and iron traces tend to be mirror images of that of nickel.

5.3 Discussion

In Figure 2 each of the chromium and nickel points shown in Figure 1 has been plotted to show that they indeed segregate in opposite directions. Similar data points for the neutron-irradiated specimen are also shown. Note that in addition to the similar trend of the two sets of data that there is an offset between the two sets. Although a small offset arises from the slight difference in composition in the two alloys, it is thought that the offset arises primarily from an ion-induced modification of the average composition at the depth examined. Johnston,[4] as well as others,[5-7] have shown that the elemental distribution along the ion path in Fe-Ni-Cr alloys is changed. This is due to the combined influence of the foil surface and the gradient in displacement rate, operating in conjunction with the Inverse Kirkendall effect and other diffusion mechanisms.' Large-area compositional scans (compiled in Table 1) confirm that the average composition at this depth was shifted from the original level.

TABLE 1

LARGE AREA MEASUREMENTS OF AVERAGE COMPOSITION

Area	Cr (wt %)	Ni (wt %)
#1	6.1	33.9
#2	5.8	33.6
#3	6.3	34.5
#4	6.6	34.8
#5	6.6	33.4
#6	6.3	33.9
Average	6.3	34.0

Another interesting point is that the composition at the end-points of the distribution in Figure 2 correspond to $(Fe,Cr)_3Ni$ and (Fe,Cr)Ni. The tendency of E37 to decompose into these two compounds is shown schematically in Figure 3. In other words, small amounts of chromium appear to be substituting for iron in the Fe_3Ni and FeNi near-stoichiometric compounds. This set of end points appears to be more than coincidental for two reasons.

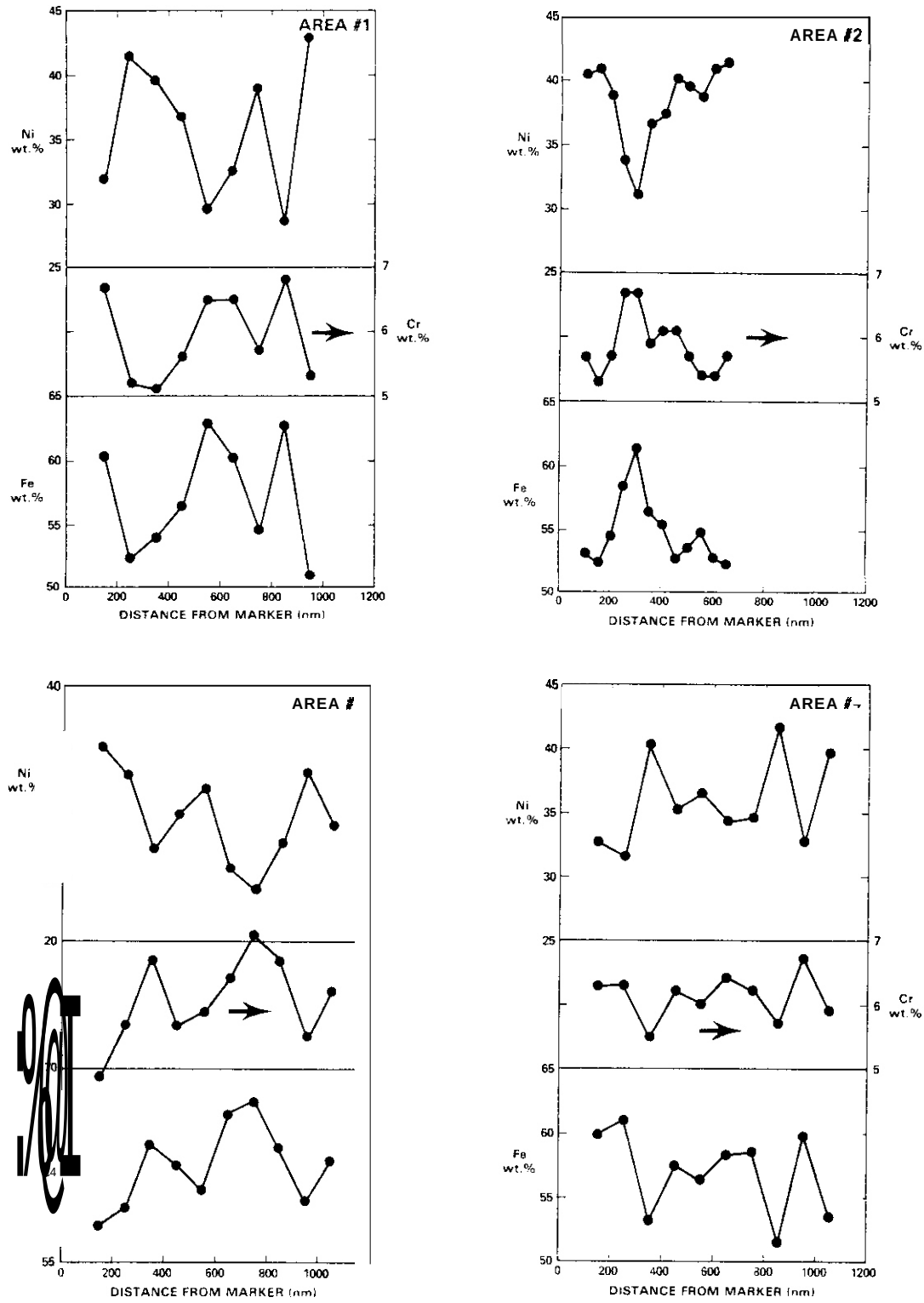

FIGURE 1. compositional Oscillations Observed in Fe-35.0Ni-7.0Cr Irradiated to 117 dpa with Ni^+ Ions at *625°C*

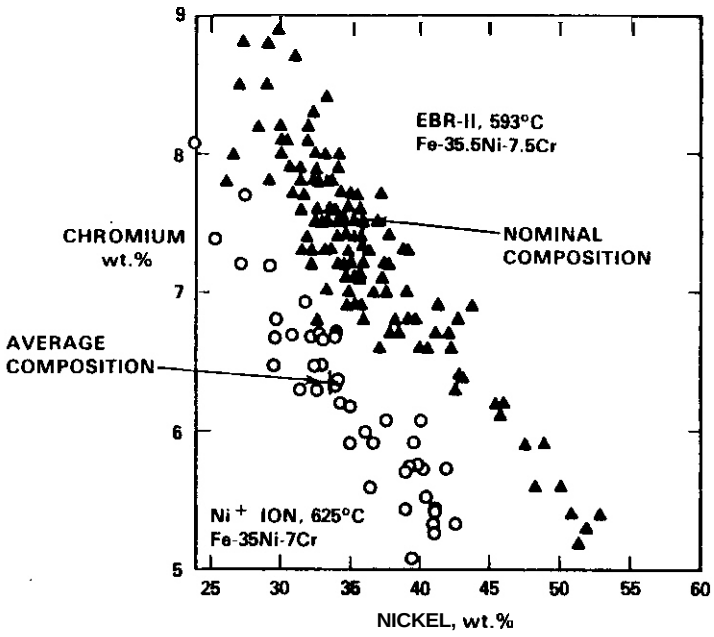

FIGURE 2. Relationship Between Local Nickel and Chromium Levels Observed in Both Neutron and Ion-Irradiated Specimens.

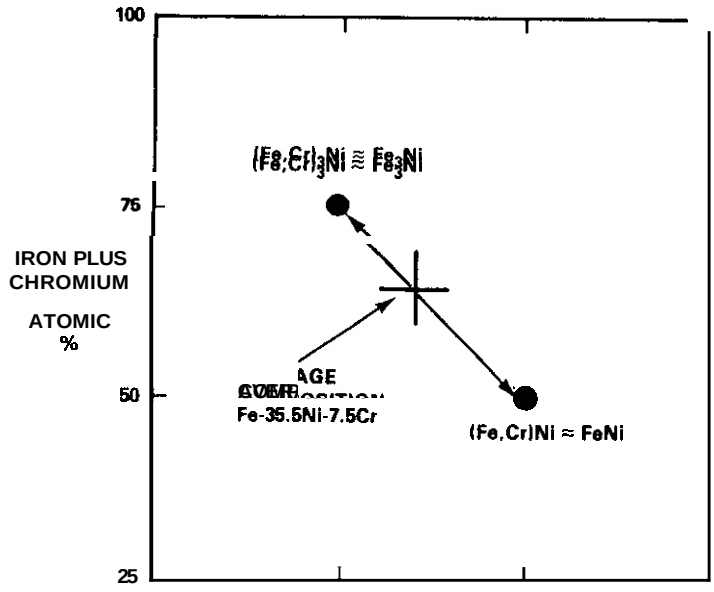

FIGURE 3. Schematic Representation of the Decomposition Process.

First, the electron beam used in the EDX analysis has an effective diameter of one-tenth of the oscillation period but beam scattering within the specimen enlarqes the volume of specimen contributing X-rays to the detector. The oscillations are also assumed to occur over the thickness of the foil. This thickness is typically ~50 nm, or about one-quarter of the oscillation period. Thus the beam tends to average the composition over a substantial volume, yielding a net composition of that volume that is closer to the centroid of the compositional distribution than it is to the actual composition at any one point. Therefore, the actual ranges of composition tend to lie more towards the ends of the distribution than indicated in Figure 2, which is distorted by the averaging of composition in the volume measured by the X-ray procedure.

Second, there is a large amount of published literature that shows that Fe-Ni alloys have a tendency, during either aging or irradiation, to decompose into two f.c.c. phases. Some of these references are listed in Ref. 8-15. Depending on the nickel level of the alloy, the split is either between Fe_3Ni and FeNi or between FeNi and Ni_3Fe. The alloys in the lnvar range (45% Ni) have been extensively studied and are known to split between Fe_3Ni and FeNi. Although chromium additions tend to suppress the ordered phases of these stoichiometric compounds,[16] 7% chromium in this alloy does not appear to totally preclude the tendency of iron and nickel to segregate to near-stoichiometric levels.

According to published literature, the tendency toward decomposition manifests itself in several ways, depending on the composition, temperature history, cold-wnrk level and the presence or absence of irradiation. Both short-range and long-range order have heen observed and several investigators have argued that spinodal decomposition should also occur.[17,18] The compositional micro-oscillations observed in this study may provide the first experimental confirmation of this prediction.

In the neutron irradiation at 593°C, the oscillation period was found to be 100-200 nm, while that of the ion-irradiated specimen at 625°C was 200-400 nm. It appears that the period of oscillation is rather sensitive to irradiation temperature and/or displacement rate.

5.4 Conclusions

The tendency of the Elinvar alloy to decompose during irradiation with spinodal-like micro-oscillations in composition appears to be a general feature of Invar-like alloys at high irradiation temperatures. The period of these oscillations is rather large, increases with temperature and seems to be subdividing the alloy matrix into near-stoichiometric zones of Fe_3Ni and FeNi with chromium substituting for a portion of the iron.

6.0 References

1. H. R. Brager and F. A. Garner, "Microsegregation Observed in Fe-35.5Ni-7.5Cr Irradiated in EBR-II," OAFS Quarterly Progress Report DOE/ER-0046/18 p. 98.

2. F. A. Garner, "A Model Describing the Compositional Dependence of Void Nucleation in Irradiated Fe-Ni-Cr Alloys," this report.

3. J. F. Bates and W. G. Johnston, "Effects of Alloy Composition on Void Swelling," Proc. Inter. Conf. on Radiation Effects on Breeder Keactor Structural Materials, June 19-23, 1977, Scottsdale, AZ, M. L. Bleiberg and J. W. Bennett, eds., AIME 1977, p. 625.

4. W. G. Johnston, W. G. Morris and A. M. Turkalo, ibid, p. 421.

5. N. Q. Lam, J. Nucl. Mater., 117 (1983) p. 106

6. V. K. Sethi and P. K. Okamoto, "Radiation-induced Segregation In Complex Alloys," in ref. 3, p. 421.

7. A. D. Marwick, R. C. Piller and M. E. Horton, "Radiation-Induced Segregation in Fe-Ni-Cr Alloys," Proc. BNES Conf. on Dimensional Stability and Mechanical Behavior of Irradiated Metals and Alloys," Brighton, England, Vol. II, paper 4, 1983.

8. Y. Tanji, Y. Nakagawa, Y. Saito, K. Nishimura and K. Nakatsuka, Phys. Stat. Sol. (a), 56 (1979) p. 513.

9. J. E. Albertson, J. M. Knudsen, N. O. Roy-Poulsen and L. Vistisen, Physica Scripta, 22 (1980) p. 171.

10. Y. Bando, J. Phys. Soc. Japan, 16 (1961) p. 2342.

11. S. Kachi, Y. Bando and S. Higuchi, Japanese J. *of* Applied Physics, 1 (1962) p. 307.

12. V. I. Gomankov, N. I. Nogin and Ye. V. Kozis, Fiz. Met. Metalloved., 55 (1983) p. 125.

13. L. Neel, J. Pauleve, R. Pauthenet, J. Laugier and D. Dautreppe, J. *of* Applied Physics, 35 (1964) p. 873.

14. J. Pauleve, A. Chamberod, K. Krebs and A. Marchand, IEEE Trans. Magnetics, MAG-2, No. 3 (1966) p. 475.

15. Yu. L. Rodionov, G. G. Isfandiyarov and O. S. Sarsenbin, Fiz. Met. Metalloved., 48 (1979) p. 979.

16. K. N. Binnatov, A. A. Katsnelson and Yu. L. Rodinov, Fiz. Met. Metalloved., 39 (1975) p. 1021.

17. J. R. C. Guimaraes, J. Danon, R. B. Scorzelli and I. Souza Arevedo, J. Phys. F, 10 (1980) p. L197.

18. P. L. Rossiter and P. J. Lawrence, Phil. Mag A, 49, (1984) p. 535.

7.0 Future Work

Examination *of* other irradiated Fe-Cr-Ni specimens will continue in order to determine the origin and consequences *of* the radiation-induced decomposition process.

8.0 Publications

None

INFLUENCE OF COLD WORK ON THE NEUTRON-INDUCED SWELLING OF SIMPLE Fe-Ni-Cr TERNARY ALLOYS

F. A. Garner and H. R. Brager (Hanford Engineering Development Laboratory)

1.0 Objective

The object of this effort is to determine the origins of the sensitivity of void swelling in irradiated metals to environmental and material variables.

2.0 *Summary*

The swelling of simple Fe-Ni-Cr ternary alloys in EBR-II appears to be sensitive to both irradiation temperature and cold-work. It is suggested that cold-work interacts with the tendency of Fe-Ni-Cr alloys to order during irradiation and thereby affects swelling.

3.0 Program

Title: Irradiation Effects Analysis (AKJ)
Principal Investigator: D. G. Doran
Affiliation: Hanford Engineering Development Laboratory

4.0 Relevant DAFS Program Plan Task/Subtask

Subtask II.C.1 Effects of Material Parameters on Microstructure

5.0 Accomplishments and Status

5.1 Introduction

In earlier reports it was shown that cold-working of solute-bearing austenitic alloys affects their phase evolution, thereby controlling the composition of the alloy matrix and the onset of void swelling.[1-3] In the absence of solutes such as carbon and silicon, there is very little tendency to form precipitate phases. It was therefore proposed that cold-work might exert no influence on swelling of f.c.c. metals and alloys in the absence of such solutes.[3] This suggestion was supported by observations that low fluence neutron irradiations of pure aluminum, copper and nickel produced either small increases in swelling with cold-work or no change.[4] Holmes[5] also showed that 50% cold-working did not influence the swelling of pure nickel over the range 399-455°C, as shown in Figure 1. To test this hypothesis the swelling of both annealed and 20% cold-worked specimens of "pure 316" (Fe-17Cr-16.7Ni-2.5Mo) designated as alloy P-7 was measured after irradiation in the Oak Ridge Research (ORR) reactor at several temperatures.[6] No effect of 20% cold-work on swelling was observed. It now appears that this result may not have been a fair test of the hypothesis, however.

It was later learned that this alloy contained in excess of 1000 appm oxygen and it appears that void nucleation was dominated by this anomalous aspect of the alloy. One possible indication of this supposition is that the swelling behavior of P-7 in the High Flux Isotope Reactor (HFIR) was completely atypical of that observed in other heats of AISI 316 as well as other Fe-Ni-Cr alloys irradiated in both HFIR and EBR-II. Whereas all Fe-Cr-Ni alloys irradiated to date have exhibited a minimum transient regime of ~10 dpa and a post-transient swelling rate of ~1%/dpa, the P-7 alloy in HFIR had no measurable transient regime and a temperature-independent swelling rate of 0.5%/dpa.[7]

Although many simple Fe-Ni-Cr ternary alloys have been irradiated in EBR-II and reported in the DAFS Quarterly Progress Report series,[8-10] all of these alloys were irradiated in the solution-annealed condition. In the AA-XI experiment, however, both annealed and 30% cold-worked conditions of alloy E20 were irradiated side-by-side in EBR-II at 425 and 540°C to fluences of 3.7 and 4.9 x 10^{22} n/cm^2 (E > 0.1 MeV) respectively. These exposures correspond to 18.5 and 24.5 dpa. Alloy E20 is Fe-24.4Ni-14.9Cr with very low levels of the usual solutes.[8]

5.2 Results

The swelling was determined by immersion density measurements and is shown in Table 1.

TABLE 1

SWELLING OBSERVED IN ALLOY E20 IN THE AA-XI EXPERIMENT

Temperature °C	Displacement Level (dpa)	Alloy Condition	Swelling %
425	18.5	Annealed	12.8*
425	18.5	30% CW	3.8*
540	24.5	Annealed	1.14*
540	24.5	30% CW	4.81**
			3.61**

*Average swelling of four identical specimens exhibiting very small differences in density.
**Separate measurements on two nominally identical specimens.

5.3 Discussion

Contrary to our previous expectations, it appears that cold-working can indeed affect the swelling of solute-free ternary alloys although the results above indicate that swelling can be either increased or decreased, depending on the irradiation temperature. Note in Figure 2 that the swelling of solution-annealed specimens in this study agrees reasonably well with the behavior observed in the same alloy in the AA-VII experiment. This is consistent with the similarity observed between specimens irradiated in the AA-VII and AD-1 experiments.[10]

With some caution, one can make another observation. Note that when the irradiation was performed in the temperature-insensitive regime (400-510°C), cold-working led to decreased swelling. When the irradiation was performed above the order-disorder transition temperature (which lies somewhere in the range 510 < T < 538°C) the effect of cold-work was to increase the swelling. While it is too early to draw definitive conclusions, it appears that this unexpected result may be due to the influence of cold-working in destroying the tendency of the alloys to exhibit short-range order. Ordering processes have recently been implicated in controlling of the swelling behavior of Fe-Ni-Cr alloys.[11-13]

6.0 References

1. Brager, H. R. and Garner, F. A., "Dependence of Void Formation on Phase Stability in Neutron Irradiated Type 316 Stainless Steel," Effects of Radiation on Structural Materials, ASTM STP *683*, J. A. Sprague and D. Kramer, Eds., American Society for Testing and Materials, 1979, pp. 207-232.

2. Garner, F. A. and Porter, D. L., "History Dependence and Consequences of the Microchemical Evolution of AISI 316," Effects of Radiation on Materials: Eleventh Conference, ASTM STP 782, H. R. Brager and J. S. Perrin, Eds., American Society for Testing and Materials, 1982, pp. 295-309.

3. Garner, F. A., "The Microchemical Evolution of Irradiated Stainless Steels," Proceedings of TMS-AIME Symposium on Phase Stability During Irradiation, Pittsburgh, PA, October 5-9, 1980, J. R. Holland, L. K. Mansur and D. I. Potter, Eds., pp. 165-189.

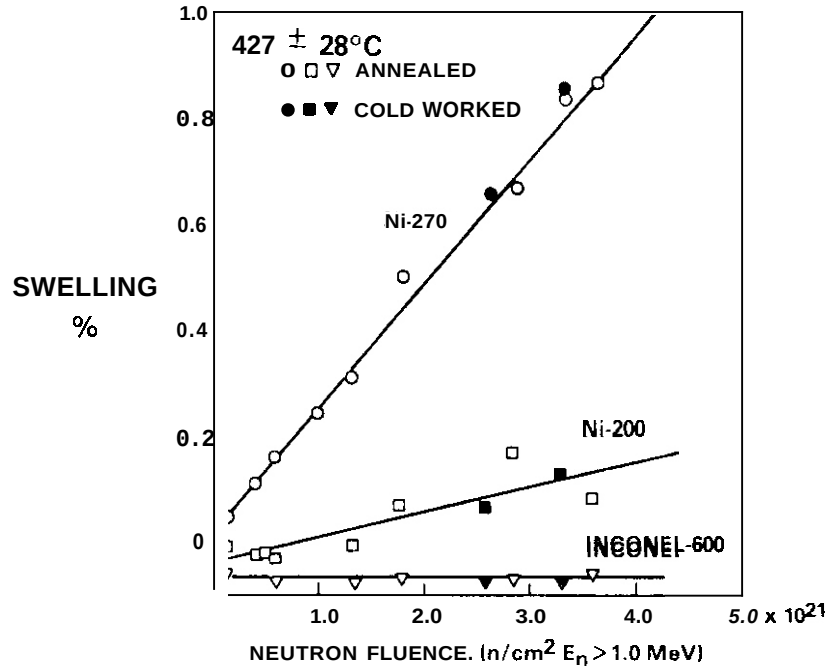

FIGURE 1. Effect of Cold-Work and Impurities on Swelling of Various Nickel Alloys in EBR-II Over the Range 379 to 455°C. (5)

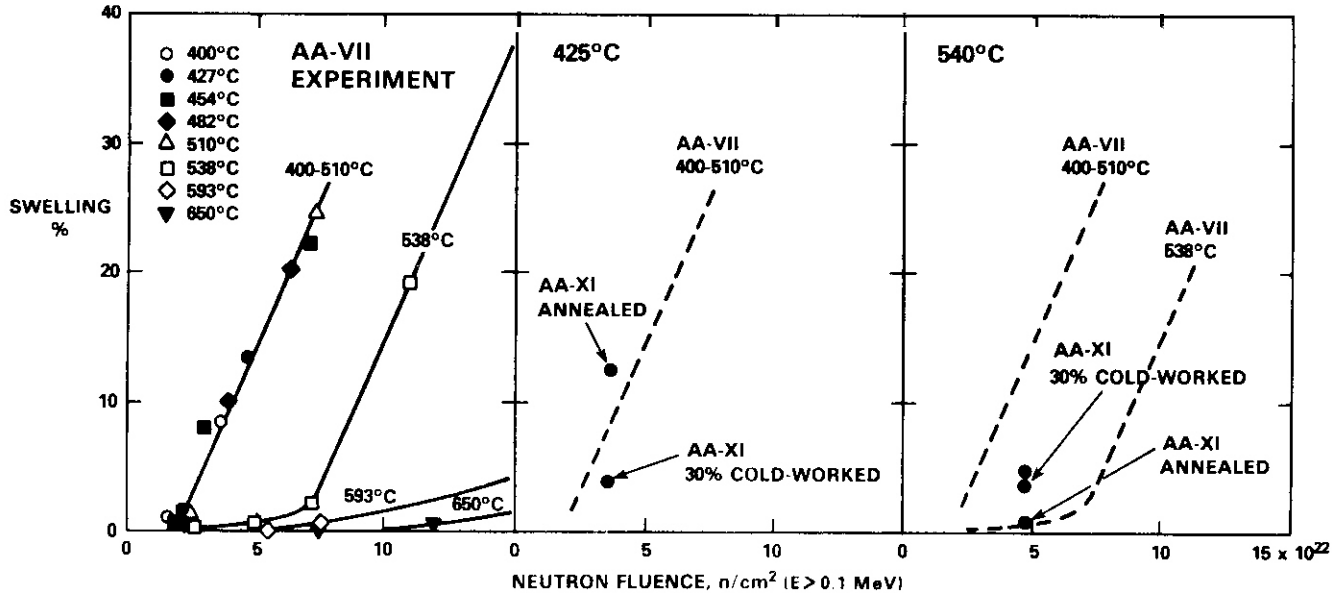

FIGURE 2. Swelling of Alloy E20 (Fe-25Ni-15Cr) in Two Separate Experiments Conducted in EBR-II. The influence of cold-work on swelling can be seen in (b) and (c).

4. Adda, Y., "Report of the CEA Program on investigations of Radiation- Induced Cavities in Metals: Presentations of Some Results," Proc. Symposium on Radiation-Induced Voids in Metals, AEC Symposium Series 26, June 9-11, 1971, Albany, NY, pp. 31-83.

5. J. J. Holmes, Trans. American Nuclear Society, 12, 1969, p. 117.

6. Brager, H. R. and Garner, F. A., "The Influence of Cold Work Level, Solute and Helium Content on the Swelling of 'Pure' AISI 316 (Fe-17Cr- 16.7Ni-2.5Mo)," Effects of Radiation on Materials: Eleventh Conference, ASTM STP 782, H. R. Brager and J. S. Perrin, Ed., American Society for Testing and Materials, 1982, pp. 152-165.

7. Appleby, W. K., Bloom, E. E., Flinn, J. E. and Garner, F. A., "Swelling in Neutron-Irradiated 300 Series-Stainless Steels," in Radiation Effects in Breeder Reactor Structural Materials, M. L. Bleiberg and J. W. Bennett, Eds., the Metallurgical Society of the American Institute of Mining, Metallurgical and Petroleum Engineers, 1977, pp. 509-552.

8. F. A. Garner, "Dependence of Swelling on Nickel and Chromium Content in Fe-Ni-Cr Ternary Alloys, "DAFS Quarterly Progress Report, DOE/ER- 0046/14, August 1983, p. 133, also H. R. Brager and F. A. Garner, ibid, p. 152.

9. F. A. Garner and H. R. Brager, "Swelling of Fe-Ni-Cr Ternary Alloys at High Exposure," DAFS Quarterly Progress Report, DOE/ER-0046/16, February 1984, p. 38.

10. H. R. Brager and F. A. Garner, "Dependence of Swelling of Fe-Ni-Cr Alloys on Chromium and Nickel Content," DAFS quarterly Progress Report, DOE/ER-0046/11, November 1982, p. 221.

11. H. R. Brager and F. A. Garner, "Microsegregation Observed in Fe-35.5Ni-7.5Cr irrddiated in EBR-II" ASTM STP 870 (in press), also in DAFS Quarterly Progress Report, DOE/ER-0046/18, August 1984, p. 98.

12. H. R. Brager, F. A. Garner and T. Lauritzen, "Compositional Micro-oscillations in Ion-Irradiated Fe-35.0Ni-7.0Cr, this report.

13. F. A. Garner, "A Model Describing the Compositional Dependence of Void Nucleation in Irradiated Fe-Ni-Cr Alloys, ASTM STP 870 (in press), also in this report.

7.0 Future Work

This effort will continue, focusing on the examination of these and other Fe-Ni-Cr ternary specimens using electron microscopy and x-ray analysis.

8.0 Publications

None.

SWELLING OF NEUTRON-IRRAOIATEU 85Ni-15Cr at 400-650°C

F.A. Garner (Hanford Engineering Development Laboratory)

1.0 Ohjective

The object of this effort is to determine the factors which control the swelling and creep of irrddiated metals.

2.0 *Summary*

The binary alloy 85Ni-15Cr swells during neutron irradiation in a manner quite unrepresentative of either Fe-Ni-Cr ternary alloys or pure nickel. Chromium additions appear to depress void nucleation in nickel but also appear to suppress the tendency of nickel to saturate in swelling at high exposure. Below a transition temperature somewhere in the range 538°C < T < 593°C the swelling is quite insensitive to irradiation teinperature. Above the transition temperature the swelling behavior is more complex. At these higher temperatures the alloy densifies at low fluences, which is also indicative of the possible occurrence of long or short-range order. **The** swelling transition temperature also appears to coincide with the critical temperature for order-disorder transformation.

3.0 Program

Title: Irradiation Effects Analysis (AKJ)
Principal Investigator: D.G. Doran
Affiliation: Hanford Engineering Development Laboratory

4.0 Relevant DAFS Proqram Plan Task/Subtask

Subtask II.C.l Effects of Material Parameters on Microstructure.

5.0 Accomplishments and Status

5.1 Introduction

In a series of earlier reports it was shown that the parametric dependence of swelling in Fe-Ni-Cr alloys lies primarily in the effect of material and environmental parameters on the duration of the transient regime of swelling.[1,2] It was also shown that the post-transient rate of swelling in all Fe-Ni-Cr alloys was ~1%/dpa, essentially independent of composition. The dependence of the transient duration on nickel content was explained in terms of the competition between the increase in the effective vacancy diffusion coefficent (which lowers the vacancy supersaturation and decreases the void nucleation rate) and the increasing tendency of Fe-Ni alloys to form short-range and long-range order with increasing nickel content.[3] One manifestation of this tendency toward ordering is the generation of compositional micro-oscillations found in both ion and neutron-irradiated Fe-35.5Ni-7.5Cr[4,5]. These micro-oscillations tend to destroy the swelling resistance of high nickel alloys by generating volumes which are enriched in chromium and depleted in nickel, both of which favor void nucleation. These micro-oscillations also lead to significant changes in lattice parameter, causing the alloy to densify. Densification is also known to be a general consequence of disorder-order transitions in the Fe-Ni[6] and Ni-Cr systems[7].

In order to study the correlation between swelling resistance and the tendency toward ordering, the swelling of 85Ni-15Cr in EBR-II was investigated. Nickel-chromium alloys are known to exhibit ordering. This alloy was irradiated in the same experiment which contained the Fe-Ni-Cr alloys described earlier.[1,2] Unfortunately, there was no pure nickel included in these studies for comparison. There are data on the swelling of pure nickel available from other fast reactor irradiations, however.

5.2 Results

Figure 1 shows that the swelling of 85Ni-15Cr in EBR-II is remarkably insensitive to temperature in the range 400-538° and that the rate of swelling increases continually with accumulated exposure. Even at 2.0 x 10^{23} n/cm^2 (E > 0.1 MeV) or ~100 dpa, however, this alloy has not yet reached the swelling rate of 1%/dpa which is characteristic of Fe-Ni-Cr alloys in their temperature-independent regime. Above 538°C the transients are longer, but not in a manner typical of Fe-Cr-Ni alloys since the transient at 650°C is shorter than that at 593°C. Note also that prior to the onset of significant swelling, the alloy densifies ~0.15% at the higher temperatures.

5.3 Discussion

There is only limited neutron irradiation data for pure nickel at high displacement levels. Figure 2 shows that the available data in the range 400-460°C[8-12] indicates that nickel initially swells at ~1%/dpa but tends to saturate in swelling shortly thereafter. This tendency toward saturation at levels below 10% has been observed also in ion and electron irradiation experiments.[13-17] An example of this behavior is shown in Figure 3.

Since the swelling rate of 85Ni-15Cr is continuously increasing, one would expect that nickel would swell more at low displacement levels hut that 85Ni-15Cr would swell more at high displacement levels. As shown in Figure 4, this behavior has actually been observed in comparative 46.5 MeV Ni^+ ion irradiations of pure nickel and Ni-27.5 Cr.[18] Note also in Figure 4 that the saturation level of swelling in nickel must be relatively insensitive to temperature since the swelling curve at 60 dpa is remarkably flat with temperature. Figure 5 shows the dependence of ion-induced swelling in Ni-27.5Cr on both temperature and displacement level. Figure 6 shows that the decrease in the onset of swelling is progressive with chromium content. The Ni-9Cr alloy was irradiated with ions at 525°C only.

Figure 7 indicates that the effect of chromium additions is to depress the void nucleation rate. This is in apparent disagreement with the effect of chromium additions on the swelling of Fe-Ni-Cr austenitic alloys[1,3]. There is one interesting difference in behavior, however, between the Ni-9Cr and Ni-27.5 alloys at 525°C. Both pure nickel and Ni-27.5Cr were observed to cease nucleation by ~2 dpa but the nucleation in Ni-9Cr at 525°C was relatively continuous. The eventual density of voids in the two Ni-Cr alloys was essentially identical however.[18]

If the depression of void nucleation by chromium additions is to be explained in terms of the previously advanced model[3], then either the effective vacancy diffusion coefficient D_V^{eff} of Ni-Cr alloys must be higher than that of pure nickel or the tendency of Ni-Cr alloys to order must be very large. As can be seen from Figure 8, however, the addition of chromium to nickel at 1100°C tends to depress rather than to enhance the diffusion of both nickel and chromium[19]. Another researcher has found that additions of 0-14% chromium to nickel at 1250°C have essentially no effect on the diffusion of either chromium or nickel.[20]

There is, however, ample evidence that both long and short-range order exist in the Ni-Cr system. Short-range order has been found in Ni-11.4Cr[21] and a review of numerous papers on ordering in a wide range of Ni-Cr alloys is contained in Ref. 22. Although short-range order has been observed by many investigators, long range order has also been observed in Ni-25Cr, Ni-29.2Cr and Ni-33.3Cr with critical ordering temperatures of 550, 580 and 590°C[23]. Thus, the Ni-27.5 Cr alloy whose ion-induced swelling is described in Figures 4-6 was irradiated in the temperature regime encompassing the critical temperature. Interpolation of the critical ordering temperatures between that of Ni-11.4Cr and Ni-25Cr yields a critical temperature of ~540°C for the 85Ni-15Cr alloy. This is coincident with the transition temperature observed in the swelling of that alloy in EBR-II.

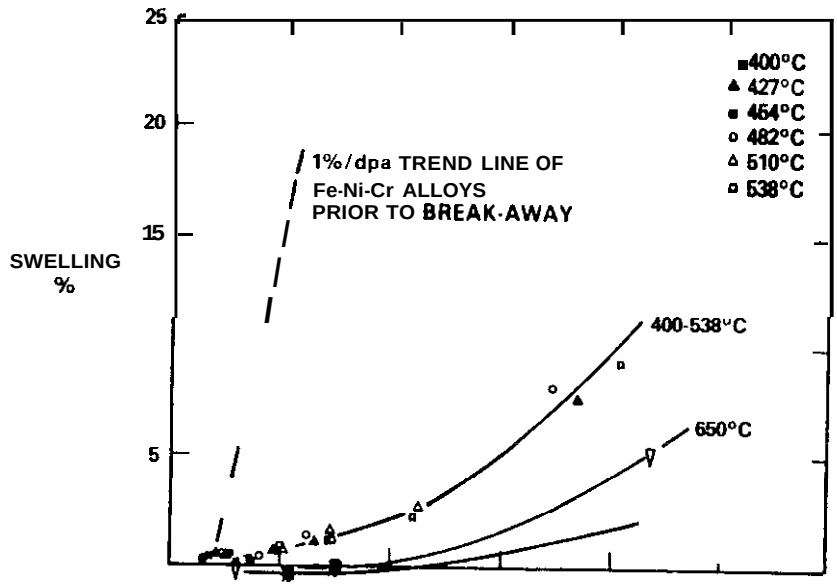

1. Swelling of 85Ni-15Cr irradiated in EBR-II, measured by immersion density.

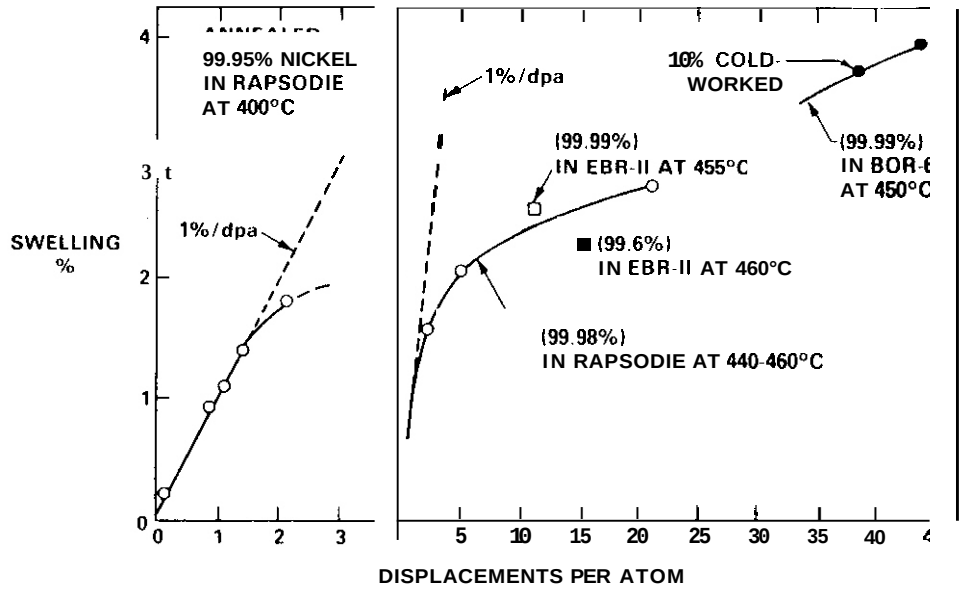

2. Swelling observed in relatively pure nickel in fast reactors at 400°C[8] and at 440-460°C[9-12]. All data are for annealed specimens except for the one 10% cold-worked datum.

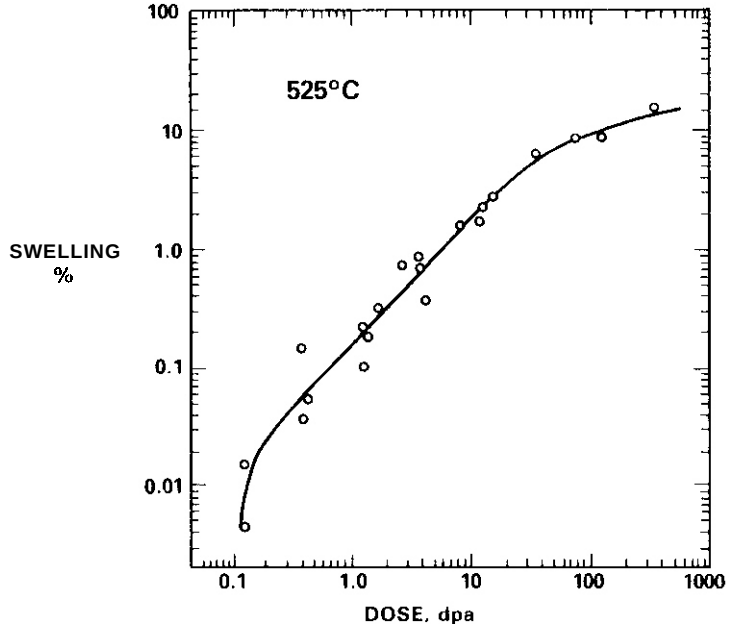

3. Swelling induced in pure nickel by 46.5 MeV Ni^+ ions at 525°C.[15,16]

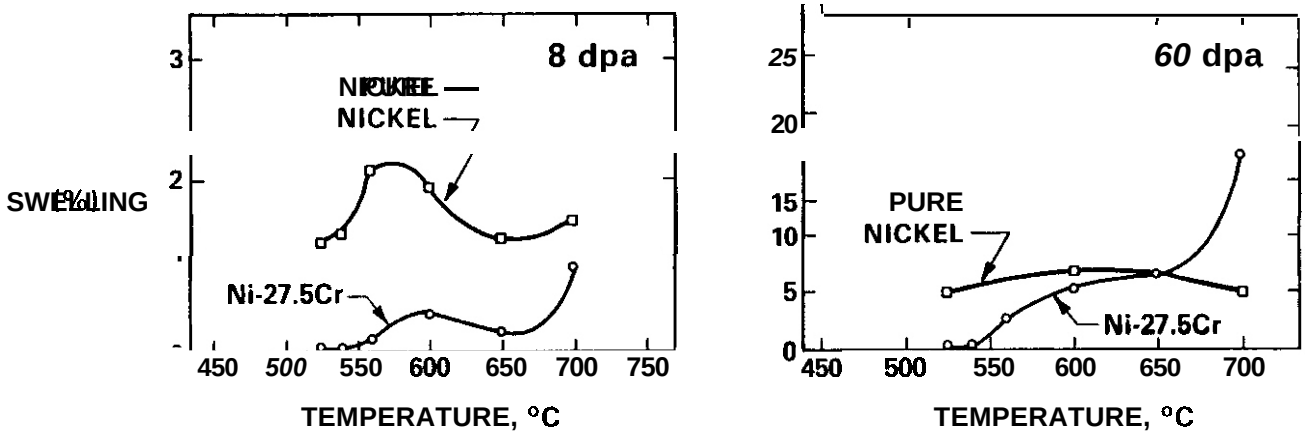

4. Swelling observed in comparative irradiations of pure nickel, Ni-9Cr and Ni-27.5Cr at 8 and 60 dpa with 46.5 MeV Ni^+ ions[18].

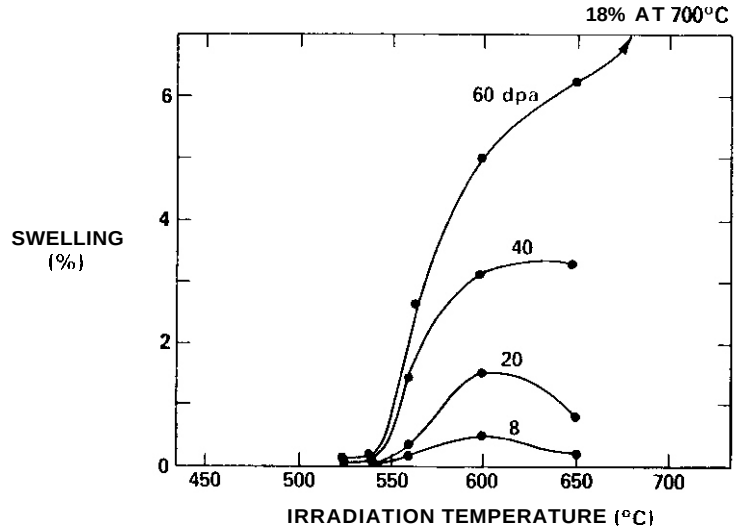

5. Temperature and dose dependence of swelling observed in Fe-27.5Cr irradiated with 46.5 MeV Ni^+ ions[18].

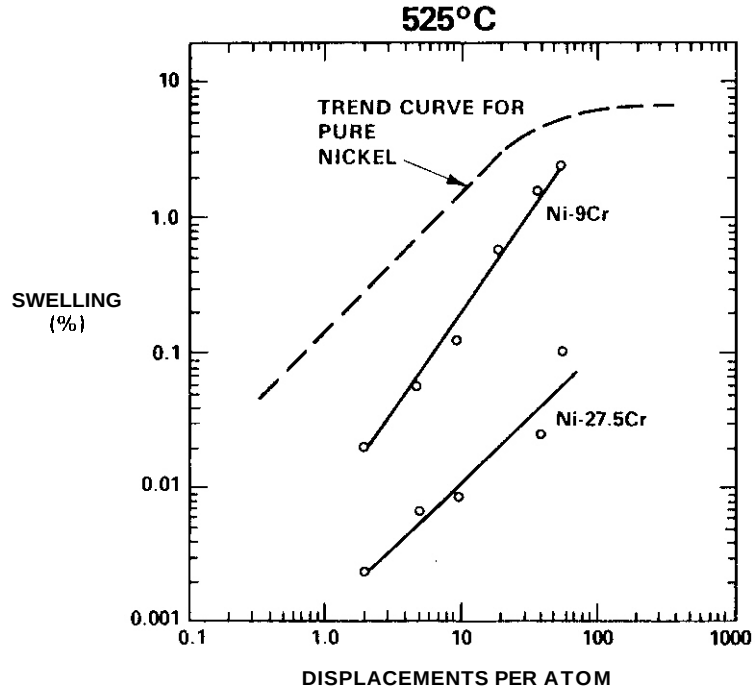

6. Comparison of Ion-induced Swelling of Nickel Alloys at 525°C[18]

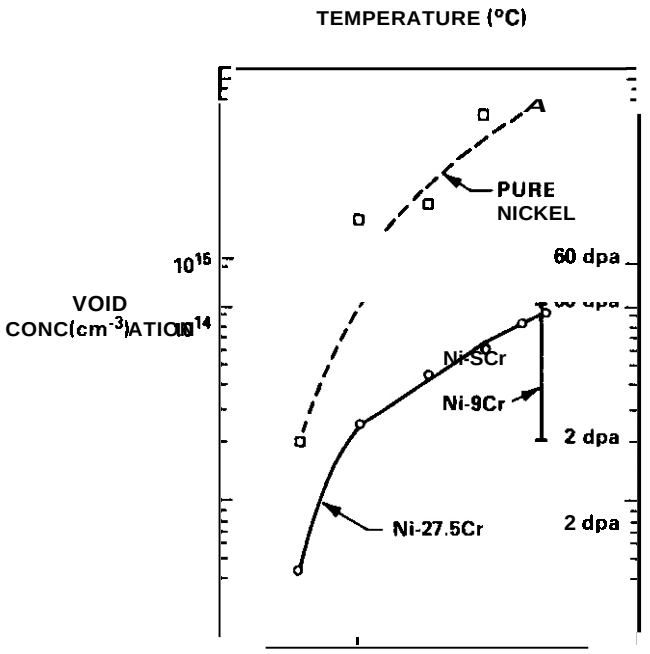

7. Void densities

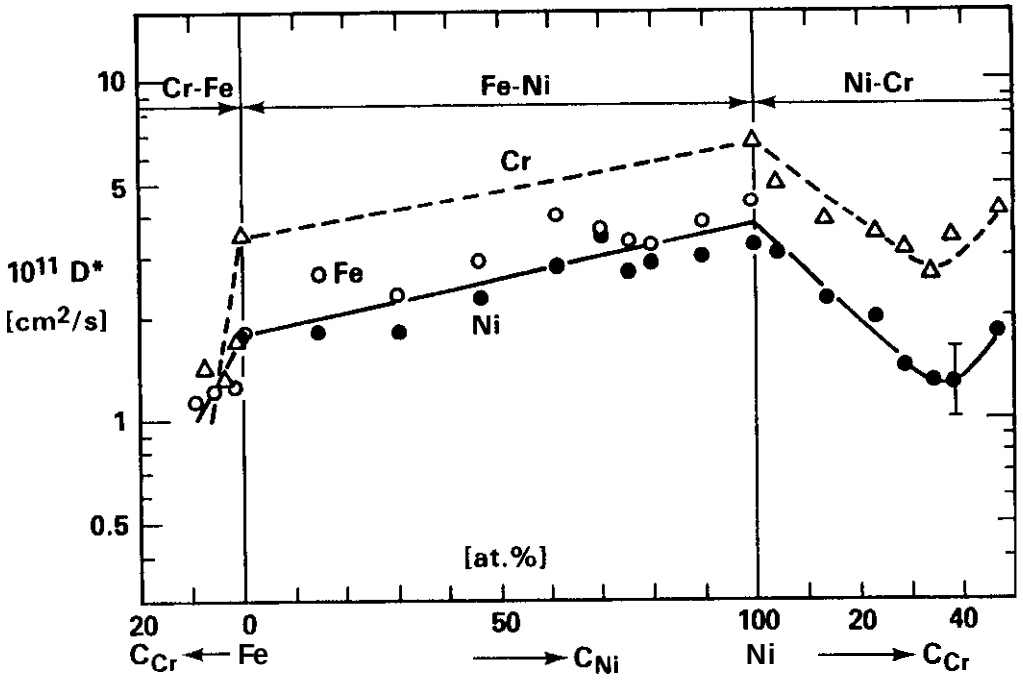

8. Diffusion of elemental components in the f.c.c. phases of binary solid solutions in the Fe-Ni-Cr system at 1100°C.(19)

Ordering has been invoked by several theoreticians as a mechanism that influences swelling. Schulson proposed that ordering impedes the mobility of irradiation-produced vacancies and thus increases the direct recombination of vacancies and interstitials[24]. Akhiezer and Davydov note that alloys which tend to order (but which are not long-range ordered) are characterized by a greater vacancy formation energy and, therefore, by a smaller thermal vacancy concentration compared with the disordered pure metal[25] This leads to larger supersaturations and greater rates of void nucleation. Alternatively, however, they note that in alloys that do not order at any temperature, the nucleation of voids is impeded compared with that of the corresponding pure metal.

Brager and Garner[4,5], however, note that another manifestation of the tendency to order is the spinodal-like formation at relatively high temperatures of micro-oscillations in compositon. These oscillations lead to relatively large regions wherein the composition favors void nucleation and other regions which do not.

5.4 Conclusion

Void formation in pure nickel tends to saturate at relatively low swelling levels during ion or neutron irradiation, but nickel-chromium alloys do not. It is postulated that chromium additions to nickel lead to some form of radiation-enhanced ordering. This increases the density of the alloy and is possibly related to the unusual swelling behavior of the alloy compared to that of pure nickel or Fe-Ni-Cr alloys. It may also be related to the abrupt extension of the transient regime of swelling above 538°C. Void nucleation appears to be impeded by chromium additions, and such additions also induce a swelling behavior that is remarkably insensitive to irradiation temperature below the order-disorder transformation temperature.

6.0 Reference

1. F.A. Garner, "Dependence of Swelling on Nickel and Chromium Content in te-Ni-Cr Ternary Alloys", OAFS Quarterly Progress Report DOE/ER-0046/14, August 1983, p. 133.

2. F.A. Garner and H.R. Brager, "Swelling *of* te-Ni-Cr Ternary Alloys at High Exposure". DAFS Quarterly Progress Report DOE/ER-0046/16, February 1984, p. 38.

3. F.A. Garner, "A Model Describing the Compositional Dependence of Void Nucleation in Irradiated Fe-Ni-Cr Alloys", ASTM STP 870 (in press), also in this report.

4. H.R. Brager and F.A. Garner, "Microsegregation Observed in Fe-35.5Ni-7.5Cr Irradiated in EBR-11", ASTM STP 870 (in press), also in OAFS Quarterly Progress Report DOE/ER-0046/18 p. 98.

5. H.R. Brager, F.A. Garner and T. Lauritzen, "Compositional Micro-oscillations in Ion-Irradiated FE-35.0Ni-7.0Cr," this report.

6. A. Chamberod, J. Laugier and J.M. Pennison, J. Magnetism and Magnetic Materials, 10 (1979) p. 139.

7. A. Marucco, E. Metcalfe and B. Nath, "The Order-Disorder Transformation is Ni-Cr Alloys", in Solid-state Phase Transformations, H.I. Aaronson, et al. Ed., The Metallurgical Society of AIME, p. 237, 1982.

8. Y. Adda, Proc. Inter. Conf. on Radiation-Induced Voids in Metals, CONF-710601, Albany N.Y., (1971) p. 31.

9. G. Silvestre, A. Silvent, C. Regnard and G. Sainfort, J. Nucl. Mater., 57 (1975) p. 175.

10. N.P. Agapova and nine coauthors, Atomnaya Energiya, 45 (6), Dec. 1978, p. 433.

11. K.B. Roarty, J.A. Sprague, R.A. Johnson and F.A. Smidt, J. Nucl. Mater. 97 (1981)p. 67.

17. H.R. Brager and J.L. Straalsund, HEDL-SA-3225 (previously unpublished data) 1972.

13. J.B. Whitley, G.L. Kulcinsky, P. Wilkes and J. Billen, J. Nucl. Mater., 85-86 (1979) p. 701.

14. G.L. Kulcinsky, J.L. Brimhall and H.E. Kissinger, in ref. 8, p. 449.

15. R.S. Nelson, J.A. Hudson, D.J. Mazey, G.P. Waiters and T.M. Williams in Ref. 8, p. 430.

16. J.A. Hudson, S. Francis, D.J. Mazey and R.S. Nelson, in Effects nf Radiation on Substructure and Mechanical Properties of Metals and Alloys, ASTM STP 529, 1973, p. 326.

17. O.I.R. Norris, J. Nucl. Mater., 40 (1971) p. 66.

18. J.A. Hudson and S.J. Ashby, "Void Formation in a Binary Nickel Alloy" in The Physics of Irradiation Produced Voids, (R.S. Nelson, Ed.) AERE-R-7934, 9-11 Sept. 1974, Harwell U.K., p. 140.

19. J. Ruzickova and B. Million, Mat. Sci and Engr., 50 (1981), p. 59.

20. G.R. Johnston, High Temperatures - High Pressures, 14 (1982) p. 695.

21. H. Heidsiek, R. Scheffel and K. Lucke, Journal de Physique, Colloque c7, n° 12, 38, Dec. 1977, p. C7-174.

22. R.L. Klueh, Mat. Sci. and Engr., 54 (1982) p. 65.

23. Ye.Z. Vintaykin and G.G. Urshadze, Fir. Met. Metalloved., 27 (5), (1969) p. 895

24a. E.M. Schulson, J. Nucl. Mater., 66 (1977) p. 322.

b. E.M. Schulson, J. Nucl. Mater., 83 (1979) p. 239.

25. I.A. Akhiezer and L.N. Oavydov, J. Nucl. Mater., 96 (1981) p. 155.

7.0 Future Work

Examination of both neutron and ion-irradiated specimens of Ni-Cr, Fe-Ni and Fe-Ni-Cr alloys will continue in an effort to determine the relationship between swelling and the tendency of alloys to order.

8.0 Publications

None.

VACANCY CLUSTEK EVOLUTION IN METALS UNDER IRRADIATION

M.F. Wehner and W.G. Wolfer (University of Wisconsin)

1.0 Objective

Void nucleation is the least understood part of radiation-induced void swelling in metals. The classical void nucleation models predict steady-state void nucleation rates which vary over orders of magnitude when small changes are made in certain critical parameters such as the surface energy and the void and dislocation bias. As a result, terminal void number densities cannot be obtained from the classical void nucleation models without arbitrarily adjusting some or all of the critical materials parameters. To remedy this situation. a new and fundamental approach has been developed. The present report gives the first account of this research.

2.0 Summary

A stochastic treatment of vacancy cluster formation in irradiated metals is formulated in terms of a Fokker-Planck equation. The Fokker-Planck coefficients are found to depend on the cluster size distribution itself. This nonlinear equation is solved by a previously developed numerical path integral solution. The nonlinear dependence provides an important feedback for the evolution of the bias. This evolution both initiates and terminates the nucleation process. The void size distribution follows a bifurcation process in which a peaked distribution of stable voids separates from a distribution of small unstable voids. The stable void number density reaches a final value which depends on temperature and dose rate. These predicted values are in close agreement with measured void number densities.

3.0 Program

Title: Radiation Damage and Performance Analysis of Ferromagnetic Steels for Fusion Applications (supported by EPRI under contract with the University of Wisconsin)
Principal Investigator: W.G. Wolfer
Affiliation: University of Wisconsin

4.0 Relevant DAFS Program Plan Task/Subtask

II.C.17 Microstructural Characterization
II.B. 2.3, Subtask C: Correlation Methodology

5.0 Accomplishments and Status

5.1 Introduction

The formation of vacancy clusters and voids in solids subject to displacement damage has in the past been treated in the context of classical nucleation theory (Katz and Wiedersich. 1971; Russell, 1971. 1970; Wolfer and Si-Ahmed, 19821. The basic assumptions of the classical theory are that an incubation period or a lag time exist during which a subcritical cluster population forms. This period is then followed by a nucleation period during which a constant flux of clusters grows beyond a critical size. An individual cluster overcomes the nucleation barrier at the critical size only as a result of growth fluctuations. Once it crosses the barrier its further growth becomes more deterministic and growth fluctuations become negligible. The second important assumption of the classical and homogeneous nucleation theory concerns the termination of the nucleation period and the cessation of the steady-state nucleation rate. This termi-

nation is generally believed to be caused by a depression of the supersaturation of the clustering species, namely the concentrations of vacancies, divacancies and self-interstitials in the present example. For a continuous irradiation, the increasing void density is believed to eventually reduce the vacancy supersaturation and thereby stop the cluster flux across the nucleation barrier. Although it is difficult to precisely specify the required reduction, Russell (1978) suggests that a lowering of the vacancy supersaturation by a factor of ten will suffice to terminate void nucleation.

In this classical approach to void nucleation, the critical size and the nucleation barrier are determined mainly by the supersaturations, the internal enersv of the cluster. and by the diffusion coefficients of the mobile species. 'The subcritical cluster population below the critical size has no direct influence on the critical size and the nucleation barrier.

It is one of the major goals of the present paper to show that this latter assumption is incorrect. To abandon it requires also to abandon the classical approach of steady-state nucleation, and to develop a time-dependent theory which describes the evolution of the entire cluster population. This population is represented by a distribution function $P(x,t)$, where t is the time and x the number of vacancies contained in a cluster. For each cluster size x, the master equation determines the change of $P(x,t)$. The most direct approach to a time-dependent nucleation theory is then to numerically solve a sufficiently large group of master equations (Courtney, 1962; Abraham, 1969, 1971). Another approach is based on the Monte Carlo method. as has been used extensively by Binder (1984).

The first approach does not seem to be practical in view of the fact that voids observed in the electron microscope range in size from about 2 nm to 200 nm in diameter. and the barely visible voids already contain 300 vacancies. The second approach does not allow the void size distribution present at any moment to influence the subsequent evolution of the void population.

Accordingly, a different approach has been developed which proceeds along the following lines. In the first step, the master equation for the cluster distribution function $P(x,t)$ is replaced by a Fokker-Planck equation in the cluster size space x. Next, a nonlinear transformation between x and the cluster radius r is applied, and a new Fokker-Planck equation is obtained for the cluster distribution function $\tilde{P}(r,t)$. This Fokker-Planck equation is then solved numerically using a recently developed technique based on the path integral (Wehner and Wolfer, 1983a, 1983b). These steps are discussed in Sections 5.2 and 5.3.

The reaction rates for the absorption and emission of mobile point defects at vacancy clusters depend most critically on three parameters, namely the so-called bias factors, the point defect concentrations, and the cluster properties. To make the paper self-contained, these parameters will be briefly summarized and discussed in Section 5.4. The results for the evolution of the vacancy cluster size distribution will then be presented in Section 5.5, and critically examined in Section 5.6.

5.2 Master and Fokker-Planck Equations

Let x denote the number of vacancies contained in a cluster and $P(x,t)$ the number density of clusters of size x at time t. If it is assumed that a cluster of size x can change its size only by the absorption of monovacancies and of self-interstitials, and by the emission of vacancies, then the following master equation holds:

$$dP(x,t)/dt = \beta(x-1)P(x-1,t) + [\alpha(x+1) + \theta(x+1)]P(x+1,t) - [\alpha(x) + \beta(x) + \theta(x)]P(x,t) \quad . \quad (1)$$

This equation is valid for $x \geq 2$, and it represents a set of rate equations as x is a discrete variable assuming only integer values. The rate coefficients $\alpha(x)$, $\beta(x)$, and $\theta(x)$ are the absorption rates for vacancies and interstitials, and the thermally induced emission rate of vacancies from a cluster of size x, respectively. The thermally induced emission rate of interstitials is so small as to be entirely negligible. Although the two absorption rates are strictly functions of time through their dependence on the point defect concentrations, this dependence can be suppressed for the following reason. The point defect concentrations, C_v and C_i for vacancies and interstitials. depend on the radiation induced production rate, P_0, and on the total sink strength S, a parameter that will be defined later. For a constant production rate P_0, the time dependence of S determines the time dependence of the concentrations C_v and C_i. These concentrations adjust to a new sink strength with a relaxation time on the order of S/D_v or less, where D_v is the diffusion coefficient for vacancy migration. Since this relaxation time is very short compared to the time scale over which S and $P(x,t)$ change, we can indeed assume that the point defect concentrations are quasi-

stationary, and $\alpha(x)$ and $\beta(x)$ are nearly time-independent. The expressions for the rate coefficients that will be used later are derived from a diffusion model of point defects to a spherical cavity. Accordingly, the size variable, x, in this model is treated as a continuous variable, and we shall therefore treat it likewise in the distribution function $P(x,t)$.

For clusters with size $x >> 1$, we may expand the first and second term into Taylor series. Retaining terms only to second order, the master equation (1) is then approximated by the Fokker-Planck equation

$$\frac{\partial P(x,t)}{\partial t} = - \frac{\partial}{\partial x} [K(x)P(x,t)] + \frac{1}{2} \frac{\partial^2}{\partial x^2} [Q(x,t)P(x,t)] \tag{2}$$

with a drift force defined as

$$K(x) = \beta(x) - \alpha(x) - \theta(x) \tag{3}$$

and a diffusion function as

$$Q(x) = \alpha(x) + \beta(x) + \theta(x) \ . \tag{4}$$

The truncation of the series expansion after the second order terms assures, according to a theorem by Pawula (19671, that the distribution function $P(x,t)$ remains positive everywhere. Because of the unit step size, the expansion for $x >> 1$ is equivalent to the so-called system size expansion of van Kampen (1981). Significant differences between the solutions to the master and to the Fokker-Planck equation would be expected in the vicinity of $x = 1$. However, we now introduce the boundary condition

$$P(1,t) = C_v \text{ for } t > 0 \ , \tag{5}$$

and thereby force the solution *of* the Fokker-Planck equation to agree with the solution to the master equation at $x = 1$. As a result we expect that the Fokker-Planck equation will provide adequate results for the entire size space $x > 1$. Additional boundary conditions are

$$P(x,0) = 0 \text{ for } x > 1 \tag{6}$$

and

$$P(\infty,t) = 0 \ . \tag{7}$$

The solution for the cluster distribution in terms of the size variable x is not convenient for two reasons. First, for large voids such as those observed in irradiated materials, x becomes on the order of 10^6. Second, void size distributions are measured in terms of the void radius. Therefore, it is desirable to introduce a new cluster distribution function

$$\tilde{P}(r,t) = P(x,t) \frac{dx}{dr} \tag{8}$$

where the cluster or void radius is defined as

$$r = (\frac{3\Omega x}{4\pi})^{1/3} + \frac{b}{2} \tag{9}$$

Here, Ω is the atomic volume, and the cluster or void surface is defined by the centers of the surface atoms. Their radii is assumed to be equal to half the Burger's vector b. The equation (9) represents a nonlinear transformation between two stochastic variables, x and r. The change in size of one individual cluster is described by the stochastic differential equation

$$dx = K(x)\, dt + \sqrt{\frac{1}{2} Q(x)}\, d\xi(t) \tag{10}$$

where $\xi(t)$ represents a Gaussian white noise. Equation (10) is strictly equivalent to the Fokker-Planck equation (2), only if it is interpreted in the Ito sense (Gardiner, 1983). Consequently, the normal rules of calculus do not apply when transforming stochastic differential equations belonging to-master equations of the birth and death type such as Eq. (1). Instead the transformation rules for the Ito stochastic calculus must be applied, hence Eq. (10) is transformed into

$$dr = \tilde{K}(r)\,dt + \sqrt{\tfrac{1}{2}\tilde{Q}(r)}\,d\xi(t)$$

where
$$\tilde{K}(r) = K[x(r)]\frac{dr}{dx} + \frac{1}{2}Q[x(r)]\frac{d^2r}{dx^2} \tag{11}$$

$$\cong K(r)\frac{\Omega}{4\pi r^2} - Q(r)\frac{\Omega^2}{(4\pi)^2 r^5}$$

$$\tilde{Q}(r) = Q[x(r)]\left(\frac{dr}{dx}\right)^2 \cong Q(r)\frac{\Omega^2}{(4\pi)^2 r^4}\,. \tag{12}$$

The transformed Fokker-Planck equation is then

$$\frac{\partial\tilde{P}(r,t)}{\partial t} = -\frac{\partial}{\partial r}\left[\tilde{K}(r)\tilde{P}(r,t)\right] + \frac{1}{2}\frac{\partial^2}{\partial r^2}\left[\tilde{Q}(r)\tilde{P}(r,t)\right]\,. \tag{13}$$

It will be shown below that the rate coefficients are all proportional to r. Hence, $K(x)$ and $Q(x)$ are both proportional to $x^{1/3}$, and the shift and diffusional broadening appear of equal importance. In contrast, the transformed drift force behaves as $\tilde{K}(r) \sim 1/r$ and the transformed diffusion function as $\tilde{Q}(r) \sim 1/r^3$. Therefore, with larger void radius, the diffusional spreading of the Size distribution diminishes and void growth becomes an increasingly deterministic process when judged by the evolution of the void radius. The dynamics of void nucleation and growth are, of course, independent of the coordinate system used. The nonlinear transformation (9) simply illustrates that large voids are subject to smaller fluctuations in size than are small voids. The experimental evidence for this observation will be discussed in Section 5.6.

5.3 Path Sum Solution

The formal solution to the Fokker-Planck equation (13) subject to the boundary conditions of Eqs. (5) and (7) can be constructed via the path sum as shown recently by Wehner and Wolfer (1983b). If the solution at time t is assumed to be known, the solution at a later time $t + \tau$ is given by

$$\tilde{P}(r,t+\tau) = \int_b^\infty dr'\,\tilde{P}(r',t)G(r,r',\tau) - \int_0^\tau d\tau'\left[\tilde{J}(b,t+\tau')G(r,b,\tau')\right.$$
$$\left. + \frac{1}{2}\tilde{P}(b,t+\tau')\tilde{Q}(b)\frac{\partial}{\partial r'}G(r,b,\tau')\right]\,. \tag{14}$$

Here,
$$\tilde{J}(r,t) = \tilde{K}(r)\tilde{P}(r,t) - \frac{1}{2}\frac{\partial}{\partial r}\left[\tilde{Q}(r)\tilde{P}(r,t)\right] \tag{15}$$

is the net cluster current, and the radius of a monovacancy ($x = 1$) is assumed to be equal to the Burgers vector b.

In the limit of small time steps τ, the propagator or Green's function can be given by (Dekker, 1976)

$$G(r,r',\tau) = (2\pi\tilde{Q}(r')\tau)^{-1/2}\exp\{-[r - r' - \tilde{K}(r')\tau]^2/2\tilde{Q}(r')\tau]\}\,. \tag{16}$$

By the repeated application of Eq. (14) for N times, the solution can be found for a finite time interval $t - t_0 = N\tau$. This solution becomes exact in the limit $\tau \to 0$ and $N \to \infty$ such that $N\tau$ remains fixed. In actual numerical calculations, a small but finite time step τ is selected based on the interval spacing employed in the numerical integration of Eq. (14). Furthermore, if τ is sufficiently small, $\tilde{P}(r,t)$ changes little in the vicinity of $r > b$, hence the cluster current $\tilde{J}(b,t+\tau')$ may be approximated by its value at

time t. As a result of the boundary condition in Eq. (5), $\tilde{P}(b,t+\tau') = C_v$. Hence, the r.h.s. of Eq. (14) is known and can be evaluated.* The details of the numerical procedure are given elsewhere (Wehner and Wolfer. 1983b). Starting with the initial condition, Eq. (6), the path sum solution of Eq. (14) then yields the evolution of the distribution function $\tilde{P}(r,t)$ with time.

5.4 Rate Coefficients, Bias Factors and Point Defect Concentrations

The fundainental process involved in the cluster formation is the diffusion of the point defects to the sinks. If we consider then a cluster as a spherical sink, and if the point defect absorption and emission at the sink is controlled by bulk diffusion, then the reaction rates are given by

$$\alpha(r) = 4\pi r D_i C_i Z_i^o(r) \tag{17}$$

$$\beta(r) = 4\pi r D_v C_v Z_v^o(r) \tag{18}$$

$$\theta(r) = 4\pi r D_v C_v^o(r) Z_v^o(r) \tag{19}$$

where $$C_v^o(r) = C_v^{eq} \exp\{4\pi[\gamma(r)r^2 - \gamma(r_-)r_-^2]/kT\} \tag{20}$$

is the vacancy concentration in local thermodynamic equilibrium with a void of radius r, $\gamma(r)$ is the surface energy, and r_- is the radius of the void with one less vacancy. The surface energy for small voids is dependent on the void radius as discussed by Si-Ahmed and Wolfer (1982).

The void bias factors $Z_i^o(r)$ and $Z_v^o(r)$ account for the effect of the stress-induced interaction of the interstitial and vacancy, respectively, with the void. They have been derived recently by Sniegowski and Wolfer (1983) for the case where segregation to voids does not occur. Both bias factors are given by

$$Z^o(r) \cong 1 + [(\sqrt{1+\eta} - 1)/2\lambda]^{1/3} \tag{21}$$

where $$\eta = 4\lambda\Gamma/(r^3 kT \ln 2) \tag{22}$$

$$\Gamma = \frac{\mu v^2 (1+\nu)^2}{36\pi(1-\nu)} \tag{23}$$

$$\lambda = \frac{7 - 5\nu}{30} - \frac{2\Gamma\mu^2}{3r\alpha^6\gamma^2} \tag{24}$$

Here, μ is the shear modulus, ν the Poisson's ratio, k the Boltzmann constant, and T the absolute temperature. By inserting the appropriate values for the relaxation volume v and the shear polarizability α, the bias factors Z_i^o and Z_v^o can be obtained for the absorption of self-interstitials and vacancies, respectively. For the materials parameters of solution-annealed nickel, listed in Table 1, the void bias factors as shown in Figure 1 are obtained. It is seen that small voids possess a significant bias for preferential interstitial absorption. However. this bias diminishes rapidly with increasing void radius, a fact that will prove to be essential for the emergence of a peaked distribution for voids above the critical size.

*Note that since Eq. (13) is a parabolic partial differential equation, both the value of the probability distribution and the current may not be specified independently at the boundary without a risk of overspecifying the problem (Morse and Feshbach, 1953).

TABLE 1

MATERIALS PARAMETERS FOR NICKEL

k	Boltzmann constant	1.38×10^{-23} J/°K
T	temperature	
a	lattice parameter	3.639×10^{-10} meter
b	Burger's vector	$a/\sqrt{2}$
Ω	atomic volume	$a^3/4$
E_v^m	vacancy migration energy	1.76×10^{-19} Joule
E_v^f	vacancy formation energy	2.832×10^{-19} Joule
D_v	vacancy diffusion coefficient	$1.286 \times 10^{-6} e^{-E_v^m/kT}$ (m^2/s)
P_o	production rate of point defects	$0.1\ \Omega \times$ (dpa rate)
R_c	recombination coefficient	$8\pi a\left(\frac{1}{D_i} + \frac{1}{D_v}\right) - \frac{8\pi a}{D_v}$
C_v^{eq}	equilibrium vacancy concentration	$\frac{1}{\Omega} e^{(1.5-E_v^f/kT)}$ (m^{-3})
ν	Poisson's ratio	$2.64 + 7.7 \times 10^{-5}$ T (°C)
E	Young's modulus	$2.097 \times 10^{-11} - 1.03 \times 10^{8}$ T (°C)
μ	shear modulus	$E/2(1 + \nu)$
v	relaxation volume	for interstitials 1.8 Ω
		for vacancies −0.2 Ω
α^G	shear polarizability	for interstitials −150 eV
		for vacancies −15 eV
γ_o	surface energy of flat surface	$2.28 + (1333 - T)0.55 \times 10^{-3}$ J/m^2
$\gamma(x)$	surface energy of a void	$\gamma_o[1.0 - (0.8/(x + 2))]$
A^d	shape factor for dislocations	
ρ^d	dislocation density	
$A^d\rho^d$	dislocation sink strength	2×10^{13}
$Z^d_{i,v}$	dislocation bias factors	

As mentioned in Section 5.2, the time scale for the relaxation of the point defect concentrations is much shorter than for significant change in the cluster population. Thus the point defect concentrations assume their stationary solutions corresponding to the existing set of material parameters, and C_i and C_v change as these parameters change. The approximation $dC_i/dt \cong dC_v/dt \cong 0$ is a statement of the "adiabatic approximation" as termed by Haken (1983). The resulting equations for the point defect concentrations become (Si-Ahmed and Wolfer. 1982)

$$D_i C_i = \frac{1}{2}\left\{\left[\left(\frac{\langle Z_v\rangle}{\langle Z_i\rangle} D_v C_v^s + \frac{S\langle Z_v\rangle}{R_c}\right)^2 + \frac{4\langle Z_i\rangle}{\langle Z_v\rangle R_c} P_o\right]^{1/2} - \left(\frac{\langle Z_v\rangle}{\langle Z_i\rangle} D_v C_v^s + \frac{S\langle Z_v\rangle}{R_c}\right)\right\} \quad (25)$$

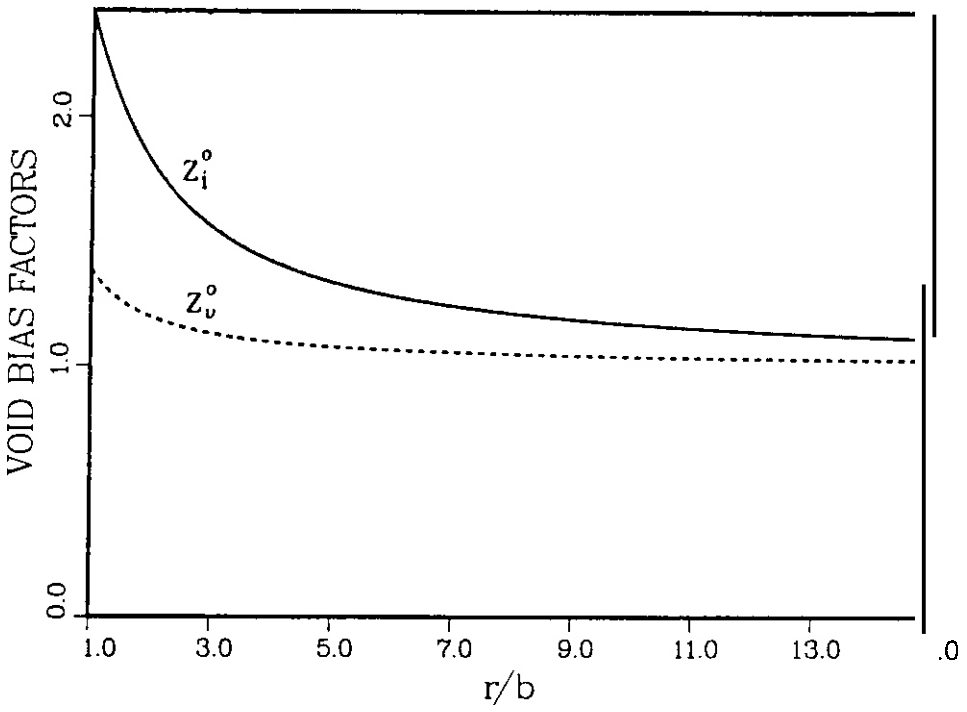

FIGURE 1. The void bias factors vs. void radii for interstitials (solid line) and for vacancies (dashed lines) evaluated from Eqs. (18) and with the parameters listed in Table 1.

$$D_C = \frac{1}{\tau_{rec}} D_i C_i + D_C C_v^S$$

Here the total sink strength is

$$S = 4\pi \int_b^\infty dr\, [r\tilde{P}(r,t)] + A^d \rho^d \tag{26}$$

the sink averaged bias factors are

$$\langle Z \rangle = \frac{4\pi \int_b^\infty dr\, [rZ^o(r)\tilde{P}(r,t)] + Z^d A^d \rho^d}{S} \tag{27}$$

and the averaged vacancy concentration in equilibrium with sinks is

$$C_v^S = \frac{4\pi \int_b^\infty dr\, [rC_v^o(r)Z_v^o(r)\tilde{P}(r,t)] + C_v^e Z_v^d A^d \rho^d}{\langle Z_v \rangle} \tag{28}$$

One may speak of the fast variables (the point defect concentrations) as being "slaved" by the slow variables (the average bias factors, the sink strength and the averaged vacancy concentration). Moreover, the dependence of the point defect concentrations on the cluster size distribution leads to another important consequence. Through Eqs. (17-19) and (25-28) one can see that this dependency removes the linearity of the Fokker-Planck equation (13). Indeed Eq. (13) is no longer a differential equation but rather an integro-differential equation. Such integral dependencies are common throughout physics whenever many-body interactions play an important role. In the present case, the integral dependence arises from the fact that the

mono-defect populations depend on weighted averages of certain functions characteristic of the system. It does not, however. depend on particular values of the size distribution function. Because of this integral dependence, this truly nonlinear equation can be solved using the numerical path integral technique by assuming that for small enough time steps the equation may be regarded as being linear. Then given the solution at a particular time, the solution a very short time later can be found. This new solution is used to recalculate the point defect concentrations (and hence the Fokker-Planck coefficients). A revised linear equation is constructed and the whole process repeated. In this manner it is possible to investigate the effect of the void size distribution on its own development.

5.5 Void Size Distributions

In order to gain an initial understanding of the dynamics of void nucleation, the nonlinear character of Eq. (13) will be suppressed. Specifically, the integral dependence in Eqs. (26-28) will be neglected. This erroneous assumption leads to the conclusion that the microstructural properties of the material remain unchanged throughout the nucleation process. Nevertheless, certain interesting characteristics of cluster nucleation become transparent in this limit.

Figures 2a and 2b show the transformed Fokker-Planck coefficients evaluated for parameters listed in Table 1 and for a case representative of ion bombardment experiments at a temperature of 873 K. The general shape of these plots is typical of that found over the entire ranges of temperature and dose rate studied. The critical size of a void is defined as that size where $\tilde{K}(r)$ crosses zero. This corresponds to the location of the peak of the nucleation barrier. In Figure 2a, this occurs at approximately $r/b = 3.0$. At this point in the discussion. it is convenient to introduce some nomenclature. Voids of less than the critical size are subject to a negative drift force, hence they are more likely to be driven back in size space across the boundary at $r/b \simeq 1$. Since a "particle" driven across a boundary in an open system is lost, these voids are referred to as "unstable." Some voids, driven by the random forces, will cross the critical size. These voids are then subject to a positive drift force and tend to grow in size. Hence, voids of a size greater than the critical size are termed "stable."

Figure 3a shows the void size distribution obtained by solving the linear equation (13) subject to the Fokker-Planck coefficients of Figure 2. As is evident, a large concentration of small unstable voids (invisible to the electron microscope) develops quite rapidly. In addition, after a certain length of time, a uniform, plateau-like distribution of larger stable voids is established. The leading edge of this plateau continues to propagate in size space as time progresses.

The nucleation barrier for the linear Fokker-Planck equation is, of course, time-independent. Accordingly, the current across this barrier quickly attains its steady-state value. This constant current, together with the slowly varying nature of the drift force of Figure 2a in the region $r/b > 5$, causes the size distribution to flatten out. Hence, the plateau-like behavior is a consequence of the suppression of the nonlinearity of Eq. (13).

Computer memory limitations prohibit extension of the calculations to total doses much higher than 0.2 dpa for the Fokker-Planck coefficients plotted in Figure 2. The trend. however, is that of a development of a population of voids uniformly distributed over a broad range in size. In addition, the void number density, defined as the area under the stable portion of the void size distribution. continues to increase with increasing dose. Both of these effects are contrary to experimental findings. Under most irradiation conditions, a very narrow size class of voids is observed, i.e. the void size distribution is sharply peaked. Also. the void number density does not vary with time after an initial nucleation period (Glasgow. Si-Ahmed, Wolfer, Garner, 1981; Mansur 1978). As Figure 3a shows, this cannot be obtained by a theoretical approach which neglects the effect of the void population itself on the microstructural properties of the metal.

To this end, the nonlinear character of Eq. (13) is considered. Figure 3b shows the void size distribution at various times solved under the same conditions as in Figure 3a except that the integrals of Eqs. (26-28) are calculated after each time step and the Fokker-Planck coefficients suitably adjusted as described in the previous section. These plots show a dramatic change in the void size distribution which now becomes very sharply peaked at the later times (note the logarithmic y axis). Also, the unstable voids diminish in number as time progresses. Furthermore, after the initial nucleation period. the stable void number density remains constant with increasing dose.

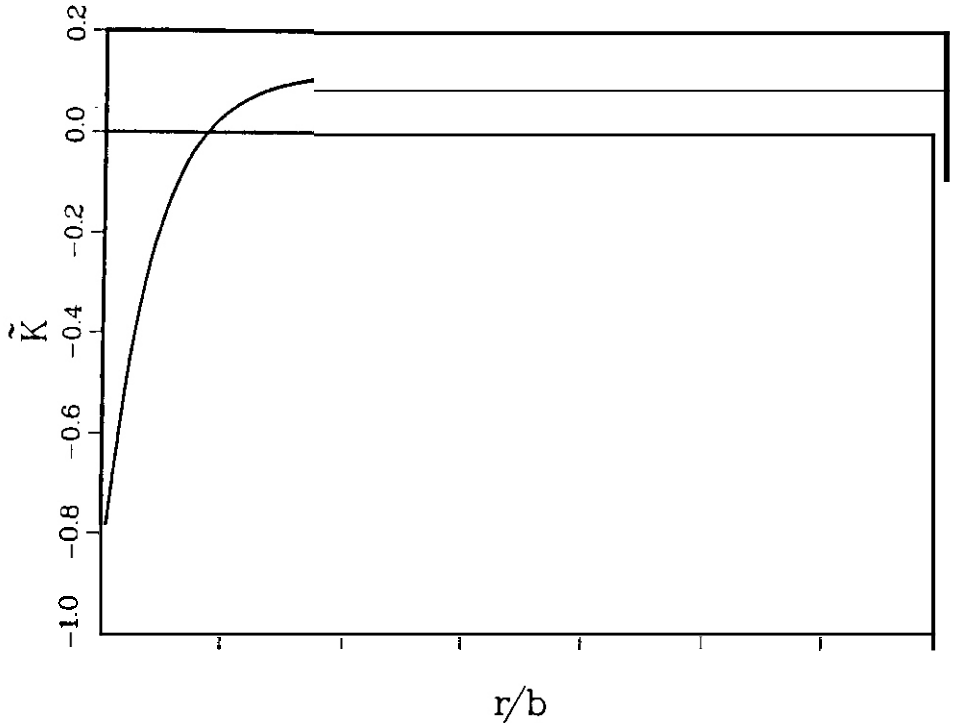

FIGURE 2a. The transformed drift function vs. void radii obtained by neglecting the effect of the void size distribution at T = 873 K and a dose rate of 0.001 dpa/s.

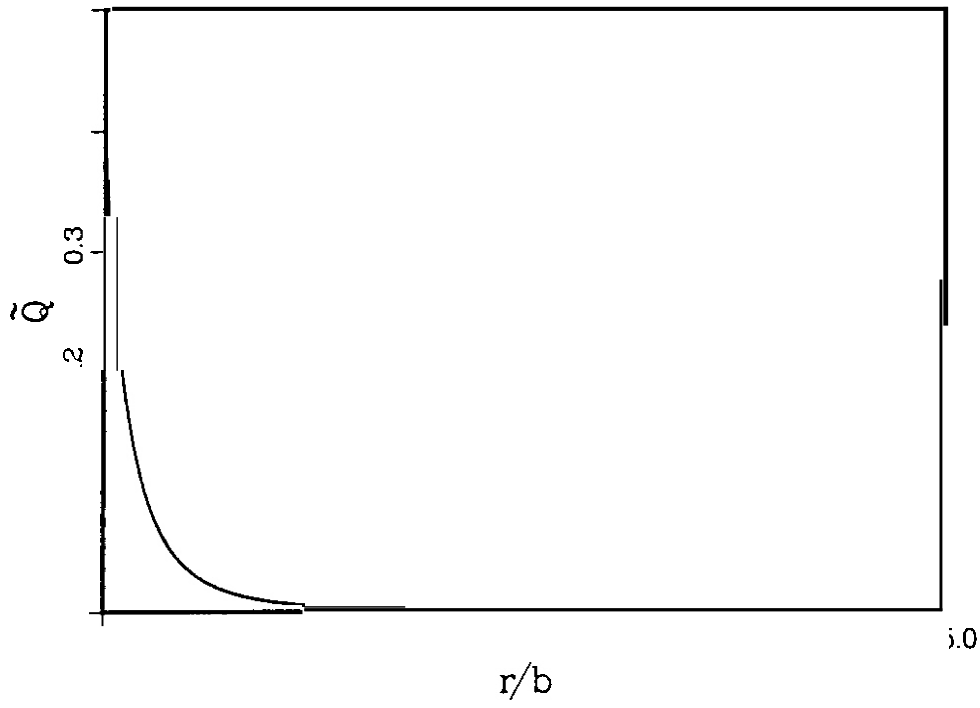

FIGURE 2b. The transformed diffusion function vs. void radii obtained by neglecting the effect of the void size distribution at T = 873 K and a dose rate of 0.001 dpa/s.

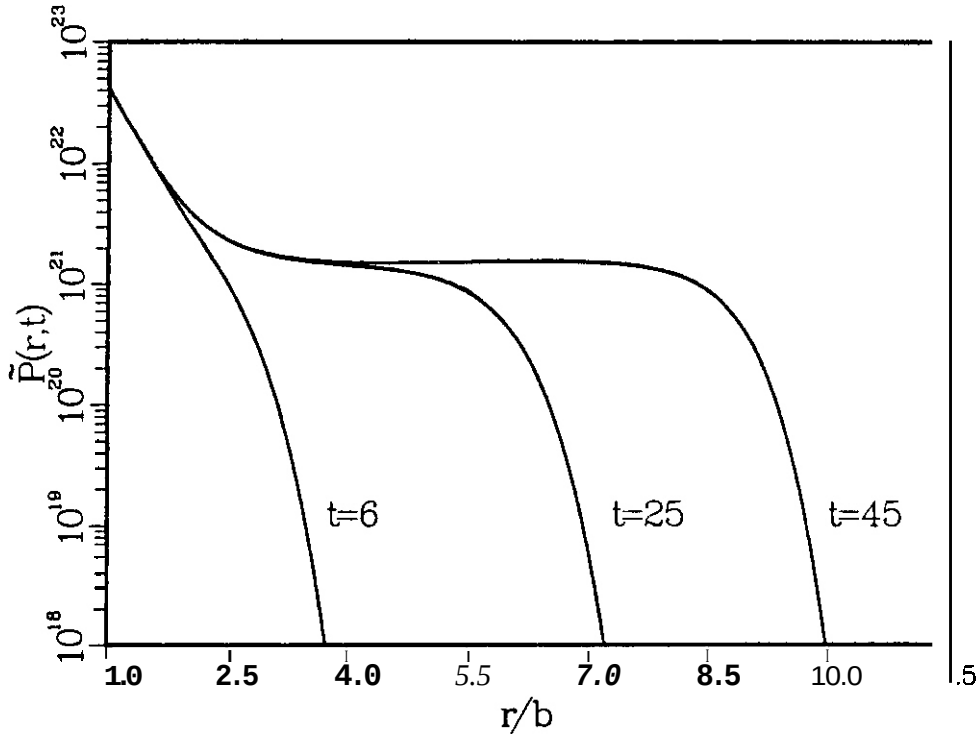

FIGURE 3a. The void size distribution vs. void radii at various times obtained by neglecting the effect of the size distribution upon itself at T = 873 K and a dose rate of 0.001 dpals. Note the high concentration of unstable voids and the plateau-like size distribution of stable voids. The times indicated are in seconds.

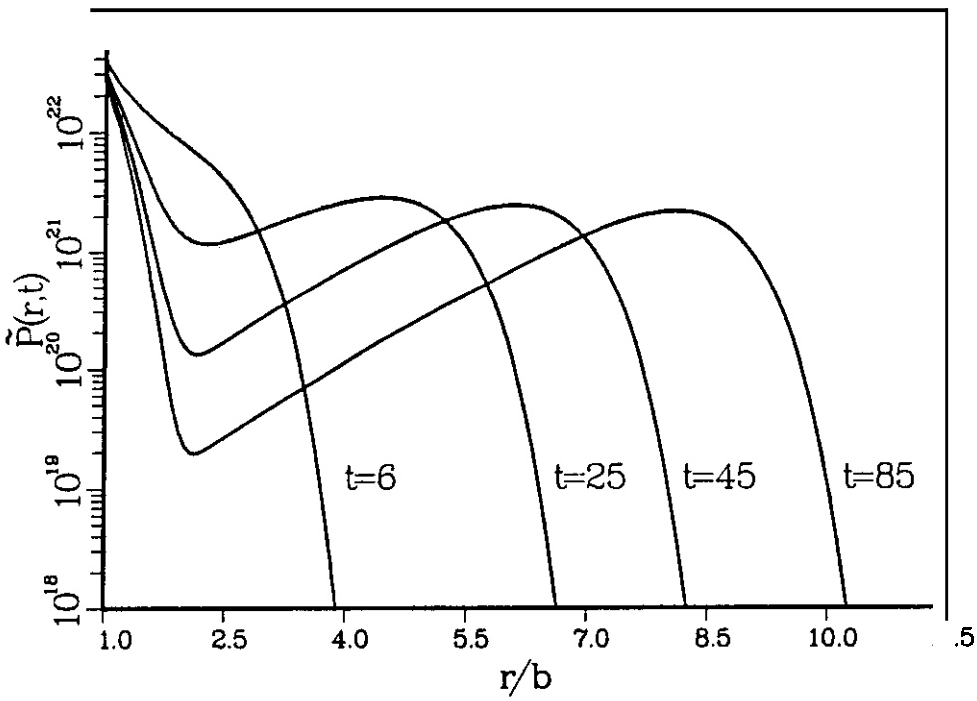

FIGURE 3b. The void size distribution vs. void radii at various times obtained by considering the effect of the void size distribution itself on the microstructural parameters at T = 873 K and a dose rate of 0.001 dpals. Note the "pinching off" of the void size distribution at later times. This results in a lowering of the concentration of unstable voids as well as the isolation of a narrow size class of stable voids. The times indicated are in seconds.

Such an extreme change in the shape of the distribution function illustrates the highly sensitive nature of void nucleation to changes in the microstructure and the rate coefficients. The feedback mechanisms responsible for the termination of void nucleation are twofold. First the increase in the void sink strength causes a decrease in the concentrations of both point defects. This feedback mechanism is however not as significant as traditionally believed. As seen from the y-intercepts in Figure 3b, the vacancy concentration changes little with time.

The second. and dominant feedback mechanism is the change in the difference of the capture rates β and α This difference is highly sensitive to changes in the average bias factors, and best illustrated by the transformed drift force $\tilde{K}(r)$. Figure 4 shows that the drift force not only changes in magnitude but the critical size increases as well with increasing dose. The transformed diffusion function. $\tilde{Q}(r)$, being a sum rather than a difference of the rate coefficients, does not change much with time and has the general shape as in Figure 2b. The changing shape of the distribution function can be further explained by defining a potential function as

$$G(r,t) = -2 \int_b^r \frac{\tilde{K}(r',t)}{\tilde{Q}(r',t)} dr' \quad . \tag{29}$$

The peak value of this potential determines the nucleation barrier, ΔG. As shown in Figure 5, this barrier increases dramatically with time. Since the steady state nucleation current over a fixed barrier is proportional to $e^{-\Delta G}$ (Russell, 1978), it is apparent that the time-dependent nucleation current corresponding to the barrier of Figure 5 is reduced significantly in a very short period of time. Clearly, the actual nucleation of voids can occur only in the very early stages of the irradiation.

The irradiation temperature of the material determines to a large degree the point defect concentrations. Accordingly, the dynamics of void nucleation and growth are also expected to be strongly affected by the temperature. Figure 6a shows the calculated void size distribution obtained for ion bombardment of nickel at a temperature of 613 K. Comparison with the higher temperature (873 K) resultant of Figure 3b, reveals two experimentally consistent observations. First. at the lower temperature, the stable void number density as well as the vacancy concentration are considerably higher. Second, the nucleation process requires more time (hence more total dose) at the lower temperature. However, the general shape of the void size distribution is the same in both figures.

The damage rate also affects the dynamics of void nucleation and growth by governing directly the point defect production. In Figure 6b, the calculated void size distribution obtained for neutron bombarded nickel at a temperature of 613 K is shown. Comparison with the previous figure reveals a lower stable void number density. and that more time but less total damage is required for the nucleation process occurring at a lower damage rate.

Again the overall shape of the void size distribution, especially in the stable size regime. is the same. A comparison with several different combinations of temperature and dose rates confirms that the shape, more specifically the width at any fraction of the maximum of the stable void population remains nearly constant over a wide range of values. In this study all other parameters characterizing the material were held constant. Other results not shown here indicate that the width of the size distribution broadens and the height diminishes as the dislocation sink strength increases significantly beyond the void sink strength. A more detailed analysis of the effect of this and other material parameters on void nucleation and growth is forthcoming.

5.6 Discussion

The present results indicate that in annealed materials subject to displacement damage, the stable void Size distribution is established at low doses. In contrast, most irradiation experiments are carried to higher doses because both measurements of void densities and void swelling can be performed with greater accuracy. These measurements are aimed at obtaining average void sizes and total number of voids per unit volume. Rarely are detailed void size distributions obtained. However, in the few cases where distributions have been measured with satisfactory statistical counts, the following characteristics are observed. The void size distribution at low doses is indeed sharply peaked in agreement with our results. However, a significant tail towards larger void sizes is often observed which is attributed to void coalescence. This process is not included in the present analysis based on the master equation (1) which allows only unit step pro-

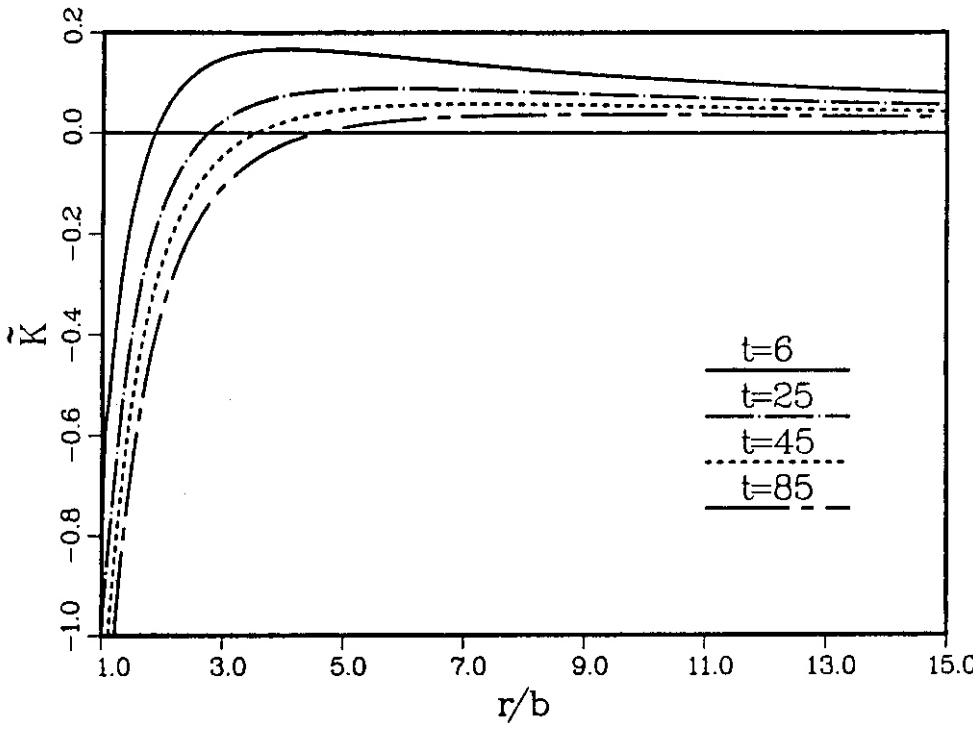

FIGURE 4. The transformed drift function vs. void radii which led to the void size distributions of Figure 3b evaluated at those times.

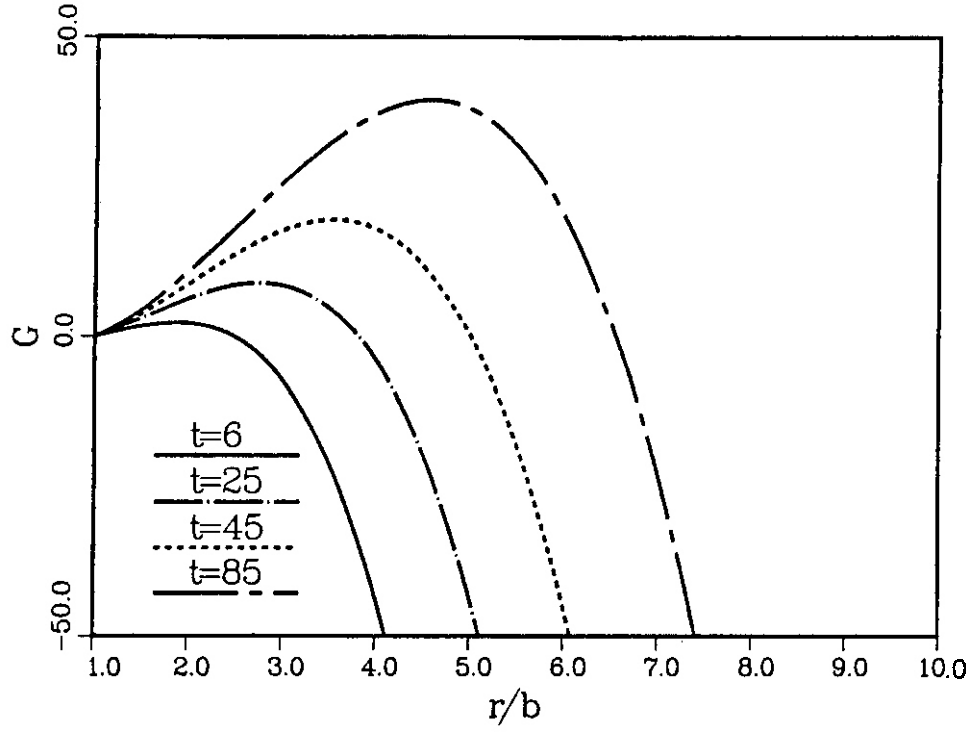

FIGURE 5. The potential function vs. void radii which led to the void size distributions of Figure 3b evaluated at those times. Note how the nucleation barrier (the peak value of the potential) increases drastically with time.

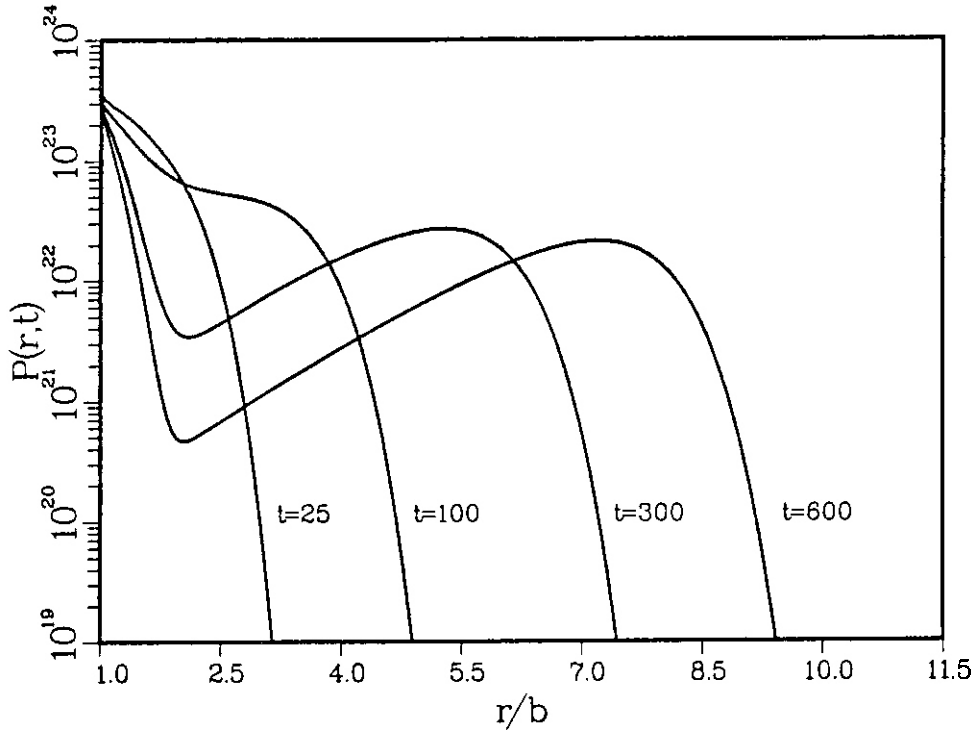

FIGURE 6a. The void size distribution vs. void radii at various times with T = 673 K and a dose rate of 0.001 dpals.

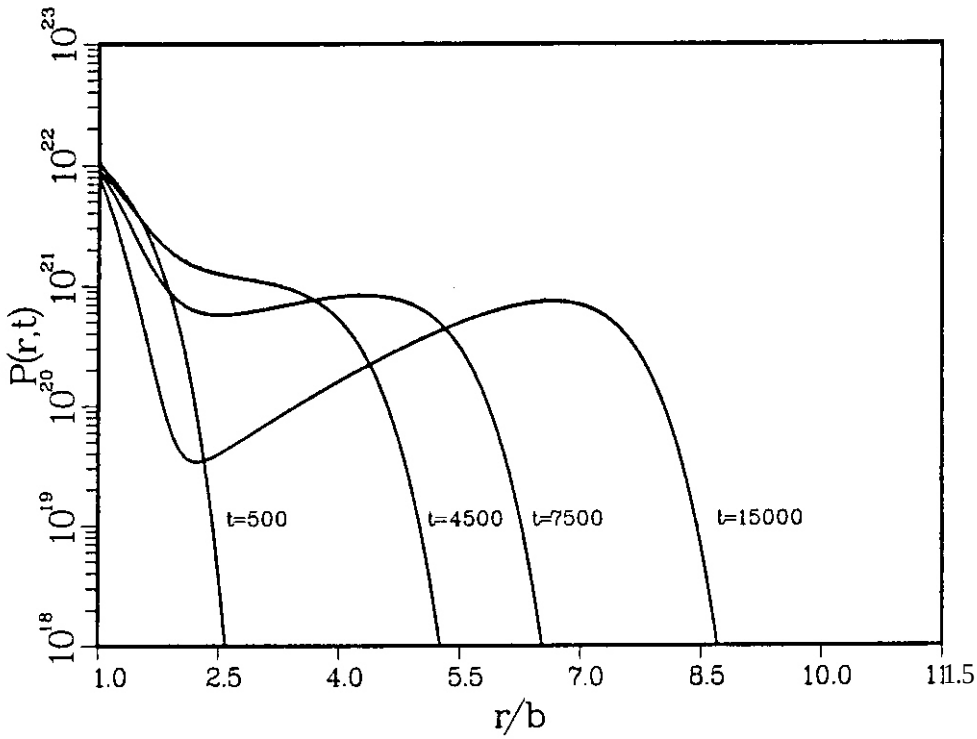

FIGURE 6b. The void size distribution vs. void radii at various times with T = 673 K and a dose rate of 10^{-6} dpa/s.

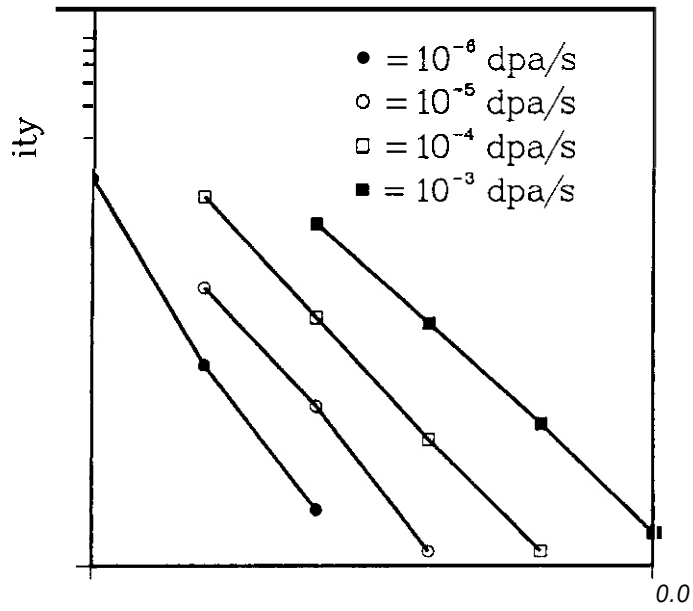

FIGURE 7. Terminal void number densities vs. temperature at various dose rates. Solid circles - 10^{-6} dpa/s; open circles - 10^{-5} dpals; open squares - 10^{-4} dpals; solid squares - 10^{-3} dpals.

cesses. Extensive coalescence can furthermore lead to bi-modal void size distributions at high doses. Renucleation at higher doses due to helium production also gives rise to bi-modal void size distributions.

It should also be noted that many materials of practical interest such as steel are highly heterogeneous, and the spatial distribution of voids reflects this varying microstructure.

Accordingly, a comparison between our theoretical predictions and experimental results is best made on pure metals. Since the most commonly observed quantity is the void number density, the stable void size distribution was integrated from a void radius of 1 nm upwards. This lower bound represents the limit of visibility in standard transmission electron microscopy. Furthermore. the calculations of the void size distribution were always carried out to a sufficiently large dose to provide the terminal void number density. This density is plotted in Figure 7 as a function of the irradiation temperature for various dose rates. It is seen that the void number density decreases sharply with temperature. With increasing dose rate, the characteristic curve for the total void number density is shifted to higher temperature. This shift is well known for the swelling-temperature relationships. When comparing heavy ion irradiations of a typical dose rate of 10^{-3} dpa with fast neutron irradiations ($\sim 10^{-6}$ dpa/s), we find a characteristic temperature shift for void nucleation ot about 200°C in the case of nickel. This shift is somewhat larger than the corresponding shift for void growth (Brailsford and Bullough, 1972). Both the temperature and dose-rate dependence of the terminal void number density are in general agreement with the experimental observations. Furthermore, the quantitative comparison illustrated in Figure 8 demonstrates that the predicted void number densities (solid line) are in excellent agreement with the measured void densities in nickel irradiated with fast neutrons at temperatures below about 500°C. The experimental data at higher irradiation temperatures reflect the presence of gas bubbles. Some of the data on void number densities reported by Packan. Farrel and Stiegler (1978) are for dose rates of 10^{-7} dpals. and therefore expected to fall below the solid curve predicted for a dose rate of 10^{-6} dpals.

The above comparison and agreement between measured and theoretically predicted void number densities is remarkable in several aspects. First, no parameter of the theoretical models required adjustment. The value of surface energy employed is the one measured for a clean surface of nickel; the bias is evaluated

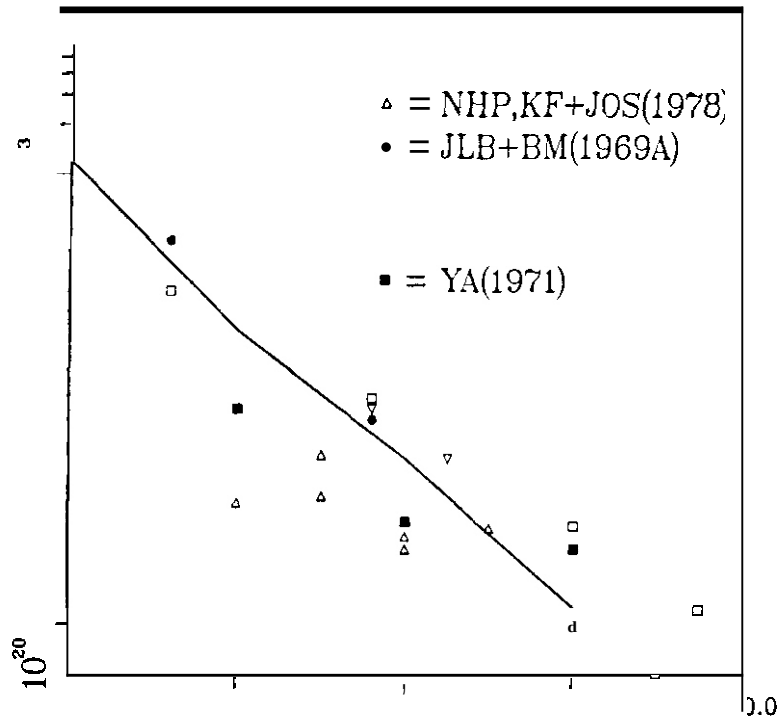

FIGURE 8. A comparison of the theoretical prediction of the terminal void number density vs. temperature with various neutron irradiation experiments.

based on the elastic constants, the Burgers vector, and the actually measured relaxation volumes for interstitials and vacancies (Sniegowski and Wolfer. 1984). Second, no gas is required in the dynamic void nucleation calculations. The void nucleation is both self-starting and self-terminating. The autonomous process for void nucleation in an annealed metal reflects the importance of the feedback mechanisms discussed in the previous section. Among these, the evolution of the average bias provides the key for the emergence of a sharply peaked void size distribution. Such an evolutionary process can no longer be treated with the traditional theory of steady state nucleation. The approach developed in the present paper, based on the time dependent solution of a truly nonlinear Fokker-Planck equation, proved very successful in treating the dynamic nucleation process and the subsequent growth stage in a unified formalism.

6.0 References

Abraham. F.F., 1969. J. Chem. Phys. 51, 1632; 1971, ibid. 54, 3874.

Adda, Y., 1978, in "Radiation-Induced Voids in Metals," Corbett and Ianniello, eds., Oak Ridge, TN: USAEC Technical Information Center. p. 31.

Binder, K., 1984, "Application of the Monte Carlo Method in Statistical Physics," (Berlin: Springer-Verlag).

Erailsford, A.D. and Bullough, R., 1972, J. Nucl. Mat. 44, 121.

Brimhall, J.L. and Mastel, B., 1968, J. Nucl. Mat. 28, 115

Brimhall, J.L. and Mastel, B., 1969a, J. Nucl. Mat. 29, 123.

Brimhall, J.L. and Mastel, E., 1969b, J. Nucl. Mat. 33, 186.

Courtney, W.G., 1962. J. Chem. Phys. 36, 2009.

Gardiner, C.W., 1983, "Handbook of Stochastic Methods." (Berlin: Springer-Verlag) p. 96.

Glasgow. B.B., Si-Ahmed, A., Wolfer. W.G. and Garner, F.A.. 1981. J. Nucl. Mat. 103 & 104, 981.

Haken, H., 1983. "Synergetics, An Introduction." 3rd ed., (Berlin: Springer-Verlag) p. 192.

Katr, J.L. and Wiedersich, H., 1971, J. Chem. Phys. 55, 1414.

Mansur, L.K.. 1978. J. Nucl. Mat. 78, 156.

Morse, P.M. and Feshbach. H., 1953, "Methods of Theoretical Physics, Volume 1," (New York: McGraw-Hill) p. 705.

Packan. N.H.. Farrel, K.. and Stiegler, J.O., 1978, J. Nucl. Mat. 78, 143.

Pawula. R.F., (1967), Phys. Rev. 162, 186.

Russell, K.C., 1971. Acta Metall. 19, 753.

Russell, K.C., 1978, Acta Metall. 26, 1615.

Si-Ahmed, A. and Wolfer, W.G.. 1982, Proceedings of the 11th International Symposium on the Effects of Radiation on Materials, ASTM STP 782 (Philadelphia: American Society for Testing Materials) p. 1008.

Sniegowski. J.J. and Wolfer, W.G.. 1983.

Van Kampen, N.G., 1981, "Stochastic Processes in Physics and Chemistry," (Amsterdam: North-Holland) p. 214.

Wehner, M.F. and Wolfer, W.G., 1983a, Phys. Rev. A 27, 2663.

Wehner, M.F. and Wolfer. W.G., 1983b, Phys. Rev. A 28, 3003,

Wolfer. W.G. and Ashkin, M., 1975, J. Appl. Phys. 46, 547.

Wolfer, W.G. and Ashkin. M., 1976. J. Appl. Phys. 47, 791.

Wolfer, W.G. and Si-Ahmed, A., 1982, Phil. Mag. A 46, 723.

7.0 Future Work

Time dependent void nucleation calculations will be reported in subsequent periods for a ferrite phase, for pure copper., and pure aluminum. Comparisons with measured void number densities will also be made in all cases.

8.0 Publications

The present progress report has been submitted as a publication to the Philosophical Magazine.

THE EFFECT OF HELIUM CLUSTERING ON ITS TRANSPORT TO GRAIN BOUNDARIES

Nasr M. Choniem, Jamal N. Alhajji (UCLA) and Dietmar Kaletta (KfK)

1.0 Objective

The purpose of this paper is to investigate the influence of helium clustering in the matrix on its transport to grain boundaries by single gas atom migration mechanisms. The work is a combined nucleation-diffusion study to understand various effects of micro processes in the matrix on the ability of helium to migrate to grain boundaries.

2.0 Summary

Using a rate theory model, we develop in this investigation a solution to the problem of the rate of helium absorption at grain boundaries. In fusion reactor conditions, helium is expected to be uniformly generated inside the grains of structural materials. With the simultaniety of displacement damage production, helium atom can be trapped in vacancies or vacancy clusters, inhibiting the migration of helium. If trapped helium is again detrapped, it will eventually find its way to grain houndaries. Helium may also be trapped on heterogeneous sites. such as precipitates. We have included both homogeneous and heterogeneous nucleation in our analysis of helium transport. It is shown that matrix clustering is an effective impediment to the transport of helium to grain boundaries only for a short irradiation time. Later, the slow leakage of helium from the matrix to grain boundaries leads to the capture of a percentage of helium produced. The role of precipitates in this mechanism is discussed. Precipitate densities below $\sim 10^{13}$ cm^{-3} may be ineffective helium traps. The effect of displacement damage on gas re-solution is discussed, and shown to have a particular significance in the determination of the average cavity density.

3.0 Program

Title: Radiation Effects on Structural Materials (DOE DE-SR03-84ER52110)
Principal Investigator: Nasr M. Ghoniem
Affiliation: University of California at Los Angeles

4.0 Relevant DAFS Program Task/Subtask

Suhtask Group C: Microstructural Characterization, Correlation Methodology

5.0 Accomplishments and Status

5.1 Introduction

When helium atoms are introduced into a solid, either by implantation or by nuclear reactions, they tend to be insoluble. Like other noble gases, the closed electronic structure results in its segregation. Because of this insolubility, there is a great tendency for helium atoms to be trapped on vacancies, impurity atoms or other helium atoms [1-13].

Unfortunately, the introduction of helium into structural materials by nuclear reactions results in a general degradation of their properties. In fast breeder reactors, as well as anticipated fusion reactors, helium generation can lead to volumetric swelling and high temperature embrittlement of structural

components. It has been shown by numerous experiments [14-26], that even small amounts of helium can lead to a severe loss of ductility. Thusby, the creep rupture lifetime of structural materials can be drastically reduced at high temperature. Failure creep ductilities on the order of less than 1% have been reported [26].

It has also been experimentally demonstrated that the location of helium production is of strategic importance 1271. Steels with a small amount of boron have shown low ductility, when boron allows precipitates near the grain boundary. Experiments have shown that when boron atoms are uniformly distributed throughout the matrix (e.g. by thermomechanical heat treatments). the loss of ductility is not so great[27].

The problem of high temperature helium embrittlement is critical for fast breeder core and vessel structural materials. If fusion reactor first walls are operated at temperatures above 500°C for steels, helium emhrittlement can also he a limiting design factor. It is therefore technically important to adress this problem. During the past two decades, there has been a significant effort to understand and solve this phenomenon (see, for example, references (14-27)). A great degree of understanding has been achieved. From a theoretical standpoint. the presence of helium in grain boundary cavities has been shown to result in growth instabilities that reduce the rupture lifetime (28-30). For these treatments, however. the presence of helium inside grain boundary cavities was always assumed. For example, Trinkaus and Ullmaier [29] assumed a constant gas pressure inside growing grain boundary cavities, while Bullough, Hayns and Harries [30] assumed a simple form of gas arrival to grain boundary cavities. Even with the greater understanding of helium effects on grain boundary cavitation, there still seems to be two weak links. The first is the method of helium transport to grain boundaries. The second issue of poor understanding. is the process of grain boundary cavity nucleation.

The migration of single gas atoms to grain boundaries is complicated by the fact that there are competing matrix processes that may hinder helium transport to boundaries. Helium atoms, which predominantly migrate by an interstitial mechanism, can he trapped at precipitate interfaces, vacancies or in vacancy-helium clusters.

We have recently developed theoretical analysis for matrix helium transport during irradiation [13]. In this paper, we develop a rate-theory based model for the study of helium migration from the matrix to the grain boundary. Helium atoms are produced in the lattice in one of the following ways:

1. Nuclear reactions or by direct implantation. This Source produces a uniform distribution of helium atoms in the matrix
2. Displacement damage (dynamic re-solution). When helium atoms are trapped, collision cascades or direct collisions with the primary particle (neutron or ion) can displace it again into the lattice. This is an internal Source of helium atoms that is also uniform over space.
3. Localised sources. In this case, when elements such as boron are segregated near grain boundaries, a high localised source of helium is introduced. However, the burnup of boron atoms due to neutron absorption reactions leads to a transient helium source.

The first source of helium is dominant for short times, while the third is transient and relevent only for the case of neutron irradiation. The transient time scale for the third mechanism is on the order of $(\sigma_a \phi)^{-1}$, where σ_a is a spectral-averaged Boron neutron absorption cross-section, and ϕ is the neutron flux. It can he shown, however, that the second mechanism is the most dominant for times longer than the time required to achieve about 1 dpa. Consider now the following simple argument.

Let us denote the external helium generation rate by G^{He}_{ext} (first mechanism), the internal helium generation rate by G^{He}_{int}, and the displacement damage rate by G. In this case, the total fractional helium concentration is $G^{He}_{ext}t$, where t is time. The total fractional helium displacement rate (internal source) is therefore,

$$\text{internal helium source rate} = G^{He}_{int} = G^{He}_{ext} tG \qquad (1)$$

For this source rate to exceed the external rate of helium introduction.

$$G^{He}_{ext}\, \tau G > G^{He}_{ext} \qquad (2)$$

Therefore, the time required to achieve this condition is on the order of

$$\tau > G^{-1} \qquad (3)$$

Of course, this is a simplified argument, and the exact value of τ will depend on the strength of the interaction between displacement damage and helium atoms [31]. However, it illustrates the point that the time required to achieve this condition is not very long, if gas re-solution rate is the same as the

displacement damage rate.

In addition to single gas atom migration to grain houndaries, helium can also be transported in migrating bubbles. In this case, hubhles can move by a variety of mechanisms and transfer helium atoms with them.Once a helium atom is trapped in a vacancy, it forms a substitutional atom until other gas atoms or vacancies react with it. If that happens, a vacancy-helium complex is said to he formed. Such a vacancy-helium complex can grow in principle hy one or all of the following three processes: (1) it can accept newly created, injected or re-dissolved gas atoms; (2) it can accept vacancies either by producing near-Frenkel pairs in the low temperature regime ($T < 0.3\ T_m$, where T_m is the melting temperature in Kelvin) or by absorbing excess radiation-produced vacancies at high temperatures; and (3) it can migrate until it coalesces with other bubbles. The first two mechanisms are likely to operate in the presence of irradiation, while the last can proceed under irradiation as well as under post-irradiation conditions. Since in this case huhhle migration is the rate-controlling step for bubble growth, bubble coalescence occurs only in the high temperature regime, i.e. above 0.5 Tm 1321.

The driving force for bubble migration can be either the Brownian motion in the absence of temperature or stress gradients, or sweeping by moving dislncations. In the first case hubhle migration is random while in the latter cases it is directed up the gradient. Rubble motion practically stops when the bubble radius becomes large (~ 100nm), or when restoring forces occur. A simple mechanism of delay is the self-pinning of bubbles by their own stress fields. This may occur when the internal gas pressure is so high as to plastically deform the surrounding matrix. Recently, gas pressures indicating solid state conditions have heen measured for aluminum and nickel [33]. Important pinning centers for buhhles are the dislocations with a restoring force assumed to he constant, precipitates and grain boundaries with forces increasing linearly with huhble radius [32].

The term "bubble" used here applies to a gas-filled cavity with a diameter above the resolution limit of the transmission electron microscope (~ 1.0 nm). Below this limit, we consider the hubhle to be a "vacancy-helium cluster". Although different theoretical mechanisms exist for huhhle re-solution, experimental observations suggest that bubbles are highly stable defects. Possibe re-solution processes are:

1. Annealing or shrinkage at high tempertures.
2. Re-solution or shrinkage by gas-displacement events.
3. Re-solution of small bubbles due to Oswald ripening.
4. Absorption of bubbles by others during coalescence.

The first three processes supply single gas atoms. thus, enhancing the gas production rate, whereas the absorption (and disappearance) of bubbles doe to coalescence does not change the gas production rate. Experimental evidence for the first process has not been reported. Also, observations supporting the re-solution of gas atoms by collision events in metals are not reported, in contrast to the re-solution of precipitates observed during irradiation. However, direct observations of fission gas bubble re-solution have heen reported [34]. We will therefore consider dynamic re-solution to exist for helium bubbles in metals as well. Rubble growth by Oswald ripening has been proposed [32], but experimental evidence is still missing. From both post-irradiation annealing experiments and irradiation experiments, the disappearance of small bubbles due to coalescence has heen concluded. Buhhle growth observations versus time growth exponent α larger than 3, when a power-law ($r \sim t^{1/\alpha}$) is applied, have been attributed to coalescence growth [32]. Theoretically, however, it could he shown that any growth exponent between 1.5 and b can he achieved under irradiation independent of the net flax of helium to huhbles [32]. Thus, it seems to be questionable, whether the growth mechanism represented by the a -value can be concluded from a simple power-law growth behavior.

In the following sections we develop and apply a theory for helium clustering and transport to grain houndaries by single gas atom motion. The theory is therefore restricted to the conditions outlined above. Section 2 deals with the rate theory of helium clustering and transport. The results of calculations are presented in Section 5. The symbols and their units are given in the Nomenclature.

5.2 Theory of Helium Clustering and Transport to Grain Roundaries

As was previously mentioned, helium production is achieved via several sources. In the present theoretical treatment, we will not include "localised" or "time-dependent''helium sources. In principle, the present work can be extended to allow for these inhomogenieties. Other important space or time inhomogenieties can he due to the nature of irradiation. The production of vacancies, self interstitials and helium are stochastic processes, since they are involved in collision cascades. Therefore, certain reactions between those primary species can be influenced by the time/space distribution of the production source. There is

some progress in this area [35-37], however, the conclusions are not yet formulated in a way to include in a rate theory-type approach. We will therefore assume that defect reactions are homogeneous in both space and time.

The mode of cavity nucleation is important to discuss here. Recent stability line analysis [38] has shown that there are two general modes of cavity nucleation. The first mode driven by helium gas, which has been termed "spontaneous" nucleation, is dominant for high helium to dpa ratios (> 5). The second mode is what is termed "delayed" nucleation by the condensation of vacancies on themselves or residual impurities. This occurs at low helium to dpa ratios. The theoretical analysis of this last case is more difficult than the spontaneous nucleation case. We will only consider spontaneous nucleation in the present work.

5.2.1 Rate Equations

We will write here appropriate rate equations for the following species: (1) unoccupied vacancies; (2) self interstitial atoms; (3) interstital helium atoms; (4) substitutional helium atoms; (5) di-interstitial helium atom clusters; (6) di-helium single vacancy clusters; (7) bubble nuclei containing 3 helium atoms; (8) large bubbles containing m helium atoms. We also develop equations for the average bubble size, the average number of helium atoms in a bubble, and the amount of helium absorbed on grain boundaries. For the case of the existence of matrix precipitates, we assume that one helium bubble is associated with each precicpitate. Therefore, we include an equation describing the average precipitate bubble radius. and another equation for the average number of helium atom in a bubble. The following are equations for the fractional concentrations of various species:

(1) Unoccupied vacancies

$$\frac{dC_v}{dt} = fG + E^h_{gv}C_{gv} + bGC_{gv} - \alpha C_v C_i - R_{g,v}C_g C_v - R_{v,s}C^v_s C_v - R_{v,2g}C_v C_{2g} - R_{v,gv}C_v C_{gv} - R_{v,2gv}C_v C_{2gv} - R_{v,*}C_v C^* \quad (4)$$

(2) Self Interstitials

$$\frac{dC_i}{dt} = fG - \alpha C_v C_i - R_{i,gv}C_i C_{gv} - R_{i,s}C_i C^i_s - R_{i,2gv}C_i C_{2gv} - R_{i,*}C_i C^* \quad (5)$$

(3) Interstitial Helium

$$\frac{dC_g}{dt} = G_H + E^h_{gv}C_{gv} + bGC_{gv} + R_{i,gv}C_i C_{gv} + m\,bGC_1 + bGM_b + bGM_{ppt} + 2R_{i,2gv}C_i C_{2gv} + E^h_{2gv}C_{2gv} + 3bGC^* + R_{i,*}C_i C^* + 2(2bG)C_{2g} + 2bGC_{2gv} - R_{g,b}C_g C_b - R_{g,v}C_g C_v - 2R_{g,g}C^2_g - R_{g,gv}C_g C_{gv} - R_{g,2gv}C_g C_{2gv} - R_{g,gb}C_g C_{gb} - R_{g,*}C_g C^* - R_{g,2g}C_g C_{2g} - R_{g,ppt}C_{ppt} C_g \quad (6)$$

(4) Substitutional Helium

$$\frac{dC_{gv}}{dt} = R_{g,v}C_g C_v + E^h_{2gv}C_{2gv} + 2bGC_{2gv} - C_{gv}\{E^h_{gv} + bG + R_{i,gv}C_i + R_{g,gv}\} \quad (7)$$

(5) A Cluster of 2-Helium Atoms and One Vacancy

$$\frac{dC_{2gv}}{dt} = R_{g,gv} C_g C_{gv} + 3bGC^* + R_{v,2g} C_v C_{2g} - R_{g,2gv} C_g C_{2gv} - 2bGC_{2gv} - \sum_h E_{2gv} C_{2gv} - R_{i,2gv} C_i C_{2gv} \quad (8)$$

(6) Di-interstitial Helium Clusters

$$\frac{dC_{2g}}{dt} = R_{g,g} C_g^2 - R_{v,2g} C_v C_{2g} - R_{g,2g} C_g C_{2g} - 2bGC_{2g} + R_{i,*} C_i C^* - \sum_h E_{2g} C_{2g} \quad (9)$$

(7) nubble Nucleus

$$\frac{dC^*}{dt} = R_{g,2gv} C_g C_{2gv} + R_{g,g} C_g C_{2g} - R_{g,*} C_g C^* - R_{v,*} C_v C^* - R_{i,*} C_i C^* - 3bGC^* \quad (10)$$

(8) Matrix Rubble Concentration

$$\frac{dC_b}{dt} = \frac{4}{m_1} R_{g,*} C_g C^* + \frac{3}{m_1} R_{v,*} C_v C^* \quad (11)$$

(9) Average Number of Gas Atoms in a Rubble

$$\frac{dm_1}{dt} = R_{g,b} C_g - bGm_1 \quad (12)$$

(10) Average Matrix Rubble Radius

$$\frac{dR}{dt} = \frac{1}{R} \{D_v C_v - D_i C_i - D_v C_v^e [\exp(\frac{\Omega}{kT}(\frac{2\gamma_b}{R} - p_1)) - 1]\} \quad (13)$$

(11) Grain Boundary Gas

$$\frac{dM_{gb}}{dt} = R_{g,gb} C_g - bGM_{gb}$$

(12) Average Precipitate Rubble Radius

$$\frac{dR_{pb}}{dt} = (\frac{r_p^2 + R_{pb}^2}{R_{pb}^2})^{1/2} \frac{1}{R_{pb}} \{D_v C_v - D_i C_i - D_v C_v^e [\exp(\frac{\Omega}{kT}(\frac{2\gamma_b}{R_{pb}} - p_2)) - 1]\} \quad (14)$$

(13) Total Gas in Precipitates

$$\frac{dM_{ppt}}{dt} = R_{g,ppt} C_{ppt} C_g - bGM_{ppt}$$

While the definitions of various symbols are given in the Nomenclature section, we give here a brief description for the basis of the previous equations. The general form of the previous reactions are: displacement damage G, thermal emission E, radiation resolution bG (b is re-solution parameter), and reactions between type A and type R mobile species $R_{A,B} C_A C_B$. The first 4 equations are given for the primary reacting species; namely vacancies, self interstitials, and helium atoms. The difference between the present equations for C_v and C_i and the conventional ones is that we include here clustering reactions with helium atoms in the conservation equations. Since it is assumed that gas atoms force cavity nucleation, we have included equations for 2 gas atoms - single vacancy, and for a di-interstitial helium cluster. It can be shown that di-interstitial helium clusters are unstable at high temperature due to the low binding energy [39], and that their contribution to cavity formation is limited to the low temperture regime. A cluster of 2 helium atoms and one or no vacancies is still not the critical nucleus size, since backward reaction rates can be strong. Therefore, we consider that the critical nucleus size is a cluster of 3 gas atoms and some vacancies (need not be exactly determined). This defines the early clustering part of the process. Another larger group of bubbles is then introduced with a concentration C_b. The formation of these bubbles is achieved either by a vacancy or helium atom impingement on the critical nucleus. For gas conservation purposes, the gas-nucleus reaction rate is reduced by a factor of $4/m_1$, and the vacancy-nucleus reaction rate by a factor of $3/m_1$. These are the ratios of the number of gas atoms in the reaction to the average number of gas atoms in the large size bubble group. With this, the first moment of the size distribution is conserved (total number of helium atoms). Alternatively, one can conserve the zeroeth moment (total bubble density), but not the first moment (total gas content) if the nucleation rate is not coupled with m_1 as done here. The effects of such a model cannot be fully explored here, but work is in progress on cavity size distributions

5.2.2 Reaction Rates

We adopt here 4 basic fequencies in the clustering system. a is the frequency of self-interstitial reaction, ß is the frequency of helium gas reaction, γ is the frequency of vacancy reaction and 6 is the radiation re-solution frequency. These are given by:

$$a = 48\, \nu_i \exp(-E_i^m/kT) \quad , s^{-1} \tag{15}$$

$$ß = 48\, \nu_g \exp(-E_g^m/kT) \quad , s^{-1} \tag{16}$$

$$\gamma = 48\, \nu_v \exp(-E_v^m/kT) \quad , s^{-1} \tag{17}$$

$$\delta = b\, G \quad , s^{-1} \tag{18}$$

Also, basic thermal emission probabilities are given by the Boltzmann factors:

$$e_1 = \exp(-E_{vh}^B/kT) \tag{19}$$

$$e_2 = \exp(-E_{v,2h}^R/kT) \tag{20}$$

$$e_3 = \exp(-E_{v,b}^B/kt) \tag{21}$$

$$e_4 = \exp(-E_v/kT) \tag{22}$$

$$e_c = \exp(-E$$

The binding energies E_{vh}^B, $E_{v,2h}^B$, E_{2g}^B are determined from experiments or computer lattice calculations. The vacancy-bubble binding energy $E_{v,b}^B$ is evaluated from the work done in emitting a vacancy as follows:

$$E_{v,b}^B = E_v^f + \Delta w \tag{24}$$

$$\Delta w = (\text{—}^{-} - P_{\cdot})\Omega$$

where Δw is the work done by the change in surface area and in compressing the gas. The gas pressure, p_1, is determined by using the Van der Waal's equation of state for helium, i.e.

$$p_1 = \frac{mkT}{(\frac{4}{3}\pi R^3 - mB)} \tag{26}$$

For high gas pressures at small radii, a virial expansion is used. The following parameters are also used in our calculations:

Vacancy diffusion coefficient = $D_v = (\frac{a}{48})^2 \gamma$ (27)

Self-interstitial diffusion coefficient = $D_1 = (\frac{a}{48})^2 \alpha$ (28)

Diffusion-control combinatorial factor for bubbles = $\varepsilon = \frac{4\pi R}{48}(\frac{R}{a})$ (29)

Equivalent dispersed vacancy sink concentration = C_s^v

Equivalent dispersed interstitial sink concentration = C^i

Equivalent grain boundary sink concentration = C_{GB}

These quantities are given hy:

$$C_s^v = (\frac{a^2}{48})[Z_v \rho + 4\pi R C_b/\Omega + 4\pi R_{pb} N_p + 4\pi r_p N_p] \tag{30}$$

$$C_s^i = (\frac{a^2}{48})[Z_i \rho + 4\pi R C_b/\Omega + 4\pi R_{pb} N_p + 4\pi r_p N_p] \tag{31}$$

$$C_{GB} = (\frac{a^2}{8d})[4\pi r_p N_p + 4\pi R C_b/\Omega + 4\pi R_{pb} N_p]^{1/2} \tag{32}$$

With the previous notations, we re-write the reaction rates for the various processes. In the following, we take the basic combinatorial number as 48, and assume that the combinatorial number with a cluster containing n particles is simply 48n. A discussion on the grain boundary loss term is given in section 2.4.

Helium Emission

$$E^h_{g,v} = \beta e_1 \tag{33}$$

$$E^h_{2g,v} = \beta e_2 \tag{34}$$

$$E^h_{2g} = \beta e_5 \tag{35}$$

Interstitial Reactions

$$\text{Recombination} = \alpha \tag{36}$$

$$\text{Distributed Sink} = \alpha C^i \tag{37}$$

$$R_{i,gv} = \alpha \tag{38}$$

$$R_{i,*} = 3\alpha \tag{39}$$

Vacancy Reactions

$$\text{Distributed Sink} = \gamma C_s^v \tag{40}$$

$$R_{v,2g} = 2\gamma \tag{41}$$

$$R_{v,*} = 3\gamma \tag{42}$$

$$R_{v,gv} = \gamma \tag{43}$$

$$R_{v,2gv} = 2\gamma \tag{44}$$

Gas Reactions

$$R_{g,v} = \beta \quad (45)$$

$$R_{g,b} = \varepsilon\beta \quad (46)$$

$$R_{g,g} = 2\beta \quad (47)$$

$$R_{g,gv} = \beta \quad (48)$$

$$R_{g,2gv} = 2\beta \quad (49)$$

$$R_{g,2g} = 2\beta \quad (50)$$

$$R_{g,*} = 3\beta \quad (51)$$

$$R_{g,gb} = C_{GB}\beta \quad (52)$$

Vacancy Emission

$$D_v C_v^e \exp\left[\frac{\Omega}{kT}\left(\frac{2\gamma}{R} - p_1\right)\right] = a^2 \gamma e_3 \quad (53)$$

$$D_v C_v^e = a^2 \gamma e_4 \quad (54)$$

Now the previous set of rate equations can be re-written in the following form:

$$\frac{dC_v}{dt} = fG + (\beta e_1 + \delta)C_{gv} - \{\alpha C_i + \beta C_g + \gamma[C_s^v + C_{gv} + 2C_{2g} + 2C_{2gv} + 3C^*]\}C_v \quad (55)$$

$$\frac{dC_i}{dt} = fG - \{C_v + C_{gv} + 2C_{2gv} + 3C^* + C_s^i\}\alpha C_i \quad (56)$$

$$\frac{dC_g}{dt} = G_H + (\beta e_1 + \delta + \alpha C_i)C_{gv} + (\beta e_2 + 2\delta)C_{2gv} + 3(\delta + \alpha C_i)C^* + 4\delta C_{2G} + 4aC_i C_{2gv} + m\delta C_b + \delta M_{gb} + \delta M_{ppt} - [\varepsilon C_b + C_v + 4C_g + C_{gv} + 2C_{2gv} + 2C_{2g} + C_{GB} + \varepsilon_{ppt} C_{ppt}]\beta C_g \quad (57)$$

$$\frac{dC_{gv}}{dt} = RC_g C_v + (\beta e_2 + 2\delta)C_{2gv} - \{\beta e_1 + \beta C_g + 6 + \alpha C_i\}C_{gv} \quad (58)$$

$$\frac{dC_{2gv}}{dt} = \beta C_g C_{gv} + 3\delta C^* + 2\gamma C_v C_{2g} - \{2\beta C_g + 2\delta + \beta e_2 + 2\alpha C_i\}C_{2gv} \quad (59)$$

$$\frac{dC_{2g}}{dt} = 2\beta C_g^2 + 3\alpha C_i C^* - \{2\gamma C_v + 2\beta C_g + 2\delta\}C_{2g} \quad (60)$$

$$\frac{dC^*}{dt} = 2(C_{2gv} + C_{2g})\beta C_g - 3(\beta C_g + \gamma C_v + \alpha C_i + \delta)C^* \quad (61)$$

$$\frac{dC_b}{dt} = (12/m_1)\beta C_g C^* + (9/m_1)\gamma C_v C^* \quad (62)$$

$$\frac{dm_1}{dt} = \varepsilon\beta C_g - \delta m_1 \quad (63)$$

$$\frac{dR}{dt} = \left(\frac{a^2}{R}\right)\{\gamma C_v - \alpha C_i - \gamma(e_3 - e_4)\} \quad (64)$$

$$\frac{dM_{ppt}}{dt} = \epsilon_{ppt}\beta C_{ppt} C_g - \delta M_{ppt} \quad (65)$$

$$\frac{dM_{gb}}{dt} = \beta C_{GB} C_g - \delta M_{gb} \quad (66)$$

$$\frac{dR_{pb}}{dt} = \left(\frac{r_p^2 + R_{pb}^2}{R_{pb}^2}\right)^{1/2}\left(\frac{a^2}{R_{pb}}\right)\{\gamma C_v - \alpha C_i - \gamma(e_3' - e_4)\} \quad (67)$$

where e'_3 is calculated for a precipitate huhhle in a similar way to e_3.

5.2.3 Gas Conservation

For the previous system of equations to have a realistic solution, total gas should be conserved. In this case, the total amount of injected gas should be accounted for in various clusters, in bubbles, on precipitates and on grain houndaries. This means that the following equation must be satisfied:

$$M_t = G_H t = C_g + C_{gv} + 2C_{2gv} + 3C^* + mC_b + M_{ppt} + M_{gb} \quad (68)$$

The time-derivative of this equation gives:

$$G_H = \frac{dC_g}{dt} + \frac{dC_{gv}}{dt} + 2\frac{dC_{2gv}}{dt} + 2\frac{dC_{2g}}{dt} + 3\frac{dC^*}{dt} + m\frac{dC_b}{dt} + C_h\frac{dm}{dt} + \frac{dM_{ppt}}{dt} + \frac{dM_{gb}}{dt} \quad (69)$$

The right hand side of equation (69) is composed of time-derivatives of various cluster concentrations. Using equations (57) through (63), and equations (65) and (66), it can be easily shown that the conservation equation (69) is strictly satisfied. We can now calculate the fraction of total injected gas that ends up on the grain houndaries.

$$f_{gb} = \frac{M_{gb}}{G_H t} \quad (70)$$

5.2.4 Grain Roundary Helium Flux

The amount of helium arriving at the grain boundary is dependent upon the matrix sink for helium. During the early stages of irradiation, matrix precipitates and bubbles are not the dominant sink and one must take into account all other helium sinks (vacancies and small size clusters). The amount of helium going to grain boundaries will be small during this phase, however. Now, suppose that helium diffuses in a medium of distributed sink strength k^2. And suppose also that the grain boundary is a perfect helium sink. The diffusion equation is then given by:

$$D_g \nabla^2 C_g + G_g - k^2 D_g C_g = \frac{\partial C_g}{\partial t} \quad (71)$$

where $k^2 = 4\pi R C_b/\Omega + 4\pi r_p N_p + \Sigma$small clusters (72)

Equation (71) may he solved analytically for cases where the gas diffusion coefficient (D_g), the gas generation rate (G_g) and the sink concentration k^2 are all constants and not functions of time or space. An eigen function solution results in a time-series representation [40]. For time-dependent variation of D_g, G_g and k^2, Mathews and Wood [41] developed a variational method for the calculation of grain boundary gas flow. For our purposes, it is sufficient to adopt the steady-state solution given by Brailsford and Bullough [42]. The following simple expression is used for the "equivalent" grain boundary sink strength:

$$C_{GB} = \frac{a^2 k}{8d} \qquad (73)$$

5.2.5 "Constrained" and "Unconstrained" Cavity Growth Modes

Due to the fact that we have included vacancy-gas reactions in our analysis, not all of the vacancies will he readily available for cavity growth by excess vacancy ahsorption. Normally, when there is only two reacting species; vacancies and interstitials, the presence of a dislocation bias toward interstitials insures a larger vacancy flux to he absorbed at cavities. The growth rate of cavities is directly related to the magnitude of dislocation bias in this case. We will term this growth behavior as "unconstrained" cavity growth mode. A new situation is encountered when helium atoms are included in this delicate balance process. In one form or another, vacancies and interstitials eventually recombine. except for some "biased" interstitials that end up preferentially on dislocations. The cavity growth is therefore dictated by the amount of interstitials absorbed. which has an equivalent net number of vacancies in cavities. When helium gas preferentially reacts with vacancies, some vacancies are then immobilized and therefore will not he available for "unconstrained" cavity growth. If vacancy-helium reactions are significant (i.e, the number of substitutional helium atoms is a large fraction of the total vacancy population), a larger flux of self-interstitials may arrive at the cavity, thereby inhibiting its growth. When this is the case, cavities can only grow by the ahsorption of helium atoms. and not by an excess vacancy flux. This is a very slow process, since helium atoms absorbed in the cavity have to produce their own Frenkel pairs due to the excessive cavity pressure. We will term the growth behavior in this case "constrained" as opposed to the unconstrained growth mode. In the following, we derive an analytical condition for the predominance of one of these modes of growth.

Suppose now that quasi-steady state conditions have heen achieved by the previous system of equations. In this *case*, the vacancy and interstitial equations can be described by:

$$\frac{dC_v}{dt} = 0 = fG - \alpha C_v C_i - \gamma C_v C_s^v - \beta C_g C_v \qquad (74)$$

$$\frac{dC_i}{dt} = 0 = fG - \alpha C_v C_i - \alpha C_i C_s^i \qquad (75)$$

In equations *(74)* and (75), we have lumped all vacancy sinks in the C_s^v term, and all equivalent intersitial sinks in the C_s^i term. Notice that in these equations there is one non-symmetric reaction rate, which is the reaction rate of helium gas with vacancies. Subtracting equation *(74)* from (75), and re-arranging, it can he easily shown that:

$$\frac{\gamma C_v}{\alpha C_i} = \frac{(C_s^i/C_s^v)}{(1 + \frac{\beta C_g}{\gamma C_s^v})} \qquad (76)$$

For "unconstrained" cavity growth (equation 64), $\gamma C_v/\alpha C_i$ must be greater than unity. Since $\langle Z_i \rangle = C_s^i/C_s^v$, where $\langle Z_i \rangle$ is the average system hias, then the "unconstrained" growth condition is expressed as:

$$\langle Z_i \rangle > (1 + \frac{\beta C_g}{\gamma C_s^v}) \qquad (77)$$

If $\langle Z_i \rangle$ is expressed as:

$$\langle Z_i \rangle = 1 + \Delta Z_i \qquad (78)$$

then, the "unconstrained" growth condition is

$$\langle \Delta Z_i \rangle > \frac{\alpha C_g}{\gamma C_s^v} \qquad (79)$$

Cavity growth can therefore by "constrained" until this condition is satisfied. In other words, the conversion condition from "constrained" to "unconstrained" growth is achieved when:

(vacancy-sink reaction rate) > $\langle \Delta Z_i \rangle$ x(vacancy-helium reaction rate) (80)

Equation (80) is the necessary condition for the conversion process.

5.3 Results of Calculations

5.3.1 Influence of Clustering on Single Cas Atom Transport to Grain Roundaries

During the early stages of irradiation, helium is generated as an interstitial atom, hut is soon trapped when vacancies become available. The concentration of untrapped helium is never very high. This trapping eventually leads to the formation of huhhles from substitutional helium. We first present the results of calculations for ion-irradiation conditions. This is intended to simulate a study conducted by Argonne using dual-ion beam irradiation at a nominal temperature of 625°C on type 316 stainless steel [43]. The displacement damage rate is 3 x 10^{-3} dpa/second, and the helium/dpa ratio is 5. While the re-solution parameter (b) has been set = I, and the dislocation bias factor to $\langle Z_i \rangle$ = 1.2; the remainder of material parameters are the standard values for 316 stainless steel, and are given in Table (1). The sensitivity of the calculations to input parameters is discussed later in this section.

We will discuss the influence of matrix clustering on the transport of helium atoms to grain boundaries. Figure (1) shows the Concentrations of single vacancies (C_v), self interstitials (C_i), interstitial helium (C), substitutional helium (C_{gv}), as well as bubbles (C_B). It *can* he seen that the time structure of C_v a d C_i is little affected by the presence of helium. However, the absolute magnitude of the vacancy concentration in this case is less than the corresponding situation without the interaction with helium gas. After a short period of irradiation time ($t > 0.1$ seconds), more helium is produced by displacement reactions leading to a second peak in the interstitial helium concentraion around 10 seconds, as can be seen in figure (1). The system comes to near dynamic equilibrium in about 1000 seconds (few dpa's). Figure (2) shows the distribution of helium in clusters, bubbles and grain boundaries as a function of time. By definition, vacancy-helium clusters are those containing 3 helium atoms or less, while huhhles contain more than 3 helium atoms. Since the helium injection rate is constant, the total amount of helium is linear in time. During early irradiation times ($\leq$ 0.01 dpa), most of injected helium resides in small helium-vacancy clusters. These are converted to bubbles at a higher dose, as shown in figure (2). The largest proportion of helium ends up in matrix bubbles at doses greater than about 10 dpa. It is observed that during the early stages of irradiation helium is contained in small clusters. Later, a large proportion goes to grain boundaries. However, the matrix bubble concentration becomes significant, when the fraction of helium at grain houndaries is only a few percent of total injected helium.

5.3.2 Comparison with Experiments

Figures *(3)* and (4) demonstrate the sensitivity of cavity evolution parameters to variations in the re-solution rate. In figure (3), a higher re-solution rate is shown to result in continuous cavity nucleation without saturation of the total number density. Low re-solution parameters (below 0.1) lead to saturation of the cavity number density after a short transient time. On the other hand, higher re-solution parameters result in continuous cavity nucleation. The exact value of the re-solution parameter is actually a function fo the PKA energy and the cavity radius 1441. This refinement is not included in the present analysis, since the exact dependence has not yet been calculated. The effects of helium re-solution on the average matrix bubble radius is shown in figure (4). A larger re-solution parameter leads to a higher concentration of substitutional helium, and hence to "constrained" cavity growth.

The influence of the bias factor Z_i on the microstructural parameters is demonstrated in figure (5). The reasonable variation in Z_i shows that the model results come in agreement with experiments. The point to note in figure (5) is the fast build-up of total cavity density. Cavity nucleation is shown to be *a* fast physical process. However, trailing nucleation may still persist beyond this fast phase, as illustrated in figure (6). The nucleation current, J, is shown as a function of irradiation time for extreme parametric conditions. It is interesting to note that nucleation during the early parts of irradiation (below ~ 0.01 dpa) *is* totally insensitive to parametric variations, and is primarily dependent upon helium and dpa generation rates. Generated helium is immediately trapped in free vacancies, or by small vacancy-helium clusters. This behavior is similar to the concept of a "nucleation pulse" as described by Trinkaus [39]. Trailing nucleation may still proceed at a slower rate, dictated by irradiation conditions, for a long time. Cavity number density may therefore increase by a "crucial" few orders of magnitude over the period of irradiation. We will therefore emphasize this mechanism as a "dynamic nucleation" mechanism for cavity formation. Such dynamic nucleation can be continuous throughout irradiation, if the re-solution rate is high, as demonstrated in figure (6).

h comparison of calculations with HFIK data [45] is shown in figures (7) and (8). The high cavity densities in HFIR experiments may be an indication of the dominance of dynamic re-solution, as well and "constrained" growth as described earlier. A comparison of this data with EBR-II data shows that cavity densities are orders of magnitude higher due to the profound effect of helium on nucleation.

5.3.3 Effects of Pre-existing Matrix Precipitates and Grain Size on Grain Roundary Helium Gas

One practical idea to prevent grain boundary cavity nucleation, and hence mitigate helium emhrittlement. is to trap the helium on matrix precipitates [26]. This idea has heen implemented in the development of Titanium modified stainless steels, that are resistant to helium embrittlement. This section describes the results of the present model regarding precipitate effects on helium trapping. Figure (9) shows the results of such calculations for simulation of the Argonne experiment. The figure shows the grain boundary gas content (appm), for a total amount of 150 appm injected helium. as a function of the matrix precipitate concentration (cm^{-3}). It is shown that the amount of grain houndary gas is an insensitive function of the matrix precipitate concentration below 10^{12} precipitate/cm^3. The precipitates were assumed here to he spherical, and of an average size R_{pt} = 100 A. The amount of gas finally residing at the grain boundaries decreases sharply as the precipitate density is increased, ahove 10^{12} cm^{-3}. However, even at relatively moderate densities (10^{14} cm^{-3}), few ppm helium still excape to the grain boundary. Figure (10) shows helium hubhle densities in the matrix, at precipitates as well as total density. The homogeneous nucleation of matrix cavities is reduced by the heterogeneous nucleation of cavities at precipitates. The total number of bubbles is, by heterogeneous nucleation, in the precipitate density reduced range of 10^{12} - 10^{15} cm^{-3}.

Figure (11) shows the grain boundary helium content (appm) as a function of grain diameter (micrometers), fur a total injected helium of 150 appm. The grain boundary gas is a strong function of grain diameter in the range of 10 - 50 micrometers. It decreases sharply from about 113 of total injected helium for a grain diameter of 15 μ m, to roughly 1/31) of injected helium at a diameter of 60 μ m, and then saturates thereafter. A moderate grain diameter of 30–60 μm is shown to be sufficient for reducing grain boundary helium trapping. Larger grain sizes do not result in a considerable improvement. The amount of helium per unit surface area is also shown on the same figure. It is shown that this quantity, which determines grain houndary bubhle density, is relatively insensitive to grain size. Precipitates have heen quantitatively shown to result in a reduction in the amount of helium trapped at grain boundaries. However, for practical precipitate densities few ppm of helium may still reside at grain boundaries. Increasing matrix precipitates is therefore concluded to be more effective in reducing helium embrittlement than increasing grain size.

5.4 CONCLUSIONS

In Chis study, we have shown reasonable agreement with available data on helium-filled cavity nucleation and growth. More important is the demonstration of the effects of several physical mechanisms that may he important in interpreting experiments, or the further development of theory on helium cavity formation. The following points are emphasized:

(1) The injection of helium gas into the solid. either via nuclear reactions or by implantation, cannot be separated from the question of vacancy mobility. It has heen shown that large helium concentrations lead to the immobilization of a large fraction of vacancies, thushy leading to a "constrained" mode of cavity growth. provided that the cavities or clusters are immobile.

(2) Helium gas re-solution due to the interaction of displacement damage with gas-filled cavities is a process of prime importance to cavity re-nucleation. At high re-solution rates, "dynamic nucleation" is a continuous process throughout irradiation.

(3) Theoretical models, and experiments are hoth needed to determine the effects of re-solution.

(4) The external source of helium injection can be less important compared to internal helium sources due to gas re-solution, effects on gas arrival rates at grain boundaries.

(5) During early irradiation, helium gas gets trapped in small vacancy clusters. A large fraction of gas goes to grain boundaries, until matrix cavity nucleation is complete. When this is achieved, the majority of introduced gas resides in buhbles and a small percentage goes to grain boundaries. It may be impossible therefore to completely suppress helium from reaching grain houndaries.

(6) In order for matrix precipitates to act as effective helium traps, their density must he high (> 10^{14} - 10^{15} cm^{-3}).

Acknowledgements

Work was partially supported by the US DOE under grant #DE-SG03-84ER52110 with UCLA during Professor Ghoniem's sabbatical leave at KfK. The financial arrangements and consultational help of the radiation damage group at KfK are greatly appreciated.

REFERENCES

(1) M.I. Baskes .Journal of Nuclear Materials 83 (1979)139.

(2) G. Carter; D.G. Armour; S.E. Donnelly; D.C. Ingram; R.P. Webb "The Injection of Inert Gas Ions into Solids: Their Trapping and Escape, Harwell Consultants Symposium, October 1979, p. 83.

(3) G. Farrell; W.A. Grant Radiation Effects 3 (1970)249.

(4) R.H.J. Fastenau; A. van Veen; P. Penning; L.M. Caspers Phys. Stat. Sol. (A) Subject Classification: 10.1;21 47 (1978)577.

(5) J.E. Inglesfield; J.R. Pendry Philosophical Magazine 34, No. 2 (1976)205.

(6) D.L. Johnson; J.R. Cost "Characterization and Behavior of Atomic Helium in Niobium" Canf. of the National Bureau of Standards on Defects and Defect Clusters in B.C.C. Metals and their Alloys, Gaithersburg, MD, August 1973, pp. 279.

(7) G.R. Odette; P.J. Maziasz; J.A. Spitznagel, Journal of Nuclear Materials, 1036104 (1981)987.

(8) Poker. D.B.; Williams, J.M. Appl. Phys. Lett, 40 (1982)851.

(9) J. Roth Journal of Nuclear Materials 63 (1976)120.

(10) W. Schilling "Diffusion of Helium in Metals" Yamada V Conference on Point Defects, Tokyo, Japan, Oct. 1981.

(11) F.A. Smidt Jr.; A.G. Pieper "Helium Mobility and Rubble Formation in Type 316 Stainless Steel, Aluminum and Vanadium Conf. of the American Society for Testing and Materials on the Properties of Reactor Structural Alloys After Neutron or Particle Irradiation, ASTM STP 570, Gatlinburg, TN, June 1974, pp. 352.

(12) W.D. Wilson; C.L. Bisson Radiation Effects 22 (1974)63.

(13) N.M. Ghoniem; S. Sharafat; J.M. Williams; L.K. Mansur, "Theory of Helium Transport and Clustering in Metals under Irradiation", J. Nucl. Mater., 117 (1983) p.96.

(14) H. Bohm; H.Hauck; W. Leo; C. Wassilew .Journal of Nuclear Materials 33 (1969)343.

(15) G.J.C. Carpenter; R.B. Nicholson "High-Temperature Embrittlement of Metals by Rare Gase Bubbles" Conf. of the International Atomic Energy Agency on the Radiation Damage in Reactor Materials, Vol. II Vienna, June 1969, p. 383.

(16) K.D. Class; L. Schaefer "In-Pile Stress Rupture Strength of three Stabilized Austenetic Stainless Steels" Conf. of the American Society for Testing and Materials on the Effects of Radiation on Substructure and Mechanical Properties of Metals and Alloys, ASIM STP 529, Los Angeles, CA, June 1972, p. 460.

(17) T. Furuta Journal of Nuclear Materials 47 (1973)65.

(18) K.R. Garr; D. Kramer; C.G. Rhodes; A.G. Pard Journal of Nuclear Materials 28 (1968)230.

(19) M. Kangilaski; F.T. Zurey; J.J. Perrin; R.A. Wullaert Journal of Nuclear Materials 39 (1971)117.

(20) R.L. Klueh; J.M. Vitek Journal of Nuclear Materials 117 (1983) 295.

(21) D. Kramer; H.R. Rrager; C.G. Rhodes; A.G. Pard Journal of Nuclear Materials 25 (1968)121.

(22) G.R. Odette, Journal of Nuclear Materials, 122 & 123 (1984) p. 435.

(23) A.A. Sagues; H. Schroeder; W. Kesternich; H. Ullmaier Journal of Nuclear Materials 78 (1978)289.

(24) H. Shiraishi Journal of Nuclear Materials 87 (1979)107.

(25) H. Trinkaus, Journal of Nuclear Materials, 118 (1983) p.39.

(26) H. Schroeder; W. Kesternich; H. Ullmaier, "Helium Effects on the Creep and Fatigue Resistance of Austenitic Stainless Steels", Nucl. Eng. and Desigh/Fusion, Nov. 1984.

(27) D.R. Harries; A.C. Roberts; G.T. Rogers; J.D.H. Hughes; M. Dewey "Role of Boron in the High-Temperature Irradiation Embrittlement of Austenitic Steel" Conf. of the International Atomic Energy Agency on the Radiation Damage in Reactor Materials, Vol. 11 Vienna, June 1969, p. 357.

(28) M.H. Wood; K.L. Kear, Journal of Nuclear Materials, 118 (1983)320.

(29) H. Trinkauss; H. Ullmaier, Phil. Mag. A., 39, No.5 (1979)563.

(30) R. Bullough; D.R. Harries; M.R. Hayns, Journal of Nucl. Materials, 88 (1980)312.

(31) N.M. Ghoniem; M.L. Takata, Journal of Nuclear Materials, 105, Nos. 263 (1982)276.

(32) D. Kaletta; Radiation Effects, 78 (1983)245.

(33) W. Jager; R. Manzke; H. Trinkaus; G. Crecelius; R. Zeller, Journal of Nuclear Materials, 111&112 (1982)674.

(34) R.W. Nelson Journal of Nuclear Materials 31 (1969)153.

(35) L.K. Mansur; W.A. Coghlan; A.D. Brailsford, Journal of Nuclear Materials, 85&86 (1979)591.

(36) A.D. Marwick, "Fluctuations in Defect Concentrations due to Inhomogeneous Production of Point Defects hy Collision Cascades", IBM Report RC9276 (#40786), IRM (1982).

(37) C.P. Chou; N.M. Ghoniem, "The Effects of Collision Cascade Properties on the Diffusion of Point Defects in Irradiated Materials", to he published, Phil. Mag.

(38) S. Sharafat; N.M. Choniem, Journal of Nuclear Materials, 122 Nos. 1-3 (1984)531.

(39) H. Trinkaus, Radiation Effects, 78 (1983)189.

(40) M.H. Wood: J.R. Matthews, Harwell Research Report, TP806 (1979).

(41) J.R. Matthews: M.H. Wood, Journal of Nuclear Materials, 56 (1980)439.

(42) A.D. Brailsford: R. Bullough. Phil. Trans. of the Royal Society of London, A. Math. and Phys. Sciences, 302, No. 1465 (1981)87.

(43) G. Ayrault; H.A. Hoff; F.V. Nolfi, Jr; A.P.L Turner, Journal of Nuclear Materials, 103&104 (1981)1035.

(44) P. Chou; N.M. Ghoniem, "An Approximate Calculation of Precipitate Dissolution Using a Diffusion-Slowing Down Theory for Charged Particles", Submitted, Physical Rev. (B).

(45) P. Maziasz, Journal of Nuclear Materials, 103&104 (1981)987.

Table (I)

Standard Material Parameters for 316 Stainless Steel

Notation	Parameter	Value	units	
a	Lattice Parameter	3.63	Å	1
K	Boltzmann's Constant	8.617×10^{-5}	eV/K	
ρ	Dislocation Density	3×10^{10}	cm/cm^2	
d	Grain Diameter 3×10^{-3}	cm	2	
	Migration Energy of Single Interstitials	0.2	eV	3
E_g^m	Migration Energy of Interstital He	0.2	eV	
m	Migration Energy of Single Vacancy	1.4	eV	3
E_{vh}^B	Detrapping Energy of a Sustitutional He	2.4	eV	
$E_{v,2h}^B$	Detrapping Energy of a Sub-He-He	3.5	eV	
E_{2g}^B	Detrapping Energy of Di-interstitial He	0.79	eV	4
E_v^F	Formation Energy of a Vacancy	1.6	eV	3
F_i^F	Formation Energy of an Interstitial	4.08	eV	3
γ_b	Surface Energy	6.24×10^{14}	eV/cm^2	3
ν_i	Interstitial Vibration Frequency	5×10^{13}	sec^{-1}	5
ν_g	Helium Vibration Frequency	5×10^{13}	sec^{-1}	
ν_v	Vacancy Vibration Frequency	5×10^{12}	sec^{-1}	6
r_p	Precipitate Radius	10^{-6}	cm	
N_p	Precipitate Number Density	10^{10}	cm^{-3}	
B	Van der Waals' Constant	1.75×10^{-23}		6
b	Resolution Parameter	1		
Z_i	Bias Factor of Interstitials	1.2		
Ω	Atomic Volume 1.1958×10^{-23}			8

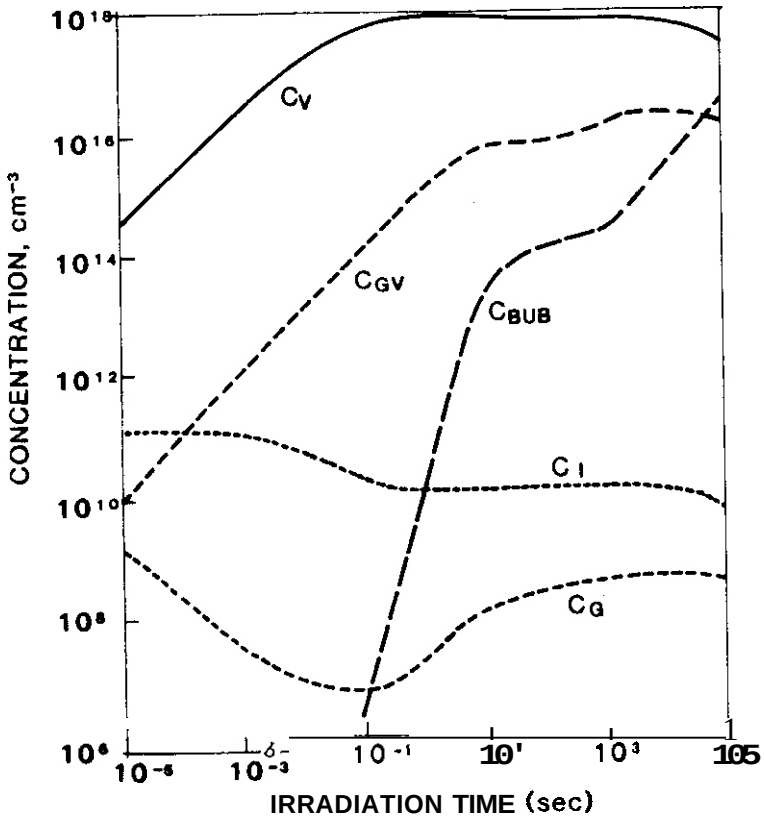

Figure (1) The evolution of clusters and hubhle concentrations as a function of irradiation time. Trradiation condition is dual ion beam with a He (appm) to dpa ratio of 5 and a damage rate of $3x10^{-3}$ dpa/sec at 625°C.

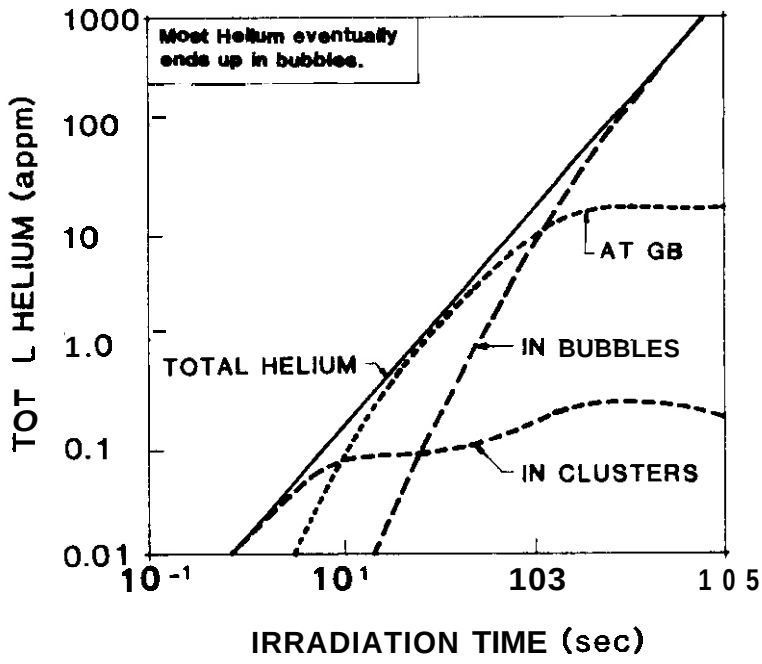

Figure (2) Helium distribution between the different traps in the material. The irrradiation condition is a He (appm)/dpa equal to 5 at $3x10^{-3}$ dpa/sec at 625°C.

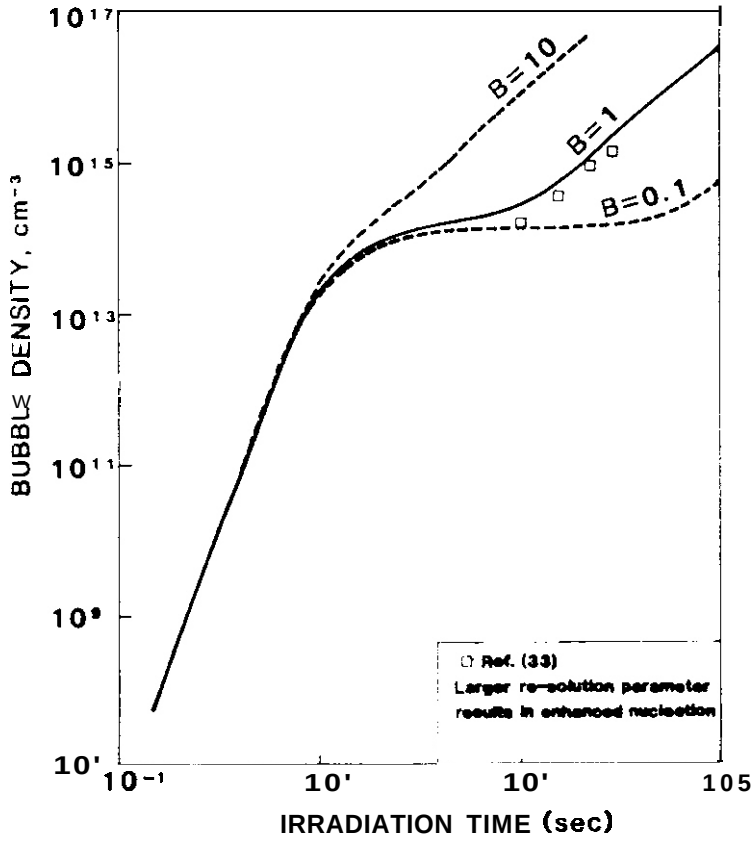

Figure (3) The effect of re-solution parameter on the hubhle concentration for dual ion beam irradiation at 625°C. The He (appm)/dpa is 5 and the damage rate is $3x10^{-3}$ dpa/sec.

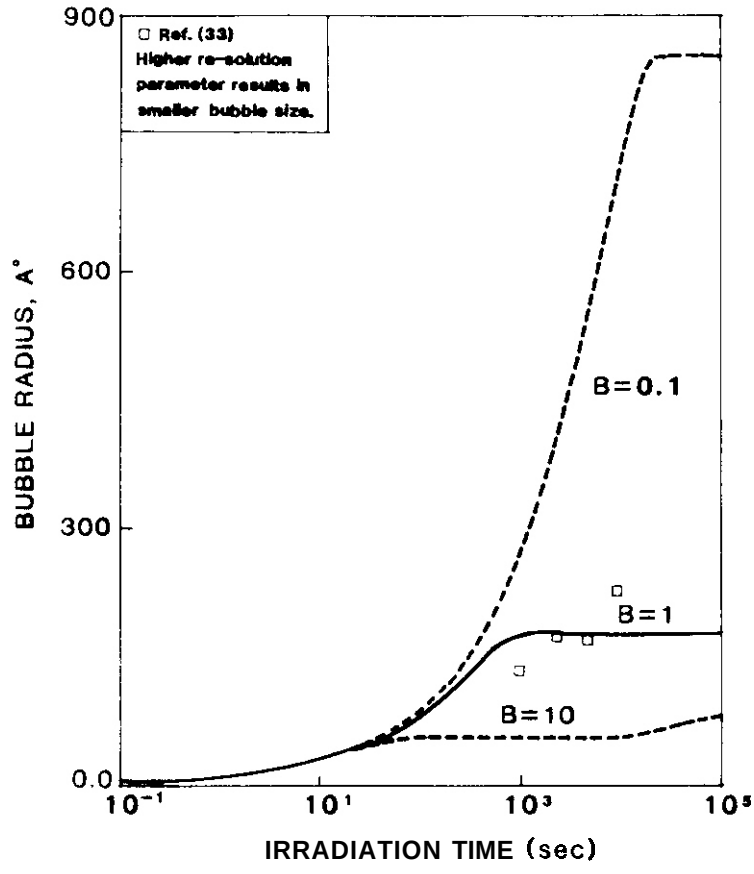

Figure (4) The effect of the re-solution parameter on bubble growth. Trradiation condition is He (appm)/dpa is 5 at 625°C and a damage rate of $3x10^{-3}$ dpa/sec.

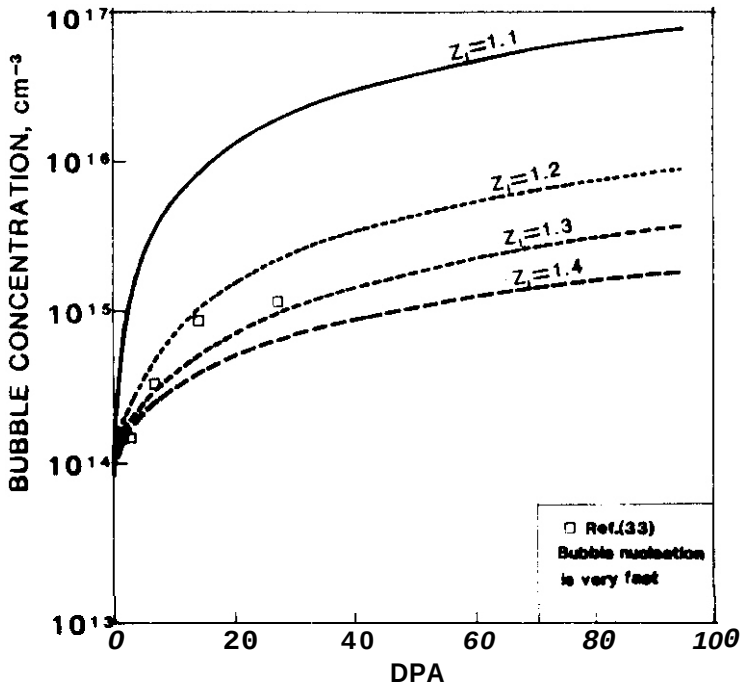

Figure (5) The number density of huhbles is strongly affected hy the interstitial bias factor Z_i. The irradiation condition is 1.5×10^{-2} appm/sec and a He (appm)/dpa of 5 at 625°C.

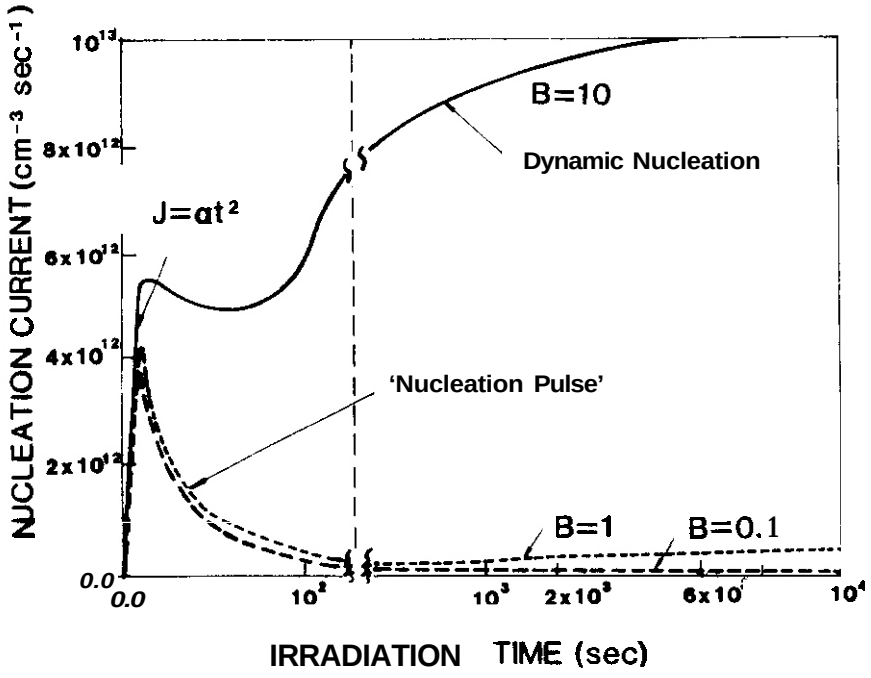

Figure (6) The nucleation behavior of bubbles under irradiation for various values of the re-solution parameter.

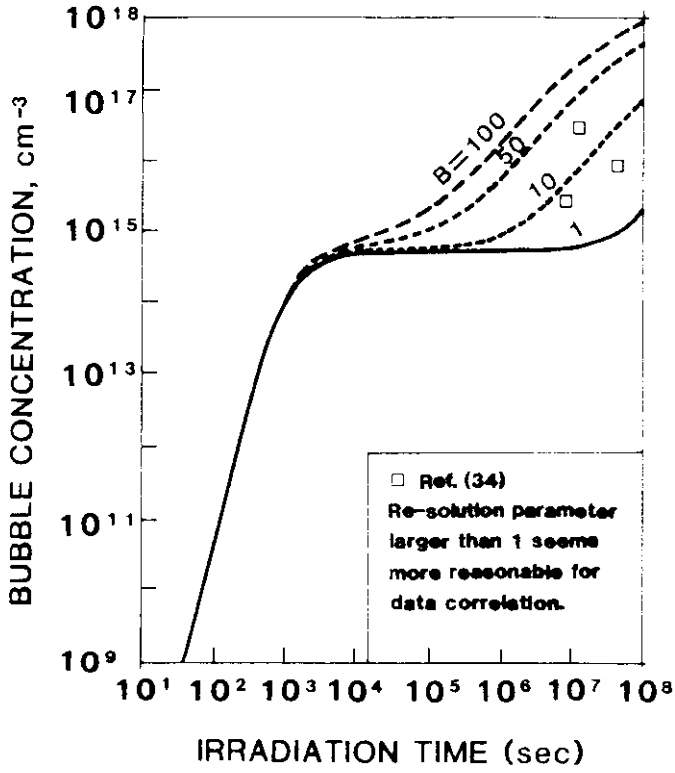

Figure (7) The effect of re-solution parameter on the huhhle concentration for HFIR at 467°C. The He (appm) to dpa ratio is 69 and the helium implantation rate is 6.9×10^{-5} appm/sec.

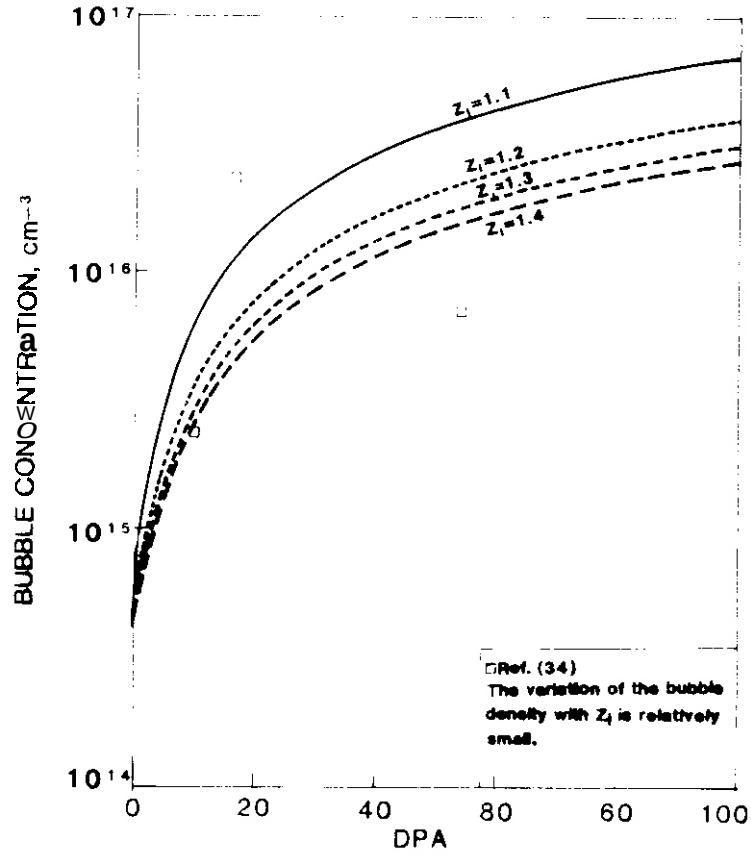

Figure (8) The dependence of the huhhle density on the hias factor as *a* function of DPA for HPIR condition at 467°C. A re-solution parameter of 10 is used in this case

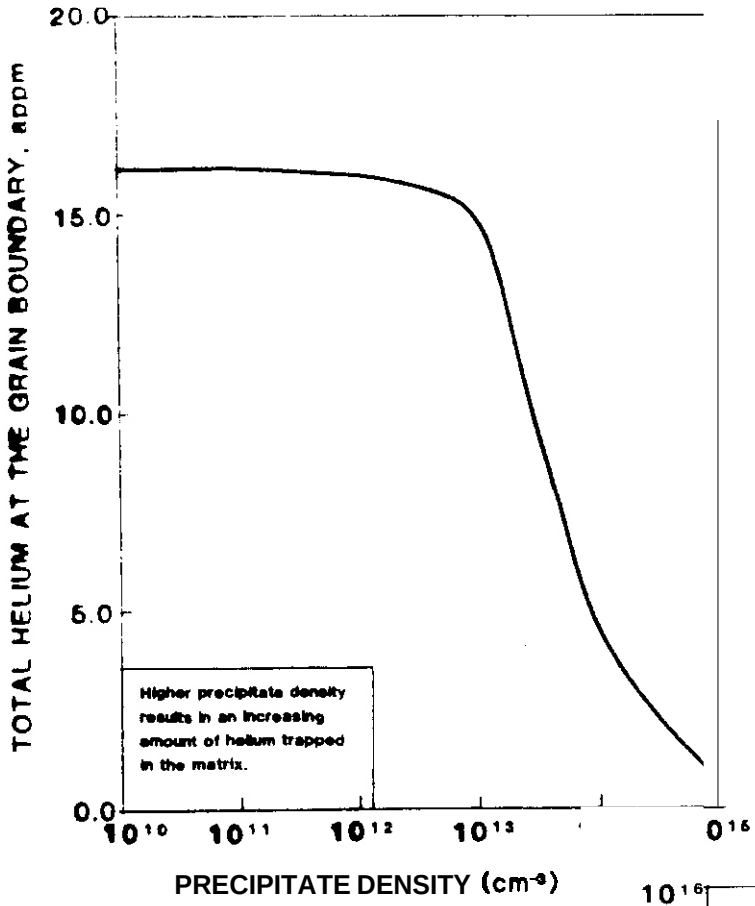

Figure (9) The effect of matrix precipitates on the amount of helium at the grain boundary. Total injected helium is 150 appm at 625°C.

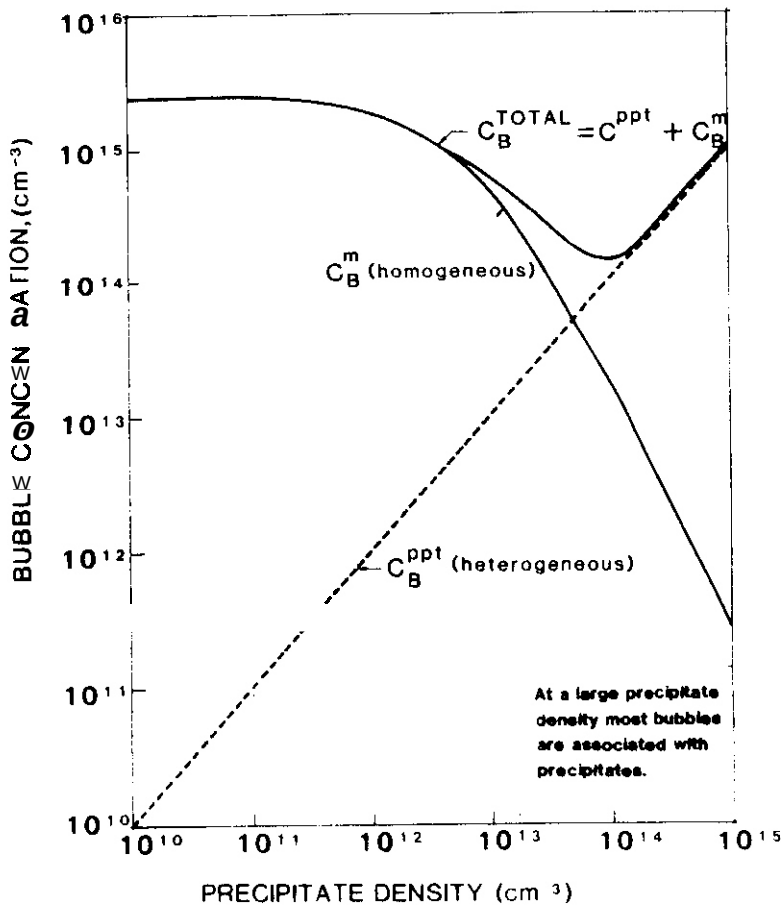

Figure (10) The effect of precipitates on the bubble concentrations. Total injected helium is 150 appm at 625°C.

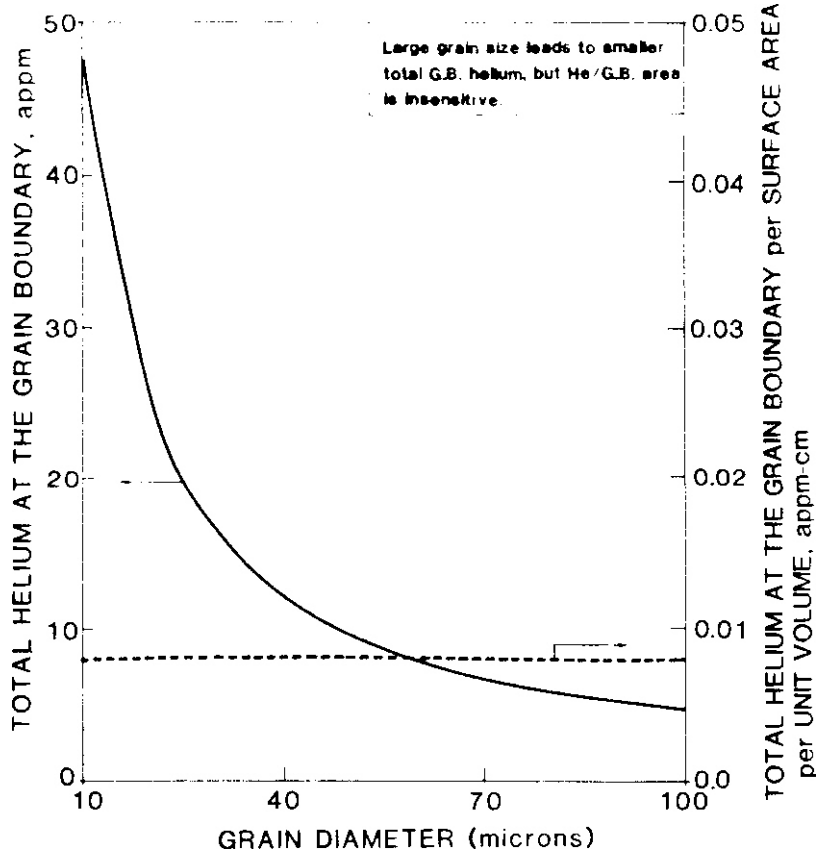

Figure (11) The influence of grain size on the amount of gas at the grain boundary. Total injected gas is 150 appm at 625°C.

5. NOMENCLATURE

SYMBOL	DESCRIPTION	UNITS
a	Lattice parameter	(cm)
B	Van der Waals' constant	(~ 1)
b	Re-solution parameter	(at/at)
C_b	Matrix hubhle concentration	(at/at)
C_g	Interstitial helium concentration	(at/at)
C_{gb}	Equivalent grain boundary sink concentration	(at/at)
C_{gv}	Substitutional helium concentration	(at/at)
C_{2g}	Di-interstitial helium cluster concentration	(at/at)
C_o	Total hhhle concentration in the grain	(at/at)
C_{2gv}	2-helium atoms and one vacancy cluster concentration	(at/at)
C_i	Self-interstitial concentration	(at/at)
D_s^i	Equivalent dispersed self-interstitials sink concentration	(at/at)
C_s^v	Equivalent dispersed vacancy sink concentration	(at/at)
C_v	Single vacancy concentration	(at/at)
C_{ppt}	Matrix precipitates Concentration	(at/at)
C*	Bubble nucleus concentration	(at/at)
C_v^e	Equilibrium vacancy concentration	(at/at)
d	Grain diameter	(cm)
D_v	Diffusion coefficient of vacancies	($cm^2 s^{-1}$)
D_i	Diffusion coefficient of interstitial	($cm^2 s^{-1}$)
e_1	Thermal emission prohahility from a substitutional helium	
e_2	Thermal emission probability from a vacancy-di-helium cluster	
e_3	Thermal emission probability from a bubble	
e_4	Thermal formation probability for a vacancy	
e_5	Dissociation probability for a di-gas atom cluster	
e_i	Thermal emmision probability from a precipitate bubble	
$\varepsilon_{g,v}^h$	Emission rate constant of a helium atom from a substitutional helium	(1/sec)
$\varepsilon_{2g,v}^h$	Emission rate constant of a helium from a di-helium single vacancy cluster	(1/sec)
E_{2g}^h	Emission rate constant of a helium from a di-helium cluster	(1/sec)
E_{vh}^B	Binding energy of a substitutional helium	(eV)
$E_{v,2h}^B$	Binding energy for a vacancy and a di-helium	(eV)
E_{2g}^B	Binding energy for a di-helium	(eV)

$E^{B}_{v,b}$	Binding energy for a vacancy and a bubble	(eV
E^{f}_{v}	vacancy formation energy	(eV)
f	Fraction of vacancies surviving the cascade	
f_{gb}	Fraction of the total gas that ends up at the grain boundary	
G	Frenkel pair generation rate	(dpa/sec)
G_{H}	Helium atom generation rate	(at/at/sec)
G^{he}_{int}	Internal He generation rate	(at/at/sec)
G^{He}_{ext}	External He generation rate	(at/at/sec)
J_{g}	Flux of helium to the grain boundary	(at/at/sec)
K	Boltzmann's Constant	(eV/K)
m_{1}	Number of gas atoms in a matrix bubble	
m_{2}	Number of gas atoms in a precipitate huhble	
M_{gb}	Total number of gas atoms at the grain boundary	
M_{ppt}	Total number of gas atoms at precipitates	
N_{gb}	Rate of bubble arrival at the grain boundary	(1/sec)
P_{1}	Pressure in a matrix hubhle	(eV/cm^3)
P_{2}	Pressure in a precipitate bubble	(eV/cm^3)
Q_{gb}	Absorption rate of helium at the grain boundary	(at/at/sec)
R	Radios of a matrix bubble	(cm)
r_{o}	Average hubhle radius	(cm)
R_{pb}	Radius of a precipitate bubble	(cm)
r_{p}	Radius of a precipitate	(cm)
$R_{g,v}$	Reaction rate between single helium and a vacancy	(1/sec)
$R_{v,s}$	Reaction rate between vacancies and the equivalent vacancy sink	(1/sec)
$R_{v,2g}$	Reaction rate between vacancies and a di-helium cluster	(1/sec)
$R_{v,gv}$	Reaction rate between vacancies and a substitutional helium	(1/sec)
$R_{v,2gv}$	Reaction rate between vacancies and a di-gas single vacancy cluster	(1/sec)
$R_{v,*}$	Reaction rate between vacancies and a critical bubble nucleus	(1/sec)
$R_{i,2gv}$	Reaction rate between interstitials and a di-gas single vacancy cluster	(1/sec)
$R_{i,*}$	Reaction rate between interstitials and a critical bubble nucleus	(1/sec)
$R_{i,s}$	Reaction rate between interstitials and the equivalent interstitial sink	(1/sec)
$R_{i,gv}$	Reaction rate between self interstitials and a substitutional helium cluster	(1/sec)
$R_{g,b}$	Reaction rate between interstitial helium and bubbles	(1/sec)
$R_{g,v}$	Reaction rate between interstitial gas atom and single vacancies	(1/sec)

$R_{g,g}$	Reaction rate between interstitial gas atoms	(1/sec)
$R_{g,gv}$	Reaction rate between interstitial gas atoms and substitutional helium clusters	(1/sec)
$R_{g,2gv}$	Reaction rate between interstitial gas and a di-gas single vacancy cluster	(1/sec)
$R_{g,gb}$	Reaction rate between interstitial gas and the equivalent grain boundary	(1/sec)
$R_{g,2g}$	Reaction rate between interstitial gas and di-pas atom clusters	(1/sec)
$R_{g,*}$	Reaction rate between interstitial pas and a critial bubble nucleus	(1/sec)
$R_{g,ppt}$	Reaction rate between interstitial gas atoms and precipitates	(1/sec)
t	Time	(sec)
T	Temperature	(°K)
Z_v	Line dislocation bias factor for vacancies	
Z_i	Line dislocation bias factor for self-interstitials	
ρ	Line dislocation density	(cm/cm^3)
Ω	Atomic volume	(cm^3)
γ_b	Bubble surface tension	(eV/cm^2)
α	Frequency factor for recombination	
β	Frequency factor for helium	
γ	Frequency factor for vacancies	
δ	Resolution frequency	(1/sec)
ϵ	Diffusion-control combinatorial factor for bubbles	

THE INFLUENCE OF SILICON ON VOID NUCLEATION IN IRRADIATED ALLOYS

B. Esmailzadeh, A. Kuinar (University of Missouri-Rolla)
F. A. Garner (Hanford Engineering Development Laboratory)

1.0 Objective

The object of this effort is to use breeder reactor data to provide models for the compositional dependence of radiatiori-induced chanqes in mechanical properties or dimensions. These models will then be used to guide the development of fusion-relevant studies.

2.0 Summary

The addition of silicon to pure nickel, Ni-Cr alloys and Fe-Ni-Cr alloys raises the diffusivity of each of the alloy components. The resultant increase in the effective vacancy diffusion coefficient causes large reductions in the nucleation rate of voids during irradiation. This extends the transient regime of swelling, which is controlled not only by the amount of silicon in solution but also hy the precipitation kinetics of precipitates rich in nickel and silicon.

3.0 Program

Title: Irradiation Effects Analysis (AKJ)
Principal: Investigator: D. G. Doran
Affiiiation: Hanford Engineering Development Lahoratory

4.0 Relevant DAFS Program Plan Task/Subtask

Subtdsk II.C.1 Effects of Material Parameters on Microstructure
Subtask II.C.14 Models of Flow and Fracture Under Irradiation

5.0 Accomplishments and Status

5.1 Introduction

It has recently heen shown that the primary influence of all environmental and material variables on the radiation-induced swelling of austenitic Fc-Cr-Ni alloys lies in the duration of the transient reqime of swelling[1-3]. In the post-transient regime the swellinq rate of austenitic alloys is ~1%/dpa and is relatively independent of those factors controllinn the transient regime. A model previously advanced by the authors relates the compositional dependence of the transient reqime to the effect of comoosition in altering the effective vacancy diffusion coefficient. This alters the void nucleation rate, particularly at higher irradiation temperatures.[4,5]

It is well known that some solutes, such as silicon, are much more rffective than other elements in rxtenaing the trdnsient regime of swelling.[2,6] The purpose of this paper is to demonstrate that silicon's effect on vacancy diffusion and void nucleation is quite strong and sufficient in itself to account for the observed suppression of swelling by silicon.

5.2 Silicon's Influence on Vacancy Diffusion

In an earlier paper Garner and Wolfer[7] demonstrated that the addition of small amounts of fast-diffusing elements to pure nickel decreased void nucleation strongly by increasinq the effective vacancy diffusion coefficient D_V^{eff}. They employed the KWR void nucleation model of Katz, Wiedersich and Russell[8,9] and used a dilute approximation model to describe the deoendence of D_V^{eff} on the tracer diffusion coefficient of the solute. Thus.

$$D_V^{eff} = (D_V + KC_S D_S)/(1 + KC_S), \qquad (1)$$

where D_V is the diffusion coefficient for migration of a free vacancy in the pure nickel and D_S is the diffusion coefficient for a solute-vacancy pair. C_S is the solute concentration, $K = 12 \exp(\varepsilon_b/kT)$ is the mass action constant for solute-vacancy dissolution in an fcc lattice, and ε_b is the solute-vacancy binding energy.

If $D_S >> D_V$ then the above formula predicts significant chanqes in D_V^{eff}. Silicon is known to have a solute diffusivity which is several orders of magnitude qreater than that of pure nickel or that of the major constituents of various austenitic steels.[10-13]

A confirmation of silicon's influence on the overall diffusivity of the solvent components of alloys has been provided by various researchers. Using radioisotope tracers Assassa and Guiraldenq[9] have shown that silicon additions to Fe-14Ni-16Cr increases the diffusivity of all three elements[14], as shown in Figure 1. Rothman, Nowicki and Murch have likewise shown a similar behavior for silicon additions to Fe-15Cr-20Ni.[15] Unfortunately neither of these qroups measured the diffusivity of silicon itself in these alloys, since there is no suitahle radioisotope for silicon. Johnston, however, has recently studied diffusion of silicon and chromium in Ni-Si and Ni-Cr-Si alloys using an electron probe microanalyzer to determine the concentration profiles that developed across the interfaces of eleven different diffusion couples[13]. He not only found silicon to be a fast-diffusing element but found that silicon had a strong effect on its own diffusion rate as well as on the diffusion rate of chromium. He inferred that the diffusion of nickel was also enhanced in the Ni-Cr-Si alloys. Johnston also found that silicon's diffusivity was slightly sensitive to the chromium concentration, but that the cross diffusion coefficient D_{SiCr} was about an order of magnitude less than D_{SiSi}.

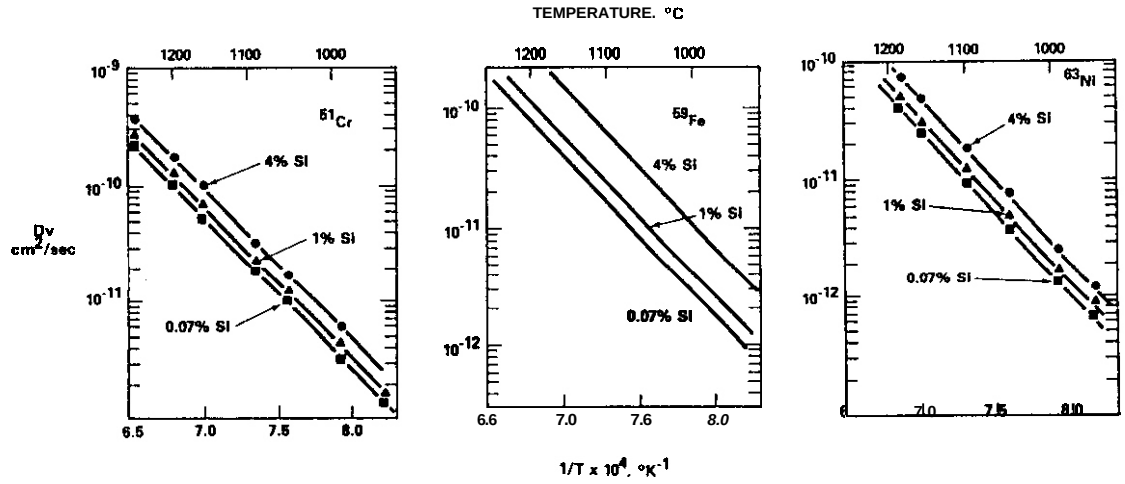

Figure 1. Influence of silicon on tracer diffusion coefficients in Fe-14Ni-16Cr[14]. A similiar effect of silicon was observed in Fe-20Ni-15Cr[15] and reveral Ni-Cr alloys[13].

To the first order, therefore, we shall assume that the diffusivity of silicon in Fe-Ni-Cr alloys is also independent of both the nickel and the iron and chromium concentrations. Rather than use a dilute approximation model for D_V^{eff}, however, we define the vacancy flux to be equal to the sum of the atomic fluxes,[16] since silicon is known to diffuse by a vacancy mechanism. Therefore,

$$D_V^{eff} = D_{vA}X_A + D_{vB}X_B + \ldots + D_{vn}X_n$$

where

$$D_{vA} = D_A^* / (C_v^{eq} \cdot f) \quad (2)$$

f 31

and

$$C_v^{eq} = \exp\left\{ (S_v^f/k) - (H_v^f/kT) \right\} \Omega^{-1} \quad (4)$$

D_{vA} is the diffusion coefficient of the component A in the matrix via a vacancy exchange mechanism. X_A is the atomic fraction of species A and f is 0.78146 for fcc lattices. D_A^* is the tracer diffusion coefficient for component A and C_v^{eq} is the free vacancy concentration. S_v^f and H_v^f are the entropy and enthalpy of vacancy formation, respectively.

5.3 Results of void nucleation calculations

Using the diffusion data published by the various researchers cited above it is possible to use equation 2 and the KWR void nucleation theory to predict the effect of silicon on void nucleation. As shown in more depth elsewhere, the major conclusions of this study are not affected by the choice of various adjustable parameters such as the dislocation bias[17]. The suppression of void nucleation is sensitive to (microstructural sink strengths, however, with the greatest effect occurring at sink strengths representative of highly irradiated alloys.

Whereas Garner and Wolfer predicted that the influence of silicon on the effective vacancy diffusion coefficient In Ni-Si alloys would saturate with increasing silicon, Figure 2 shows that it continues to increasr due to silicon's influence on its own diffusion. Figures 3-5 show the impact of silicon on calculated voia nucleation rates for pure nickel and for Fe-14Ni-16Cr and Fe-20Ni-15Cr alloys.

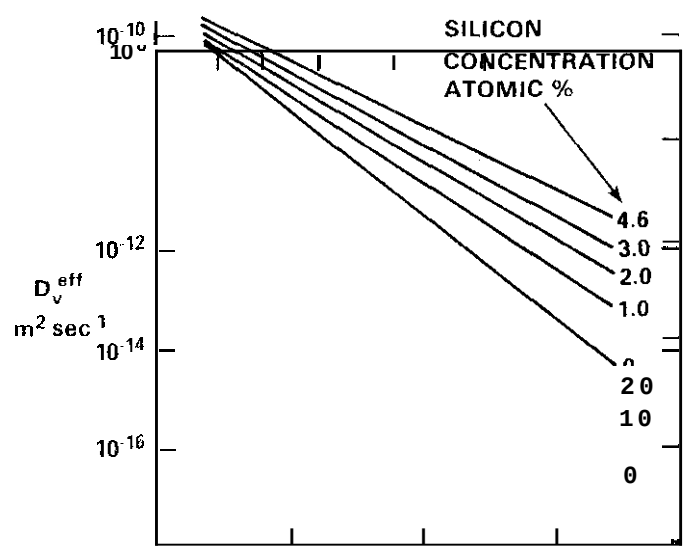

Figure 2. Calculated influence of silicon on D_V^{eff} in Ni-Si alloys.

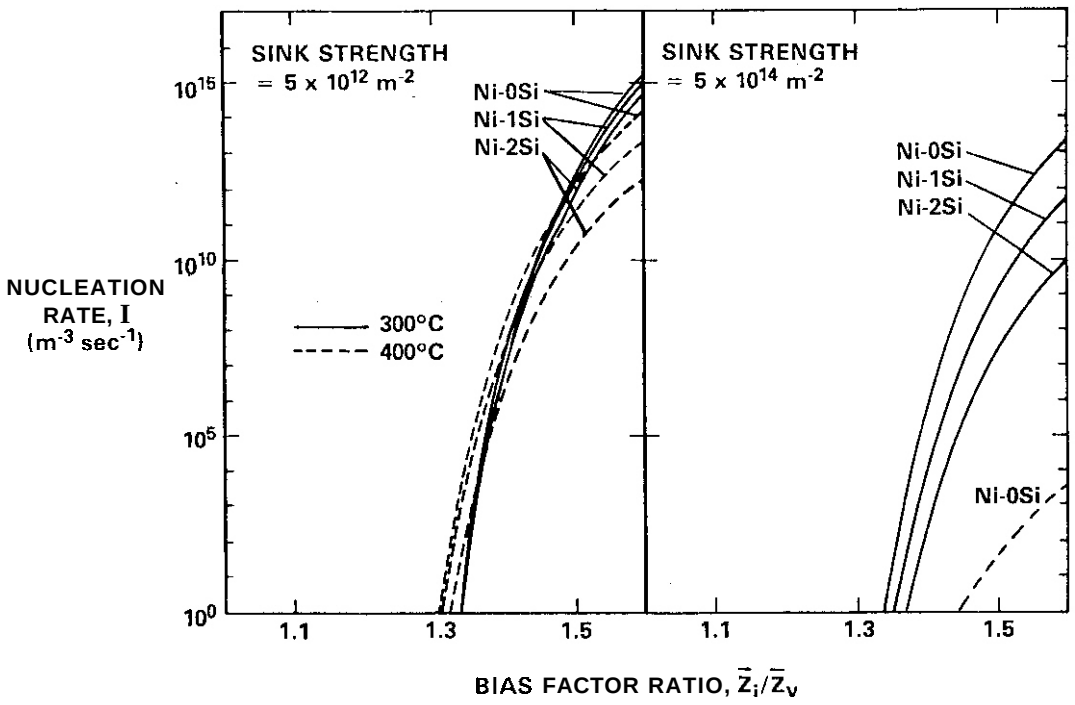

Figure 3. Calculated absolute void nucleation rates versus the average bias ratio for various silicon contents at both 300°C and 400°C and sink strengths of 5 x 10^{12} m^{-2} and 5 x 10^{14} m^{-2}. The displacement rate is 10^{-6} dpa/s.

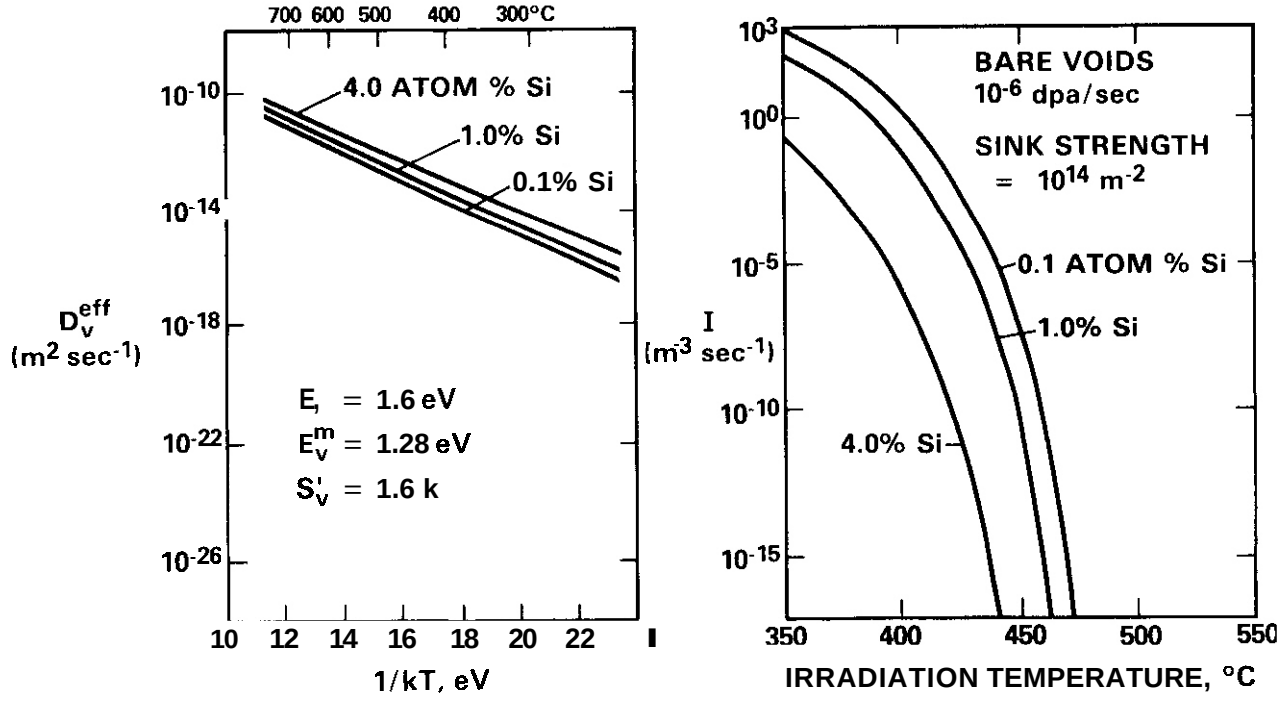

Figure 4. Calculated influence of silicon on vacancy diffusivity and void nucleation rate in Fe-14Ni-16Cr.

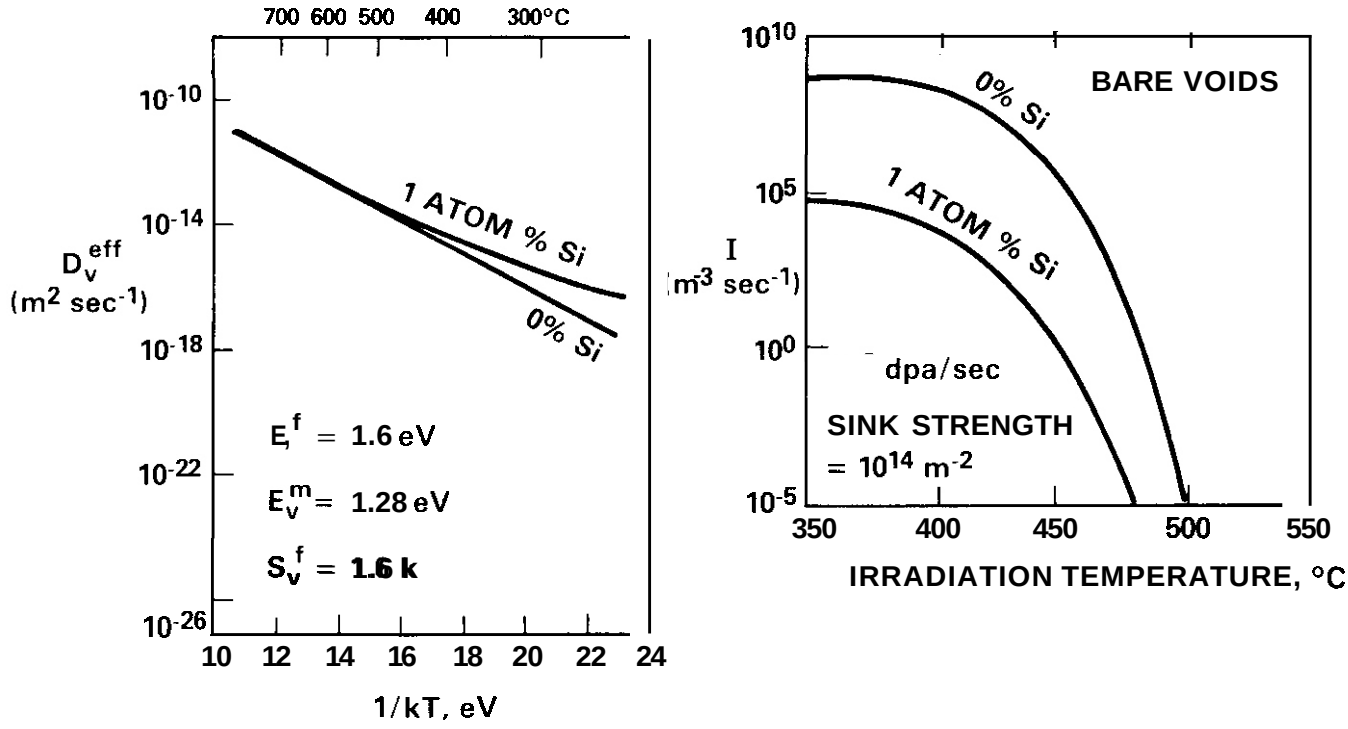

Figure 5. Calculated influence of silicon on vacancy diffusivity and void nucleation rate in Fe-20Ni-15Cr.

5.4 Discussion

This paper demonstrates a simple mechanism for the strong role of silicon in suppression of void nucleatiun in irradiated metals. Silicon's influence on D_v^{eff} is sufficient to account for the majority of the experimental observations of void suppression by silicon. As discussed in depth elsewhere,[7] there is no conflict concerning the action of this mechanism in opposition with other postulated mechanisms, i.e., solute migration by bound interstitial complexes. At concentration levels of 0.1 to 4.0 dtomic percent, the majority of silicon atoms at any one instant are not interacting with either vacancies or interstitials. Thus, both mechanisms could be operating independently. In addition, however, it must be recognized that large silicon levels quickly lead to heavy precipitation of nickel and silicon-rich precipitates[18]. This depletes the matrix of two elements known to affect void nucleation[2,4,19,20] and also substantially changes the sink density. All of these factors must be considered as manifestations of silicon's influence on void nucleation kinetics and the subsequent duration of the transient regime of swelling.

5.5 Acknowledgements

B. Esmailzadeh and A. Kumar were supported by the University of Missouri-Rolla and F. A. Garner by the U.S. Department of Energy.

6.0 References

1. F. A. Garner, J. Nucl. Mater., 122 & 123 (1984) 459-471

2. F. A. Garner and W. G. Wolfer, J. Nucl. Mater., 122 & 123 (1984) 201-206.

3. F. A. Garner and H. R. Brager, "Swelling of Fe-Ni-Cr Ternary Alloys During Fast Neutron Irradiation", ASTM STP 870, in press.

4. F. A. Garner, "A Model Describing the Compositional Dependence of Void Nucleation in Irradiated Fe-Ni-Cr Alloys", ibid.

5. B. Esmailzadeh and A. Kumar, "Influence of Composition on Steady-State Void Nucleation in Irradiated Alloys," ibid.

6. W. G. Johnston, et al., J. Nucl. Mater., 54 (1974) 24.

7. F. A. Garner and W. G. Wolfer, J. Nucl. Mater., 102 (1981) 143-150.

8. J. L. Katz and H. Wiedersich, J. of Chem. Phys., 55, No. 3 (1971) 1414-1425.

9. K. C. Russell, Acta Met., 19 (1971) 753-758.

10. H. W. Allison and H. Samelson, J. Appl. Phys., 30, No. 9, (1959) 1419-1424.

11. R. A. Swalin, A. Martin and R. Olsen, Trans. AIME (1957) 936.

12. M. A. Kristal and A. M. Mokrova, Uch. Zap. Tul. Gos. Pedagog. Inst., Fir-Tekhn. Nauki 1 (1967) 93-100.

13. G. R. Johnston, High Temperatures - High Pressures, 14 (1982) 695-707.

14. W. Assassa and P. Guiraldenq, Met. Sci., 12 (1978) 123-128.

15. S. J. Rothman, L. J. Nowicki and G. E. Murch, J. Phys. F, 10 (1980) 383-398.

16. J. Kucera and K. Stransky, Mat. Sci. Engr., 52 (1982) 1-38.

17. B. Esmailzadeh, "The Compositional and Temperature Dependence of Radiation-Induced Void Nucleation and Swelling in Austenitic Alloys," Masters Thesis, University of Missouri-Rolla, 1984.

18. H. R. Brager and F. A. Garner, in Proc. TMS-RIME Symposium on Irradiation Phase Stability, 5-9 Oct. 1980, Pittsburgh, PA., 219-235.

19. F. A. Garner, ibid., 165-189.

20. H. R. Brager and F. A. Garner, J. Nucl. Mater., 73 (1978) 9-19

DUAL ION IRRADIATION: IMPACT OF THE CONFLICTING ROLES OF HELIUM ON VOID NUCLEATION

A. Kumar (University of Missouri-Rollaiand F. A. Garner (Hanford Engineering Development Laboratory)

1.0 Objective

The object of this effort is to determine the limitations of the experimental tools used to simulate the fusion environment and also to provide guidance on the application of simulation data to design of fusion devices.

7.0 Summary

It has recently been demonstrated that ion simulations of neutron-induced swelling are strongly affected by the presence of the injected ion acting as an extra interstitial atom. The injected interstitial has been shown to exert a strong influence on both the void nucleation and steady-state regimes of swelling. In dual-ion irradiations where helium anti self-ions are injected simultaneously, the helium acts as a nucleation-assisting gas atom once it finds a vacancy cluster. While diffusing to the cluster, however, helium has a high probahility of trapping a vacancy and creating an unpaired interstitial. In this latter role, large **levels** of coinjected helium tend to strongly suppress void nucleation, not only at the lower irradiation temperatures cited by other researchers, but also at higher temperatures. The major consequence of the injected interstitial effect of large helium levels is to increase the duration of the transient reqime of swelling. A similar helium-generated interstitial effect also occurs in neutron irradiations, but the impact is negligible under most conditions due to the non-linearity of the injected interstitial effect and to the absence of the larger influence of injected ions.

3.0 Program

Title: Irradiation Effects Analysis (AKJ)
Principal Investigator: D. G. Doran
Affiliation: Hanford Engineering Development Laboratory

4.0 Relevant Program Plan Task/Subtask

Suhtask II.C.2 Effects of Helium on Microstructure

Suhtask II.C.16 Composite Correlation Models and Experiments

5.0 Accomplishments and Status

5.1 Introduction

Ion bombardment has often been used in both the fission and fusion reactor materials programs to simulate the consequences of neutron-induced atomic displacements. It has also been employed to study the action of an important fusion-relevant variable, that of large amounts of transmuted helium. The introduction of helium is accomplished either by preinjection or by simultaneous coinjection at a rate appropriate to that of the environment being simulated. The latter method is generally acknowledged as being the most realistic approach.

There are two features of the ion bombardment technique that require carefiil evaluation of the results. First, the confident use of this approach requires that one assess the impact on the ion-neutron correlation of the trade-offs and shortcomings inherent in such simulation studies.[1-3] The major shortcomings of the ion technique are the strong influence of the surface, the compressive and atypical stress-state in the bombarded region, and the influence of the bombarding ion acting as an injected interstitial. Second, there is the possibility that the neutron-relevant variable being studied in the simulation may interact with one of these shortcomings in a manner which strongly distorts the influence of that variable. This paper brings to light an example of the latter consideratian.

Helium in relatively large quantities is known, or in some cases, thought to cause suhstantial alteration of the microstructural evolution of metals during irradiation. In several recent reviews[4,5] helium is invoked to directly stabilize the cavity and change the critical radius far promotion of vacancy clusters into hias-driven growth, and to indirectly change the critical radius by altering the sink strengths of other components such as dislocations. Helium also appears to prolong the transient regime of dislocation loop evolution,[4] but not to change the eventual network density.[6-8] In addition to a refinement of cavity microstructure, it has also heen suggested that the radiation-induced segregation that precedes swelling in solute-hearing alloys may he altered hy the presence of higher loop and cavity densities.[4] Injected helium may also slow the loss of dislocations to the specimen surface, particularly in relatively soft metals without solute-hardening elements. The net result of all these roles for helium can he either an increase or decrease in swelling, depending on the alloy and the environmental conditions.

There is another role of helium which should he Considered. The production of neutron-induced helium from an (n,α) reaction represents the introduction of two new atoms and the loss of only one original atom. At its birth the helium atom is in effect an extra interstitial atom that is not mdtched with a corresponding vacancy. In typical fast reactor irradiations, the influence of helium in this role is negligible compared to its role as a gas atom acting to stabilize small cavities against dissolution by thermal emission of vacancies.

It has recently become clear, however, that in charged particle irradiations the injected interstitial represented by the bombarding ion has a strong effect on void nucleation and growth in austenitic alloys.[3,9-12] Garner has shown that the injected interstitial effect not only appears to prolong the transient regime of swelling, hut that it also depresses the magnitude and distorts the temperature dependence of the post-transient swelling rate.[3] It is now known that in the absence of injected interstitials the post-transient swelling rate of austenitic alloys is ~1%/dpa, relatively independent of compositional, fabricational and environmental variables.[13] Furthermore, Brager and Garner have shown that the post-transient swelling rate at temperatures above 500°C is not altered by large levels of helium.[14]

While Plumton and coworkers have demonstrated theoretically and experimentally the influence of injected interstitials on void nucleation,[10-12] Mansur and coworkers have shown that the post-transient swelling is also affected,[15-16] although to a lesser extent. Figure 1 shows the strong effect of injected interstitials on void nucleation predicted by Plumton and Wolfer.

It is important to note, however, that the coimplanted helium in dual ion irradiations also generates an extra interstitial whose influence is additive to that of the homharding ion. This occurs because helium atoms quickly interact with vacancies by trapping and immohilizing them, but the corresponding self-interstitial is not immobilized. While helium-as-stabilizer acts after finding the vacancy cluster, the helium-generated interstitial exerts its influence on void nucleation prior to the time helium reaches the cluster. Even if the immobilized vacancy interacts with another interstitial and recombines, releasing the helium atom, another trapping event will quickly occur, preserving the extra interstitial.

Due to the strong nonlinearity in the response of void nucleation to extra interstitials, the influence of helium-generated interstitials is amplified in ion irradiations beyond that which would occur in highly thermalized fission reactors which produce large levels of helium and which also are used to simulate fusion environments. Due to the delay involved in the first stage of the $^{58}Ni(n,\gamma)\ ^{59}Ni(n,\alpha)^{56}Fe$ reaction,[17] a substantial number of voids nucleate at lower levels of helium/dpa in thermal reactors, a consideration which further magnifies the difference hetween the response of metals to helium's influence in dual ion and fission soectrum irradiations.

In order to illustrate the impact of helium-generated interstitial, the nucleation theory will be briefly outlined, then the results of calculations will he presented. Experimental examples of helium-delayed transient swelling will then be discussed.

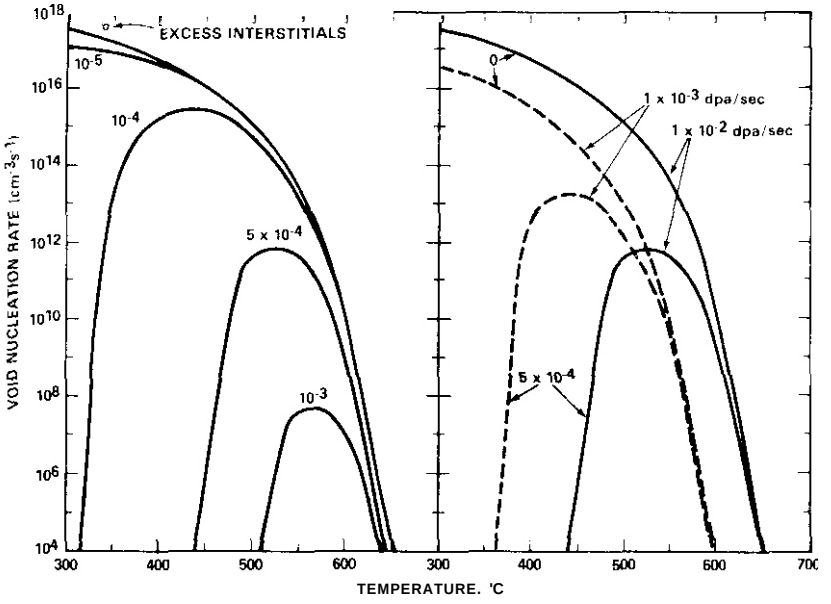

FIGURE 1. The effect of injected interstitials on void nucleation, as predicted by Plumton and Wolfer.[10] The curves shown in (a) correspond to 14 MeV nickel ion irradiation of pure nickel at a displacement rate of 10^{-2} dpa/s. 75% of the Frenkel pairs are assumed to recombine within the cascade and this factor is included in the *excess* interstitial fraction cited above. The fractional amount of defects which are injected interstitials is 10^{-5} near the surface, 5×10^{-4} near the peak and 10^{-3} near the end of range. The interaction of displacement rate variations and injected interstitials is shown in (b).

5.2 Nucleation Theory

The steady-state void nucleation theory employed here was developed by Katz, Wiedersich and Russell,[18,19] and extended by Wolfer.[20] The steady-state nucleation rate is

$$I_s = \{\sum_{x=1}^{N-1} \beta^{-1}(x) \exp[-\Delta G(x)/kT]\}^{-1} \quad (1)$$

where N is a cluster size which is large compared to the critical cluster size, and the critical size is defined at the maximum of $\Delta G(x)$, which represents the nonequilibrium counterpart of the Gibbs free energy for a cluster containing x vacancies.

$$\Delta G(x) = -kT \sum_{j=2}^{x} \ln \{[\alpha(j) + \gamma(j)]/\beta(j-1)\}, \quad (2)$$

where $\alpha(j)$, $\beta(j)$ and $\gamma(j)$ are the reaction rates for interstitial absorption, vacancy absorption and vacancy re-emission at the cluster surface. These reaction rates depend on the point defect fluxes.

$$\alpha(x) = 4\pi r(x)\, Z_i^0(x)\, D_i C_i \quad (3)$$

$$\beta(x) = 4\pi r(x)\, Z_v^0(x)\, D_v C_v \quad (4)$$

$$\gamma(x) = 4\pi r(x)\, Z_v^0(x)\, D_v C_v^0(x) \quad (5)$$

where $r(x)$ is the void radius, $Z_i^0(x)$ and $Z_v^0(x)$ are the void bias factors for interstitial and vacancy capture, D_i and D_v are the diffusion coefficients for interstitial and vacancy migration, C_i and C_v

are the average point defect concentrations in the alloy matrix and C_v^0 is the equilibrium vacancy concentration at the cluster surface. C_v^0 depends on the gas pressure in the cavity, the surface energy and radius of the cavity.

The concentrations C_i and C_v are given by the solution of the rate equations describing the partition of point defects between recombination events and the various microstructural sinks. The sum of the various loss terms must equal the production rates, P_i and P_v, which in this analysis are not considered to be equal due to the presence of the injected interstitials represented by the bombarding ions. P_i and P_v in this analysis are the original displacement rates prior to any form of in-cascade or post-cascade recombination event.

$$D_i C_i = D_v \bar{Z}_v F \tag{6}$$

and

$$D_v C_v = D_v(\bar{Z}_i F + \bar{C}_v) - (P_i - P_v)\,\bar{Z}_v S. \tag{7}$$

In these equations S is the total sink stength, $\bar{Z}_i$ and $\bar{Z}_v$ are the sink-averaged bias factors and $\bar{C}_v$ is the average vacancy concentration in thermodynamic equilibrium at all sinks. The factor F is described in detail elsewhere[10] and contains factors describing the balance of sinks and sources, including the injected interstitials as well.

Note in Equation 7 that the vacancy flux to the cluster is diminished by any imbalance between interstitial and vacancy production rates. Under most circumstances the number of extra interstitials is small, approaching at the most an excess interstitial fraction ε_i of $\sim 10^{-3}$, where

$$\varepsilon_i = \frac{P_i - P_v}{P_v} . \tag{8}$$

The influence of such small fractions is magnified in a very non-linear manner, however, by the approximately ten-fold reduction in displacements due to in-cascade recombination, and is further magnified by any process that significantly reduces the net flow of vacancies to the cluster. Recombination events at lower temperatures are very effective in this respect and so is the increased vacancy re-emission at higher temperatures.

In this paper we define ε_i to have two components, one due to the bombarding ion (assumed to be Ni^+) and the other generated by the presence of the coimplanted helium.

$$\varepsilon_i = \varepsilon_i^{Ni^+} + \varepsilon_i^{He} \tag{9}$$

5.3 Calculation of the Helium-Generated Interstitial Effect

There are three minor problems to be surmounted prior to initiating the calculation, which was performed using the same nucleation code employed by Plumton and coworkers.[10-12] First, there are a variety of adjustable parameters to be chosen. For all physical and diffusional properties of the matrix, the values chosen by Plumton and Wolfer[10] were employed to allow a direct comparison with their results. Likewise, point defect properties and bias factors were also chosen to be the same. However, their work investigated a range of in-cascade survivability fractions. We chose this fraction to be 0.08. This value is a factor of 1.3-2.0 below that usually chosen and is based on the work of English and coworkers who showed that the solutes in commercial alloys serve to defocus atomic collision sequences and enhance vacancy-interstitial recombination in cascades.[21] We also chose a displacement rate of 3×10^{-3} dpa/s to match a 3.0 MeV Ni^+ dual ion data set to be considered in the next section.

The injected interstitial fraction is very sensitive to the choice of damage calculational code employed, the energy of the ion and the depth within the specimen where the comparison is made.[22] For 3 MeV Ni+ ions it appears that the injected interstitial fraction ε_i^{Ni+} ranges between 1×10^{-4} and 5×10^{-4} in the region from which data are usually derived. The displacement damage created by the coinjected helium

is small and is ignored in the calculation. Coinjection rates of 5, 16 and 55 appm helium per dpa were chosen to match a particular dual-ion experiment[7] and to span the range covered by various fusion devices and the HFIR mixed-spectrum reactor. The total sink strengths employed in the calculation are also representative of those that existed in the dual-ion experiment of reference 7 during the transient regime of swelling.

The second obstacle to surmount is to decide how to illustrate the helium-as-interstitial effect separately from helium's gas-stabilization role. It has heen shown earlier that one can study the relative influence of one mechanism or variable on nucleation while ignoring the action of another mechanism, providing the results are expressed in relative nucleation rates where the relative effect of other variables cancels.[20,23] At low temperatures the influence of gas-stabilization on nucleation is not large, but at relatively high temperatures this mechanism is much more important. Wiedersich and Hall showed that, when cavities are treated as neutral sinks, the influence of gas stabilization at high temperatures is strongest at low helium levels and that little enhancement of nucleation was achieved for concentrations in excess of 10 appm.[24] When the hias of small cavities toward interstitials is taken into account, it is found that considerably more gas is required to stabilize cavities at relatively high irradiation temperatures but the tendency toward saturation of void density with increasing helium level is still preserved.[25] Therefore, it appears to be appropriate to study the helium-as-interstitial effect while ignoring the gas-stabilization role. There will, of course, be some cancellation by the two conflicting roles, the degree of which will be determined later.

Finally, there are a number of other parameters that determine the shape of an ion-induced profile of swelling vs. depth. Some of these are the strong influence of the specimen surface on point defect and dislocation densities, diffusional spreading of point defects, gradients in both the displacement rate and the injected interstitial profile, and the presence of swelling-induced compressive stresses. Many of these effects have been included in various rate theory or nucleation theory calculations hut are not necessary here to illustrate the strong and non-linear parametric dependence of the helium-generated interstitial effect. Therefore these other considerations have not been included in this study, even though they often act synergistically to change the influence of the interstitial effect.

Figure 2 shows the parametric influence on void nucleation of an injected interstitial fraction ε_i^{Ni+} = 5 x 10^{-4} and a helium injection rate of 55 appm/dpa. Three points should he noted. First, the effect is largest at low sink densities characteristic of the early stages of an annealed specimen under irradiation. (Conversely, cold-worked specimens would experience a lesser influence of injected interstitials.) Second, 55 appm helium per dpa represents a value of ε_i^{He} = 0.55 x 10^{-4}, which produces a strong additive but non-linear effect of the helium-generated interstitial. At low temperatures, the nucleation rate drops roughly four orders of magnitude due to 55 appm/dpa helium. At the peak nucleation rate temperature, the suppression effect varies from ~0.5 to ~1.5 orders of magnitude, increasing as the total sink strength decreases.

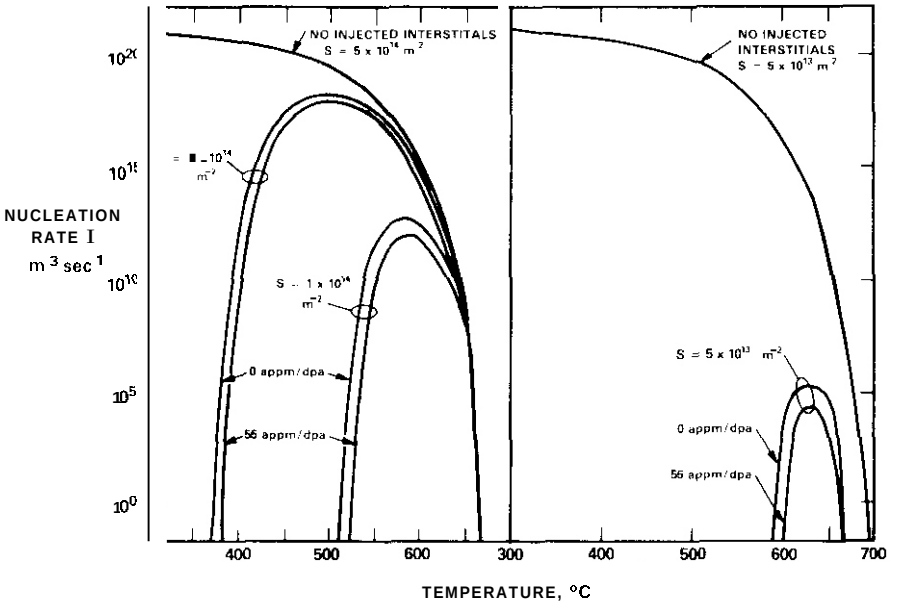

FIGURE 2. The influence on void nucleation of injected interstitials due to both bombarding ions (ε_i^{Ni+} = 5 x 10^{-4}) and helium atoms at 55 appm/dpa and 3 x 10 dpa/s. The suppression is sensitive to both sink strength and temperature.

Third, note that under some conditions the suppression effect of helium-generated interstitial increases again at higher temperatures. Earlier studies[10-12] focused only on the suppression at low temperature, reflecting attempts to model experimental results at relatively low temperature. The increase of suppression again at high temperatures reflects the large role of thermal vacancy emission in reducing the net flow of vacancies into the cluster, producing a condition where the influence of the extra interstitial again becomes relatively large.

Figure 3 emphasizes the strong dependence of the suppression by 55 appm/dpa on both irradiation temperature and sink strength. Figure 4 demonstrates the dependence of the suppression of nucleation on helium/dpa ratio, injected interstitial fraction and temperature.

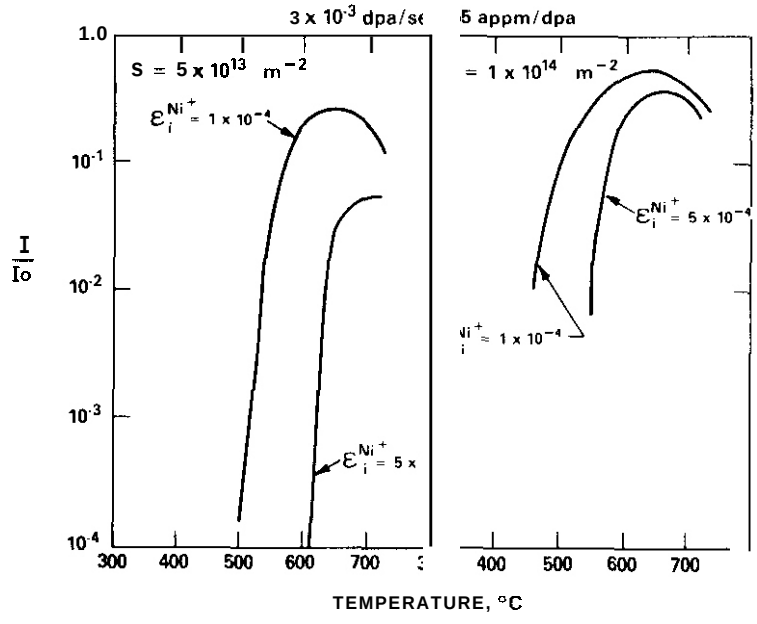

FIGURE 3. Relative Void Nucleation Rate I/I_0 for coinjection of 55 appm/dpa helium, where I_0 is the nucleation rate without helium, but one which is already suppressed by the injected interstitial represented by the bombarding Ni+ ion.

5.4 Discussion

The strong nonlinearity of the injected interstitial effect is most pronounced at relatively low irradiation temperatures but reasserts itself again at relatively high temperatures, particularly for low sink strengths which are characteristic of annealed specimens. These low sink strengths are also characteristic of low displacement rates, high temperature and low energy ions of shallow penetration.[8] This nonlinearity of response allows high helium/dpa rates to significantly reduce the steady-state nucleation rate and thereby prolong the transient regime of swelling. Note in Figure 1 that a value of $\varepsilon_i^{He} = 1 \times 10^{-5}$ (10 appm/dpa) would influence swelling rates only below ~400°C. Therefore, little effect of large levels of helium would be expected for helium-generated interstitials acting alone in a mixed spectrum reactor such as HFIR, although helium-as-stabilizer does enhance void densities in AISI 316 by one to two orders of magnitude.[14] However, since most of the helium was produced relatively late in the irradiation, both the transient duration and post-transient swelling rate at ~600°C were unaffected by helium acting in any role.[14]

Agarwal and coworkers showed that a helium/dpa ratio of 5.0 shortened the duration of the transient regime of swelling relative to that obtained by 15 appm preinjection (no coinjection) in annealed Fe-20Ni-15Cr (Figure 5). However, they also showed that helium/dpa ratios of 16 and 55 then increased the transient regime.[7] Note that the entire range of helium influence in both its conflicting roles is relatively small compared to a change in nickel level from 20 to 25%.[3] The results for Fe-25Ni-15Cr also show that a variation almost as large as that due to helium is achieved merely by decreasing the displacement rate by a factor of four.[3] This implies that helium's influence is a second order effect on void nucleation at 700°C compared to that of nickel, and is comparable to moderate changes in displacement rate.

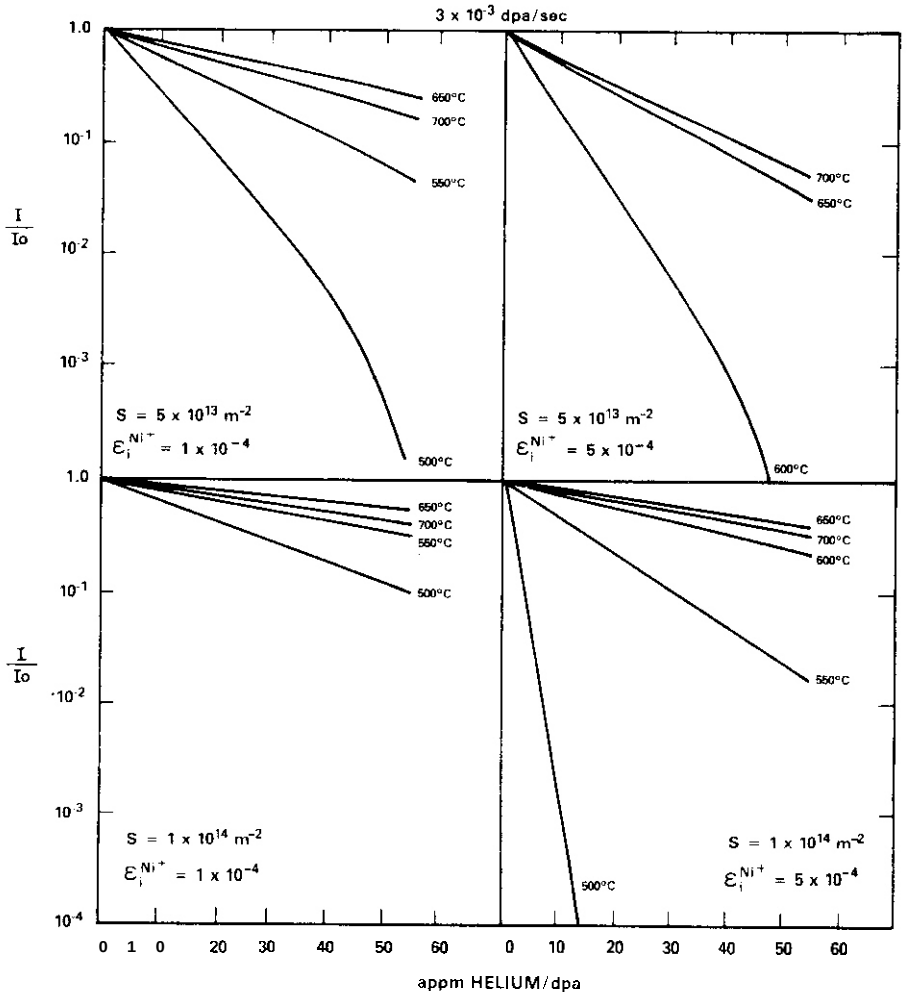

FIGURE 4. Influence on void nucleation of temperature, total sink strength, helium/dpa ratio and injected interstitials represented by bombarding Ni+ ions.

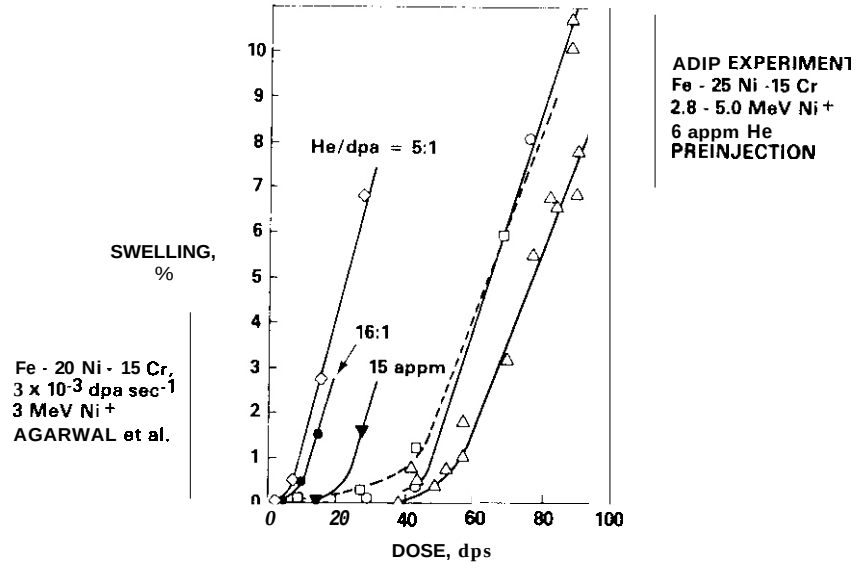

FIGURE 5. Relative influence of helium, nickel content and displacement rate on swelling of Fe-Ni-Cr alloys at 700°C.[3] All data were taken at comparable values of ε_i^{Ni+}. This ADIP cooperative experiment was conducted by three separate laboratories at 2 x 10^{-2} dpa/s, except for one (designated by triangles) which was conducted at 5 x 10^{-3} dpa/s.

It is important to note, however, that the transient regimes observed for the ion-irradiated Fe-25Ni-15Cr alloy were much longer than that of the neutron-irradiated alloy at all temperatures studied,[2,26] probably due to the combined influence of injected interstitials and surface effects. As shown in Figure 6, the temperature dependence of the transient regime for the Fe-25Ni-15Cr alloy also looks very much like that expected from the temperature dependence of the injected interstitial, although a strong surface influence is also suspected to be operating on the high temperature end of the swelling regime.

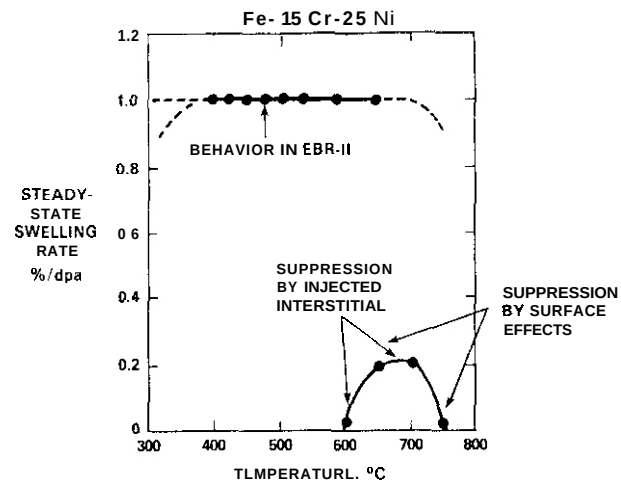

FIGURE 6. Comparison of the steady-state swelling rates of Fe-25Ni-15Cr observed in EBR-II and Ni+ ion irradiation experiments.[3] No coinjection of helium was involved in these experiments. Note the limited and much more temperature-dependent range of ion-induced swelling compared to that of neutron-induced swelling.

Anpther conclusion can be drawn from this work. In those instances where the injected interstitial ϵ_i^{Ni+} fraction is much larger ($\geq 1 \times 10^{-3}$) one would expect the helium suppression effect to become more pronounced, perhaps outweighing completely the gas stabilization role. For 0.5 MeV Ni^+ ions it is impossible to examine any irradiated portion of the foil that is not dominated by such large ϵ_i^{Ni+}.[11] Gilbon, Rivera and Levy reported recently on single ion and dual-ion studies of AISI 316 using 0.5 MeV Ni+ ions.[27] Their results show that annealed AISI 316 with no helium exhibits a relatively long transient regime (~50 dpa) but that 10 appm/dpa coinjection extended the transient regime by ~20 dpa. The post-transient swelling rates were comparable, however.

It is obvious that helium plays mare than one role in microstructural evolution, and that some effects of helium must cancel the influence of others. Helium-as-stabilizer probably saturates quickly while the helium-generated interstitial role clearly does not. However, the indirect effects of helium on dislocation, loop and precipitate evolution probably increase at a wide range of rates, depending on the balance of other environmental and material parameters. While we cannot with certainty point to a clear example of helium acting in the single dominant role of injected interstitial, neither are we justified in ignoring it or selecting another role as being dominant. The calculations show that the helium-generated interstitial role can be as large or larger than that of all other mechanisms advanced to date. The important consideration is the realization that ion irradiation experiments are already so perturbed by factors atypical of the neutron environment that the balance can easily be further shifted by another factor such as coinjected helium acting to generate extra interstitials. Thus we must accept the possibility that the often observed depression of ion-induced swelling by coinjected helium may in itself be an artifact of the simulation procedure rather than representing a neutron-relevant phenomenon.

When helium is preinjected, the helium-generated interstitial mechanism is not expected to operate. The helium will quickly find sinks such ds vacancies or dislocations, and vacancy equilibrium will be reestablished prior to the heginning of the ion bombardment. The total cavity and loop sink strength early in the irradiation will be changed by preinjection, however, and may affect nucleation as a consequence. Mansur and coworkers assert that for large levels of helium preinjection the cavity influence can become so large compared to that of dislocations that the post-transient swelling rate can also he strongly depressed.(4,5)

There is an interesting parallel between helium-generated interstitials operating on void nucleation and a quite similar role proposed for helium in the nucleation of Frank loops. Mansur and Coghlan suggested that one consequence of coinjected helium would be enhanced loop nucleation in the very early stages of irradiation.(5) Trapping of helium atoms by vacancies would free additiondl self-interstitials that would then augment loop nucleation. While Mansur and Coghlan did not specifically lahel this mechanism in terns of injected interstitials, it is directly analoqous in nature but opposite in consequence to the mechanism proposed in this paper for void nucleation.

5.5 Conclusions

Helium, when coinjected into ion-bombarded specimens, acts both in a gas-stabilization role and as a suppressor of void nucleation via its icfluence as a generator of an extra mobile interstitial. When compounded with the influence of the bombarding ion used to create the hulk of the damage, large amounts of coinjected helium tend to act more as an inhibitor of void nucleation. This inhibitor role exhibits a minimum with temperature and increases whenever recombination or vacancy re-emission strongly reduces the net flow of vacancies to void embryos. Since the rate of void nucleation determines the duration of the transient regime, it is expected that the temperature regime of dual ion-induced sweliing will be much smaller at a given damage level than that obtained in neutron irraditions. The helium-as-inhibitor effect is also expected to be smaller in cold-worked specimens.

6.0 References

1. Garner, F. A. and Laidler, J. J., in: Proc. Workshop of Neutron and Charged Particle Damage, CONF-760673, Oak Ridge National Laboratory, Oak Ridge, TN, June 8-10, 1976, pp. 177-240.

2. Garner, F. A., Powell, R. W., Diamond, S., Lauritren, T., Rowcliffe, A. F., Sprague, J. A. and Keefer, D., Radiation Effects in Breeder Reactor Structural Materials, eds., M. L. Bleiberg and J. W. Bennett, The Metallurgical Society of AIMC, 1977, pp. 543-569.

3. Garner, F. A., J. Nuci. Mater., Vol. 117, 1983, pp. 177-197.

4 Farrell, K., Mariasz, P. J., Lee, E. H. and Mansur L. K., Radiation Effects, Vol. 78, 1983, pp. 277-295.

5. Mansur, L. K. and Coghlan, W. A., J. Nucl. Mater., Vol. 119, 1983, pp. 1-25.

6. Farrell, K. and Packan, N. H., J. Nucl. Mater., Vol. 85 & 86, 1979, pp. 683-687.

7. Agarwal, S. C., Ayrault, G., Potter, D. I., Taylor, A. and Nolfi, F. V. Jr., ibid, pp. 653-657.

8. Garner, F. A. and Wolfer, W. G., "A Model for the Evolution of Network Dislocation Density in Irradiated Metals," Effects of Radiation on Materials: Eleventh Conference, ASTM STP 782, H. R. Brager and J. S. Perrin, Eds., American Society for Testing and Materials, 1982, pp. 1073-1087.

9. Lee, E. H., Mansur, L. K. and Yoo, M. H., J. Nucl. Mater., Vol. 85 & 86, 1979, pp. 577-581.

10. Plumton, D. L. and Wolfer, W. G., Damage Analysis and Fundamental Studies Quarterly Progress Report DOE/ER-0046/12, August 1983, pp. 216-231. A similar set of curves for different diffusion conditions appears in J. Nucl. Mater., Vol. 120, 1984, pp. 245-253.

11. Plumton, D. L., Attaya, W., and Wolfer, W. G., J. Nucl. Mater., Vol. 122 & 123, 1984, pp. 650-653

12. Badger, B. Jr., Plumton, D. L., Zinkle, S. J., Sindelar, R. L., Kulcinski, G. L., Uodd, R. A. and Wolfer, W. G., "Experimental Investigation of the Effect of Injected Interstitials on Void Formation," ASTM STP 870, (in press).

13. Garner, F. A., J. Nucl. Mater., Vol. 122 & 123, 1984, pp. 459-471.

14. Brager, H. R. and Garner, F. A., J. Nucl. Mater., Vol. 117, 1983, pp. 159-176.

15. Brailsford, A. D. and Mansur, L. K., J. Nucl. Mater., Vol. 71, 1977, pp. 110-116.

16. Mansur, L. K. and Yoo, M. H., J. Nucl. Mater., Vol. 85 & 86, 1919, pp. 523-532.

17. Wiffen, F. W., Allen, E. J., Farrar, H., Bloom, E. E., Gabrial, T. A., Kerr, H. T., and Perey, F. G., "Production Rate of Helium During Irradiation of Nickel In Thermal Spectrum Fission Reactors," accepted for publication *in* J. Nucl. Mater.

18. Katz, J. L., and Wiedersich, H. J., Chem. Phys., Vol. 55, 1971, pp. 1414-1425.

19. Russell, K. C., Acta. Met., Vol. 19, 1971, pp. 753-758.

20. Wolfer, W. G., Mansur, L. K., and Sprague, J. A., in ref. 2, pp. 841-864.

21. English, C. A., Eyre, B. L., Shoaih, K., and Williams, T. M., J. Nucl. Mater. Vol. 58, 1915, pp. 220-226.

22. Plumton, D. L., Attaya, H. and Wolfer W. G., in Damage Analysis and Fundamental Studies Quarterly Progress Report, DOE/ER-0046/14, August 1983, pp. 111-119.

23. Garner, F. A. and Wolfer, W. G., J. Nucl. Mater., Val. 102, 1981, pp. 143-150.

24. Wiedersich, H. and Hall, B. O., J. Nucl. Mater., Vol. 66, 1971, pp. 187-192.

25. Wolfer, W. G., J. Nucl. Mater., Vol. 122 & 123, 1984, pp. 367-318.

26. Garner, F. A. and seventeen co-authors, in Proc. Workshop on Correlation of Neutron and Charged Particle Damage, CONF-760673, Oak Ridge National Laboratory, Oak Ridge, TN, June 8-10, 1976, pp. 147-175.

27. Gilbon, D., Rivera, C., and Levy, V., "Influence of Helium on Swelling of Steels," ASTM STP 870, (in press).

7.0 Future Work

This effort is complete.

8.0 Publications

This paper will be published in the Proceedings of the 12th International ASTM Conference on Effects of Radiation in Materials, ASTM STP 870, June 1984, Williamsburg, VA, F. A. Garner and J. S. Perrin, Eds.

CHAPTER 6

FUNDAMENTAL STUDIES OF SPECIAL PURPOSE MATERIALS

SWELLING OF COMMERCIAL COPPER ALLOYS AND NiBe IRRADIATED IN FFTF

H. R. Brager and F. A. Garner (Hanford Engineering Development Laboratory)

1.0 Objective

The object of this effort is to provide data on the swelling of high conductivity alloys in response to high fluence fast reactor irradiation and thereby predict their behavior in anticipated fusion environments.

2.0 Summary

The swelling of tensile specimens irradiated in the MOTA-1B experiment at ~450°C has been measured using immersion density. The majority of these specimens were fabricated from various commercial copper alloys and exhibited volume changes ranging from -0.66% to 16.6% swelling. The latter was obtained in a copper-0.1% silver specimen that reached 16 dpa, implying a swelling rate of at least 1%/dpa.

3.0 *Program*

Title: Irradiation Effects Analysis (AKJ)
Principal Investigator: D. G. Doran
Affiliation: Hanford Engineering Development Laboratory

4.0 Relevant DAFS Program Plan Task/Subtask

Subtask II.C.1, Effects of Material Parameters on Microstructure.

5.0 Status and Accomplishments

5.1 Introduction

In an earlier report[1] it was noted that nine copper-base alloys in thirteen material conditions had been inserted into the MOTA-10 experiment for irradiation in FFTF at ~450°C. Ni-1.9Be and AISI 316 were also included. The experiment involved both TEM disks and miniature tensile specimens. The tensile specimens do not include all of the alloy treatment conditions that are included in the TEM disks. The first discharge of MOTA-1B has occurred with the average fluence in the 450°C capsule at ~2.5 x 10^{22} n/cm^2 (E > 0.1 MeV). For stainless steel this exposure corresponds to ~12 dpa, but for copper, which has a lower displacement threshold energy, it corresponds to ~16 dpa. The tensile specimens have been measured for changes in density, using standard immersion density techniques.

5.2 Results

The measured changes in swelling of the miniature tensile specimens are given below:

TABLE 1

SWELLING OF VARIOUS COMMERCIAL COPPER ALLOYS, Ni-1.9Be AND AISI 316 IN MOTA-1B AT ~450°C AND 2.5 x 10^{22} n/cm^2 (E > 0.1 MeV)

Alloy	Condition	% Swelling
Cu (99.999%)	Annealed	6.5
Cu-0.1 Ag	20% CW	16.6%
Cu-0.3 Ag-0.06 P-.08 Mg	20% CW	7.9
Cu-1.8 Ni-0.3 Be (A)	20% CW & Aged (1/2 HT)	1.70
Cu-1.8 Ni-0.3 Be (B)	Annealed & Aged (AT)	0.29
Cu-2.0 Be (A)	20% CW & Aged (1/2 HT)	-0.18
Cu-2.0 Be (B)	Annealed & Aged	-0.66
Cu-0.9 Cr-0.1 Zr-0.05 Mg	Aged & 90% CW	1.03
Cu-0.25 Al_2O_3	20% CW	0.13
Ni-1.9 Be	Annealed & Aged	-0.37
AISI 316 (lot CN-13)*	Annealed	-0.70

*Included as a standard reference material

5.3 Discussion

The 16.6% swelling observed in the 20% cold-worked Cu-0.1 Ag alloy represents a swelling rate of at least 1%/dpa which is comparable to that ohserved in pure nickel and Fe-Ni-Cr simple ternary alloys.[2] Zone-refined copper in the annealed condition swelled only 6.5%, however, which is initially surprising since most solutes added to pure metals result in a reduction of swelling. The addition of silver to copper is known to he an exception, however. As shown in figure 1, Makin found that the addition of 1% silver greatly suppresses the tendency of copper to saturate in swelling during electron irradiation at 250°C.[3] Barlow also studied copper with 0.1 and 1.0 wt.% silver using electron irradiation.[4] He found that the 0.1% alloy behaved like pure copper at all temperatures, hut the 1% Ag alloy swelled at a hiaher rate than pure copper at 150-250°C. In the range 350-450°C the swelling rate of the electron irradiated pure copper and copper +1% silver were the same.

Since the influence of the solute silver was shown in HVEM studies to be dependent on its concentration, it is not surprising that the Cu-0.3 Ag-0.06 P-0.08 Mg alloy swelled in MOTA to a level intermediate to that of pure copper and Cu-0.1% Ag. The phosphorus and mdgnesium probably also played a role. No data are available for phosphorus, hut the addition of 0.7% magnesium at 600°C led to a slight reduction in the swelling of copper irradiated with 150 KeV Cu^+ ions.[5]

The data in Table 1 show that beryllium is an effective suppressor of swelling in copper, particularly at the 2% level. Makin also showed in his electron irradiation studies that the addition of 1% beryllium at 250°C resulted in a total suppression of swelling to 100 dpa.[3] One clue to beryllium's effectiveness in suppressing swelling lies in the large densification observed in the Cu-2% Be alloy. Such changes in density are usually associated with segregation and/or formation of ordered phases, particularly when substantial solute-solvent misfit is involved. Indeed, beryllium has a large negative misfit of -26% and forms CuBe precipitates during ion irradiation of Cu-1.35 at % Be in the range of 300-700°K.[6,7] Beryllium additions were also shown to strongly enhance diffusion in copper during irradiation.[7]

Nickel has a smaller misfit (-8%) and diffuses slower than does copper in Cu-Ni alloys.[7] Void formation was found to he inhibited by nickel additions during 46.5 MeV Ni^+ irradiation at 400°C.[8] In electron irradiations of various copper-nickel alloys, Barlow[4] and Leffers and coworkers[9] showed that nickel additions could hoth increase or decrease swelling, depending on the irradiation temperature and nickel level. In the MOTA experiment, the combined effect of 1.8% nickel and small (0.3%) heryllium additions led tn a reduction hut not total suppression of swelling.

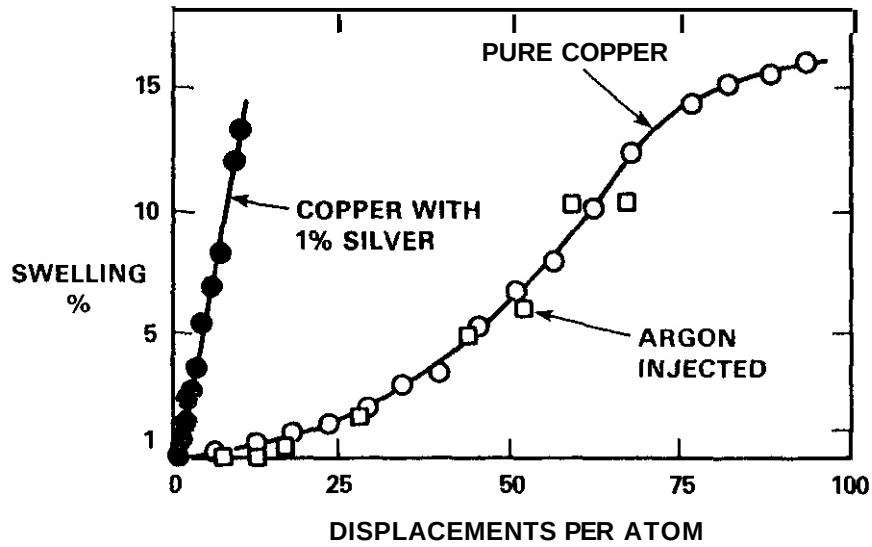

FIGURE 1. Swelling of Pure Copper and Copper +1% Silver During Irradiation With 1.0 MeV Elections at 250°C.(3)

The most interesting swelling response in the MOTA experiment was that of Cu-0.25 Al_2O_3. Alumina additions should be inert at this temperature and yet the swelling was reduced from the 6.5% level of pure copper to only 0.13%.

Since the tensile specimens do not include the entire range of alloy conditions covered by the TEM disks, we cannot at this time make definitive statements about the effect of cold-work on swelling. Such conclusions must await the measurement of density changes in the TEM disks.

Table I also shows that a substantial densification occurred in the strong and moderately conductive Ni-1.9 Be alloy irradiated in MOTA at 450°C. The suppression of swelling in ion-irradiated nickel with beryllium additions has been demonstrated by several authors.(10,11) Ordered precipitates of NiBe were also found to develop during irradiation.(11) The swelling of pure nickel during fast neutron irradiation is covered in another report.(12)

5.4 Conclusions

Copper alloys have the potential for swelling at a rate of about 1%/dpa during neutron irradiation at 450°C. Zone-refined copper tends to swell to lower levels, however, and may he saturating at levels of swelling which are at least as large as 8%. Additions of various alloying elements can delay or suppress swelling, hut the addition of silver tends to increase swelling, apparently by precluding the possibility of saturation. The data developed in this report show that the response of various copper alloys to either charged particle or neutron irradiation is quite similar.

6.0 References

1. H. R. Brager and F. A. Garner, "Irradiation of Copper Alloys in FFTF," DAFS quarterly Progress Report DOE/ER-0046/17, May 1984, p. 133.

2. F. A. Garner, J. Nucl. Mater., 122 & 123, 1984, p. 459.

3. M. J. Makin in Voids Formed hy Irradiation of Reactor Materials, S. F. Pugh, Ed., British Nuclear Energy Soc., 1971, p. 269.

4. P. Barlow, Radiation Damage in Pure FCC Metals and Alloys in HVEM, Ph.D. Thesis, 1977, University of Sussex, England.

5. H. Venker, P. Giesecke, and K. Ehrlich, in AIME Symp. on Radiation Effects in Breeder Reactor Structural Materials, Scottsdale AZ, 1977, p. 415.

6. R. Koch, R. P. Wahi, and H. Wollenberger, J. Nucl. Mater., 103 & 104, 1981, p. 1211.

7. M. P. Macht, V. Naundorf, R. P. Wahi, and H. Wollenherger, J. Nucl. Mater., 122 & 123, 1984, p. 698.

8. 0. J. Mazey and F. Menzinger, J. Nucl. Mater., 48, 1973, p. 15.

9. T. leffers, B. N. Singh, and P. Barlow, RISO-M-1937, RISO Research Establishment, Roskilde, Denmark, May 1977.

10. T. D. Ryan, Ph.D. Thesis, University of Michigan, 1975.

11. P. R. Okamoto, A. Taylor, and H. Wiedrrsich, in Fundamental Aspects of Radiation Damage in Metals, CONF-751006-P2, 1975, p. 1188.

12. F. A. Garner, "Swelling nf Neutron-Irradiated 85Ni-15Cr at 400-650°C," this report.

7.0 Future Work

Density change data will continue to he generated on the ?EM disks. Tensile, resistivity measurements and electron microscopy examination will also he performed.

8.0 Publications

None

TENSILE PROPERTY CHANGES OF COMMEKCIAL COPPER ALLOYS NEUTRON IRKADIATEU AT 450°C

H. L. Heinisch and H. R. Brager (Hanford Engineering Development Laboratory)

1.0 Objective

The object of this effort is to provide data on the changes in mechanical properties of high conductivity alloys in response to high fluence fast reactor irradiation and thereby predict their behavior in anticipated fusion environments.

2.0 Summary

Tensile tests were performed on miniature Specimens of high-purity copper and eight copper alloys that were irradiated to ∿16 dpa at ∿450°C in the MOTA experiment in FFTF. Tensile properties of these alloys were also examined after aging at 400°C for 1000 hours. The results of these tests are presented here. Changes in tensile properties of most, but not all, of the irradiated alloys seem to be primarilv dependent on thermal effects rather than the effect of atomic displacements.

3.0 Program

Title: Irradiation Effects Analysis (AKJ)
Principal Investigator: D. G. Doran
Affiliation: Hanford Engineering Development Laboratory

4.0 Relevant DAFS Program Plan Task/Subtask

Subtask II.C.l, Effects of Material Parameters on Microstructure.

5.0 Accomplishments and Status

5.1 Introduction

A series of representative commercial copper alloys is now being irradiated in the Materials Open Test Assembly (MOTA) in the Fast Flux Test Facility (FFTF). The first of four discharges of this experiment has occurred for specimens irradiated to 2.5 x 10^{22} n/cm^2 (E > 0.1 MeV). This corresponds to ∿16 dpa in pure copper. Only data for one temperature, ∿450°C, is currently available.

The alloys were irradiated in the form of miniature tensile specimens and standard microscopy disks, both of which were punched from the same sheet. While the disks will be used only for microscopy, the tensile specimens provide data on changes in density, electrical conductivity and tensile properties, all measured at room temperature. The copper specimens span four classes: pure metal, and solution-strengthened, precipitation-hardened and dispersion-strengthened alloys. The electrical conductivity and density changes are described in companion reports in this volume. The report on conductivity included a full description of the alloy compositions and starting conditions. Identical tensile specimens were also subjected to thermal aging at 400, 500, 600 and 700°C for 1000 hours and others are being aged to 10,000 and 30,000 hours. Those specimens aged at 400°C for 1000 hours have been examined in order to partially separate the effects of temperature and irradiation.

5.2 Measurements and Results

Miniature tensile specimens nominally 1.27 cm long by 0.25 cm wide (0.5 x 0.1 inch) were punched from sheets of about 0.025 cm (10 mils) thickness. The widths and thicknesses of the gauge sections of all non-irradiated specimens were measured prior to testing. The thicknesses of the irradiated specimens were measured, but their widths were assumed to he the average of the unirradiated specimens of the same type (which had only about 2% variation).

All specimens were tested in the mini-tensile frame especially designed for that purpose.[1] The results are shown in Table 1. The yield stress, ultimate tensile strength, uniform elongation and total elongation (elastic plus plastic) were determined from plots of load versus deflection. The values in Table 1 are for one specimen only for each condition. Control specimens of 304 stainless steel were tested intermittently, giving yield and ultimate strength values within an established two-sigma control band of ±6%.

The irradiated specimens were measured and tested behind lead body shielding, using long tweezers. The hottest specimens, those containing Ni and Be, measured up to 300 mR/hr at contact, while the others were factors of 10 to 20 below that. Specimens from the higher fluence FFTF irradiations now in progress will be tested in a hot cell, a situdtion for which the mini-tensile frame was specifically designed.

All the alloys showed a reduction in strength after irradiation or aging. However, for most of the alloys, the differences between the strengths of aged and irradiated specimens were small. For these alloys the changes during irradiation were apparently due primarily to thermal effects rather than displacement damage.

6.0 References

1. N. F. Panayotou, R. J. Puigh and E. K. Opperman, "Miniature Specimen Tensile Data for High Energy Neutron Source Experiments," J. Nucl. Mat., 103 & 104, 1523 (1981).

7.0 Future Work

Relationships between the changes in density, electrical conductivity and tensile properties of these alloys due to irradiation and thermal effects are being investigated.

TABLE 1

TENSILE PROPERTIES OF VARIOUS COPPER ALLOYS

	Yield Strength (MPa)			Ultimate Tensile Strength (MPa)			Uniform Elongation (%)			Total Elongation (%)		
	Unirrad.	Aged*	Irrad.**	Unirrad.	Aged*	Irrad.**	Unirrad.	Aged*	Irrad.**	Unirrad.	Aged*	Irrad.**
Copper (99.999%) Zone-Refined	58	58	43	208	178	154	28	20	10	38	29	16
Solution-Strengthened CuAg	254	78	57	330	210	157	22	34	11	5.6	39	12
CuAgP	408	115	109	473	268	197	21	24	9 8	5.7	34	10
Dispersion-Strengthened CuAl25	483	476	396	534	501	429	1.8	5 5	5.9	5.3	11	13
Precipitate-Strengthened MZC (HT)	450	401	267	517	498	364	2.5	6.2	8.7	5.6	10	11
CuBeNi (1_Z HT)	563	308	211	678	459	400	3 2	8 9	12	7.5	11	12
CuBeNi (AT)	561	566	451	670	610	495	3 4	1 3	0 9	3.9	1.5	1.1
CuBe (1/2 HT)	647	403	351	697	550	548	2 7	15	11	7.5	19	12

*Aged 1000 hours @ 400°C.
**Irradiated at ~450°C to ~16 dpa 2 5 x n cm^2 (E > 0 1 MeV) in the MOTA of the FFTF

CONDUCTIVITY CHANGES IN NEUTRON-IRRADIATED COMMERCIAL COPPER ALLOYS AT ~450°C

H. R. Brager and F. A. Garner (Hanford Engineering Development Laboratory)

1.0 Objective

The object of this effort is to determine the response of high-conductivity high-strength copper alloys to high fluence neutron irradiation.

2.0 Sumnary

The electrical conductivity changes induced in nine copper-base alloys during irradiation at 450°C in FFTF have been measured. Alloys which contain beryllium as one of their constituents exhibit an increase in electrical conductivity, while those that do not contain beryllium exhibit a decrease in conductivity. The change in conductivity appears to correlate with the original conductivity of the alloy.

3.0 Program

Title: Irradiation Effects Analysis (AKJ)
Principal Investigator: D. G. Doran
Affiliation: Hanford Engineering Development Laboratory

4.0 Relevant DAFS Program Plan Task/Subtask

II.C.l Effects of Material Parameters on Microstructure.

5.0 Accomplishments and Status

5.1 Introduction

In an earlier report[1] it was noted that a series of commercial copper alloys were inserted into the MOTA irradiation experiment in FFTF at the lowest temperature available, ~450°C. The first discharge at 2.5 x 10^{22} n cm^{-2} (E > 0.1 MeV) corresponds to a displacement dose of ~16 dpa for copper. Measurements of room temperature conductivity have been made on miniature tensile specimens both prior to and after irradiation using a four-point resistivity measuring device.

5.2 Results and Discussion

Table 1 shows the resistivity measurements obtained prior to and after the irradiation. Figure 1 demonstrates that the conductivity changes can be positive or negative but that the percentage change in conductivity appears to be related to the original conductivity of the unirradiated alloy.

Another point to notice is that the positive changes in conductivity are all associated with highly precipitation-hardened alloys containing beryllium. Cu-2.0 Be alloys had changes of 58-61% while the Cu-1.8 Ni-0.3 Be had changes of 14-17%. This implies that the radiation-induced change is not linear with beryllium content, at least in the presence of nickel. It is anticipated that the tensile properties of these specimens will show some reduction of alloy strength due to a redistribution in size and concentration of second phase particles.

5.0 References

(1) H. R. Brager and F. A. Garner, "irradiation of Copper Alloys in FFTF," DAFS Quarterly Progress Report DOE/ER-0046/17, May 1984, 133.

7.0 Future Work

Tensile tests on these specimens will continue. Examination of irradiated TEM disks by electron microscopy will also proceed. Additional data will also be available at several higher fluence levels.

8.0 Publications

None

TABLE 1

CONDUCTIVITY MEASUREMENTS ON COPPER ALLOYS

Material	Composition	Condition*	Electrical Conductivity (% IACS @ 20°C) Preirradiation	Post-Irradiation
Cu	Cu (99.99%)	CW	101	86
Cu Ag	Cu - 0.1 Ag	CW	97	77
Cu Ag P	Cu - 0.03 Ag - 0.06 P - 0.08 Mg	CWA	96	RO
A1-25	Cu - 0.25 Al_2O_3	CW	84	73
MZC	Cu - 0.9 Cr - 0.1 Zr - 0.05 Mg	CWA	83	77
Cu Be Ni	Cu - 1.8 Ni - 0.3 Be	CWA (1/2 HT)	74	84
Cu Be Ni	Cu - 1.8 Ni - 0.3 Be	SAA (AT)	61	71
Cu Be	Cu - 2.0 Be	CWA (1/2 HT)	18	29
Cu Be	Cu - 2.0 Be	SAA (AT)	20	37

*CW = cold worked, CWA = cold worked and aged, SAA = solution annealed and aqed, 1/2 HT and AT are industry designations for "half-hard and tempered" and "annealed and tempered," respectively.

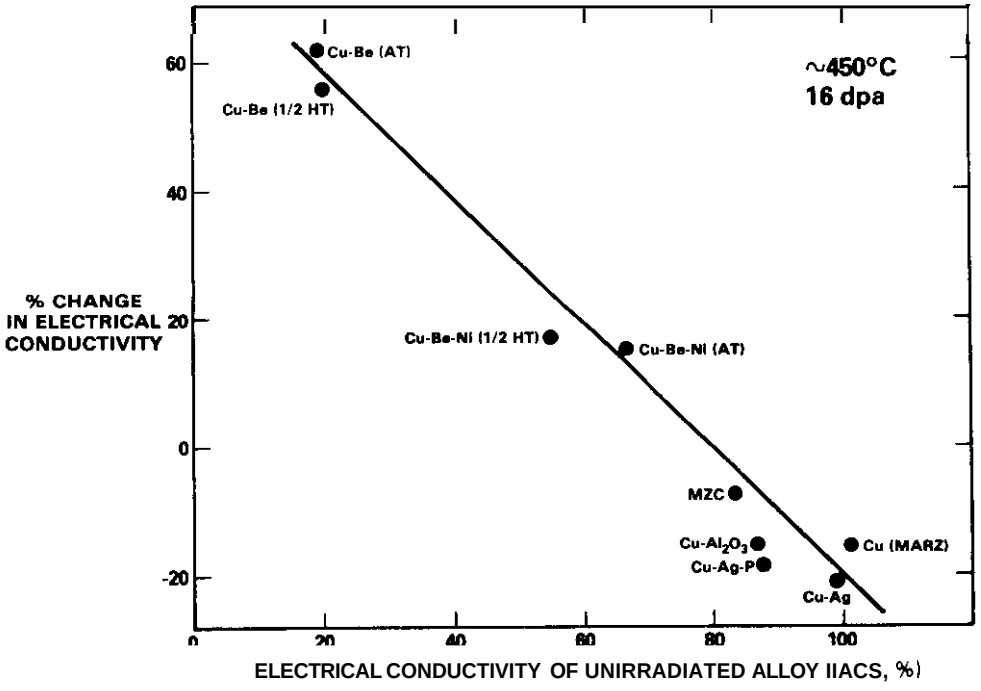

Figure 1. Conductivity Changes Observed in Copper **Alloys** After Irradiation to 16 dpa in FFTF at ~450°C.

SWELLING OF BERYLLIUM

W.G. Wolfer (University of Wisconsin-Madison) and T.J. McCarville (TRW, Energy Development Group)

1.0 Objective

Beryllium is considered as a possible material for limiters in JET as well as future fusion reactors. Accordingly, it is of interest to assess the radiation-induced swelling and the predominant mechanism for it.

2.0 *Summary*

A comparison of the displacement rate and the helium production rate produced in beryllium by 14 MeV neutrons shows that the helium production rate is the predominant mechanism for swelling. A simple model is developed which reproduces the data for swelling produced in fission reactors.

3.0 Program

Title: Effects of Radiation and High Heat Flux on the Performance of First-Wall Components
Principal Investigator: W.G. Wolfer

4.0 Relevant DAFS Program Plan Task/Subtask

Task II.C.17 Microstructural Characterization
Subtdsk II.B.2.3 Correlation Methodology

5.0 Accomplishments and Status

5.1 Introduction

Beryllium and graphite are two leading candidates for limiter materials in immediate contact with the plasma in tokamak devices. In fact, recent experiments on the ISX-B device with a beryllium limiter demonstrated the suitability of this material, and it is therefore being considered also for use in the JET device. Beryllium has the lowest atomic number of any metal suitable for structural application, and its presence in the plasma as an impurity minimizes the Bremsstrahlung losses.

With regard to future fusion reactors, its potential use depends critically on its radiation resistance to fast neutrons. Because of its large cross section for the (n,2n) reaction with the associated helium production, and because of the high PKA energy created by the 14 MeV neutrons, swelling is of major concern.

At the present time, no data on the effects of fast neutron, high-fluence irradiation on the dimensional changes of beryllium exists. However, data on beryllium specimens irradiated in both the ETR and ATR have been reported by Beeston and coworkers.[1,2] The specimens in ETK were irradiated at about 100°C to fluences up to about 3.5×10^{22} n/cm^2 ($E > 1$ MeV), and some were subsequently annealed to higher temperatures to study the formation of helium bubbles. These data provide an important source of information to test the models of radiation-induced dimensional changes in beryllium which were developed during the course of this study. However, it is important to first discuss some basic aspects of diffusion, displacement damage, helium production, and radiation-induced dimensional changes.

Since beryllium is an anisotropic metal with a hexagonal closed-packed crystal structure, the following dimensional changes can be produced by neutron irradiation:

a) void swelling.
b) bubble swelling,
c) anisotropic or irradiation growth,
d) irradiation creep,
e) microcrack formation.

Void swelling has been observed to occur in most metals subject to fast-neutron irradiation at elevated temperatures. Two conditions must, in general, be met for void swelling to occur. First, the irradiation temperature must be higher than the temperature for vacancy migration but lower than the temperature for significant self-diffusion. Second. the ratio of Heldpa must be small or else swelling will be gas-driven (i.e., bubble swelling will be the dominant mechanism for swelling at high Heldpa ratios).

During void swelling, self-interstitials form dislocation loops or are absorbed at edge dislocations. If the dislocation loops and the edge dislocations have a preferred crystallographic orientation. as expected for anisotropic metals such as beryllium. void swelling is accompanied by anisotropic growth or irradiation growth. The latter may even occur in the absence of void formation if vacancies are absorbed preferentially at dislocations with Burgers vectors of different orientation than those for dislocations which capture self-interstitials. Anisotropic growth in polycrystalline mterials will eventually lead to microcrack formation, and hence, swelling. At the same time, the fracture strength will be reduced.

Radiation-enhanced creep requires displacement damage, and it increases with the void swelling rate.

For an assessment of all these dimensional changes, three processes are of crucial importance: the vacancy diffusion rate, the displacement rate, and the helium production rate. It might be expected that the helium production rate in beryllium dominates all other considerations.

5.2 Diffusion Properties of Beryllium

Self-diffusion data in pure metals have recently been reviewed by Peterson.[3] For self-diffusion parallel to the C-axis in Be

$$D_{\parallel} = 0.62 \exp(-1.71\ \text{eV}/kT)\ \text{cm}^2/\text{s} .$$

and perpendicular to the C-axis,

$$D_{\perp} = 0.52 \exp(-1.63\ \text{eV}/kT)\ \text{cm}^2/\text{s} .$$

In comparison to the melting point of Be, T_m = 1550 K, the activation energies for self-diffusion are low. For example, the activation energy for nickel is 2.8 eV, so that at about half of its melting point or at 873 K, the self-diffusion coefficient is equal to 2.2×10^{-17} cm^2/s. In comparison. $D_{\perp} = 2.1 \times 10^{-17}$ cm^2/s and $D_{\perp} = 1.03 \times 10^{-16}$ cm^2/s in Be at 523 K. As a result of the low activation energy, self-diffusion becomes a significant process in Be at about 250°C.

5.3 Displacement and Helium Production Rates

The energy of primary recoil atoms (PKA) produced in beryllium by fast neutrons is large compared to other metals as a result of the small atomic weight. As seen from Table 1, the average primary recoil energy produced by 1 MeV and 14 MeV neutrons is 0.18 MeV and 2.52 MeV, respectively. For these high PKA energies, the electronic stopping power is dominant for beryllium, which results in the very low damage efficiencies shown in the third column of Table 1. The number of displacements were obtained by estimating the displacement energy from the empirical relationship $E_d \cong 150\ k_B T_m$, where k_B is the Boltzmann constant in eV, and T_m is the melting point. For beryllium, this estimate gives E_d = 19 eV. The elastic scattering cross section of neutrons with beryllium is about 1 barn and 2.5 barn for 1 MeV and 14 MeV neutrons, respectively. As a

TABLE 1

DISPLACEMENTS IN BERYLLIUM

Neutron Energy (MeV)	Average Primary Recoil Energy (MeV)	Damage Efficiency	Number of Displacements
1	0.18	0.075	355
14	2.52	0.010	663

result, a neutron fluence of 10^{22} n/cm^2 (E = 1 MeV) produces about 3.5 dpa, whereas a fusion fluence of 10^{22} n/cm^2 (E = 14 MeV) generates about **16.6** dpa.

The production rate of helium in the ATR and ETR was estimated by Beeston' to be about 4700 appm He per 10^{22} n/cm^2 (E > 1 MeV). Hence in these fission reactors, the Heldpa ratio is on the order of 1300 appm He/dpan, where dpan indicates that only displacements by neutrons and excluding those by the decay of the nucleus are taken into account.

In the beryllium moderated fusion breeder blanket, Beeston' estimates the helium production rate to be in the range of 5500-7000 appm per 10^{22} n/cm^2 (E > 1 MeV). The higher value corresponds to the front of the blanket where the neutron spectrum is faster. In this case, the Heldpa ratio is expected to be substantially greater than 420 He/dpan in the front of the blanket (where the neutron spectrum is fastest, but not 14 MeV) and somewhat less than 1570 He/dpan in the back of the blanket (where the uncollided fusion source strength is low).

To put these helium production and displacement rates in proper perspective, we note that helium ion implantation for blistering studies results in a ratio of about 1000 appm He/dpa.[4] As these studies have shown, swelling in this regime is dominated by gas-driven or bubble swelling for all irradiation temperatures. We conclude, therefore, that the predominant damage mechanism in both fission and fusion neutron irradiations of Be is helium bubble swelling. All other processes mentioned above will play a minor role in determining the radiation lifetime of beryllium components in fusion reactors.

5.4 Helium Bubble Swelling of Neutron Irradiated Beryllium

The formation and growth of helium bubbles in metals can take place by both athermal and thermal processes, depending on the irradiation temperature. When self-diffusion is insignificant. the growth proceeds by the emission of self-interstitials which remained trapped near the bubble, or by the punching of interstitial loops. For both cases there exists a pressure in the bubble which greatly exceeds the bubble equilibrium pressure of $2\gamma/r$, where r is the bubble radius and γ the surface energy. In fact, the helium density within the bubble remains nearly equal to the solid packing density, and swelling is simply equal to

$$\frac{\Delta V}{V_o} = \frac{V_{He}}{\Omega} C_{He} \qquad (1)$$

where Ω is the atomic volume of the host metal, V_{He} is the molar volume of dissolved helium, and C_{He} is the atomic fraction of helium.

Equation (1) has been fitted to the swelling data reported by Beeston[2] for beryllium irradiated at about 100°C, with the result that

$$\frac{\Delta V}{V_o}(\%) = 10.52 \pm 0.23]\phi t \ , \qquad (2)$$

where ϕt is in units of 10^{22} n/cm^2 (E > 1 MeV). Per unit of this fluence, about 0.9 at.% of helium is produced, so that Eq. (2) can also be written

$$\frac{\Delta V}{V_o}(\%) = 10.58 \pm 0.25]C_{He}(at.\%) \ . \qquad (3)$$

This equation implies a molar volume of helium in Be of

$$V_{He} = C0.58 \pm 0.25]\Omega \qquad (4)$$

which is in excellent ayreement with the value of 0.62 Ω obtained from computer simulation studies of helium clusters in Cu by Baskes and Holbrook.[5] Equation (3) is expected to be applicable for irradiation temperatures $ 250°C based on the arguments given above on self-diffusion.

At higher temperatures self-diffusion allows bubbles to grow by absorption of thermal vacancies. In this case. the bubble pressure remains close to the equilibrium pressure

$$P = 2\gamma/r \ .$$

If this equation is multiplied by the bubble fractional volume then the left hand side becomes equal to $C_{He}kT$ if an ideal gas law is assumed. Since the bubble volume can also be written as $\Delta V/V_o = (4\pi/3)Nr^3$, where N is the bubble density, we obtain

$$\frac{\Delta V}{V}(\%) = 100\ (\frac{3}{4\pi N})^{1/2}\ (\frac{C_{He}kT}{2\gamma})^{3/2} \ . \qquad (5)$$

Beeston[2] has experimentally determined the bubble density in post-irradiation annealed beryllium samples. For samples irradiated at about 100°C no visible bubbles were found until the annealing temperatures exceeded 300°C, which is close to the estimated temperature where self-diffusion becomes important.

The measured bubble densities for annealing temperatures between 400°C and 600°C are given by the empirical equation

$$N = 1.4 \times 10^{14} \exp(0.41\ eV/kT)\ cm^{-3} \ . \qquad (6)$$

The reported measurements of the surface energy γ of beryllium are 1 J/m^2,[6] and 1.6 J/m^2.[7] However, Muir[8] list a value of 2 J/m^2, which would be in better agreement with empirical correlations based upon melting temperature and cohesive energy.

Accordingly, bubble swelling predictions were made for surface energy values of 1 J/m^2 and 2 J/m^2 by using Eqs. (5) and (6). At low temperatures. Eq. (5) predicts swelling values below the values obtained with Eq. (3). Hence, it is assumed that the actual bubble swelling is determined by whichever equation provides the largest value. The results are shown in Figures 1 and 2 for a surface energy of 1 J/m^2 and 2 J/m^2, respectively. Measured swelling values for the annealed samples are also indicated in these figures together with the estimated helium concentrations.

It is seen that better agreement between the theoretical predictions and the measured data is obtained when a value of 2 J/m^2 is assumed for the surface energy of beryllium. It is also found that the transition temperature where equilibrium bubble swelling becomes equal to the "solid helium" swelling shifts to lower values with the increase in the helium concentration.

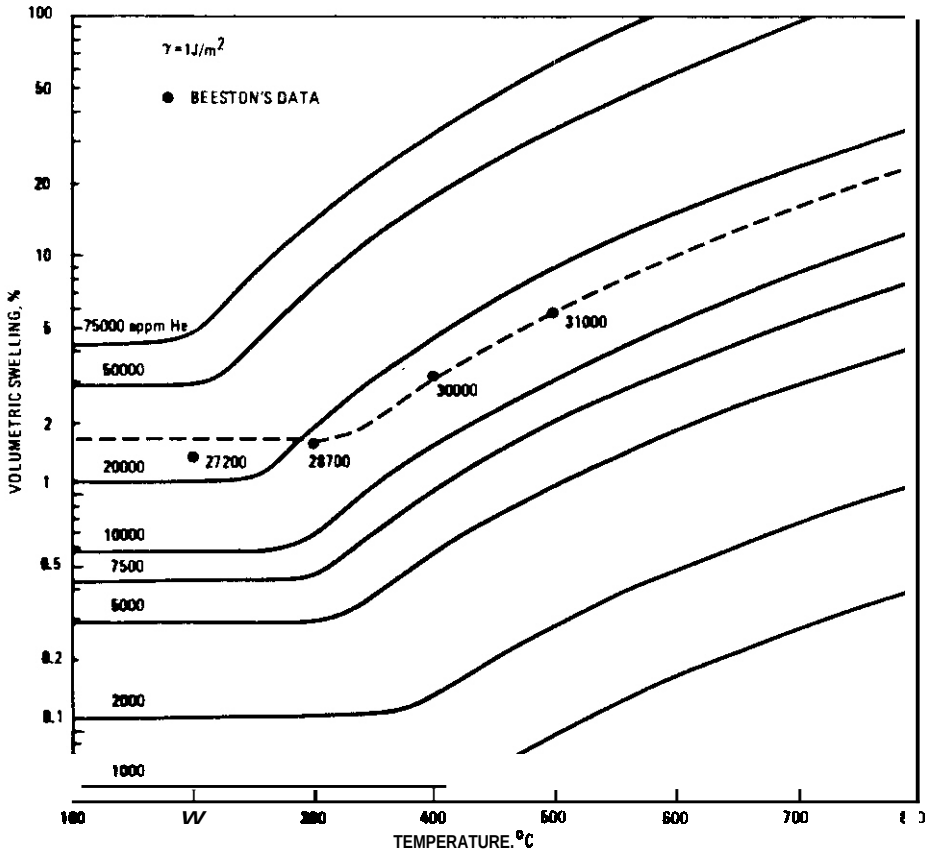

FIGURE 1. Results of the Swelling Model Assuming a Surface Energy of 1 J/cm^2.

6.0 References

1. J.M. Beeston, M.R. Martin, C.R. Brickman, G.E. Korth, and W.C. Francis, in Symp. on Materials Performance in Operating Nuclear Systems, Ames Laboratory, **Ames,** Iowa. August 1978. Nuclear Metallurgy 19, CONF-730801, pp. 59-87.

2. J.M. Beeston et al., "Comparison of Compression Properties and Swelling of Beryllium Irradiated at Various Temperatures," EGG-FT-6608, Idaho National Engineering Laboratory (19841.

3. N.L. Peterson, J. Nucl. Matls. 69 & 70, p. 3, 1970.

4. W.G. Wolfer, J. Nucl. Matls. 93 & 94, p. 713 , 1980.

5. M. Baskes and J.H. Holbrook, Phys. Rev. B17, p. 422, 1978.

6. R.S. Barnes and **G.B.** Redding, Nuclear Energy 10, p. 22, 1959.

7. J.B. Rich, G.B. Redding and R.S. Barnes, J. Nucl. Matls. 1, p. 73, 1959.

8. L.E. Muir, Interfacial Phenomena in Metals and Alloys, Addison-Wesley Publ. Corp., Reading, **MA,** 1975. p 124.

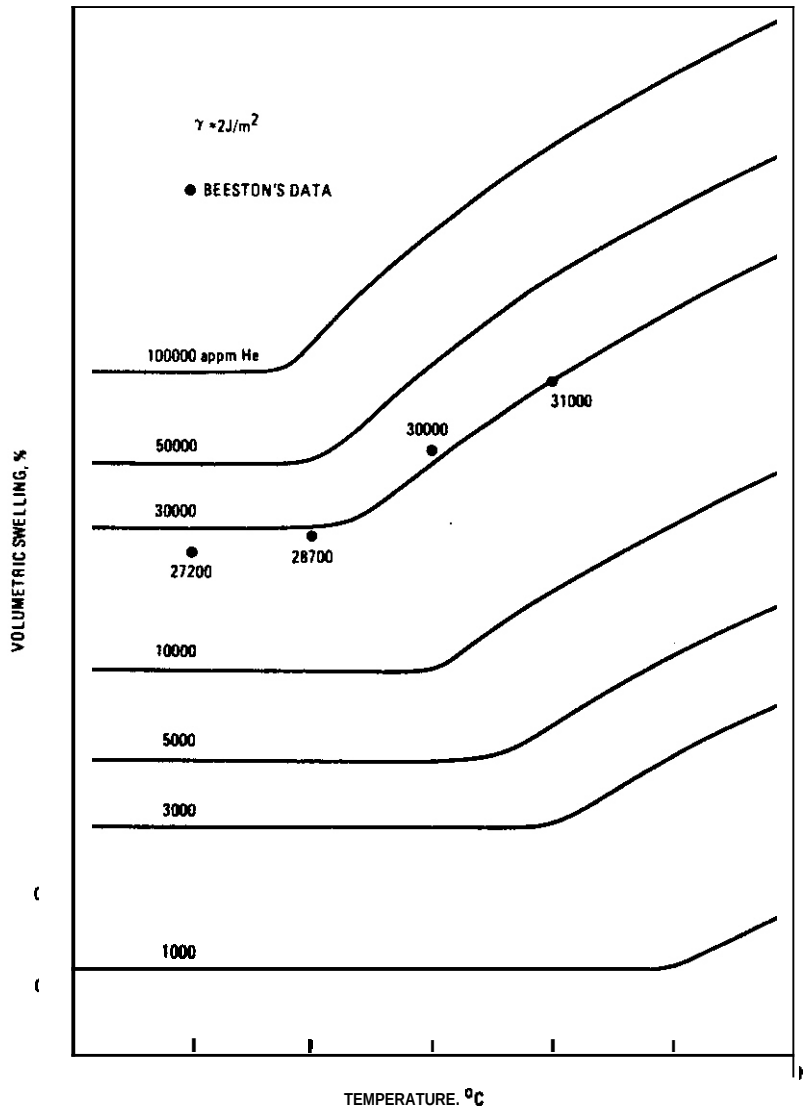

FIGURE 2. **Results** *of* **the Swelling Model** Assuming *a* **Surface Energy** *of* 2 J/cm^2.

CHAPTER 7

FUNDAMENTAL STUDIES SUPPORTED BY OTHER AGENCIES

BASIC RADIATION EFFECTS RESEARCH AT OAK RIDGE NATIONAL LARORATORY

L. K. Mansur (Oak Ridge National Laboratory)

The basic radiation effects program at Oak Ridge National Laboratory is a large effort with the dual objectives of understanding the atomic and microstructural defect mechanisms underlyinq radiation effects, and of determining principles for the design of radiation resistant materials. This program is sponsored by the Division of Materials sciences of the U.S. Department of mergy. A strength of this effort is the parallel and integrated theoretical and experimental approach to each major research area. The experimental effort is active in analytical electron microscopy, ion irradiations and ion beam techniques, neutron irradiations, surface analysis, mechanical testing and other areas. The theoretical effort is active in developing the theory of radiation effects based on defect mechanisms for a broad range of phenomena, and in applying it to the design and interpretation of experiments as well as to allay design.

Because of the importance and relative lack of mechanistic understandinq of anticipated materials problems in fusion reactors, a significant fraction of this research addresses the special characteristics, materials, and phenomena to be encountered there. The program interacts with the Alloy Development for Irradiation Performance and the Damage Analysis and Fundamental Studies programs of the office of Fusion Energy.

Aspects of the work in Which significant progress has been made recently are in the mechanisms of helium interaction with swelling and in related mechanisms of swelling variation with alloy type and composition. The following contributions describe two research efforts in this area.

EXPERIMENTAL DETERMINATION OF THE CRITICAL CAVITY RADIUS IN FE-10% Cr FOR ION IRRADIATION*

L. L. Horton and L. K. Mansur, Metals and Ceramics Division (Oak Ridge National Laboratory)

1.0 Abstract

An ion bombardment experiment was designed tu investigate the minimum critical radius, r_c^*, for the ferritic alloy Fe-10% Cr. Specimens were implanted with 300 appm Helium, annealed, and then irradiated to 30 dpa at 850K with 4 MeV Fe^{++} ions. The specimens contained a bimodal cavity distribution consisting of a population of larger Cavities (average radius 7.6 nm) and a population of smaller cavities (average radius 1.2 nm). The upper Cut-Off of the cavity radii for the smaller cavities, 2.5 nm, is interpreted as r_c^*. Theoretical calculations of r_c^* for physically allowable combinations of bias, surface energy, vacancy migration energy, and vacancy formation energy and entropy were performed using the measured minimum critical radius and microstructural data. Thus, an estimation of these fundamental parameters was made for this alloy. The results Suggest that a bias of ~0.2 is reasonable. An assessment of the possible values of the other fundamental parameters is given. In addition, the low irradiation-induced dislocation density (1×10^{13} m^{-2}), which results in the ratio of the dislocation and Cavity sink strengths, Q, being much less than unity, may be partially responsible for the low cavity growth rate in this alloy.

2.0 Introduction

An important parameter in the cavity growth process in the radius above which the cavity exhibits bias-driven growth. When bias-driven growth occurs, large values for the cavitational swelling can result. The value for the cavity radrus above which bias-driven growth occurs is referred to as the critical cavity radius. A development of the equations for the critical cavity radius and related concepts, as well as a review of previous work in the area, is given in Reference 1. Calculations of this type have demonstrated that the critical cavity radius is sensitive to many experimental parameters, including dose rate[2], irradiation temperature[2,3], dislocation density[4] and the gas pressure within the cavity. The latter has a particularly interesting effect. As the number of gas atoms in a cavity increases, the critical cavity radius decreases. As first discussed by Sears[5], if the number of gas atoms within a cavity exceeds a critical value, the critical radius effectively disappears and bias-driven cavity growth occurs regardless of the cavity radius. The size for which the critical radius disappears upon the addition of more gas atoms is termed the minimum critical radius. Coghlan and Mansur[3] have shown how the calculated values for both the critical number of gas atoms and the minimum critical radius are dependent on the gas law used in the calculations.

Experimentally, the effect of the critical cavity radius can be seen in the bimodal cavity distributions that are often observed in irradiated materials containing helium. Bimodal cavity distributions typically contain a ppulation of cavities with an average diameter of a few nanometers as well as a second population of cavities with a much larger diameter. An explanation for these distributions based on the critical radius concept suggests that the smaller cavities did not achieve bias-driven growth because their radii are less than the critical value. Thus, the upper cut-off radius for the smaller cavities approximately equals the theoretical minimum critical radius. The larger cavities are believed to have radii greater than the critical radius and thus have grown in a bias-driven mode.

*Research sponsored by the Division of Materials Sciences, U.S. Department of Energy, under contract DE-AC05-84OR21400 with Martin Marietta Energy Systems, Inc.

In this investigation, an ion bombardment experiment was designed to study the critical cavity radius in the ferritic alloy Fe-10% Cr. The objective was to begin with a pre-existing population of gas bubbles that spanned the minimum critical radius and critical number of gas atoms. This allowed observation of the spontaneous separation of the distribution into a bimodal distribution upon irradiation. The Separation and consequent determination of the minimum critical radius were then related, via the theory and observed microstructures, to basic material parameters, thus providing an estimate of vacancy migration energy, vacancy formation energy and entropy. surface energy, and bias for this material. In order to generate a population of bubbles, specimens were implanted with helium and subsequently annealed. The specimens were then bombarded with heavy ions to form the bimodal distribution. This procedure is similar to that used by Mazey and Nelson[6] and Lee and Mansur[7] to investigate the critical radius in austenitic alloys. While other investigations have provided determinations of the critical cavity radius for austenitic materials, the present results are among the first available for ferritic materials.

2.1 Experimental Procedure

The Fe-10% Cr alloy used for this investigation was fabricated at Oak Ridge National Laboratory. A full description of the fabrication procedure can be found in Reference R. Briefly, rod stock (3-mm-dia) was annealed in flowing dry hydrogen for 24 h at 1400 K, furnace cooled to loo0 K, held at lo00 K for 2 h, and then furnace cooled. The specimens had a b.c.c. structure with a grain size of ~200μm and a dislocation density of $<10^{12} m^{-2}$. Impurity concentrations for the alloy after annealing are shown in Table 1. Disk specimens of ~0.5 mm thickness were sliced from the rods and prepared tor ion bombardment using Standard techniques[8]. Final specimen thicknesses were 0.3 mm.

TABLE 1

IMPURITY CONCENTRATIONS IN Fe—10% Cr SPECIMEN MATERIALS (wt ppm)

C	34	K	7
H	2	Mg	<3
N	4	Mn	10
O	6	Mo	<2
Ag	2	Na	4
AS	20	Nb	2
B	2	Ni	20
Ba	4	P	10
Br	5	S	20
Cl	40	Sb	2
Ca	4	S''	70
Co	4	Ta	<3
C''	30	V	
Ga	50	W	<10
Ge	20	Zn	10

A 3 x 3 array of specimens was implanted with 300 appm helium at room temperature followed by a 2 h heat treatment at 1000 K. During the implantation, the energy of the helium ion beam was ramped sinusoidally at 2.5 $\times 10^{-2}$ Hz between n.2 and 0.4 MeV in order to implant the helium evenly over a region extending from about 0.65 to 0.95 μm from the specimen surface. After the 2 h heat treatment, the specimen temperature was reduced to 850 K and six of the specimens were irradiated with 4 MeV Fe^{++} ions to a damage level of 30 dpa. The damage rate during the heavy ion bombardment was ~8 $\times 10^{-3}$ dpa/sec. The remaining specimens were covered by a mask during the irradiation. The ion irradiations and heat treatment were performed in the target chamber of the Van de Graaff facility at ORNL.

Specimens were prepared for transmission electron microscopy by electropolishing to remove a 0.85 μm thick layer from the irradiated surface ("sectioning") followed by backthinning to perforation. The sectioning depth was selected based on the damage-depth profile for ion-irradiated iron[9]. The specimens were sectioned in a vertical jet apparatus with an 80% ethanol-20% perchloric acid solution cooled to 225 K. Backthinning was performed at 285 K with a Tenupol electropolishing apparatus and an electrolyte of 900 ml acetic acid, 100 ml methanol, and 100 ml perchloric acid. The specimens were examined at 120 kV in JEM 120C and JEM 120CX transmission electron microscopes (TEM). The JEM 120C THM was equipped with a special objective lens pole-piece for the observation of magnetic materials.

2.2 Experimental Results

The specimens that were implanted with helium and annealed contained a homogeneous distribution of small cavities, or bubbles. with an average diameter, $\bar{d}_b$, of 2.7 nm and a concentration of 6×10^{21} m^{-3}. A histogram Of the cavity diameters is shown in Fig. 1. As expected, bubbles were also found along dislocations and grain boundaries.

The heavy ion damage caused the formation of a bimodal cavity distribution as shown in the histogram of the cavity diameters in Fig. 2 and the micrographs in Fig. 3. The dislocation density in these specimens was ~1 x 10^{13} m^{-2}. The larger cavities have a concentration of 6.7 x 10^{20} m^{-3} and an average diameter, $\bar{d}_c$, of 15.2 nm, yielding a cavitational swelling of 0.2% (volume-averaged cavity diameter of 17.7 nm). The smaller cavities in the distribution have a concentration of 3 x 10^{22} m^{-3} and an average diameter, $\bar{d}_s$, of 2.3 nm. As shown in Fig. 2, the upper cut-off for the small cavity diameters for the bubble ppulation is ~5 nm. Therefore, assuming that the smaller cavities have not achieved the critical radius and the larger cavities have exceeded the critical radius, the minimum critical radius indicated by the experimental data is ~2.5 nm.

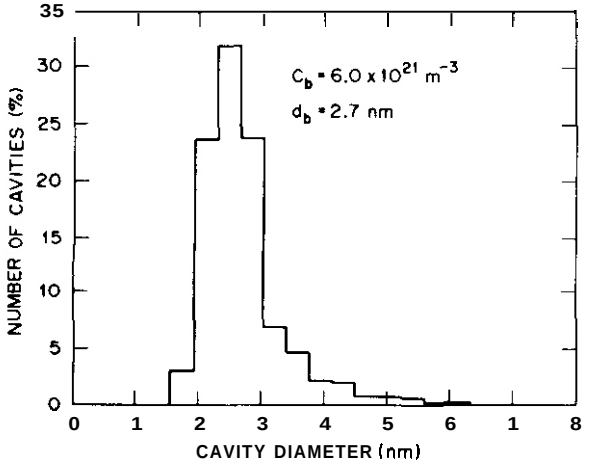

FIGURE 1. Histogram of the cavity diameters prior to irradiation for Fe-10% Cr implanted with 300 appm helium and annealed.

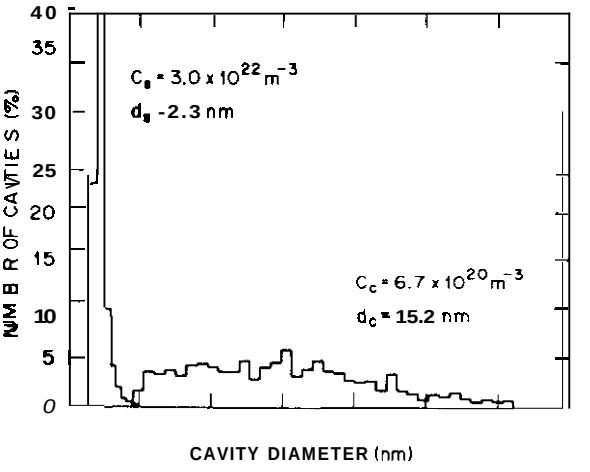

FIGURE 2. Superimposed histogram of the cavity diameters for the two Cavity populations making up the bimodal distribution found in Fe-10% Cr implanted with 300 appm helium, annealed, and irradiated to 30 dpa.

2.3 Theoretical Calculations

2.3.1 Background

The calculations performed in this study are based on equations given by Mansur and Coghlan[1]. The growth rate of a cavity, dr_c/dt, was calculated with the expression:

$$dr_c/dt = \frac{\Omega}{r_c}[Z_v^c D_v C_v - Z_i^c D_i C_i - Z_v^c D_v C_v^e(r_c)] \quad (1)$$

where the subscripts v and i refer to vacancies and interstitials, respectively; r_c is the cavity radius; Ω is the atomic volume; $Z_{i,v}^c$ are the cavity capture efficiencies; $D_{i,v}$ are the diffusion coefficients; $C_{i,v}$ are the point defect concentrations; and $C_v^e(r_c)$ is the thermal vacancy concentration near a cavity of radius r_c. The variables $C_{i,v}$ and $C_v^e(r_c)$ are determined by the sink strengths, point defect generation

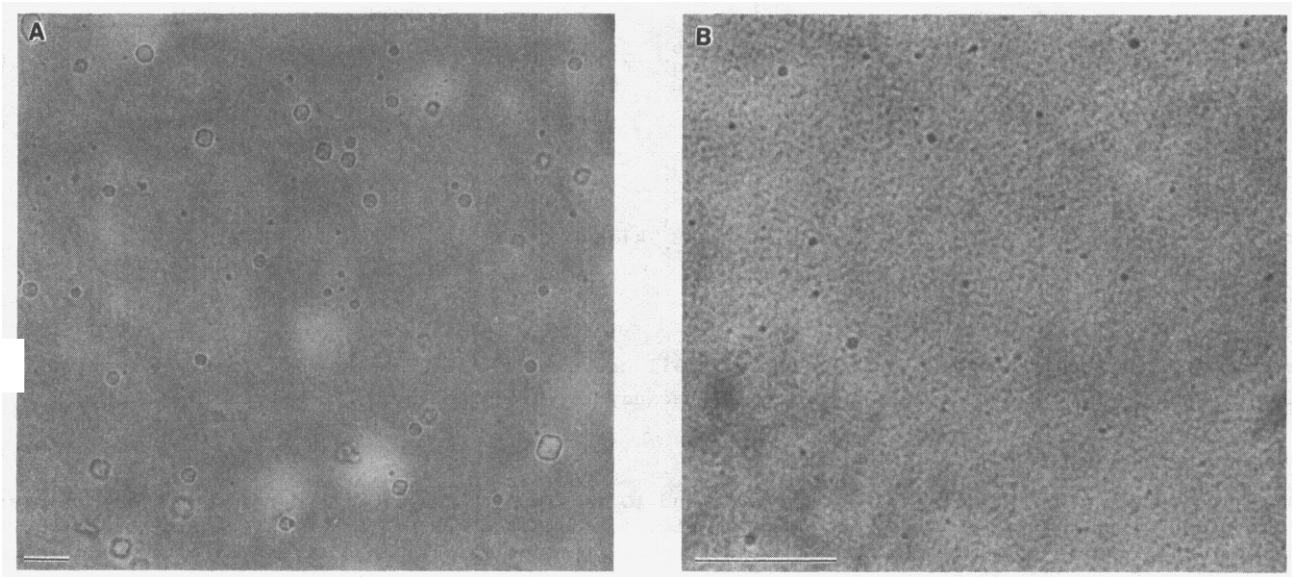

FIGURE 3. Micrographs of the cavities in the bimodal size distribution. Scale marker length is 50 nm. A) Large cavities, specimen thickness of 95 nm; B) small cavities, specimen thickness 25 nm.

rates, point defect formation energies, point defect migration energies, pressure within the cavities, thermal vacancy emission rate, etc. The complete expressions for these variables are given in Reference 4. The pressure within a cavity was assumed to obey a modified Van der Waals gas law given by:

$$P_g = n_g kT/(\frac{4}{3}\pi r_c^3 - n_g B) \quad (2)$$

where n_g is the number of gas atoms in the cavity, k is Boltzmann's constant, T is the irradiation temperature, and B is a constant given by:

$$B = 6.65 \times 10^{-27} [4.5 \times 10^{-4} + 5.42/(1890 + T)] \ m^3/atom \quad (3)$$

for helium[10].

In calculating the sink strengths and the rate of vacancy emission from the sinks, the measured dislocation and cavity parameters observed in the specimens irradiated to 30 dpa were used. Due to the bimodal nature of the cavity distribution, the smaller and the larger cavities were considered separately in calculating the sink strengths. The Sink strengths, S, for point defects are given by:

$$S_{v,i} = 4\pi(\bar{r}_s N_s Z^s_{v,i}(r_s) + \bar{r}_c N_c Z^c_{v,i}(r_c)) + LZ^d_{v,i} \quad (4)$$

where the subscripts and superscripts s and c refer to small and large cavities, respectively, N is the concentration, r is the average radius, and L is the dislocation density. The capture efficiencies were assumed to be the same for the small cavities and the larae cavities. The rate of thermal vacancy emission from the sinks, G_T [Eq. (5) in Reference 1], is given by

$$G_T = D_v C_v^o \left\{ Z_v^d L + 4\pi Z_v^c \left[\bar{r}_s N_s \exp[-(P_g^s - \frac{2\gamma}{r_s})\Omega/kT] + \bar{r}_c N_c \exp[-(P_g^c - \frac{2\gamma}{r_c})\Omega/kT] \right] \right\} \quad (5)$$

where

$$C_v^o = \Omega^{-1} \exp(S_v^f/k) \exp(-E_v^f/kT) \quad , \quad (6)$$

P_g^c and P_g^s are the gas pressures in the large and small cavities and γ is the Surface tension. In Eq. (6), S_v^f is the vacancy formation entropy and E_v^f is the vacancy formation energy.

To more accurately define G_T, Eq. (5) can he expanded to incorporate the radii and concentrations of cavities for each division of the histograms shown in Fig. 2, instead of using the average cavity radii for the small and large cavity populations. For the observed cavity populations, this expansion alters the calculated value of G_T by less than 0.6%.

For the calculation of G_T, values for P_g^s and P_g^c must he assumed. If the implanted helium is partitioned to the cavities and dislocations—according to the sink strengths ($S_v^d = Z_v^d L = 1 \times 10^{13} m^{-2}$, $S_v^c = Z_v^c 4\pi \bar{r}_c N_c = 6.4 \times 10^{13}\ m^{-2}$, and $S_v^s = Z_v^c 4\pi \bar{r}_s N_s = 4.2 \times 10^{14}\ m^{-2}$ for $Z_v^d = Z_v^c = 1$) then ~255 appm helium is partitioned to the small cavities, ~39 appm to the large cavities, and ~6 appm to the dislocations. However, only ~100 appm helium is required in order for the pressure in the small cavities to equal the equilibrium bubble pressure, $P_{eq}^s = 2\gamma/r_s$ (assuming $\gamma = 1\ J/m^2$). If the remaining 200 appm helium is partitioned between the large cavities and the dislocations, ~170 appm helium is available to pressurize the large cavities. This translates to ~2.2 x 10^4 helium atoms/cavity or a pressure of ~0.6 of P_{eq}^c. The above discussion assumes that all of the partitioned to visible sinks. If a portion of the implanted helium is attached to small vacancy–helium clusters, the helium available to pressurize the cavities would be reduced. For the calculations of G_T, $P_g^s = P_{eq}^s$ and $P_g^c = 0$ were assumed. The actual value for P_g^c has little effect on G_T because thermal vacancy emission from cavities of large radius of curvature approaches that for flat surfaces [Eq. (5)]. For $P_g^c = 0$, $G_T = 5.218 \times 10^{24} m^{-3} sec^{-1}$ while for $P_g^c = 0.6\ P_{eq}^c$, $G_T = 5.129 \times 10^{24} m^{-3} sec^{-1}$, a change of Of <2%.

When the critical cavity radius, r_c^c, or the critical number of gas atoms, n_g^* is attained, dr_c/dt is equal to zero. Figure 4 shows typical results for the present calculations. When n_g is less than n_g^*, $dr_c/dt = 0$ for two values of r_c. The lower of these values is r_c^s, the radius for which the cavity is stable, while the larger value is r_c^c. A cavity with $n_g < n_g^*$ and a radius between r_c^s and r_c^c will shrink (i.e., $dr_c/dt < 0$) to r_c^s. The cavity will exhibit bias–driven growth only when $r_c > r_c^c$. when $n_g = n_g^*$, as is also shown in Fig. 4, $dr_c/dt = 0$ for only one value of r_c, referred to as r_c^{c*}. For $n_g > n_g^*$, the cavity will exhibit bias-driven cavity growth regardless of the cavity radius.

In this investigation, values for n_g^* and r_c^{c*} were determined for a range of point defect and other fundamental parameters. The parameters that were held constant in the calculations are summarized in Table 2. The parameters in Table 2 are necessary to perform calculations with Eq. (1) (see Ref. 11. In addition, the vacancy formation energy, E_v^f, was assumed to be equal to the difference between the self-diffusion energy, E^{SD}, and the vacancy migration energy, E_v^m. Analytical solutions[3,4] for n_g^* and r_c^{c*} have teen obtained assuming that the dislocation sink strength was much greater than the cavity sink strength. However, the experimental data for the dislocations and cavities observed for Fe-10% Cr indicates that this assumption is invalid here. Therefore, a numerical approach was used to determine the values for r_c^{c*} and n_g^*.

2.4 Theoretical Results

The values of r_c^{c*} and n_g^* determined for a self-diffusion energy of 2.6 eV and a number of values for y, E_v^m, bias and S_v^f are shown in Table 3. Here, the bias is defined as $Z_i^d Z_v^c - Z_i^c Z_v^d$. In this table, S_v^f is listed in terms of Boltzmann's constant, i.e., $S_v^f = 0.5k = 4.308 \times 10^{-5}$ ev/K. Tabte 4 summarizes a series of calculations assuming that E^{SD} = 2.7, 2.8 or 2.9, $\gamma > 1\ J/m^2$, and $S_v^f = 1.5$ k. The basis for the selection of parameter values is discussed in the next section. As shown in Tables 3 and 4, r_c^{c*} is equal to 25 nm, the experimentally determined value for the minimum critical radius, for several combinations of y, E^{SD}, E_v^m, Z_r^d and S_v^f. The bias ranges from 0.05—0.4.

Plots of dr_c/dt, the radial growth rate, as a function of the Cavity radius are shown for several biases in Figure 5. For larger cavities in calculations with r_c^{c*} = 2.5 nm, the value for dr_c/dt is primarily dependent on the bias. For example, although each of the curves shown in Fig. 5 for a bias of 0.4 used different combinations Of the rest Of the fundamental parameters, the radial growth rate indicated for a cavity with a radius >5 nm is about 5 pm/sec. In terms of displacement rate, this growth rate is 0.62 nm/dpa for a displacement rate of 8×10^{-3} dpa/sec. Similarly the radial growth rate is about 0.38 nm/dpa for a bias of 0.2, 0.17 nm/dpa for a bias of 0.1 and 0.08 nm/dpa for a bias of 0.05.

2.5 Discussion

The helium implantation/anneal/heavy ion bombardment sequence successfully generated a bimodal Cavity distribution in Fe-10% Cr. For the 850 K irradiation temperature, the experimental value for the minimum Critical cavity radius indicated by this distribution is ~2.5 nm. Calculations of r_c^{c*} and n_g^* were performed for a range of values for the parameters γ, E^{SD}, E_v^m, S_v^f and the bias. As shown in Table 3, when traditional values are assumed for these parameters (γ = 1 J/m^2, S_v^f = 1.5 k, bias = 0.05, E^{SD} = 2.6 eV and E_v^m = 1.2 eV), extremely high values are calculated for both r_c^{c*} and n_g^*. In order for r_c^{c*} to equal 2.5 nm for E^{SD} = 2.6, the bias is 0.2 or greater, γ is <1 J/m^2 and S_v^f is equal to or less than k. These are relatively low values for γ and S_v^f. For a temperature of 1723 K, the surface energy for free, clean

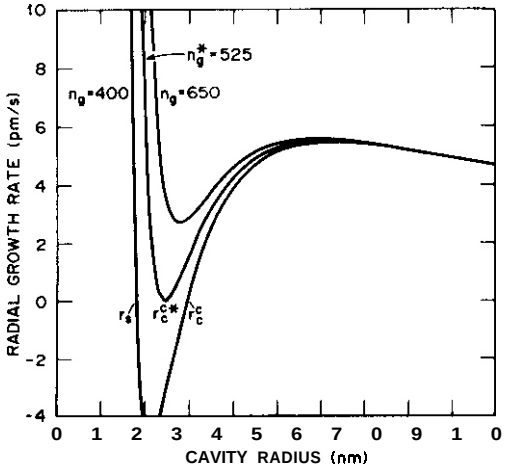

FIGURE 4. Typical plots of the radial growth rate as a function of cavity radius for $n_g < n_g^*$, $n_g = n_g^*$, and $n_g > n_g^*$.

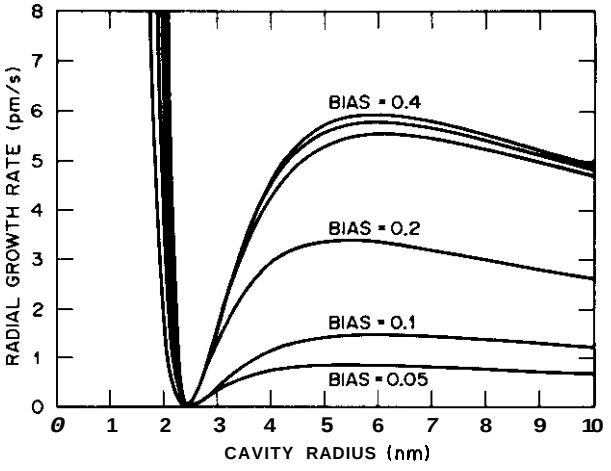

FIGURE 5. Plot of the radial growth rate as a function of cavity radius calculated for Fe-10% Cr with r_c^{c*} = 2.5 nm and biases ranging from 0.05 to 0.40.

TABLE 2

values for parameters used in calculations for r_c^{c*} and n_g^*.

Displacement rate, G	6.8×10^{26} m^{-3}sec^{-1} (8×10^{-3} dpa/sec)
point defect survival fraction, f	0.5
Recombination radius, r_r	0.344 nm
Diffusion pre-exponentials, D_v^o	1.9×10^{-4} m^2/sec
D_i^o	10^{-6} m^2/sec
Interstitial migration energy, E_i^m	0.26 eV
Sink efficiencies	$Z_v^d = Z_i^c = Z_v^c = 1$
Experimental sink parameters	r_s = 1.65 nm, $N_s = 3\times10^{22}$ m^{-3}
	r_c = 7.6 nm, $N_c = 6.7\times10^{20}$ m^{-3}
	L = 1×10^{13} m^{-2}

TABLE 3

values for r_c^{c*} and n_g^* calculated for the parameters listed and assuming E^{SD} = 2.6 eV.

γ_2 (J/m^2)	E_v^m (ev)	$S_v^{f\ddagger}$ (k)	Bias	r_c^{c*} (nm)	n_g^*
1	1.2	1.5	.05	24	131,000
1	0.7	1.5	.05	22	108,000
1	0.7	1.0	.05	18	69,000
1	0.7	0.5	.05	14	39,500
0.75	0.7	0.5	.05	11	20,500
0.75	0.7	0.5	.2	4.1	2,300
0.5	0.7	0.5	.2	2.8	730
0.75	0.7	0.5	.4	2.5	719
0.5	0.7	1.0	.4	2.5	525
0.6	1.2	0.5	.4	2.5	595

*values for S_v^f are shown in terms of Boltzmann's constant, k.

TABLE 4

values for r_c^{c*} and n_g^* calculated for the parameters listed and assuminq S_v^f = 1.5 k.

γ_2 (J/m^2)	E_v^m (ev)	E^{SD} (ev)	Bias	r_c^{c*} (nm)	n_g
1	0.7	2.7	.4	2.5	900
2	1.2	2.R	.4	2.5	1400
1.5	0.7	2.8	.2	2.5	1070
1	0.7	2R	.1	2.5	935
2	1.2	2.9	.1	2.5	1425
1.5	0.7	2.9	.05	2.5	1100
1.25	1.2	2.9	.05	2.5	950

surfaces in iron has been measured as 1.95 J/m^2 with a calculated temperature coefficient (a-iron) of -1.4×10^{-4} J/m^2-K.[11] with these parameters, $\gamma_{calc} = 1.95 - 1.4 \times 10^{-4}$ (T-1723) J/m^2 or, for 850K, $\gamma_{calc} \approx 2.1$ J/m^2. Since many impurity species adsorbed on the void surfaces would result in $\gamma < \gamma_{calc}$, a value of γ t2.1 J/m^2 would not be surprising. However, it is usually assumed that the maximum reduction in γ_{calc} due to segregation is about 50%, yielding an expected range for γ of ~1 to 2 J/m^2, rather than γ <1 as suggested above. Likewise, although no measured values for S_v^f are available, S_v^f < k may be unlikely. If S_v^f is assumed to be 1.5 k and γ is assumed to be within the 1 to 2 J/m^2 range, r_c^{c*} = 2.5 nm can be calculated only for E^{SD} >2.6 eV as shown in Table 4. Reported values for E^{SD} for pure iron range from 2.5 ev[12] to 2.9 ev[13]. Likewise, several values have been proposed for the vacancy migration energy for iron. As discussed in Reference 14, these range from high values, 1.2-1.4 ev, to low values, 0.6~0.8 eV. For E^{SD} = 2.h eV (Table 3), a low value for E_v^m, 0.7 eV, allows higher, and possibly more reasonable, values for γ and S_v^f when r_c^{c*} = 2.5 nm than are possible with E_v^m = 1.2 eV. For higher values of E^{SD}, however, r_c^{c*} = 2.5 nm can be obtained with reasonable values for γ and S_v^f for both E_v^m = 0.7 and 1.2 eV.

The cavity growth rate is dictated by many of the Same parameters as the critical cavity radius. However, the functional forms of the parametric dependences are different. Thus, a comparison Of theoretical and experimental cavity growth rates can be used to advantage. Sets of parametric values that do not give reasonable values for both critical cavity radius and cavity growth rate can be eliminated. with the parameter combinations given in Tables 3 and 4, the bias ranges from 0.05 to 0.4 when r_c^{c*} = 2.5 nm, with the lowest biases possible only when E^{SD} = 2.9 eV. If the Cavity growth rates indicated by the calculations are assumed to apply for the entire irradiation time up to 30 dpa, a growth rate of 0.62 nm/dpa (bias of 0.41 yields a cavity diameter of 37 nm, a radial growth rate of 0.38 nm/dpa (bias of 0.2) yields a Cavity diameter of 23 nm, and a growth rate of 0.17 nm/dpa (bias of 0.1) yields a cavity diameter of 11 nm. while the above assumption fails to consider the larger growth rates for small cavities and the variation in the sink strength with dose, the purpose of the above calculation is only to obtain an order of magnitude estimate. With this understanding, the growth rate for bias of 0.1 to 0.2 yields a cavity diameter close to the average Cavity diameter of 15.2 nm found experimentally. Therefore, it Seems that a bias of $\leq$0.2 may be more valid for Fe-10% Cr than a bias of 0.4. A bias of 0.2 is also in approximate agreement with the net bias suggested by Sniegowski and Wolfer[15] for ferritic alloys. Based on vacancy and interstitial relaxation volumes, they calculated that the net bias is 0.2 to 0.28 for Cavity radii of 2 nm to 50 nm, respectively. Sniegowski and Wolfer define the net bias, B(r), as a function of the cavity radius, as

$Z_i^d/Z_v^d - Z_i^c(r)/Z_v^c(r)$. To compare this bias to the net bias term used in this study, it is only necessary multiply $^{\sim}B(r)$ by $Z_v^d Z_v^c(r)$. For $Z_v^d \approx Z_v^c(r) \approx 1$, a good approximation for cavities with r>2 nm, the values for the bias can be directly compared. The bias suggested by both of these studies is relatively low, which results in a low cavity growth rate. as discussed above. Thus a low bias could be responsible for the low swelling rates for the ferritic alloys.

At this pint, a brief discussion of the impact of the value of f, the defect survival fraction, on the calculations is relevant. In the calculations presented here, f was assumed to be 0.5. If a lower value is assumed, e.g. f = 0.2, r_c^{c*} = 2.5 nm cannot he calculated for E^{SD} = 2.6 eV unless $\gamma < 0.5$ J/m^2 and $S_v^f < 0.5$ k. with f = 0.2 and $E^{SD} \geq 2.8$ eV, r_c^{c*} = 2.5 nm can be calculated with $S_v^f \approx 1.5$ k and $\gamma \geq 1$ J/m^2. With this lower value for f, the radial growth rates are lower than those reported for calculations with f = 0.5. Comparison of the calculated and experimental radial growth rates Suggests that a bias of 0.2 to 0.3 is most reasonable with f = 0.2.

The value for r_c^{c*} determined experimentally for Fe-10% Cr, 2.5 nm, is Similar to values for r_c^{c*} reported for some austenitic materials; for nickel-ion irradiation of specimens preinjected with helium, a minimum critical radius of ~3 nm is reported for PE16 irradiated at 898 K[6] and a value of ~5 nm is reported for a Fe-Cr-Ni ternary alloy irradiated at 948 K.[7] It should be noted, however, that, for the Same fundamental parameters and sink strengths, the calculated value for r_c^{c*} would be about an order of magnitude higher (~25 nm) for Fe-10% Cr if the irradiation temperature had been 950 K, the peak swelling temperature for ion-irradiated austenitic alloys, rather than 850 K, the peak swelling temperature for ion-irradiated €e-10% Cr.

The cavitational swelling reported in the studies of the austenitic materials is much higher than the swelling observed in Fe-10% Cr. For example. a 2.7% swelling was observed in PE16 after 30 dpa[6] compared to the 0.2% swelling reported here for Fe-10% Cr. After 40 dpa, the swelling in the Fe-Ni-Cr alloy. a low swelling austenitic alloy, was 1.17%.[7] The swelling differences may be related to the values for Q, the ratio of the dislocation sink strength to the cavity Sink strength, for the materials. while the Cavity sink strengths for all the materials are in the range of 1.2 to 5 x 10^{14} m^{-2}, the dislocation sink strengths vary from 10^{14} – 10^{15} m^{-2} for the austenitic materials compared to only 10^{13} m^{-2} for Fe-10% Cr. The corresponding values for Q are ~4.5 for PE16, ~1 for Fe-Cr-Ni, and ~0.02 for Fe-10% Cr. For Q>1, Q~1, and Q>1, the respective swelling is expected to be greater than linear, linear and less than linear in dose.[1] Also, for either Q<<1 or Q>>1 the magnitude of the swelling rate is expected to be low. For Fe-10% Cr, if Q were to be made equal to unity by Somehow increasing the dislocation density, i.e., L ≈ 4.88 x 10^{14} m^{-2}, then for r_c^{c*} = 2.5 nm, the calculated cavity growth rate for r>5 nm is ~10 pm/sec or 2.5 nm/dpa for a bias of 0.05. For this bias and Q ~0.02, the calculated cavity growth rate is ~.06 nm/dpa. Thus, the lower swelling in the Fe-10% Cr may be due, in part, to the low density of the irradiation-produced dislocations, which leads to Q<<1 and consequently to a low swelling rate.

One feature of the experimental results that is not addressed with the present calculations is the observation that the cavity concentration increases after heavy ion bombardment. This Suggests that all of helium/vacancy complexes are not visible after helium implantation and annealing. Further calculations are in progress to derive the cavity distribution observed after irradiation from the pre-irradiation bubble distribution.[16]

2.6 Summary

The major results of this investigation include: 1) A bimodal cavity size distribution was observed in a Fe-10% Cr alloy implanted with 300 appm Helium, annealed and irradiated with 4 MeV Fe^{++} ions at 850 K to 30 dpa. The minimum Critical cavity radius indicated by this distribution is 2.5 nm and is comparable to that reported for ion-irradiated austenitic materials for the peak swelling temperature. 2) Calculations have shown that, while a unique set of fundamental parameters cannot be established based on the present measurement of the minimum critical radius, the bias is ≤ 0.4. Comparisons of both experimental and calculated cavity growth rates, as well as experimental and calculated values of the minimum critical radius, can be used to greatly reduce the number of sets of parameters. This approach suggests that a bias of ~0.2 may be reasonable for ferritic alloys. 3) This experiment also suggests that the low cavity growth rate in Fe-10% Cr is due, in part, to the low irradiation-induced dislocation density (low Q) in addition to the relatively low bias.

Further experiments are clearly necessary to establish better values for the self-diffusion energy, vacancy migration energy, etc., for ferritic alloys. An experiment similar to that reported here with a different irradiation temperature would be expected to reduce the number of possible combinations of values for these

parameters. Similarly. if this experiment was repeated with the same alloy but with a high dislocation density introduced after the bubble population was formed, the explanation for the low swelling rate based on low Q could be tested directly.

2.7 Acknowledgments

The authors wish to thank M. B. Lewis and S. Cook for assistance with the ion irradiations, E. H. Lee and J. M. Vitek for technical discussions, and W. E. Gilliam for manuscript preparation.

3.0 References

1. L. K. Mansur and W. A. Coghlan, "Mechanisms of Helium Interaction with Radiation Effects in Metals and Alloys: A Review," J. Nucl. Mater. 119 (1983) 1-25.

2. J. R. Townsend, "Critical Cavity Sizes in Dual-Ion Bombarded 304SS, Part II: Theoretical," J. Nucl. Mater. 108/109 (1982) 544-549.

3. W. A. Coghlan and L. K. Mansur, "Critical Radius and Critical Number of Gas Atoms for Cavities Containing a Van der Waals Gas," to be published, J. Nucl. Mater.

4. W. A. Coghlan and L. K. Mansur, "The Effect of Microstructure on the Minimum Critical Radius and critical Number of Gas Atoms for Swelling," 12th International Symposium on the Effects of Radiation on Materials, Williamsburg, VA, June 18-20, 1984.

5. V. F. sears, "Kinetics of void Growth in Irradiated Metals," J. Nucl. Mater. 39 (1971) 18-26.

6. D. J. Mazey and R. S. Nelson, "Observations of Bubble-void Transition Effects in Nickel Alloys," J. Nucl. Hater. 85/86 (1979) 1127.

7. E. H. Lee and L. K. Mansur, "Evidence for a Mechanisms of Swelling Variation with Composition in Irradiated Fe-Cr-Ni Alloys," this report.

8. L. L. Horton, "A Transmission Electron Microscope Study of Fusion Environment Radiation Damage in Iron and Iron-Chromium Alloys," ORNL/TM-8303 (July 1982).

9. L. L. Horton, J. Bentley, and W. A. Jesser, "The Depth Distribution of Displacement Damage in α-Iron under 'Triple-Beam' Ion Irradiation," J. Nucl. Mater. 103/104 (1981) 1343-1348.

10. N. V. Tsederberg et. al, "Thermodynamic and Thermophysical Properties of Helium," (Keter Press, Jerusalem, Israel, 1971) p. 18.

11. J. E. Murr, Interfacial Phenomena in Metals and Alloys, (Addison-Wesley Publishing Co., Reading, Mass, 19751 p. 183.

12. D. W. James and G. M. Leak. Phil. Hag. 14 (1966) 701.

13. G. Hettich, H. Mehrer, and K. Maier, "Self-diffusion in Ferromagnetic-Iron," Scripta Met. 11 (1977) 795-802.

14. Papers included in Yamada Conf V Proceedings, "Point Defects and Defect Interactions in Metals," ed. by J. Takamura, M. Doyama, and M. Kiritani (U. Of Tokyo Press, 1982).

15. J. J. Sniegowski and W. G. Wolfer, "Bias in Ferritic and Austenitic Alloys," to be published in Ferritic steels in Nuclear Technologies, ed. by J. W. Davis and D. J. Michel (AIME, Warrendale, PA).

16. D. Fainstein Pedraza, unpublished work.

EVIDENCE FOR A MECHANISM OF SWELLING VARIATION WITH COMPOSITION IN IRRADIATED Fe–Cr–Ni ALLOYS*

E. H. Lee and L. K. Mansur (Oak Ridge National Laboratory)

1.0 Abstract

irradiations with 4 MeV Ni ions and 200–400 kev He ions were carried out on two alloys, Fe-15Cr-15Ni and Fe-15Cr-35Ni, at 675°C and doses up to 84 dpa. Both dual-ion irradiation experiments and sequenced He injection-anneal-Ni irradiations were used. The dual-ion experiment showed that the two alloys exhibited large differences in microstructural development, with the low nickel alloy having significantly greater swelling. The injection-anneal-irradiation experiment was designed to test the hypothesis, suggested by our earlier work, that the lower swelling of the high nickel alloy may result from a larger critical radius/critical number of gas atoms required to achieve bias driven swelling. This experiment provided a direct measurement of these critical quantities by the induction of a bimodal Cavity size distribution. The measurement gave minimum critical radii of about 5 nm for the high nickel alloy and t0.5 nm for the low nickel alloy, values consistent with the hypothesized mechanism. The basis of this difference in critical quantities was further investigated. Evidence suggests that interstitial absorption at interstitial type dislocation loops is significantly more difficult in the high nickel alloy.

2.0 Introduction

Austenitic Fe–Cr–Ni ternary alloys are the basis of stainless steels and related alloys for structural materials both in fast reactors and in designs for fusion reactors, and thus have been the subject of a number of investigations. Johnson et al.[1] performed an extensive characterization of the swelling behavior as a function of composition using 5 MeV Ni-ion irradiation, and found a trend of swelling reduction with increasing nickel or decreasing chromium. Similar observations were made for Fe–Cr–Ni ternary alloys neutron irradiated in the Experimental Breeder Reactor (EBR-II) by Bates and Johnston.[2] Hishinuma et al.[3,4] studied high purity Fe-17Cr-xNi with x=12, 35, 50 wt. % using 1 MeV electron irradiations and found an increasing trend in the dose to the onset of swelling as nickel was increased. Recently Garner and Wolfer,[5] and Garner and Brager[6] presented additional data and reported that swelling rate was insensitive to composition, confirming that the compositional sensitivity resided mainly upon the difference in the period to the onset of swelling.

The question of the mechanism(s) underlying this compositional Sensitivity is a long standing and important one. A number of studies have been made to shed light on this question. Changes in the diffusional properties of the alloying elements with composition have been studied in relation to swelling.[7-9] Changes in overall shear modulus with composition have also been correlated with swelling behavior.[10] The effects on swelling of local changes in elastic or diffusional properties around sinks, which are induced when solute Segregation changes the local composition with reference to the bulk average values have been examined in detail over the past several years.[11-15]

The purpose of the present paper is to further investigate the mechanisms for swelling variation with nickel content. The theory of cavity swelling predicts that rapid Swelling occurs only when cavities achieve a critical radius or accumulate a critical number of gas atoms. Our recent work in this area has led us to the hypothesis that the proximate cause of swelling variation with nickel content may be a dependence of the Critical quantities on nickel content. Higher nickel alloys would require larger critical cavity Size and critical numbers of gas atoms, and thus should begin swelling later in dose. Experiments have been carried out to measure critical cavity sizes. The results are consistent with the proposed hypothesis. Further microstructural evidence is discussed regarding the basis of the variation in critical quantities.

*Research sponsored by the Division of Materials Sciences, U.S. Department of Energy, under contract DE-AC05-84OR21400 with Martin Marietta mergy Systems, Inc.

3.0 Background

3.1 Theory

A well known result of the theory of cavity formation is that rapid cavity growth can begin only when a cavity surpasses a critical radius.[16-24] The critical radius depends on the number of gas atoms contained in the cavity, as well as on materials properties and irradiation conditions. The theory has been reviewed and further developed with respect to applications in the present context by Mansur and Coghlan.[16] For a number of contained gas atoms, n_g, the cavity will reside at a stable radius $r_c^s(n_g)$, and the corresponding critical radius that must be achieved for bias-driven growth is $r_c^c(n_g)$. Fluctuations in size occur about r_c^s by stochastic clustering processes. The cavity tends to return to r_c^s after any fluctuation unless an upward fluctuation leads to a size above r_c^c, after which the cavity will grow inexorably. As more gas is added, r_c^s increases and r_c^c decreases. When a critical number of gas atoms n_g^* is accumulated, r_c^s and r_c^c meet at what is termed the minimum Critical radius r_c^*. If any more gas is added, the critical radius abruptly disappears and bias-driven growth is ensured. It has been shown that r_c^* is never less than 2/3 of r_c, the Critical radius corresponding to gas-free swelling.[16] Thus, when we refer in general terms to the critical radius without qualification regarding the number of contained gas atoms there is little ambiquity.

Two qualitatively different paths are available therefore for nucleation of bias driven cavities. Fluctuations may take cavities containing various quantities of gas, n_g, from their Stable radius $r_c^s(n_g)$ to their corresponding critical radius $r_c^c(n_g)$, or beyond. Alternatively, enough gas may be absorbed to accumulate n_g^* gas atoms, at which point the critical cavity radius drops from its minimum finite value r_c^* to zero. When this latter path is followed, bias driven growth is ensured. no fluctuations are required. when the critical radius is small, corresponding to cavities containing tens to hundreds of vacancies. the fluctuation path is likely and few cavities may remain to accumulate enough gas to reach Stable sizes that are nearly equal to r_c^*. However. when r_c^* is large, a few nanometers, corresponding to cavity volumes of tens of thousands to hundreds of thousands of vacancies, the situation is different. Cavities must accumulate nearly n_g^* gas atoms, so that r_c^s is nearly equal to r_c^* before appreciable nucleation of bias driven cavities can begin. Fluctuations are ineffective at bridging volumes corresponding to nanometers in cavity radius.

The Occurrence of r_c^s and r_c^c in the theoretical solutions give rise to the expectation of bimodal Cavity size distributions. The cavities in the group of the bimodal at smaller size reside at their r_c^s corresponding to their n_g. The cavities in the group of the bimodal at larger sizes have achieved critical size and continue to grow. In general the upper radius cutoff of the smaller group in the bimodal can be interpreted as a lower limit to the minimum critical radius, r_c^*.

3.2 Experiment Design

Through application of the above concepts it is clear that when a bimodal cavity size distribution is induced by the introduction of gas, a measure of the critical radius can be obtained. A sequenced He injection-anneal-Ni ion irradiation experiment was designed to measure the critical radii in both the high and low nickel alloys. A similar experiment has recently been reported on the ferritic alloy Fe-10%Cr.[25] The object here is to create similar distributions of helium bubbles in each alloy by the injection and anneal steps, Spanning the critical radii in both alloys. Subsequent irradiation should cause the cavity size distributions to split into two parts, with the upper Cutoff of the lower group in each alloy giving a measure of the corresponding critical radius.*

*There is a rearrangement of the distributions under irradiation. If the distribution after annealing consisted of equilibrium bubbles, for example, the equilibrium bubble at the size that would coincide with r_c^* upon irradiation would contain three times (ideal gas) or more (non-ideal gas) as much gas as required for bias driven growth (n_g^*). A much smaller equilibrium bubble would move up to r_c^* upon irradiation. where the relation between the initial equilibrium bubble size and the cavity size at the minimum critical radius upon irradiation is $r_c^{eq} = r_c^*/3^{1/3}$, for ideal gas behavior.[16] During irradiation smaller bubbles may also dissolve by ejecting gas atoms resulting from energetic collisions or disappear by coalescing with other cavities; and by these processes larger bubbles may be promoted to above critical size at the expense of smaller bubbles, consequently reducing the small bubble population.

Figure 1 is a schematic illustration of the expected results from the sequenced experiment that was carried out. The upper plot shows the bubble size distribution after the injection and annealing steps. The initial distribution is shown as the same in both alloys for simplicity. The lower plots show that the distributions break up in the two alloys after irradiation. The resolution limit of the electron microscope is also shown. If the breakup occurs below this size a unimodal cavity size distribution will be observed in that alloy.

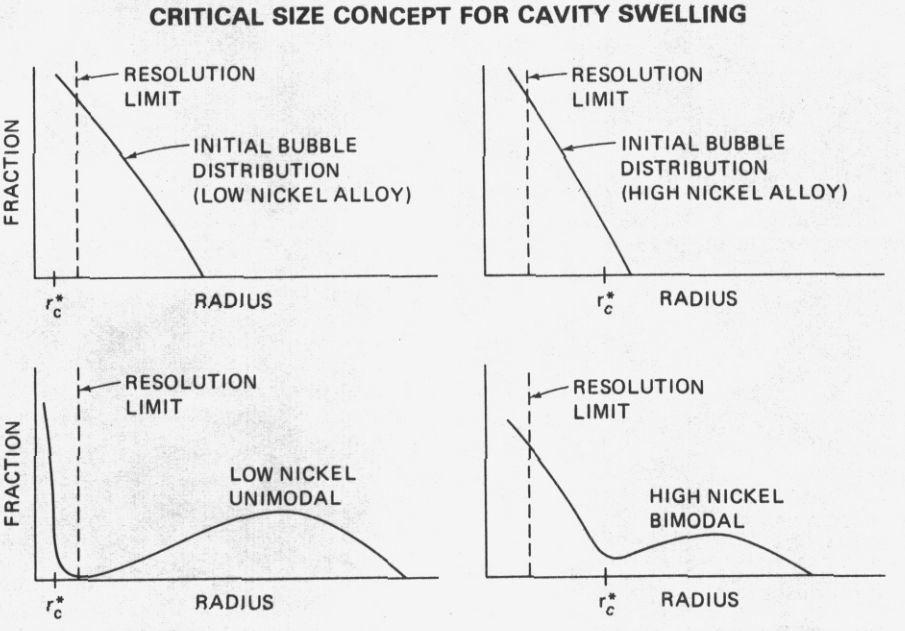

FIGURE 1. Schematic representation of cavity size distribution for small and large r_c^*.

4.0 Experimental

Two ternary austenitic stainless steels, Fe-15Cr-15Ni and Fe-15Cr-35Ni were irradiated in the ORNL van de Graaff accelerator using 4 MeV Ni-ions. Both alloys had impurities at levels less than 0.003 carbon, 0.02 oxygen, and 0.002 nitrogen (weight percent). Two irradiation methods were applied: (1) Ni-ion irradiation simultaneously with helium ions whose energy was ramped between 0.2–0.4 MeV to produce a uniform implantation profile at a ratio of 0.4 appm/dpa, and (2) 400 appm helium implantation followed by one hour aging and subsequent Ni-ion irradiation. All irradiations were performed at 675 C. Specimens were irradiated to doses in the range 1 to 84 dpa. The irradiated disk specimens, 3 mm diameter, were then sectioned to a depth of 0.6 μm from the front surface to expose the peak damage region, and perforated from the back side of the disk to electron transparency. A JEM-120CX microscope with an energy dispersive x-ray detector was used for TEM and microchemical analysis. The details of accelerator facility, sample preparation technique, and Energy Dispersive Spectroscopy (EDS) analysis method were described elsewhere.[26,27,28]

5.0 Results

5.1 Simultaneous Irradiation

The alloys in the solution annealed condition (1038 C/1 h) were irradiated with dual ions at a ratio of 0.4 appm/dpa at 675 C. Figure 2 illustrates the damage microstructures with dose, and Table 1 summarizes the measured data for loops, dislocations, and cavities for the two alloys. An examination of the micrographs revealed a clear disparity in the evolution of dislocation and cavity microstructures between the alloys. In the low nickel alloy, dislocations and cavities developed very rapidly with dose. At 1 dpa, loops were already unfaulted and were developing into network dislocations. Cavity swelling reached 2% at 52.6 dpa. Dislocation density appeared to saturate at a level of 4–5 $\times 10^{13}$ m^{-2}. On the other hand in the high nickel alloy, the evolution of dislocations and cavities was extremely sluggish. Dislocation loops constituted the major feature in the microstructure at 1.0 dpa. The unfaulting of these loops was very slow and some of the remnant loop structure was still visible at 83.5 dpa as shown in Fig. 2. The final dislocation

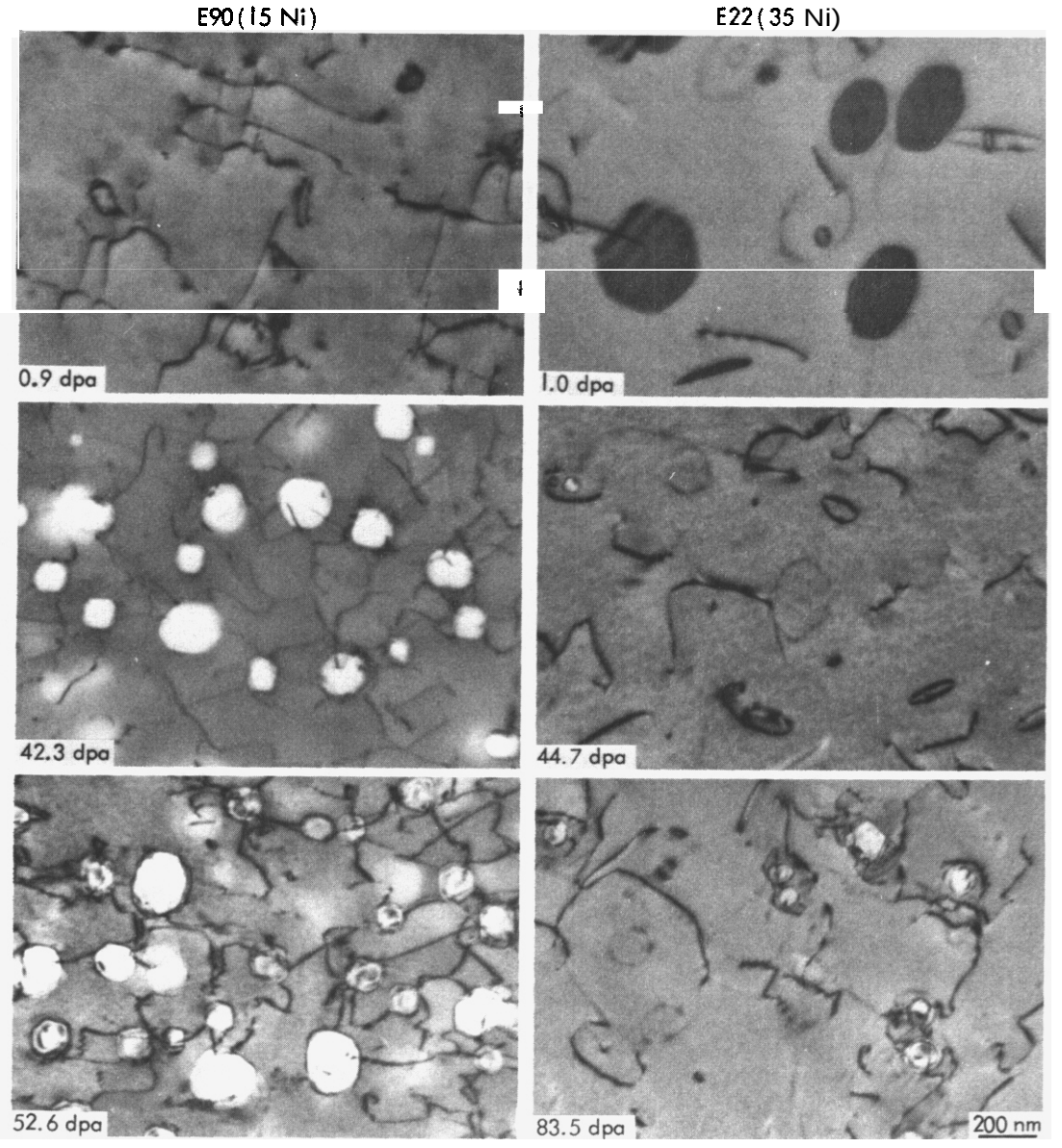

FIGURE 2. Dose dependence of microstructures for 15Ni and 35Ni alloys irradiated with 4 MeV Ni-ions and injected with 0.4 appm/dpa helium at 675°C.

density, however again approached a similar value of 4-5 × 10^{13} m^{-2}. A few cavities were found at 44.7 dpa, but cavity welling was still quite low with a value of 0.5% at 83.5 dpa.

The nature of dislocation loops was determined for a 35 Ni alloy specimen irradiated to 1 dpa. The loop analysis was carried out by using $\bar{g}\cdot\bar{b}$ invisibility criteria and the "inside-outside" contrast method according to the procedure described by Loretto and Smallman.[29] For instance with the FS/RH convention, an interstitial loop has a Burgers vector upward with respect to the plane of the loop and gives a strong outside contrast for $(\bar{g}\cdot\bar{b})>0$ or $(\bar{g}\cdot\bar{b})s_g>0$ when the deviation parameter, s_g is taken as positive. Changing the g direction only then gives a weak inside contrast with $(\bar{g}\cdot\bar{b})s_g<0$ condition. Some of these examples are depicted in Fig. 3, and the results of the detailed analyses of the loops are presented in Table 2. The analysis indicated that all loops were extrinsic (interstitial) in nature. The faulted loops had b=a<111>/3 displacement vectors and the unfaulted loops had b=a<110>/2 displacement vectors. Interestingly, loops were found frequently as doublets (Fig. 3) or occassionally as triplets (Fig. 4). These loops were arranged one within the other but were never coplanar. The smaller loops were on alternate {110} planes. Figure 4

TABLE 1

MICROSTRUCTURAL DATA AFTER ION IRRADIATION WITH 0.4 appm/dpa HELIUM INJECTION

		Loop		ocation	Cavity		
Alloy	dpa		Diam	Density m^{-2}	Density m^{-3}	Diam nm	Swelling %
E90	0.9	---	---	2.7×10^{13}	---	---	---
(15 Ni)	42.3	---	---	6.1×10^{13}	2.6×10^{19}	87	1.1
	52.6	---	---	4.3×10^{13}	4.5×10^{19}	86	2.0
E22				---	---	---	---
(35 Ni)				5×10^{13}	3×10^{18}	20	0.001
	83.5	---	---	4.7×10^{13}	1.2×10^{19}	77	0.5

TABLE 2

RESULTS OF BURGERS VECTOR ANALYSIS (g•b)

Approx. Zone Axis	[001]			[111]			[112]			[012]	
g / b	$0\bar{2}0$	$\bar{2}20$	220	$0\bar{2}2$	$\bar{2}02$	$20\bar{2}$	$\bar{1}\bar{1}1$	$\bar{2}20$	$\bar{1}31$	$\bar{2}00$	200
a[011]/2	-1	-1	+1	0	+1	-1	0	+1	-1	0	0
Observed	S	S_i	S_o	W	S_o	S_i	W	S	S	W	W
a[$\bar{1}$01]/2	0	+1	-1	+1	+2	-2	+1	+1	0	+1	-1
Observed	W	S_o	S_i	S	S	S	S	S	W	S_o	S_i
a[101]/2	0	-1	+1	+1	0	0	0	-1	+1	-1	+1
Observed	W	S_i	S_o	S	W	W	W	S	S	S_i	S_o
a[1$\bar{1}$0]/2	+1	0	0	+1	-1	+1	0	-2	+2	-1	+1
Observed	S	W	W	S	S_o	S_i	W	S	S	S_o	S_i
a[$\bar{1}$11]/3	-2/3	0	0	0	+4/3	-4/3	+1/3	+4/3	-1	+2/3	-2/3
Observed	S	W	W	W	S_o	S_i	S	S	S	S_o	S_i
a[1$\bar{1}$1]/3	+2/3	0	0	+4/3	0	0	+1/3	-4/3	+5/3	-2/3	+2/3
Observed	S	W	W	S	W	W	S	S	W	S_i	S_o

W = weak or invisible
S = strong or medium
i, o = inside, outside

illustrates the spatial arrangement. The loops were imaged by tilts of 55 degrees along the tilt axis shown on the micrographs. Surprisingly, most larger loops (~200 nm diameter) were still faulted with the faults on $\{111\}$ planes, while almost all smaller secondary loops (~50 nm diameter) were already unfaulted with the loops on $\{110\}$ planes.

Energy dispersive X-ray spectroscopy (EDS) analysis was also carried out to investigate the local compositional changes during microstructural evolution. The results showed that nickel was enriched at loops and around cavities. Figure 5 shows the relative Fe, Cr, and Ni peak heights at matrix, loop, and cavity regions after 83.5 dpa irradiation of the 35 Ni alloy. Similar nickel enrichment was observed around cavities in the 15 Ni alloy, Fig 6. Although the absolute peak height of nickel around the cavity appeared to to be higher in the high nickel alloy than in the low nickel alloy, the actual extent of nickel segregation around cavities in the alloys could not be determined because of the varying matrix contribution from the foil.

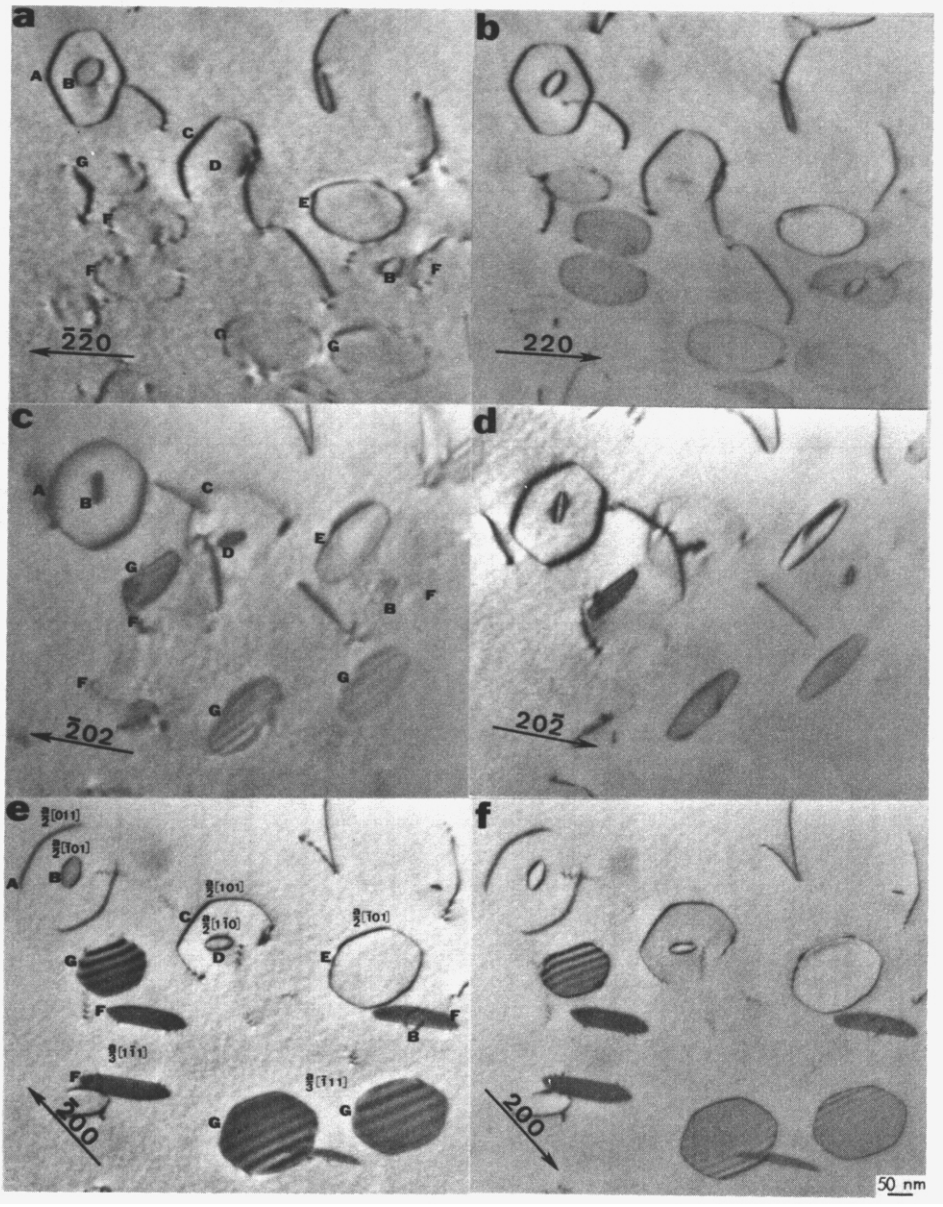

FIGURE 3. Selected micrographs used in Burgers vector analysis of dislocation loops in 35Ni alloy. Irradiation conditions are the Same as Fig. 2. (a) $\bar{g}$ = [$\bar{2}\bar{2}$0], B~[001], (b) $\bar{g}$ = [220], B~[001], (c) $\bar{g}$ = [$\bar{2}$02], B~[111], (d) $\bar{g}$ = [20$\bar{2}$], B~[111], (e) g = [200], B~[012], and (f) $\bar{g}$ = [200], B~[012].

5.2 Sequenced Irradiation

Helium was implanted to a level of 400 appm during a one hour period at 675 C, and the specimens were then aged for an additional hour at 675 C prior to ion bombardment, to coarsen a bubble microstructure. TEM examination of as-implanted and aged samples revealed that bubble distributions were uniform and their densities were also similar for both alloys, being in the range 3 to 5 × 10^{21} m^{-3}, Fig. 7. However, the average bubble diameter in the 15Ni alloy was ~7.5 nm, about 50% larger than that of the 35Ni alloy (~4.9 nm), Table 3. About 0.03 dpa displacement damage was produced by helium implantation, which led to dislocation loops in both alloys. However the loop density and size was different in the two alloys. In the low nickel alloy, the loop density was ~5 × 10^{19} m^{-3} with an average diameter of 30 nm. The high nickel alloy showed only a few large loops (~100 nm dia.), whose density was estimated to be less than 1 × 10^{18} m^{-3}.

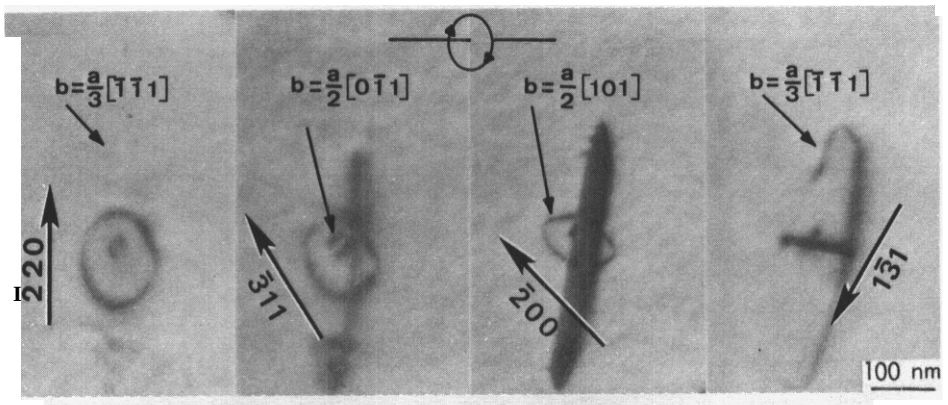

FIGURE 4. Micrographs showing the sequence of image changes of triple loops during tilt of 55° along the tilt axis shown. The loops are nested but not coplanar. Irradiation conditions are the same as Fig. 2.

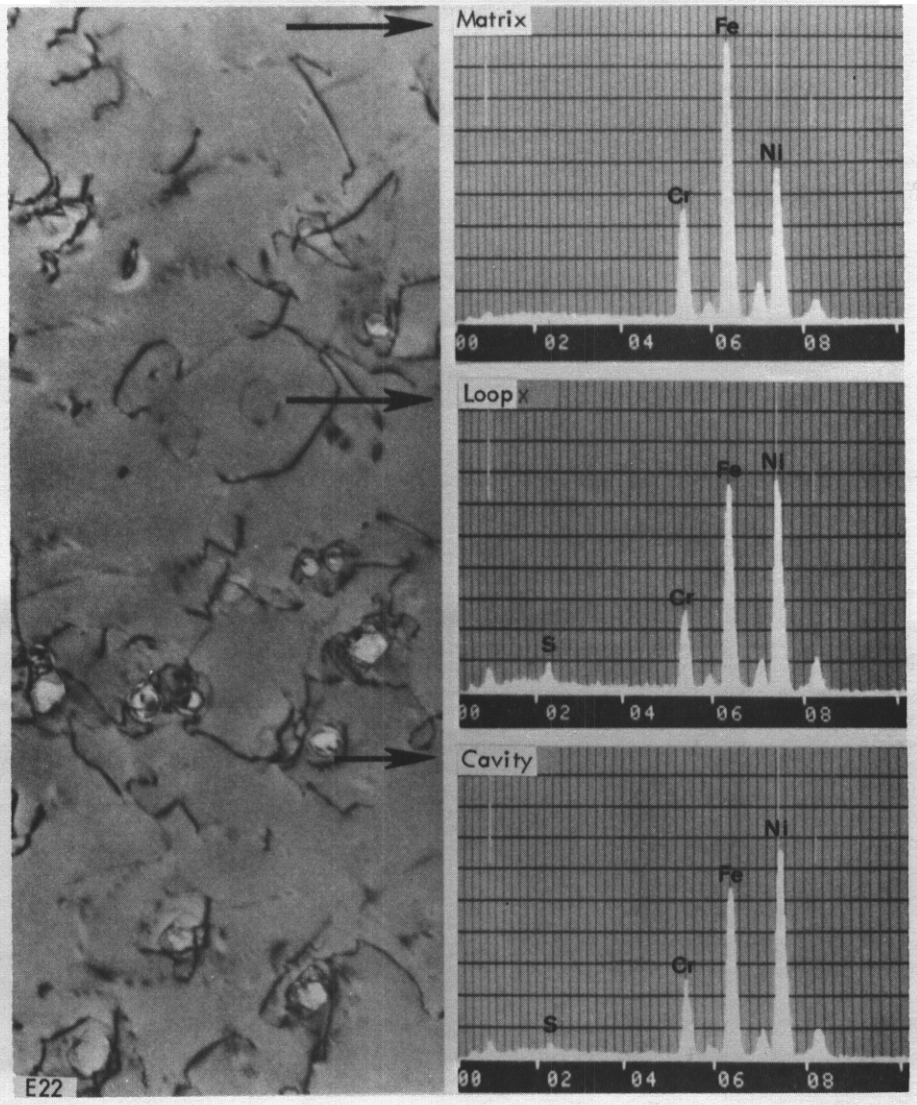

FIGURE 5. EDS analysis of chemical composition at matrix, loop, and cavity in 35Ni alloy irradiated to 83.5 dpa. Irradiation conditions are the same as Fig. 2.

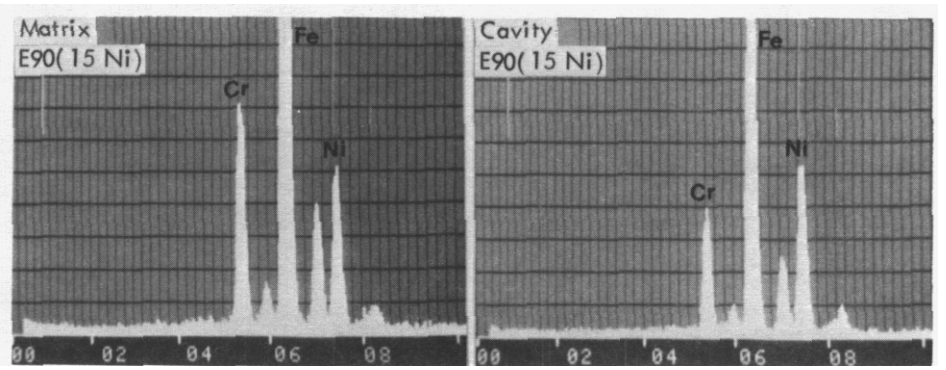

FIGURE 6. EDS analysis of chemical composition at matrix and cavity in 15Ni alloy irradiated to 52.6 dpa with 0.4 appm/dpa helium injection rate at 675°C.

TABLE 3

MICROSTRUCTURAL DATA AFTER ION IRRADIATION WITH 400 appm HELIUM PREINJECTION

Alloy	Fluence dpa	Loop Density m^{-3}	Loop Diam nm	Dislocation Density m^{-2}	Bubble Density m^{-3}	Bubble Diam nm	Cavity Density m^{-3}	Cavity Diam nm	swelling %
E90	0.03*	5×10^{19}	30	---	3.4×10^{21}	7.5	---	---	---
(15Ni)	15.0	---	---	1.3×10^{14}			5.3×10^{20}	37.1	1.63
	39.4	---	---	1.0×10^{14}			5.4×10^{20}	36.8	1.71
E22	0.03*	$<1\times10^{18}$	~100	---	4.8×10^{21}	4.9	---	---	---
(35Ni)	24.1	---	---	2.1×10^{14}	1.8×10^{21}	4.0	2.3×10^{20}	28.9	0.38
	40.6	---	---	1.2×10^{14}	1.0×10^{21}	4.4	5.2×10^{20}	32.4	1.19

*Helium only

Although the initial bubble distributions were fairly similar in the two alloys, subsequent Ni-ion irradiation produced striking contrasts in cavity microstructures. In the low nickel alloy, the initial bubble density was 3.4×10^{21} m^{-3}, but these small bubbles disappeared completely during subsequent ion irradiation. After irradiation, only a unimodal cavity size distribution was observed, as shown in Fig. 8(a). Cavity density saturated at a value of 5.3×10^{20} m^{-3} at 15 dpa, an order of magnitude lower than the initial bubble density. The cavity swelling rate was more rapid at the beginning but slowed down as dose increased: 1.63% cavity swelling at 15 dpa increased to only 1.71% at 39.4 dpa. In the high nickel alloy, however, the bubble density decreased gradually but not completely as cavities developed, thus leading to a bimodal size distribution. Figure 8(b) shows the distribution after 40.6 dpa. The upper cut-off diameter of the small size group is seen to be about 10 nm. Cavity swelling was 0.38% at 24.1 dpa and 1.19% at 40.6 dpa, thus exhibiting a rather sharp increase. The growth was apparently not too different in the two alloys for cavities above the critical size.

In both alloys, the final cavity density approached 5×10^{20} m^{-3} and the dislocation density approached 1×10^{14} m^{-2}, irrespective of composition. Both cavity and dislocation densities were higher than those of the irradiation with simultaneous helium injection, hinting that the initial high density of bubbles may have affected the microstructural evolution in the implanted specimens.

6.0 Discussion

When the Fe-15Cr-15Ni and Fe-15Cr-35Ni alloys were irradiated with simultaneous helium injection, it was found that the 35Ni alloy was more resistant to swelling. The lower swelling was primarily a result of a

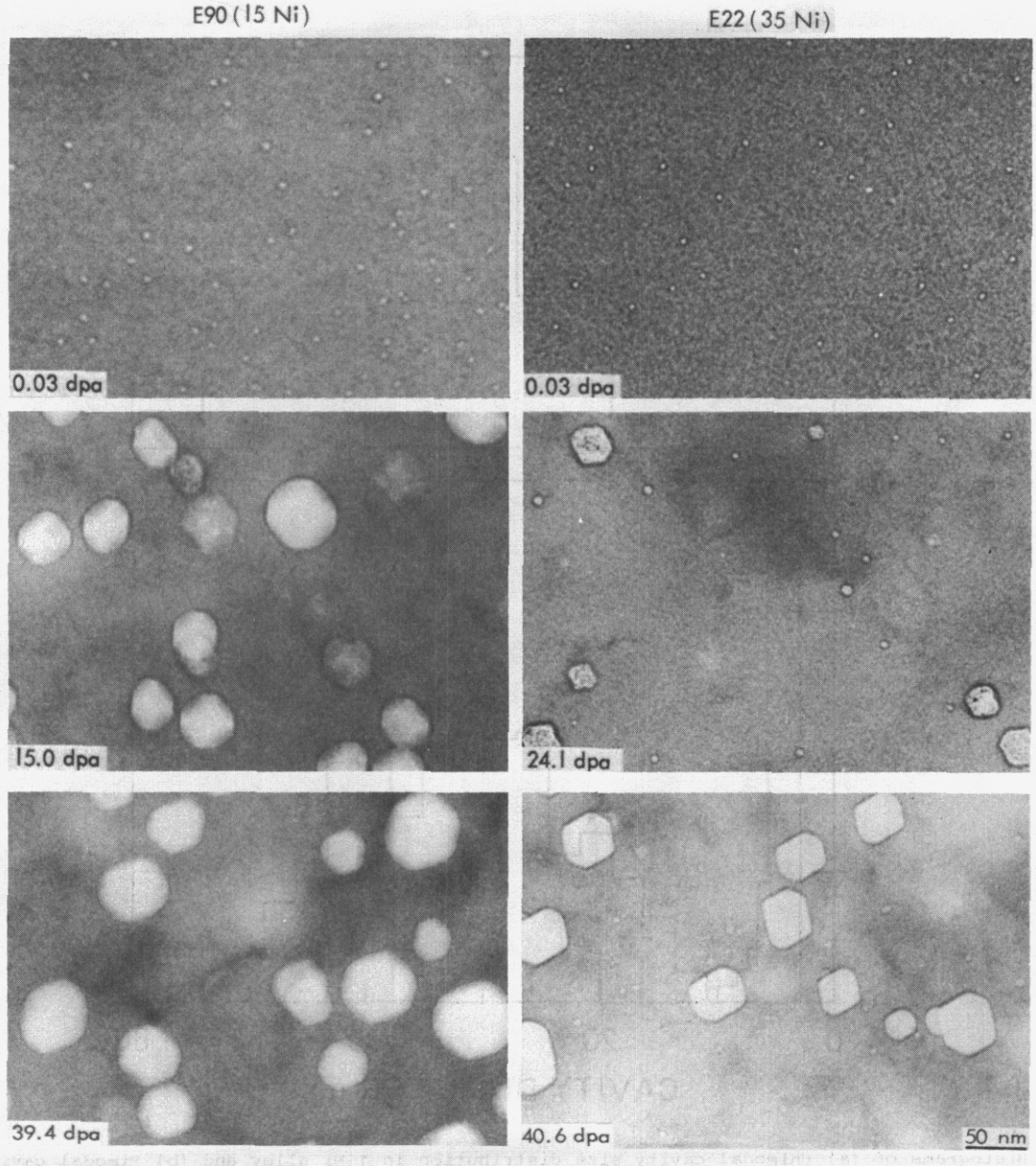

FIGURE 7. Dose dependence of microstructures for 15Ni and 35Ni alloys implanted with 400 appm helium a aged for 1 h at 675°C (top) and 4 MeV Ni-ion irradiated at 657°C to two subsequent doses (m and bottom).

longer interval to the onset of swelling, in agreement with earlier work.[1-6] In Ref. [2] it was repor that increasing nickel increased this transient period. This was also the result of Ref. [5] where it also reported that the swelling rate was essentially independent of composition at high dose, achievi rate of about 1%/dpa. No microstructural data was reported in either case, however. The present resu show that in the high nickel alloy of the present experiments this long transient period was characte by slow faulted interstitial loop growth, and an absence of network dislocation evolution. The low ni alloy began swelling much earlier and the dislocation evolution also began very early. The helium injection-anneal-irradiation experiment was designed to investigate the possibility that this delay wa associated with a much larger critical number of gas atoms (critical radius) for bias driven growth i high nickel alloy. The minimum critical radius was measured, by the induction of a bimodal cavity si *distribution*, to be about 5 nm in the high nickel alloy. In the low nickel alloy the minimum critica radius could not be measured. It is believed that the reason for this is that it is below the resolut limit of electron microscopy, <1 nm for the present conditions. However, the actual critical radius alloy has yet to be confirmed by other means.

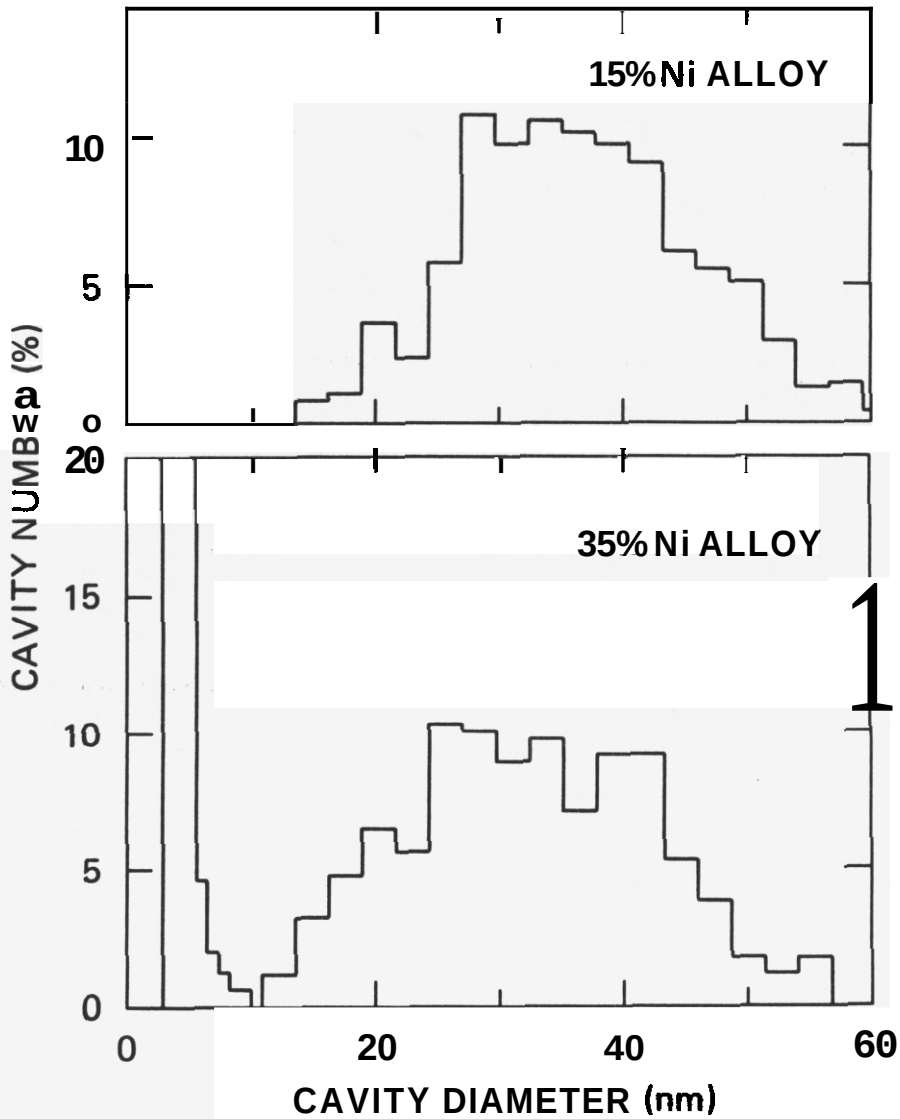

FIGURE 8. Histograms of (a) Unimodal cavity size distribution in 15Ni alloy and (b) Bimodal cavity size distribution in 35Ni alloy after ~40 dpa irradiation in sequenced heium injection-annealing-irradiation experiment.

The experimental results are consistent with the hypothesis that the proximate cause of the difference in the swelling behavior of the two alloys is that the minimum critical radii, and correspondingly the critical number of gas atoms necessary for bias driven swelling, differ by a large factor. The measured critical radius of 5 nm in the high nickel alloy in the sequenced irradiation corresponds to a critical number of gas atoms of 1.1×10^4 (Ref. 16), or 560 appm. Using these figures directly, and based on the cavity density at high dose in the simultaneous experiment, swelling should have begun when each cavity accumulated 1.1×10^4 gas atoms corresponding to a dose of 15 dpa at a rate of 0.4 appm per dpa. This is of the same order as the observed result, where swelling was found to begin somewhat below 45 dpa, and reinforces the idea that the high nickel alloy waited to begin swelling until a relatively large value of n_g^* was accumulated. Differences in detail with the sequenced experiment arise because of different sink densities and counting of very small bubbles. The question to be addressed in turn is why the critical radii in the two alloys are so different. We address this by appealing to the theory. Specifically, the derived equation for the minimum critical radius in terms of irradiation and materials parameters can be used to shed light on this question. The exact result for a modified Van der Waals gas[30] can be expressed in the simple exact form[16]

$$r_c^* = \frac{4\gamma}{3f}\left(\frac{3}{2}\frac{1+\delta}{2+\delta}\right), \quad (1)$$

where

$$f = \frac{kT}{\Omega} \ln S, \quad (2)$$

where S is the quantity $(Z_v^c D_v D_v - Z_i^c D_i C_i)/D_v C_v^e$. The symbols are defined as follows: γ is the surface free energy, $\delta \approx \sqrt{1+3\beta}$, where $\beta = Bf/kT$, B is the van der Waals volume exclusion correction, kT has its usual meaning, D is the diffusion coefficient, C is the concentration, C_v is the thermal vacancy concentration and Z^c is the cavity capture efficiency for point defects. The symbols D, C and Z^c are specialized by the subscripts v and i, which denote vacancies and interstitials, respectively. Detailed expressions for these quantities in terms of material and irradiation parameters are given in Ref. [16]. Eq. (1) reveals the sensitivities of the critical radius to all the irradiation and materials parameters that can affect it.

In examining these sensitivities, we have explored physically reasonable ranges for the parameters. From this work it became clear that only a reasonable difference in the bias could change the critical radius so strongly from the low to the high nickel alloy. The bias is defined as $(Z_i^d Z_v^c - Z_v^d Z_i^c)$ and is implicit in S of Eq. (2). Here Z^d denotes the capture efficiency of dislocations for point defects. However. we know that the cavity growth rate also is dictated by some of the same parameters affecting r_c^*, although with different dependencies. We noted from the high dose data that the Cavity growth rate, the swelling rate and the final dislocation densities were not greatly different in the two alloys. Thus, the parameter(s) we select as most likely to exhibit a difference in the two alloys and to have a Sensitive enough dependence to he responsible for the large difference in critical radius in the two alloys, must also give rise to the prediction of relatively little difference in Cavity growth rate. Specifically, the cavity growth rate is directly proportional to bias[16], when Cavities are large enough to render thermal emission unimportant.

We are therefore confronted with an apparent paradox. From the theoretical expression (1), we deduce that the most likely parameter responsible for the difference in critical radius is the bias. Our calculations using Eq. (1) show that to achieve the measured difference requires a difference in bias of a factor of 150. However, this large a difference in bias also produces a factor of change of the Same order of magnitude in the cavity growth rate when the sink densities are the same in both cases. Such a large difference in cavity growth rates was not ohserved. We believe this problem is resolved by reference to the microstructure. At low and moderate doses in the high nickel alloy, when swelling is not occurring, the microstructure is dominated by faulted dislocation loops. At the highest dose in the high nickel alloy, line dislocations are predominant and the material swells readily. In the low nickel allay, line dislocations are predominant at all doses and the material swells readily. We take this correlation as a clue that the long lived faulted loop microstructure in the high nickel alloy may be correlated with low bias, while after evolving after very high dose to a dislocation network, the bias achieves a value necessary for ready swelling.

These deductions are made based on analysis of the experimental data in terms of the theory. There is independent evidence in the microstructure that may be interpreted as an indication of low bias in the faulted loop microstructure. Many observations of double and triple interstitial loops were made in the high nickel alloy, for example, refer to Figs. 3 and 4. If the initial interstitial loop in one of these groups were a good absorber of interstitials, we would expect that interstitiah diffusing into the region would be readily absorbed at the dislocation core of the loop. However, evidently this is not always the case. Some interstitials diffusing into the region nucleate new loops rather than attaching to the original loop. This is a process we would only expect to happen if the interstitiah were attracted by the stress field of the initial loop but upon arriving were not absorbed. This therefore may be regarded as independent microstructural evidence Suggesting that interstitial absorption at the faulted interstitial loops, a process responsible for bias driving Swelling, is difficult in the high nickel alloy.

Having traced the difference in swelling in the alloys to two successively more fundamental causes, we are confronted with yet another underlyinq question of why the dislocation loops in the high nickel alloy are pour absorbers of interstitials. The answer to this is probably beyond the observational capabilities of electron microscopy, as it has to do with the absorption mechanisms of point defects at the dislocation core. Several speculative possibilities suggest themselves. The density of jogs, where defects are preferentially absorbed, may depend on composition. The extreme smoothness of the dislocation loop peripheries

in the very sharp images of the high nickel alloy may lend Some credence to this possibility. The extent of the dislocation core may be different in the two alloys. This possibility is motivated by the fact that stacking fault energy is known to vary with nickel Content. For example, in Fe-18Cr-XNi alloys, it was found that stacking fault energy increased nearly linearly from 0.015 to 0.05 J/m^2 when X increased from 15 to 35.[31] of course, the loops in the Present experiments find themselves in highly nickel rich regions in hoth alloys, as shown by Figures 5 and 6. This consideration must be factored in to any discussion of stacking fault energy dependence on composition. Changes in elastic interactions and local changes of diffusivities of point defects with segregation to loops may also produce large changes in dislocation loop capture efficiencies. Similar results have been demonstrated theoretically for segregation effects on the capture efficiency of cavities.[11—15] Elastic interaction effects rather than changes in diffusivity may be the more important, however. This view is also supported by Rothman et al. bulk diffusion data.[9] They measured partial diffusion coefficients of Fe, Cr, and Ni and found that the diffusion coefficients decreased in the order Cr, Fe, Ni, but that their activation energies for diffusion were invariant between the compositions Fe-15Cr-22Ni and Fe-15Cr-45Ni. They thus concluded that there was no correlation between swelling and the diffusional behavior of the major components. In any case, however, the observed insensitivity of cavity growth to alloy composition at high dose suggests that segregation affected capture efficiencies, at least at that stage, of cavities and dislocations in the two different alloys do not result in substantially different biases.

In examining the influence of physical parameters on the critical radius via Eq. (1), several possibilities that were eliminated as a main underlying cause of the difference between high and low nickel alloys are worthy of discussion. The first is surface energy. As Can be seen from Eq. (1), the critical radius is proportional to the surface energy. Thus to produce the measured result of a factor greater than 3 in critical radius. the surface energy would have to vary by a similar factor. We believe this is unlikely. The Surface energies Of Fe-Cr-Ni base steels and of each of the pure components Fe, Cr, and Ni are all in the same range about 2 J/m^2.[32] A second physical parameter to consider is the vacancy migration energy. It is implicit in S and variations in it have a very strong effect on the point defect concentration and consequently on r_c^*. However, we find that to produce the factor of 10 variation in r_c^* produces a substantial substantial change in the overall importance of point defect recombination. This in turn changes the cavity growth rate substantially. an effect that is absent in the high dose data.

An analysis of point defect retention at the very lowest doses, especially for the sequenced experiment where the injection of helium produces a small displacement dose, shows a major difference between the two alloys even at that stage. At the low doses achieved during He injection, point defects that survive recombination partition mostly to bubbles and interstitial dislocation loops. Thus, the retained defect fraction can be estimated. The number of retained vacancies is given by $N_v = 4\pi r_c^3/3\Omega$ where r_c is the volume averaged bubble radius N_c the corresponding cavity density and Ω is the atomic volume. similarly the number of retained inteestitials is $N_i = \pi r_\ell^2 N_\ell/\alpha$, where r_ℓ is the area averaged loop radius, N_ℓ is the corresponding loop density and α is the area per atom in the platelet. The results at 0.03 dpa give $N_v = 6.4 \times 10^{25} m^{-3}$ and $N_i = 6.1 \times 10^{25} m^{-3}$ for the low nickel alloy and $N_v = 2.5 \times 10^{25} m^{-3}$ and $N_i = 1.4 \times 10^{25} m^{-3}$ for the high nickel alloy. The point defect retention rate was about three times higher in the low nickel alloy. These values correspond to about 2% and 0.7% retention rate in low and nickel alloys, respectively.

7.0 summary

Two types of ion irradiation experiments were performed on the alloys Fe-15Cr-15Ni and Fe-15Cr-35Ni to investigate the mechanisms responsible for the large difference in swelling behavior between the two alloys. The first was a dual-ion irradiation with 4 MeV Ni ions together with 200—400 keV He ions to give a helium implantation rate of 0.4 appm/dpa. This experiment showed that the high nickel alloy swelled substantially less than the low nickel allay. The difference in swelling appears to be mainly in the dose interval to the onset of swelling. Substantial differences in the dislocation Structures were observed. Dislocation loops were unfaulted and forming networks in the low nickel alloy at 1 dpa, while dislocation loop growth and unfaulting were very slow in the high nickel alloy, with loops persisting up to doses of 84 dpa.

The second experiment consisted of sequenced helium injection, annealing, and irradiation. The experiment was designed on the basis of theoretical considerations that show a bimodal cavity distribution should result and that from it a measure of the critical cavity radius can be obtained. The experiment was motivated by the hypothesis that the critical radii and correspondingly the critical number of gas atoms may he Substantially different in the two alloys and that this might explain the different dose intervals to the onset of swelling. In the high nickel alloy, a bimodal was observed while in the low nickel alloy only a unimodal was observed. In the high nickel alloy, the critical radius was measured as 5 nm and in the low nickel alloy it is believed to be <0.5 nm, the resolution limit of electron microscopy used in this study.

It is Concluded that the basis for the different Swelling behavior in the two alloys a large difference in the critical radius and critical number of gas atoms required for bias driven swelling. The underlying cause for this difference in critical quantities has teen investigated using both derived theoretical expressions and analysis of microstructures. It is suggested that a Substantial difference in hias is responsible. In the high nickel alloy, it *appears* that interstitial dislocation loops do not absorb interstitials readily, thus eliminating the possibility of excess vacancy absorption at cavities, while in the low nickel alloy ready absorption is evident. Multiple interstitial loop formation in the high nickel alloy was observed and is taken as evidence of poor interstitial ahsorption at interstitial loops. Several possibilities for the differences in interstitial absorption at interstitial loops are suggested.

8.0 Acknowledgments

We thank Dr. R. W. Powell Of the Hanford Engineering Development Laboratory for Supplying the alloys, Dr. K. Farrell for stimulating discussions, Dr. M. B. Lewis, and Mr. S. W. Cook for accelerator operations, and Wanda Gilliam for typing the manuscript.

9.0 References

1. W. G. Johnston, J. H. Rosolowski, A. M. Turkalo, and T. Lauritzen, J. Nucl. Mater. 54, p. 24, 1974.

2. J. F. Bates and W. G. Johnston, Proc. AIME Conf. on Radiation Effects in Breeder Reactor Structural Materials, Scottsdale, AZ, June 1977, p. 625.

3. A. Hishinuma, Y. Katano, and K. Shiraishi, J. Nucl. Sci. Technol. 15(9), p. 690, 1978.

4. A. Hishinuma, Y. Katano, and K. Shiraishi, J. Nucl. Mater. 103&104, p. 1063, 1981.

5. F. A. Garner and W. G. Wolfer, J. Nucl. Mater. 122&123, p. 201, 1984.

6. F. A. Garner and H. R. Rrager, to be published in Proc. of ASIM Meeting, Williamsburg, VA. June 1—20, 1984.

7. H. Venker and K. Ehrlich, J. Nucl. Mater. 60, p. 347, 1976.

8. A. D. Marwick, J. Phys. F: Metal Phys. 8, p. 1849, 1978.

9. S. J. Rothman, L. J. Nowick, and G. E. Murch, J. Phys. F: Metal Phys. 10, p. 383, 1980.

10. J. F. Bates, J. Nucl. Mater. 87, p. 409, 1979.

11. L. K. Mansur and W. G. Wolfer, J. Nucl. Mater. 69/70, p. 825, 1978.

12. W. G. Wolfer and L. K. Mansur, J. Nucl. Mater. 91, p. 265, 1980.

13. Si-Ahmed and W. G. Wolfer, Effects on Radiation on Materials: 11th Conf., ASTM STP 782, p. 1008, Eds. H. R. Brager and J. S. Perrin, 1982.

14. W. G. Wolfer, F. A. Garner, and L. E. Thomas, Effects on Radiation on Materials: 11th Conf., ASTM STP 782, p. 1023, Eds. H. R. Brager and J. S. Perrin, 1982.

15. J. S. Watkins, J. Standring, A. D. Miodowick, and J. H. Gittus, Proc. Int. Conf. on Radiation *Behavior.* of Cladding and Structural Materials for Fast Breeder Reactors, Ajaccio Corsica, p. 123, 1979.

16. L. K. Mansur and W. A. Coghlan, J. Nucl. Mater. 119, p. 1, 1983.

17. V. F. sears, J. Nucl. Mater. 39, p. 18, 1971.

18. G. R. Odette and S. C. Langley, Proc. Int. Conf. on Radiation Effects and Tritium Technology for Fusion Reactors, Gatlinburg, TN, October 1975, CONF-750989, Eds. J. S. Watson and F. W. Wiffen, p. 1-395.

19. M. R. Hayns, M. H. Wood, and R. Bullough, J. Nucl. Mater. 75, p. 241, 1978.

20. J. R. mwnsend, J. Nucl. Mater. 108-109, p. 544, 1982.

21. A. Hishinuma and L. K. Mansur, J. Nucl. Mater. 118, p. 91, 1983.

22. R. Stoller and G. R. Odette, Effects on Radiation on Materials: 11th Conf., ASTM STP 782, p. 275, Eds. H. R. Brager and J. S. Perrin. 1982.

23. K. C. Russell, Acta Metall. 19, p. 753, 1971.

24. J. Katz and H. Wiedersich, J. Chem. Phys. 55, p. 1414, 1971.

25. L. L. Horton and L. K. Mansur, to be published in Proc. of ASTM, Williamsburg, VA, June 18–20, 1984.

26. M. B. Levis. N. H. Packan. G. F. wells, and R. A. Buhl, Nucl. Instr. and Methods, 167, p. 233, 1979.

27. E. H. Lee and A. F. Rowcliffe, Microstructural Science 7, p. 403, 1979.

28. N. J. Zaluzec, Introduction to Analytical Electron Microscopy, Eds. J. J. Hern, J. I. Goldstein, and D. C. JOY, Plenum, New York, 1979, p. 121.

29. M. H. Loretto and R. E. Smallman, Defect Analysis in Electron Microscopy, Chapman and Hall, London, 1975.

30. H. Trinkaus and L. K. Mansur, unpublished, equivalent rearrangement of van der Waals results in Ref. 16.

31. D. Dulien and J. Nutting. Iron and Steel Inst. Spec., Rept. NO. 86, p. 140, 1964.

32. L. E. Murr, Interfacial Phenomena in Metals and Alloys, Addison-Wesley Publishing Co., p. 124, 1975.

AN APPROXIMATE ANALYTICAI. CALCULATION OF PRECIPITATE DISSOLUTION RATE USING A SLOWING DOWN-DIFFUSION THEORY FOR CHARGED PARTICLES*

Philip CHOU and Nasr M. GHONIEM (UCLA)

1.0. Objective

The purpose of this paper is to develop an approximate analytical solution to the calculation of the dissolution rate of precipitates due to collision cascades.

2.0. Summary

The dynamic dissolution of microstructures by radiation induced collision cascades is theoretically calculated. Coupled cascade-slowing down diffusion equations are formulated. The resulting equations are decoupled and analytically solved by using the Neumann series expansion for total particle fluxes. Specific examples illustrating the dependence of precipitate dissolution rate on its size and the incident PKA energy are given. Spatial fluxes and currents of precipitate and matrix atoms are calculated. Dissolution parameters which control the stability of precipitates show that the concept of a modified "escape zone" for preciptate atoms from its surface is a valid representation of the phenomenon. It is shown that, for large precipitates, the dissolution rate is approximately proportional to the incident ion energy and inversely proportional to the precipitate radius.

3.0. Program

Title: Radiation Effects on Structural Materials
Principal Investigator: Nasr M. Ghoniem
Affiliation: University of California at Los Angeles

4.0. Relevant DAFS Program Task/Subtask

Suhtask Group C: Microstructural Characterization, Correlation Methodolgy

5.0. Accomplishments and Status

5.1. Introduction

The evolution of microstructural features during irradiation involves complex physical phenomena. Dynamic, diffusional and microchemical processes cooperate synergisticlly to produce changes in the properties of these features. Atomic diffusional processes can now be adequately modeled by the rate theory of chemical kinetics. Microchemical changes during irradiation are more complex to describe, but can be accounted for hy using chemical thermodynamics. However, the effects of radiation on microstructural features through dynamic collisions is a relatively unexplored area. Neutron collisions with materials create PKA's (Primary Knock-on Atoms) which in turn lead to atomic displacements. Average energy PKA's emerging from collisions with *14* MeV neutrons can cause atomic displacements on the order of a few thousands. It is therefore conceivable that if these displacements lead to the ejection of precipitate atoms into the matrix, precipitates would he unstable under irradiation. Ralance hetween microstructural processes, such as is dissolution due to high energy collision events and re-formation rate by atomic diffusion, eventually control precipitate stability.[1,2]

*Work supported by National Science Foundation Grant CPE 81 11571.

The strength of dynamic dissolution processes can be measured by a dissolution parameter, This can be defined as the ratio of precipitate atomic ejection rate to matrix displacement rate. When this ratio is unity, every displacement of a precipitate atom leads to its permanent implantation into the matrix. This process is, in a way, similar to atomic displacements. However, the energy involved in a dissolution event is much higher than the displacement energy. due to the fact that energies are required for the displacement of precipitate atoms as well as the transport of those atoms into the matrix. Therefore, it is expected that such long-range displacement events are much more difficult as compared to traditional atomic displacement events. In an earlier paper[3], we developed a Monte Carlo computer program, TRIPOS, to study the TRansport of Ions in POlyatomic Solids. The interaction between collision cascades and precipitates was numerically simulated. In this paper, an approximate analytical theory is developed for the study of the dynamic interaction between Primary Knock-On Atoms (PKA's) and microstructural features. A diffusion formulation, derived from transport theory, is given. Coupled particle slowing-diffusion equations are solved by expanding the flux in Neumann series. The dissolution paramter is evaluated based upon an average PKA generated from neutrons at different energies. Finally. an empirical formula for the dissolution parameter is given, together with a comparison with results by Nelson.[4]

5.2. Diffusion-Slowing Down Representation

Consider charged particle balance in differential space $d\vec{r}dEd\vec{\Omega}$ about position $\vec{r}$, energy E, and direction $\vec{\Omega}$. At steady state, by equating losses from leakage elastic collisions, slowing down by electronic interactions, and particle production: the following form of the Boltzmann transport equation is obtained [5,6]:

$$\vec{\Omega}\cdot\nabla\phi(\vec{r},E,\vec{\Omega}) + \Sigma_t(\vec{r},E,\vec{\Omega})\phi(\vec{r},E,\vec{\Omega}) = \frac{\partial[S(\vec{E})\phi(\vec{r},E,\vec{\Omega})]}{\partial E} + \int d\vec{\Omega}'\int dE'\Sigma_s(\vec{r},E'\to E,\vec{\Omega}'\to\vec{\Omega})\phi(\vec{r},E,\vec{\Omega}) + Q(\vec{r},E,\vec{\Omega}) \quad (1)$$

where

$\phi(\vec{r},E,\vec{\Omega})$ = particle angular flux = (particle speed) x (particle number density)

$\vec{\Omega}\cdot\nabla\phi(\vec{r},E,\vec{\Omega})d\vec{r}dEd\vec{\Omega}$ = net rate at which particles are lost from $d\vec{r}dEd\vec{\Omega}$ due to leakage

$\Sigma_t(E)$ = total macroscopic cross section

$\Sigma_t(E)\phi(\vec{r},E,\vec{\Omega})d\vec{r}dEd\vec{\Omega}$ = rate at which particles undergo nuclear interactions in $d\vec{r}dEd\vec{\Omega}$.

$\Sigma_s(E'\to E,\vec{\Omega}'\to\vec{\Omega})$ = differential scattering cross section

$[\int d\vec{\Omega}'\int dE'\Sigma_s(E'\to E,\vec{\Omega}'\to\vec{\Omega})\phi(\vec{r},E',\vec{\Omega}')]d\vec{r}dEd\vec{\Omega}$ = rate at which particles scatter into $d\vec{r}dEd\vec{\Omega}$

$\frac{\partial[S(E)\phi(\vec{r},E,\vec{\Omega})]}{\partial E}d\vec{r}dEd\vec{\Omega}$ = net rate at which particles slow down into $d\vec{r}dEd\vec{\Omega}$ due to Coulomb interactions with electrons.

$S(E)$ = electronic stopping cross section.

For charged particle transport problems such as the slowing down of PKA's in materials, scattering processes are due to nuclear as well as electronic interactions. Nuclear interactions occur mainly by screened Coulomb collisions hetween a moving atom and background atoms. Electronic interactions are of Coulomb type collisions between moving atoms and the background electron cloud. Due to the fact that electronic collisions are highly forward, we were able to replace the electronic inscattering integral in the transport equation by substituting an electronic stopping term for the integral in the transport equation (1).

The previous transport equation has six degrees of freedom; namely, three spatial, one energy and the remainder from velocity direction cosine dependence. Assuming that the angular flux has nearly isotropic distribution, diffusion equations can be derived from the transport equation. Such simplification leads to the elimination of two independent variables (velocity direction cosines) and the reduction af degrees of freedom from 6 to 4. Computer simulations have shown that displacement collisions are isotropic in cascades over most of the energy range. Also PKA sources have isotropic and homogeneous distributions. We will therefore use the simpler diffusion approximation in our attempt to calculate a dissolution parameter. The only independent variables in these equations are space and energy. In order to simplify mathematics, and for the sake of obtaining approximate analytical solutions, we will assume that nuclear scattering is approximately isotropic. However, electronic stopping is highly anisotropic. and we will take account of this by using an average scattering cosine of unity for electronic stopping. Since the PKA Source is spatially isotropic, the error in the assumption of isotropic nuclear scattering is expected to be very small, as is the *case* in neutron transport calculations.[7] The diffusion approximation has the following expression, where the angular dependence is eliminated from the transport formulation:

$$\vec{J}(\vec{r},E) = -\frac{1}{3\Sigma_t}\nabla\phi(\vec{r},E) \qquad (2)$$

$$= -D\,\vec{\nabla}\,\phi(\vec{r},E)$$

where D is the diffusion coefficient, and Σ_t is the total cross section.

$$D = \frac{1}{3\Sigma_t}$$

Ry integrating Equation (1) over $d\vec{\Omega}$ and substituting Equation (2), we obtain

$$-D\,\nabla^2\phi + \Sigma_t\phi = Q + \frac{d}{dE}(S\phi) + \int_0^\infty dE'\Sigma_s(E'\rightarrow E)\phi(\vec{r},E') \qquad (3)$$

where ∇^2 describes spatial diffusion, $\vec{J}$ is the energy current and ϕ is the energy flux.

This equation is strictly valid for monoatomic homogeneous media. For an inhomogeneous polyatomic medium, coupled diffusion equations must be used. Let us consider a precipitate embedded in an infinite matrix, an example is the *carbide* precipitate $M_{23}C_6$ in steel. In order to simplify the treatment, an average atom type will be used to represent the two types of atoms, M and C, in the precipitate. Furthermore, we expand the self atom inscattering term into deflected and recoil terms. We also seperate the recoil terms due to atoms coming from different spatial regions from those due to self atoms. With this coupling between different atonic species and different spatial regions, the analytical solution of equation (3) is still a dificult task. We will invoke here one more assumption for the sake of simplicity, and that is to render the electronic energy loss rate zero, but subsume its effect in a modified diffusion length as evaluated from the Monte Carlo range calculations. The coupled diffusion equations for a precipitate in an infinite matrix are then given below

$$-D_{PP}\nabla^2\phi_p + \Sigma_{tpp}\phi_p = \int\Sigma_{spp}(E'\rightarrow E)\phi_p(E')dE' + \int\Sigma_{spp}(E'\rightarrow E'-E)\phi_p(E')dE' + \int\Sigma_{spm}(E'\rightarrow E'-E)\phi_m(E')dE' + S_p(E) \qquad (4)$$

$$-D_{pm}\nabla^2\phi_m + \Sigma_{tpm}\phi_m = \int\Sigma_{spm}(E'\rightarrow E)\phi_m(E')dE' \qquad (5)$$

$$-D_{mp}\nabla^2\phi_p + \Sigma_{tmp}\phi_p = \int\Sigma_{smp}(E'\rightarrow E)\phi_p(E')dE' \qquad (6)$$

$$-D_{mm}\nabla^2\phi_m + \Sigma_{tmm}\phi_m = \int\Sigma_{smm}(E'\rightarrow E)\phi_m(E')dE' + \int\Sigma_{smm}(E'\rightarrow E'-E)\phi_m(E')dE' + \int\Sigma_{smp}(E'\rightarrow E'-E)\phi_p(E')dE' + S_m(E) \qquad (7)$$

Two subscripts are used for physical parameters in Eq. (4) - (7). "p" *stands* for precipitate and "m" stands for matrix. The first subscript depicts the region where the equation is valid and the second subscript represents the atom type being studied.Equation (4) *is* for the diffusion of precipitate atoms in the precipitate, Equation (5) is for the diffusion of matrix atom in the precipitate, Equation (6) is for precipitate atoms in the matrix, and Equation (7) is for matrix atoms in the matrix. Equations (5) and (6) can not be neglected due to the fact that foreign recoils in the local medium do contribute greatly to the generation of local recoils around the interface. Four boundary conditions are required to solve *for* either matrix or precipitate atom fluxes; these are:

$$\phi(\infty) = \text{finite} \tag{8}$$

$$\phi(\vec{r}_b) = \phi(\vec{r}_b) \tag{9}$$

$$\vec{J}(\vec{r}_b) = \vec{J}(\vec{r}_b) \tag{10}$$

$$\vec{J}(0) = 0 \tag{11}$$

where $\vec{r}_b$ is a vector defining the microstructure surface.

If the mass of precipitate atoms is drastically different from matrix atoms, as is the general case, this can lead to different slowing down behaviors for these atoms. In order to consider mass differences among the interacting particles, slowing down energy ranges will have to be modified and the solution is more complex, as is the case for neutron slowing down in non-hydrogenous media (referred to as Plazec's wiggle)[8]. A good measure for the mass disparity among interacting particles is the kinetic energy transfer factor. A , which describes the maximum fraction of energy that an incident particle of mass M_1 can transfer to a recoil particle with mass M_2. It is defined as

$$A = \frac{4M_1M_2}{(M_1 + M_2)^2} \tag{12}$$

if the masses are the same, A is unity, and if the masses are drastically different, A approaches zero. Also, α , the minimum fraction of energy that an incident particle can emerge with after a collision, is given as

$$\alpha = I - A = \left(\frac{M_1 - M_2}{M_1 + M_2}\right)^2 \tag{13}$$

This factor affects the slowing down energy range; if a equals zero an incident particle can lose all of its energy in a single collision, while for the case a approaches unity it needs a large number of collisions before the incident particle can be slowed down to a small energy. Fortunately, far the case of precipitate $M_{23}C_6$, such as pure molybdenum carbide, in steel, the average mass for precipitate atoms is about 1.5 times that of iron atoms. This gives a A of 0.97 and ana of 0.03. These two parameters are very close to those of the case when precipitate and steel atom have the same mass. Therefore. we can use the formulation of equal masses for this analysis. This can considerably simplify the problem as what is faced in neutron slowing down problem [8].

5.3. Method of Solution: Neumann Expansion

We can solve the coupled diffusion equations by expanding the energy fluxes for precipitate and matrix atoms into a Neumann series of the following form

$$\phi(\vec{r},E) = \sum_{n=0}^{\infty} \phi_n(\vec{r},E) \tag{14}$$

where ϕ_n is the succesive corrections to the zeroth order solution. Each term in the Neumann series expansion has the analogy of collided flux as from transport equations. By applying a Neumann expansion for the fluxes. we can decouple the inscattering integral from the spatial dependence terms. However, a new series of diffusion equations arise as shown below

zeroth order equations

$$-D_{pp}\nabla^2\phi_{p,o} + \Sigma_{tpp}\phi_{p,o} = S_p(E) \tag{15}$$

$$-D_{pm}\nabla^2\phi_{m,o} + \Sigma_{tpm}\phi_{m,o} = 0 \qquad (16)$$

$$-D_{mp}\nabla^2\phi_{p,o} + \Sigma_{tmp}\phi_{p,o} = 0 \qquad (17)$$

$$-D_{mm}\nabla^2\phi_{m,o} + \Sigma_{tmm}\phi_{m,o} = S_m(E) \qquad (18)$$

for n ≥ 1

$$-D_{pp}\nabla^2\phi_{p,n} + \Sigma_{tpp}\phi_{p,n} = \int\Sigma_{spp}(E'\to E)\phi_{p,n-1}(E')dE' + \int\Sigma_{spp}(E'\to E'-E)\phi_{p,n-1}(E')dE' + \int\Sigma_{spm}(E'\to E'-E)\phi_{m,n-1}(E')dE' \qquad (19)$$

$$-D_{pm}\nabla^2\phi_{m,n} + \Sigma_{tpm}\phi_{m,n} = \int\Sigma_{spm}(E'\to E)\phi_{m,n-1}(E')dE' \qquad (20)$$

$$-D_{mp}\nabla^2\phi_{p,n} + \Sigma_{tmp}\phi_{p,n} = \int\Sigma_{smp}(E'\to E)\phi_{p,n-1}(E')dE' \qquad (21)$$

$$-D_{mm}\nabla^2\phi_{m,n} + \Sigma_{tmm}\phi_{m,n} = \int\Sigma_{smm}(E'\to E)\phi_{m,n-1}(E')dE' + \int\Sigma_{smm}(E'\to E'-E)\phi_{m,n-1}(E')dE' + \int\Sigma_{smp}(E'\to E'-E)\phi_{p,n-1}(E')dE' \qquad (22)$$

with the houndary conditions (8-11) applied to each flux component.

In the present analysis, two different geometries for precipitate shapes are considered; namely, plane and spherical. with the corresponding appropriate expression for the operator ∇^2 . The operator for spherical geometry causes some difficulties. Ry a change of variable such as:

$$\phi = \frac{\Psi}{r}, \qquad (23)$$

we obtain similar diffusion equations to those of the planar case with Ψ in place of ϕ . However, the external PKA source term is rQ for spherical geometry rather than Q as for plane geometry.

The solution to the previous set of equations still requires a numerical approach, if complicated nuclear scattering cross-sections are used. Our major objective is to obtain a simple analytical approximation, rather than involved numerical calculations. For this purpose, we will assume the existence of an "equivalent" hard sphere cross-section, that is valid over the entire energy range. It is known that the interaction potential *goes* from nearly pure Coulomb scattering at high energy to a Born-Meyer type interaction potential at low *energies*. In *our* simplified analysis, the "equivalent" hard-sphere cross-section *is* only a model of the entire interaction range. The value of this cross-section is deterimined such that the atomic displacement rate is normalised to the more sophisticated Monte Carlo numerical simulations of our *code TRIPOS* [3]. *Hence,* the results of the present calculations give only "relative" values of dissolution to displacement rates.

For hard sphere nuclear scattering, we have

$$\Sigma_s(E'\to E) = \Sigma(E')/E' \qquad (24)$$

Also in the process of slowing down for PKA's, the total cross section is essentially the same as the scattering cross section, i.e., $\Sigma_s = \Sigma_t$, until the energy falls below a certain energy limit when the slowing down process is terminated and the particle is considered to be absorbed. Also from the fact that precipitate atoms have similar masses and atomic numbers as those of matrix atoms, it follows that they have similar atomic scattering and diffusional behaviors. Therefore, we have

$$\Sigma = \Sigma_{tpp} = \Sigma_{tpm} = \Sigma_{tmp} = \Sigma_{tmm} = \Sigma_{spp} = \Sigma_{spm} = \Sigma_{smp} = \Sigma_{smm} \qquad (25)$$

and

$$D = D_{pp} = D_{pm} = D_{mp} = D_{mm} \tag{26}$$

Equations (19) to (22) can be further simplified by combining the deflected and recoil inscattering terms for self atoms. The simplified diffusion-slowing down equations are:

for $n \geq 1$

in precipitate:

$$-D\nabla^2\phi_{p,n} + \Sigma\phi_{p,n} = 2\int \frac{\Sigma(\vec{r},E')\phi_{p,n-1}(\vec{r},E')dE'}{E'} + \int \frac{\Sigma(\vec{r},E')\phi_{m,n-1}(\vec{r},E')dE'}{E'} \tag{27}$$

$$-D\nabla^2\phi_{m,n} + \Sigma\phi_{m,n} = \int \frac{\Sigma(\vec{r},E')\phi_{m,n-1}(\vec{r},E')dE'}{E'} \tag{28}$$

in matrix:

$$-D\nabla^2\phi_{p,n} + \Sigma\phi_{p,n} = \int \frac{\Sigma(r,E')\phi_{p,n-1}(\vec{r},E')dE'}{E'} \tag{29}$$

$$-D\nabla^2\phi_{m,n} + \Sigma\phi_{m,n} = 2\int \frac{\Sigma(\vec{r},E')\phi_{m,n-1}(\vec{r},E')dE'}{E'} + \int \frac{\Sigma(\vec{r},E')\phi_{n-1}(\vec{r},E')dE'}{E'} \tag{30}$$

for n=0, we don't have the inscattering terms on the right side. However, we have a precipitate source term for Equation (27) and matrix source term for Equation (30).

Let all the PKA's start with energy E_o, using the following transformations,

$$y = r/L \tag{31}$$

$$\epsilon = E/E_o \tag{32}$$

where $L_n = \sqrt{D_n/\Sigma_n}$ is the diffusion length, E_o is the PKA source energy. Equations (27-30) can be rewritten as below (for plane geometry) in dimensionless units,

for $n \geq 1$

$$(y,\epsilon) + \phi \quad (y,\epsilon) = 2\int^1 \frac{\phi_{p,n-1}(y,\epsilon')}{} \qquad 1\,\frac{\phi_{m,n-1}}{} \tag{33}$$

$$-\nabla_y^2\phi_{m,n}(y,\epsilon) + \phi_{m,n}(y,\epsilon) = \int_\epsilon^1 \frac{\phi_{m,n-1}(y,\epsilon')}{\epsilon'}\,d\epsilon' \tag{34}$$

$$-\nabla_y^2\phi_{p,n}(y,\epsilon) + \phi_{p,n}(y,\epsilon) = \int_\epsilon^1 \frac{\phi_{p,n-1}(y,\epsilon')}{\epsilon'}\,d\epsilon' \tag{35}$$

$$-\nabla_y^2\phi_{m,n}(y,\epsilon) + \phi_{m,n}(y,\epsilon) = 2\int_\epsilon^1 \frac{\phi_{m,n-1}(y,\epsilon')}{\epsilon'}\,d\epsilon' + \int_\epsilon^1 \frac{\phi_{p,n-1}(y,\epsilon')}{\epsilon'}\,d\epsilon' \tag{36}$$

For n=0 again, we don't have the inscattering term on the right side of the above four equations, however precipitate source and matrix source terms do exist on the right side of Equations (33) and (36), respectively. The following solutions are obtained for plane and spherical geometries, when the ∇^2 operator is replaced hy its appropriate representation:

Plane Geometry

$$\phi_{p,o} = (d_{p,o} + a_{p,o,o}e^{-y} + b_{p,o,o}e^{y})\ \delta(\varepsilon - 1) \tag{37}$$

$$\phi_{m,o} = (a_{m,o,o}e^{-y} + b_{m,o,o}e^{y})\ \delta(\varepsilon - 1) \tag{38}$$

$$\phi_{p,o} = c_{p,o,o}e^{-y}\delta(\varepsilon - 1) \tag{39}$$

$$\phi_{m,o} = (d_{m,o} + c_{m,o,o}e^{-y})\ \delta(\varepsilon - 1) \tag{40}$$

while for n>0, the following solution is obtained:

$$\phi_{p,n} = [d_{p,n} + \sum_{k=0}^{n} (a_{p,n,k}e^{-y} + b_{p,n,k}e^{y})\ y^k]\ \ln^{n-1}(\varepsilon) \tag{41}$$

$$\phi_{m,n} = \sum_{k=0}^{n} (a_{p,n,k}e^{-y} + b_{p,n,k}e^{y})\ y^k\ \ln^{n-1}(\varepsilon) \tag{42}$$

$$\phi_{p,n} = \sum_{k=0}^{n} c_{p,n,k}e^{-y}\ y^k\ \ln^{n-1}(\varepsilon) \tag{43}$$

$$\phi_{m,n} = [d_{m,n} + \sum_{k=0}^{n} c_{m,n,k}e^{-y}\ y^k]\ \ln^{n-1}(\varepsilon) \tag{44}$$

The solution coefficients, a,b,c and d, for both plane and spherical geometries,, are given in appendix A.

The total precipitate and matrix atom fluxes and currents are the sum of component fluxes and currents for each type over the whole PKA slowing down energy regime, as defined in equation (14).

$$\Phi_{Tot}(\vec{r}) = \int \phi(\vec{r},E')dE' = \sum_{n=0}^{\infty} \int \phi_n(\vec{r},E')dE' \tag{45}$$

$$\vec{J}_{Tot}(\vec{r}) = \int \vec{J}(\vec{r},E')dE' = \sum_{n=0}^{\infty} \int \vec{J}_n(\vec{r},E')dE' \tag{46}$$

The dissolution rate of the precipitate is proportional to the total precipitate atom current that crosses the precipitate surface. And the dissolution parameter, b, can now be calculated as:

$$b = \frac{J_{Tot}A}{V} = \frac{3J_{Tot}}{r_{eq}} \tag{47}$$

where V and A are the volumes and surface area for the precipitate and r_{eq} is the equivalent radius for the precipitate.

5.4. Results

In these calculations, we consider a precipitate of the $M_{23}C_6$ type and the steel matrix is considered to contain iron atoms only. Average atoms are used for the representation of precipitate atoms. In other

words, an average mass and an average atomic number are used to characterize precipitate atoms. In the present method, it is not possible to calculate preferential dissolution rates of precipitate components, as has been accomplished using the Monte Carlo Method [1]. Average PKA's are used in the slowing down-diffusion theory calculations. For instance, the average PKA energy is about 0.5 MeV for the Rotating Target Neuton Source (RTNS) fusion neutrons and 37 keV for fission neutrons. The cutoff energy is taken to be the bulk displacement energy which equals 25 eV. By solving the previous set of coupled equations, precipitate atom fluxes and matrix atom fluxes are obtained throughout the medium. Neumann series of up to 45 terms was found necessary before fluxes would converge.

Figure (1) shows the flux profiles for hoth matrix and precipitate atoms for a plane precipitate with half thickness of 5 diffusion lengths. For the case considered, precipitate and matrix atoms are of similar masses, similar atomic numbers. and same source strength. The combined flux for precipitate and matrix atoms, that is, ϕ_p and ϕ_m is essentially the Same as that for an infinite medium. For more detail on the flux in the infinite medium, the reader is referred to Appendix B at the end of this paper. Figure (1) illustrates that the sum of precipitate and matrix fluxes does converge to the infinite medium flux. Figures (2) and (3) show the fluxes in Neumann series terms. Figure (2) gives the 6^{th} to the 10^{th} term and Figure (3) gives the 31^{st} to the 35^{th} terms. A plane precipitate is considered for the above evaluations. However, it is known that generally precipitates have spherical shapes. Therefore a question arises regarding the validity of plane geometry calculations for spherical precipitates. An "effective radius" for a planar precipitate is calculated by conserving the volume to surface ratio of the precipitate. Let t equal half thickness of the planar precipitate, then the associated effective radius is $3t/2$. Figure (4) shows a comparison of fluxes at the precipitate surface between plane and spherical geometries as functions of equivalent radii. It shows that for large sizes, precipitate fluxes for spherical and planar models are similar while for small sizes, precipitate fluxes for the spherical model are smaller than those for the planar models. However, the physical entity that depicts the dissolution processes is the current that crosses the precipitate surface. The dissolution parameter can be evaluated by using Equation (47) along with the current. The best way to represent the dissolution parameter is to express it as a fraction of the dpa rate. As we know, for very small precipitates, the dissolution rate is essentially equal to the dpa rate. The dissolution parameter can then be normalized to the dpa rate at very small radii. Figure (5) shows a comparison of dissolution parameters between plane and spherical model. The results are about the same for large and small radii and within a difference of 2% for intermediate radii.

In the five figures above, the distance is expressed in units of diffusion length. In order to make the results have experimental significance. it is necessary to measure and convert the diffusion length into real units. A rule of thumb for the diffusion length is that it is about one seventh to one sixth that of the PKA ranges. Our earlier work on the contribution of direct dissolution from the self collision cascade has shown that the direct dissolution parameter peaks for planar precipitate with half thickness corresponding to 6–7 diffusion lengths. The peak corresponds to the ranges of PKA's. Furthermore, expansions for Neumann series of up to about *40* terms are required for the flux calculation to reach convergence. This suggests that it takes about 40 collisions for PKA to slow down if we remember that the n'th term in the Neumann series expansion in diffusion theory corresponds to the n'th collided term from transport theory. This also suggests that 6–1 diffusion lengths correspond to the range of a PKA from random work theory. That is, the square of the travel distance is equal to the number of jumps (collisions) times the square of the jump step (diffusion length). We have therefore taken the diffusion lengths as 1/6.5 of the ranges of PKA's. The ranges of those PKA's are calculated by using a Monte Carlo computing program, TRIPOS (TRansport of Ions in POlyatomic Solids).

Figure (5) shows the dissolution rate as a function of the equivalent precipitate radius. PKA's at different energies have the same slowing down behavior. A group of dissolution parameter curves can be obtained by using the real units in place of diffusion lengths for PKA's at different energies. Figure (6). The figure shows five curves from left to right with PKA energies of 1 keV, 10 keV, 37 keV (fission), 0.2 MeV, and 0.5 MeV (fusion), respectively. By examination of the dissolution parameters plotted in Log-Log scales, it can be observed that the plot has two asymptotic limits, one with zero slope for small precipitates and the other with a slope of –1. The intersection of those two asymptotic lines is at an equivalent radius of about 1.0 diffusion length or, 0.588 diffusion length, to be exact. The ranges of PKA's at different energies calculated by using TRIPOS for Fe on Fe can be approximated by

$$R\ (\text{range}) = 5.3[E(\text{keV})]^{0.911} \tag{48}$$

where R is in the units of angstroms and E is the average PKA energy. And the diffusion length is therefore given

$$L = R\ (\text{range})/6.5 = 0.815E^{0.911} \tag{49}$$

The dissolution parameter, b, can then he empirically given by

$$b \approx 1 \qquad r < 0.588L \tag{50}$$

$$\approx \frac{E^{0.911}}{2r_b} \qquad r > 0.588L$$

where r_b is the radius of the precipitate in angstroms and E is the PKA energy in KeV. The "escape zone" concept proposed by Nelson[4] for resolution of fission gas bubbles in fission environments has the expression as below,

$$b = 1 \qquad r_b < d \tag{51}$$

$$= \frac{r_b^3 - (r_b - d)^3}{r_b^3} \qquad r_b > d$$

where r_b is the bubble radius and d is an empirical escape distance on the order of 15Å .

By examination of equations (50) and (51), it is shown that the original Nelson concept of an "escape-zone" for fission gas huhhles can now be extended to precipitate dissolution. The dissolution rate is approximately linear with incident PKA energy and inversely proportional to the precipitate radius.

6.0. References

(1) Wilkes, P., J. Nucl. Mater., 83, (1979)66.

(2) Nelson. R.S., Hudson, J.A., and Mazey, D.J., J Nucl. Mater., 44, (1972)318.

(3) Chou, P.S., and Ghoniem, N.M., J. Nucl. Mater., 117, (1983)55.

(4) Nelson, R.S., J. Nucl. Mater., 31, (1968)153.

(5) Bartine, D.E., Alsmiller, R.G., Mynatt, F.R., Engle, W.W. and Barish, J., Nucl. Sci. Eng., 48, (1972)159.

(6) Hoffman, J.J., Dodds, H.L., Robinson, M.J., and Holmes, D.K., Nucl. Sci. Eng., 68, (1976)204.

(7) Pomraning, G., UCLA, private communication.

(8) Duderstadt, J.J., and Hamilton, L.J., Nuclear Reactor Analysis, John Wiley & Sons, Inc., NY, 1916, p. 319.

Acknowledgement

Work is supported by the National Science Foundation Grant No. CPE 81 11571 at UCLA. The authors wish to thank Dr. A. Prinja for his critique of the manuscript.

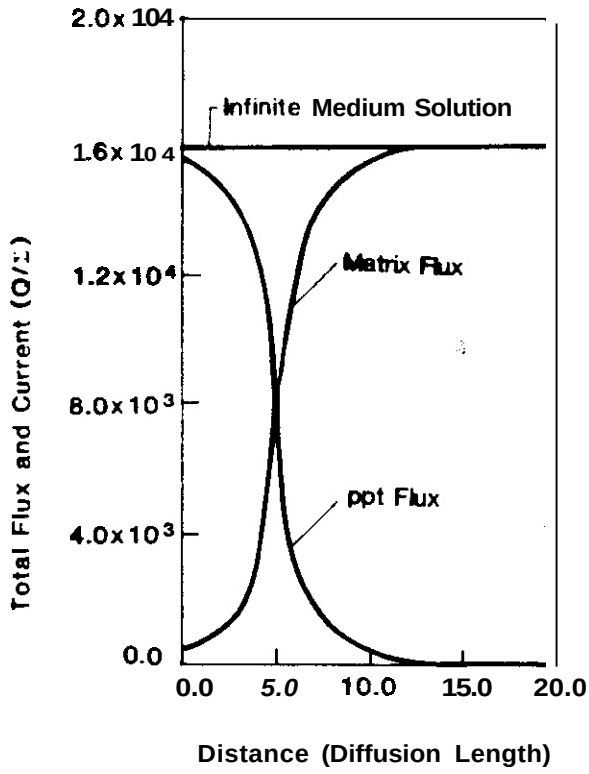

Figure 1. Precipitate (ppt) and matrix fluxes as functions of distance from the center of a slab precipitate with half-thickness equal to 5 diffusion lengths. The sum of precipitate and matrix fluxes converges to the flux for an infinite medium.

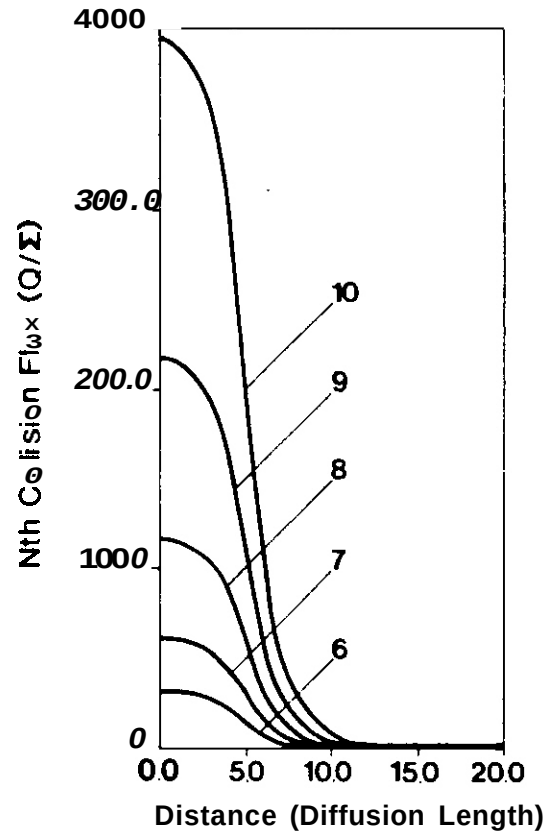

Figure 2. 6^{th} - 10^{th} Neumann expansion collision fluxes as functions of distance from the center of a slab precipitate with half-thickness equal to 5 diffusion lengths.

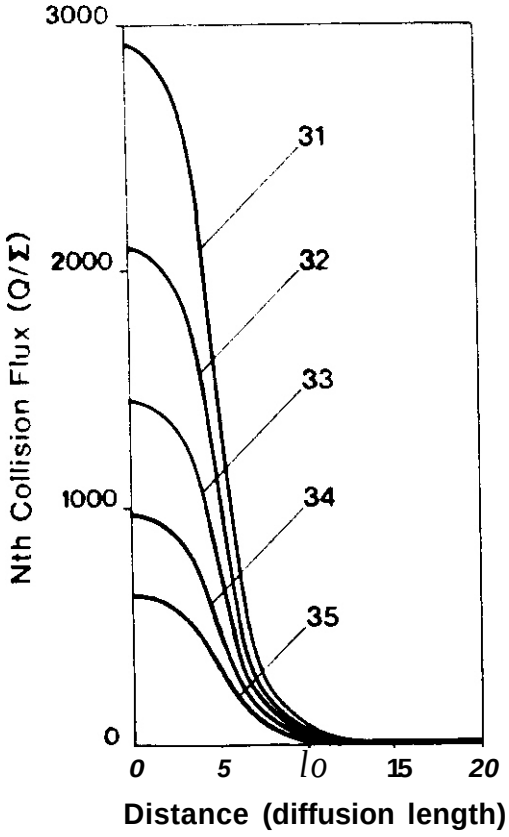

Figure 3. 31^{st} - 35^{th} Neumann expansion collision fluxes as functions of distance from the center of a slab precipitate with half-thickness equal to 5 diffusion lengths.

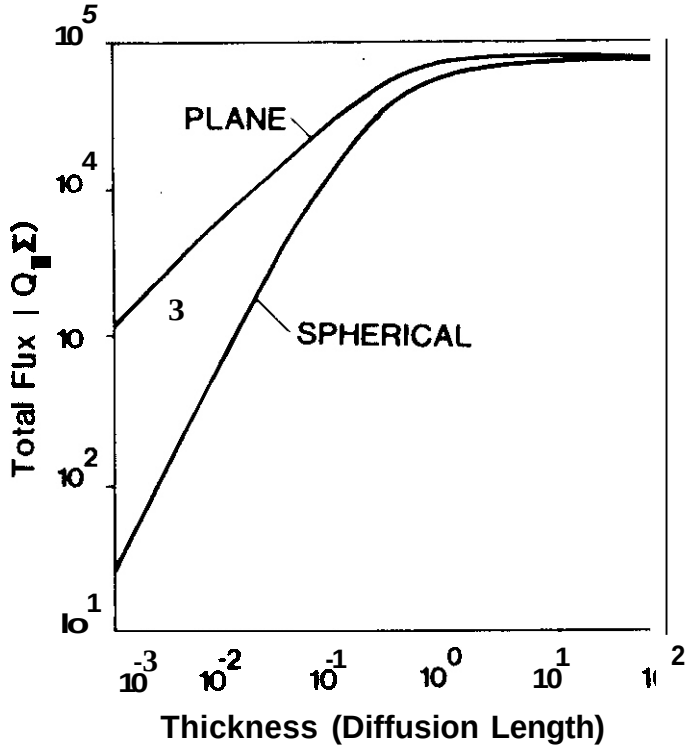

Figure 4. Total fluxes on plane and spherical precipitate surfaces as functions of equivalent precipitate thickness in diffusion lengths.

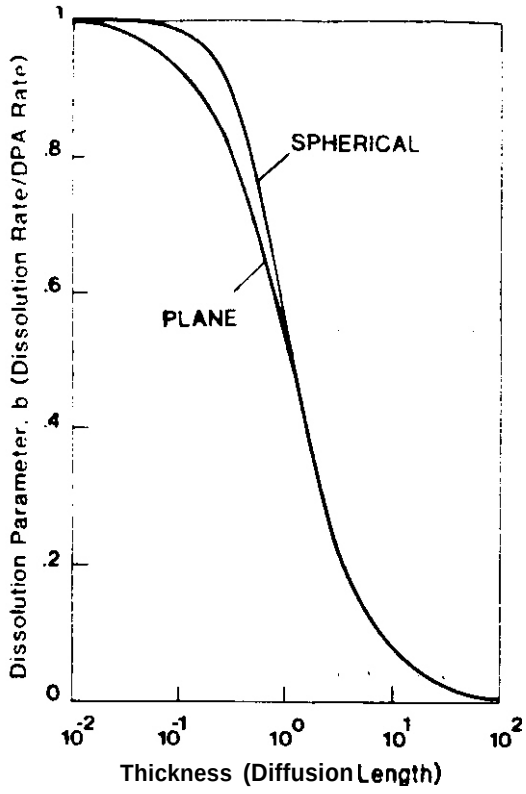

Figure 5. Dissolution parameters for plane and spherical precipitates as functions of equivalent precipitate thickness in diffusion lengths.

Figure 6. Dissolution parameters for different PKA energies a8 a function of precipitate radius in angstroms.

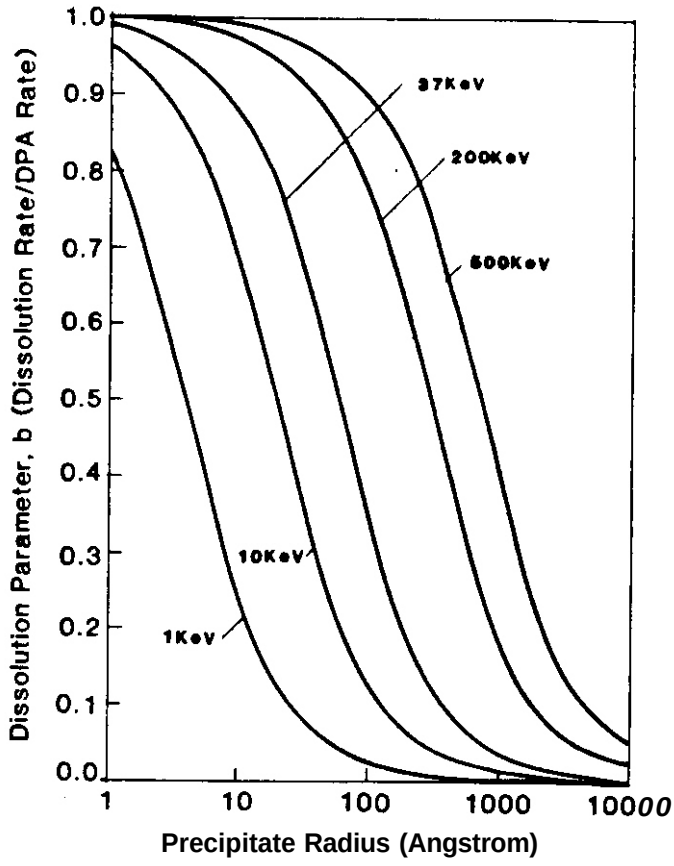

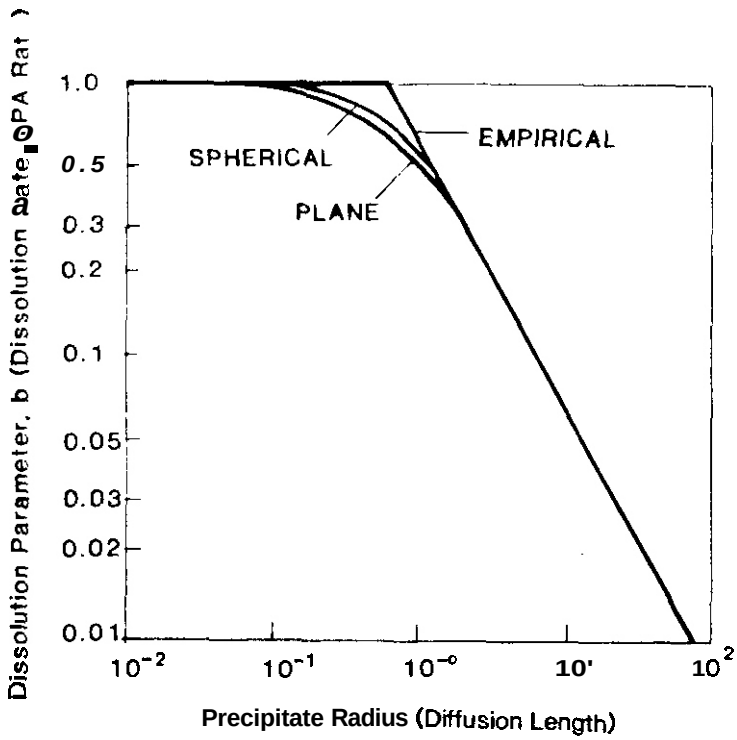

FIGURE 7. Empirical Dissolution Parameter Compared with Dissolution Parameters for Sperical and Plane Precipitates as a Function of Equivalent Radius in Diffusion Lengths.

APPENDIX A: Solution Constants

The constants a,b,c and d in the Neumann series expansion can be solved by using the houndary conditions as well as the recursive relationship. In Table I, solution constants for the zeroth Neumann expansion are given for both planar and spherical geometries.

y_b is the radius (half thickness) of the precipitate. For higher order *Neumann* series expansion, the recursive relationships are given as below.

$$d_{p,n} = 2d_{p,n-1}/(n-1) \qquad (A-1)$$

$$a_{p,n,n} = (a_{p,n-1,n-1} + a_{m,n-1,n-1}/2)/n(n-1) \qquad (A-2)$$

$$b_{p,n,n} = (b_{p,n-1,n-1} + b_{m,n-1,n-1}/2)/n(n-1) \qquad (A-3)$$

$$c_{p,n,n} = c_{p,n-1,n-1}/2n(n-1) \qquad (A-4)$$

$$d_{m,n} = 2d_{m,n-1}/(n-1) \qquad (A-5)$$

$$a_{m,n,n} = a_{m,n-1,n-1}/2n(n-1) \qquad (A-6)$$

$$b_{m,n,n} = b_{m,n-1,n-1}/2n(n-1) \qquad (A-7)$$

$$c_{m,n,n} = (c_{m,n-1,n-1} + c_{p,n-1,n-1}/2)/n(n-1) \qquad \text{(A-8)}$$

for $k < n$

$$a_{p,n,k} = (a_{p,n-1,k-1} + a_{m,n-1,k-1}/2)/k(n-1) + \frac{k+1}{2} a_{p,n,k+1} \qquad \text{(A-9)}$$

$$b_{p,n,k} = (b_{p,n-1,k-1} + b_{m,n-1,k-1}/2)/k(n-1) + \frac{k+1}{2} b_{p,n,k+1} \qquad \text{(A-10)}$$

$$c_{p,n,k} = c_{p,n-1,k-1}/2k(n-1) + \frac{k+1}{2} c_{p,n-1,k-1} \qquad \text{(A-11)}$$

$$a_{m,n,k} = a_{m,n-1,k-1}/2k(n-1) + \frac{k+1}{2} a_{m,n,k+1} \qquad \text{(A-12)}$$

$$b_{m,n,k} = b_{m,n-1,k-1}/2k(n-1) + \frac{k+1}{2} b_{m,n,k+1} \qquad \text{(A-13)}$$

$$c_{m,n,k} = (c_{m,n-1,k-1} + c_{p,n-1,k-1}/2)/k(n-1) + \frac{k+1}{2} a_{m,n,k+1} \qquad \text{(A-14)}$$

TABLE I. Solution Constants for Zeroth Neumann Solution

	Plane Geometry	Spherical Geometry
$a_{p,o,o}$	$0.5e^{-y_b}Q_p$	$0.5(1+y_b)e^{-y_b}Q_m$
$a_{m,o,o}$	$-0.5e^{-y_b}Q$	$-0.5(1+y_b)e^{-y_b}Q_p$
$b_{p,o,o}$	$a_{p,o,o}$	$-a_{p,o,o}$
$b_{m,o,o}$	$a_{m,o,o}$	$-a_{m,o,o}$
$c_{p,o,o}$	$0.5Q_p(e^{-y_b} - e^{y_b})$	$0.5Q_p(1 + y_b)(e^{-y_b} + e^{y_b})$
$c_{m,o,o}$	$0.5Q_m(e^{y_b} - e^{-y_b})$	$-0.5Q_m(1 + y_b)(e^{-y_b} + e^{y_b})$
$d_{p,o}$	Q_p	y_bQ_p
$d_{m,o}$	Q_m	y_bQ_m

Appendix B: Flux in Infinite Medium

For the case of Cascade slowing down in infinite medium, there is no space diffusion term. Therefore we have

$$\Sigma_t(E)\phi(E) = 2\int \Sigma_s(E'\to E)\phi(E')dE' + Q\delta(E-E_o) \qquad (B-1)$$

where the dependence on $\vec{r}$ has been removed. Let us assume consant cross-section and hard sphere scattering, we then have

$$\Sigma_s(E) = \Sigma_t(E) = \Sigma \qquad (B-2)$$

$$\Sigma_s(E'\to E) = \Sigma_s(E')/E' = \Sigma/E' \qquad (B-3)$$

Equation (B-1) can be rewritten as

$$\Sigma\phi(E) = 2\int_E^{E_o} \frac{\Sigma\phi(E')dE'}{dE'} + Q\delta(E-E_o) \qquad (B-4)$$

$$\text{Let } \Sigma\phi(E) = F(E) \qquad (B-5)$$

Again Eq. (B-4) has the new form

$$F(E) = 2\int_E^{E_o} \frac{F(E')}{E'}dE' + Q\delta(E-E_o) \qquad (B-6)$$

Define a new variahle, G(E), as

$$G(E) = F(E) - Q\delta(E-E_o) \qquad (B-7a)$$

i.e.

$$F(E) = G(E) + Q\delta(E-E_o) \qquad (B-7b)$$

Substitute Eq. (B-7b) in Eq. (B-6), we have

$$G(E) = \frac{2Q}{E_o} + \int_E^{E_o} \frac{G(E')}{E'}dE' \qquad (B-8)$$

Equation (B-8) can be simplified by differentiating it with respect to E, we have

$$\frac{dG(E)}{dE} = -\frac{2G(E)}{E} \qquad (B-9)$$

The solution for Eq. (B-9) is

$$G(E) = CE^{-2} \qquad (B-10)$$

by $G(E_o) = 2Q/E_o$, we know

$$C = 2QE_o \qquad (B-11)$$

therefore

$$\Sigma\phi(E) = \frac{2QE_o}{E^2} + Q\delta(E-E_o) \qquad (B-12)$$

$$\phi(E) = \frac{2QE_o}{\Sigma E^2} + \frac{Q}{\Sigma}\delta(E-E_o)$$

Therefore, we know that $\phi(E)$ has a $1/E^2$ dependence for $E<E_o$

The total flux is

$$\phi_T = \int_{E_c}^{E_o} \phi(E)dE = \frac{2QE_o}{\Sigma E_c} - \frac{Q}{\Sigma} \qquad \text{(B-13)}$$

$$\approx \frac{2QE_o}{\Sigma E_c} \quad \text{if } E_o > E_c$$

EXTERNAL DISTRIBUTION

UC-20 (106), 20c (69)

DOE-HQ/Office of Fusion Energy
ER-62
Washington, DC 20545

SE Parket

DOE-HQ/Office of
International Security Affairs
DP-33, Mail Stop 4C-024
Washington, DC 20585

DW Darn

Argonne National Laboratory (3)
9700 South Cass Avenue
Argonne, IL 60439

LR Greenwood, CMT-205
A. Taylor, MST-212
BA Loomis, MST-212

Battelle
Pacific Northwest Laboratory (2)
P.O. Box 999
Richland, WA 99352

JL Brimhall 306W/210
TD Chikalla PSL/1277

Columbia University
School of Engineering & Applied Science
New York, NY 10027

RA Gross

Commission of the European Comnunities
Rue de la Loi 200
E-1049 Bruxelles, Belgium

J. Darvas

Commission of the European Communities
Joint Research Center
Materials Science Division
I-21020 Ispra, Varese, Italia

P. Schiller

Department of the Navy
Naval Research Laboratory (2)
Washington, DC 20375

JA Sprague, Code 6395
LE Steele, Code 6390

Energieonderzoek Centrum Nederland (2)
hetnerlanns Energy Research Foundation
Westerduinweg 3, Postbus 1
NL-1755 ZG, Petten (NH), The Netherlands

B. vanderSchaaf
W. vanWitzenburg, Materials Dept

GA Technologies Inc (3)
P.O. Box 85608
San Diego, CA 92138

JR Gilleland
GR Hopkins
T. Lechtenberg

General Dynamics/Convair
P.O. Box 85377
San Diego, CA 92138

H. Gurol, MZ 92-1072

General Electric
Advanced Nuclear Technology Operation (2)
310 DeGuigne Drive
Sunnyvale, CA 94088

ANTO Library, M/C F-02
S. Vaidyanathan, M/C 5-53

Hahn-Meitner Institut fur Kernforschung Berlin GmbH
Arbeitsgruppe C2
Glienickerstrasse 100
D-1000 Berlin 39, Federal Republic of Germany

H. Wollenberger

Hokkaido University (2)
Facility of Engineering
Kita-hu, Sapporo, 060 Japan

Michio Kiritani, Precision Engineering
Taro Takeyama, Metals Research Institute

Institüt für Festkörperforschung der
Kernforschungsanlage Jülich GmbH
Postfach 1913
D-5170 Jülich 1, Federal Republic of Germany

P. Jung

Japan Atomic Energy Research Institute (2)
Physical Metallurgy Laboratory
Tokai Research Establishment
Tokai-mura, Naka-gun, Ibaraki-ken, 319-11 Japan

Tadao Iwata, Physics
Kensuke Shiraishi, Fuels Materials Research

Kernforschungszentrum Karlsruhe GmbH
Institiit fur Material und Festkorperforschung II
Postfach 3640
D-7500 Karlsruhe 1, Federal Republic of Germany

K. Ehrlich

Kyushu University
Research Institute for Applied Mechanics
6 Kasuga-koen Kasuga-shi,
Fukuoka, 816 Japan

Kazunori Kitajima

EXTERNAL DISTRIBUTION (Cont'd)

Lawrence Livermore National Laboratory (2)
P.O. Box 808
Livermore, CA 94550

MW Guinan, L-396
CM Logan, L-397

Lawrence Livermore National Laboratory
P.O. Box 5511
Livermore, CA 94550

EC Dalder, L-643

Los Alamos National Laboratory
P.O. Box 1663
Los Alamos, NM 87544

DJ Dudziak, S-41F611

Massachusetts Institute of Technology (2)
77 Massachusetts Avenue
Cambridge, MA 02139

I-Wei Chen, 13-5118
NJ Grant, 8-407

Massachusetts Institute of Technology
Nuclear Reactor Laboratory
138 Albany St
Cambridge, MA 02139

OK Harling, NW12-204

Max-Planck-Institut für Plasma Physik
The NET Team, IPP/NET
0-8049 Garching bei München,
Federal Republic of Germany

R. Toschi

McDonnell-Douglas Astronautics Co
P.O. Box 516
St. Louis, MO 63166

JW Davis

Nagoya University
Institute of Plasma Physics
Furo-chyo, Chikusa-ku,
Nagoya, 464 Japan

Taijiro Uchida

National Research Institute for Metals
Tsukuba Laboratories
1-2-1 Sengen, Sakura-mura,
Nihari-gun, Ibaraki, 305 Japan

H. Shiraishi

North Carolina State University
Box 7907
Materials Engineering Department
Raleigh, NC 27695-7907

JR Beeler Jr

Oak Ridge National Laboratory (8)
P.O. BOX X
Oak Ridge, TN 37831

ML Grossbeck
MCG Hall
LK Mansur
PJ Maziasz
NH Packan
M. Roberts
RE Stoller
FW Wiffen

Oak Ridge National Laboratory
P.O. BOX Y
Oak Ridge, TN 37831

LA Berry

Osaka University
2-1 Yamada-oka, Suita,
Osaka, 565 Japan

Kenji Sumita, Nuclear Engineering

Osaka University
8-1 Mihogaoka
Ibaraki, Osaka, 567 Japan

Toichi Okada, Institute of
Scientific & Industrial Research

Pacific Sierra Research Corp
11048 Camino Del Mar
Del Mar, CA 92014

RO Stevenson

Princeton University (2)
Plasma Physics Laooratory
Forrestal Campus
P.O. Box 451
Princeton, NJ 08544

JPF Conrads
Long-poe Ku

Risø National Laboratory
Postfach 49
OK-4000 Roskilde, Denmark

BN Singh

Rockwell International Corp
Rocketdyne Division
6633 Canoga Avenue
Canoga Park, CA 91304

DW Kneff, NA02

EXTERNAL DISTRIBUTION (Cont'd)

Sandia National Laboratories
Livermore, CA 94550

W. Garrison, Div 8314

Science University of Tokyo
Faculty of Engineering
Kagurazaka, Shinjuku-ku,
Tokyo, 162 Japan

RR Hasiguti

Studiecentrum voor Kernenergie
Centre d'Etude de 1'Energie Nucleaire
Boeretang 200
B-2400 Mol, Belgium

J. Nihoul

Swiss Federal Institute
for Reactor Research (2)
CH-5303 Wurenlingen, Switzerland

WV Green
M. Victoria

Tohoku University (2)
Research Institute for Iron,
Steel and Other Metals
2-1-1 Katahira, Sendai, 980 Japan

Katunori Abe
Hideki Matsui

Tokyo Institute of Technology
Research Laboratory for Nuclear Reactors
12-1, 2-chome, O-Okayama
Meguro-ku, Tokyo, 152 Japan

Kazutaka Kawamura

United Kingdom Atomic Energy Authority
Atomic Energy Research Establishment (2)
Oxfordshire OX11 ORA, UK

R. Bullough, Theoretical Physics

United Kingdom Atomic Energy Authority
Culham Laboratory
Applied Physics & Technology Division
Abingdon, Oxfordshire OX14 3DB, UK

GJ Butterworth

University of California (2)
School of Engineering and Applied Science
Boelter Hall
Los Angeles, CA 90024

RW Conn, KL-98
NM Ghoniem, KH-01

University of Michigan
Nuclear Engineering
Ann Arbor, MI 48109

T. Kammash

University of Missouri
Mechanical & Aerospace Engineering
1006 Engineering Bldg
Columbia, MO 65211

M. Jolles

University of Missouri
Dept of Nuclear Engineering
Rolla, MO 65401

A. Kumar

University of Tokyo (3)
3-1. Hongo 7-chome.
Bunkyo-ku, Tokyo, 113 Japan

Naohira Igata, Met & Materials Science
Shiori Ishino, Nuclear Engineering
Shuichi Iwata, Nuclear Engineering

University of Virginia
Dept of Materials Science
Thornton Hall
Charlottesville, VA 22901

WA Jesser

University of Wisconsin
1500 W. Johnson Drive
Madison, WI 53706

WG Wolfer

Westinghouse
Advanced Energy Systems Division
Fuels Materials Technology
P.O. Box 10864
Pittsburgh, PA 15236

A. Boltax, Manager

Westinghouse
Research and Development Center
1310 Beulah Road
Pittsburgh, PA 15235

JA Spitznagel

DOE-RL/AME
Breeder Technology Division
Technology Development & Engineering Branches
FED/210

KR Absher, Chief

INTERNAL DISTRIBUTION

DOE-RL/AME
Breeder Technology Division
Technology Development & Engineering Branches
FED/210

KR Absher, Chief

HEDL *(28)*

SD Atkin	WIA-58	C. Martinez	W/A-58
HR Brager	W/A-58	WN McElroy	W/C-39
LL Carter	W/B-47	EK Opperman	W/A-58
DG Ooran	WIA-57	RW Powell	W/A-58
MJ Korenko	W/C-27	RJ Puigh	WIA-58
FA Garner	W/A-58	FH Ruddy	W/C-39
OS Gelles	W/A-58	FA Schmittroth	W/A-4
R. Gold	W/C-39	WF Sheely	W/C-62
HL Heinisch	WIA-58	RL Simons	WIA-57
DL Johnson	W/A-4	JL Straalsund	WIA-61
GD Johnson	WIA-65	HH Yoshikawa	W/C-44
NE Kenny	W/C-115	Central Files (3)	W/C-110
FM Mann	W/A-4	Documentation Services	W/C-123

*GPO 593 - 083 (1985)